

Synthesis and Characterization of Inorganic Nanomaterials for Applications in Energy Storage and Catalysis

By

Jiří Kulhavý

690991

St Peter's College

A dissertation submitted for the degree of Doctor of Philosophy at the

Inorganic Chemistry Laboratory, Department of Chemistry,

University of Oxford

2022

Synthesis and Characterization of Inorganic Nanomaterials for Applications in Energy Storage and Catalysis

By

Jiří Kulhavý

690991

St Peter's College

Supervisor

Prof. S. C. Edman Tsang

A dissertation submitted for the degree of Doctor of Philosophy at the

Inorganic Chemistry Laboratory, Department of Chemistry,

University of Oxford

2022

DECLARATION

I confirm that this is my own work and the use of all materials from other sources has been properly and fully acknowledged.

Jiří Kulhavý

DEDICATION

To my family, and in particular to my supportive partner Ms. Christine Juliet Hawkins.

Acknowledgements

Firstly, I would like to thank my supervisor Professor Edman Tsang for his guidance and support throughout the course of my DPhil project. I would also like to express my gratitude to Johnson Matthey and the Engineering and Physical Sciences Research Council for providing the funding for this research, without which this project would not have been possible. I would also like to thank to my industrial supervisors Dr James Cookson, Dr James Stevens, Dr Joanna Clark, and in particular Dr Gary Evans from Johnson Matthey. In addition, I would like to thank Oxford University, Johnson Matthey and the Research Complex at Harwell for providing the research equipment and facilities needed in order to complete this research project.

I would like to thank Professor Peter Nellist, Dr Gerardo Martinez Alanis and Dr Colum O'Leary of Oxford Materials department for their collaboration and help with the STEM experiments and Ptychographic analysis of MoS_2 nanosheets, as well as Dr Jianei Zheng, Dr Tianyi Chen and Dr Elizabeth Raine for their assistance with all other STEM and TEM experiments. In addition, I would like to thank Dr Yung Kang Peng for training and assistance with solid-state NMR, and Dr Tatchamapan Yoskamtorn for her detailed training on equipment use and characterisation analysis of BET surface analysis method.

I would like to thank to Dr Ian McPherson for his insights into electrochemistry, and his expertise in setting up synthetic experiments in the laboratory, and Dr Colin Johnson and Dr Philip Holdway of Oxford Materials department for expert XPS data acquisition. In addition, I would like to thank Dr Haohong Duan for training and technical support with maintenance of and running experiments on Gas Chromatography and High-Performance Liquid Chromatography experiments.

I would like to thank Yiyang Li for training and help with the EPR measurements and Dr Simson Wu for help with EXAFS analysis and data fittings. In addition, many thanks go to Dr Chiu Tang and Dr Sarah Day of Beamline I11 laboratory at Diamond Light Source, Harwell, for the beamtimes and their expert help with running samples on and analysing data of High-Resolution Powder XRD experiments, as well as the ability to use the in house preparatory laboratory and electrochemical setup for battery testing.

I would like to express my sincere gratitude to Dr Tugce Ayvali for her help with XPS analysis and with technical aspects running various laboratory characterisation techniques, and in particular for her incredible scientific and personal support throughout the length of this project.

I would like to thank all other members of the Tsang group, both past and present, for their discussions, support, and scientific enlightenment throughout my time in the group, namely, I would like to thank Dr Hannah Kriessl, Dr Ieuan Ellis, Dr Tim Sudmeier, Dr Josh Fellowes, Dr Jiaying Mo, Dr Pu Zhao, Dr Wei-Che Lin, Dr Benedict Tsz Lo, Dr Kirsty Purchase, Dr Ivo Teixeira, Dr Eduardo Barbosa, William Vickery, Christopher Foo and Baron Ho for discussion and friendship throughout the course of this project. I would also like to thank all those in Oxford University Dancesport Club and Salsa Society who have ensured my free time has been busy, entertaining and unforgettable.

A very special thanks goes to Christine Hawkins, who spent many hours attempting to understand project background in order to help with proofreading and grammatical correctness. Finally, and perhaps most importantly, I would like to thank my family for their continual support, motivation and encouragement, without which it would not have been possible for me to complete this project.

Synthesis and Characterization of Inorganic Nanomaterials for Applications in Energy Storage and Catalysis

A thesis submitted for the degree of Doctor of Philosophy

Jiří Kulhavý, St Peter's College, 2022

Abstract

Inorganic nanomaterials are defined as materials with one or more dimension within 1 – 100 nm range. These materials possess unique optical, electronic, thermo-physical, physicochemical and mechanical properties, and represent intensively explored, studied and sought-after commodities for a large variety of applications and manufacturing processes. Heterogeneous catalysts are vital for many industrial processes and often take advantage of the unique reactivity properties of nanomaterials, while battery electrode materials composed of nanomaterials are explored to solve current limitations with higher power densities via stable rapid ion and electron transport, and with high energy density via maximization of the charge storage capability. This thesis provides an insight into synthetic methods, detailed characterization and properties study, and exemplary applications of engineered 2D MoS_2 nanomaterials in Li and Na ion batteries, palladium nanoparticles supported on 2D MoS_2 nanosheets as heterogeneous catalysts in Suzuki and Heck C-C coupling and 1-pentyne hydrogenation reactions and sulphate functionalized titanium oxide nanoparticles as solid superacid catalysts in the esterification reaction of levulinic acid and pyruvaldehyde Cannizzaro reactions.

Keywords: Heterogeneous catalyst, Li-ion Batteries, 2D MoS_2 nanomaterials, nanoparticles, solid acids, Organic coupling reaction, Alkyne hydrogenation, Pd on support catalysis, Esterification reaction.

Table of Contents

Acknowledgements....4

Abstract....6

Table of Contents....7

Chapter 1 Introduction....23

1.1 Nanomaterials and nanotechnology....23

1.2 Inorganic nanoparticles....26

1.2.1 Inorganic nanoparticles in heterogeneous catalysis....28

1.2.2 Inorganic nanostructures in battery applications....30

1.3 Titania nanoparticles....31

1.3.1 Properties of Titania....32

1.3.2 Sulphated titania as solid acid catalysts....33

1.3.3 Solid Acid Characterisation....35

1.3.3.1 NMR as a powerful characterisation tool for solid acids....37

1.4 Palladium nanoparticles....40

1.4.1 Palladium chemistry....40

1.4.2 Palladium nanoparticle synthesis....43

1.4.3 Palladium nanoparticles as catalysts in organic synthesis....44

1.4.3.1 Palladium and cross-coupling reactions....45

1.4.3.2 Palladium and hydrogenation reactions....47

1.5 Two-dimensional nanomaterials in lithium-ion batteries 51

1.5.1 Global climate change and societal need for energy solutions 51

1.5.2 Lithium-ion batteries 53

1.5.3 Advantages and drawbacks of using lithium-ion batteries 54

1.5.4 Selection of anode materials for lithium-ion batteries 58

1.5.5 Li-ion battery aging mechanisms 59

1.5.6 Molybdenum disulphide as an alternative to graphite/graphene 63

1.6 The Objective of the Thesis 68

Chapter 2 Analytical techniques 71

2.1 Introduction 71

2.2 Powder x-ray diffraction 72

2.3 Transmission electron microscopy 74

2.4 Scanning transmission electron microscopy and ptychography 77

2.5 X-ray photoelectron spectroscopy 79

2.6 Energy-dispersive x-ray spectroscopy 81

2.7 Magic angle spinning nuclear magnetic resonance 82

2.8 Trimethylphosphine (TMP) adsorbed probe for ^{13}P MAS NMR 83

2.9 Electron paramagnetic resonance 84

2.10 Inductive coupled plasma-atomic emission spectroscopy (ICP-AES) 86

2.11 Raman spectroscopy 87

2.12 Thermogravimetric analysis (TGA) 88

2.13 Bet isotherm - surface area measurement 88

2.14 Temperature programmed reduction (TPR) 89

2.15 Gas chromatography-mass spectrometry (GC-MS) 90

2.16 Electrochemical cycling 91

Chapter 3 Experimental Methods 94

3.1 Liquid exfoliation of MoS_2 via n-butyllithium intercalation 94

3.2 Liquid exfoliation of MoS_2 via physical exfoliation with help of hydrazine decomposition 95

3.3 Tetrabutylammonium (TBA) functionalisation of exfoliated MoS_2 95

3.4 Palladium deposition on exfoliated MoS_2 96

3.5 Silicon deposition on exfoliated MoS_2 96

3.6 Tin deposition on exfoliated MoS_2 97

3.7 Heat reduction of doped MoS_2 nanosheets 97

3.8 Electrode preparation for Li-ion battery testing 98

3.9 Electrochemical cycling 98

3.10 Suzuki coupling reaction 99

3.11 Heck coupling reaction 99

3.12 Vapour-phase hydrogenation of 1-pentyne 100

3.13 Synthesis of titania anatase nanoparticles 100

3.14 Functionalization of solid acid catalysts with sulphuric acid 101

3.15 Cannizzaro reaction of pyruvaldehyde to lactic acid 102

3.16 Esterification reaction of levulinic acid to ethyl levulinate 102

3.17 Continuous-wave electron paramagnetic resonance 103

3.18 Powder X-ray diffraction (XRD) 103

3.19 Trimethylphosphine (TMP) / trimethylphosphine oxide (TMPO) adsorbed sample for ^{31}P MAS NMR 104

3.20 NMR spectrum deconvolution 105

3.21 High-angle annular dark field scanning transition electron microscopy (HAADF-STEM.) 106

3.22 Electron ptychographic phase imaging 106

3.23 Gas chromatography mass spectrometry 107

3.24 High performance liquid chromatography (HPLC) 107

3.25 Brunauer-Emmett-Teller (BET) surface analysis 108

3.26 X-ray photoelectron spectroscopy 108

3.27 Transmission electron microscopy (TEM) with energy-dispersive x-ray spectroscopy (EDX) 108

3.28 Temperature programmed reduction (TPR) 109

3.29 Thermogravimetric analysis (TGA) 109

3.30 Inductive coupled plasma – atomic emission spectroscopy 110

3.31 Raman spectroscopy 110

Chapter 4 Functionalised anatase titania nanoparticles as a highly efficient solid acid catalyst…….....111

4.1 Introduction.....111

4.2 Results and discussion.....114

4.2.1 Sulphated P25 TiO_2 Nanoparticles as Solid Acid Catalysts 115

4.2.2 Preparation, Characterisation and Catalytic Testing of High Surface Area Anatase Titania Nanostructures.....120

4.2.2.1 Morphological, Structural and Physicochemical Properties 121

4.2.2.2 Investigation of Acidic Properties of Sulphated Titania Nanoparticles....135

4.2.2.3 Catalytic Testing.....143

4.3 Conclusion 150

Chapter 5 Pd-doped 1T-Phase Single Layer Molybdenum Disulphide Nanosheets and Their Catalytic Activity in Organic Reactions 155

5.1 Introduction.....155

5.2 Results and discussion.....162

5.2.1 Structural and Morphological Characterisation of the Catalysts 164

5.2.2 Catalytic Activity of Pd-doped MoS_2 Samples 182

5.2.2.1 Pd-doped MoS2 as Catalysts for Coupling Reactions.....182

5.2.2.2 Pd-doped MoS_2 as Highly Selective Catalysts in 1-Pentyne Hydrogenation……..196

5.3 Conclusion 201

5.4 Future Outlook 204

Chapter 6 Molybdenum disulfide nanosheets for high performance energy storage.....205

6.1 Introduction.....205

6.2 Results and discussion.....210

6.2.1 Structural Characterisation of as-prepared MoS_2 Nanosheets 211

6.2.2 Performance of MoS_2 Nanosheets as Anode Materials for Lithium-Ion Batteries… 221

6.2.3 Impact of calender press on the electrochemical performance of single-layer MoS_2 electrodes in Lithium-Ion Batteries 232

6.2.4 Performance of MoS_2 Nanosheets as Anode Materials for Sodium-Ion Batteries… 234

6.2.5 Tin-doped MoS_2 Nanocomposite as Anode Materials for Lithium-Ion Batteries….. 240

6.3 Conclusion 250

6.4 Future Outlook 255

General Conclusions 257

Future perspectives 260

References 261

Appendix 293

List of Figures

Figure 1.1 Synthetic strategies and engineering techniques used in nanotechnology.....25

Figure 1.2 Structure of the anatase TiO_2 polymorph.....33

Figure 1.3 Possible reaction mechanisms of palladium nanoparticles.....45

Figure 1.4 General Mechanism of Cross-Coupling Reactions.....46

Figure 1.5 Synthesis of palladium core and silver shell nanoparticles and their role in selective hydrogenation of alkynes in comparison to pure palladium nanoparticles.....50

Figure 1.6 Ragone plot for different energy storage technologies 52

Figure 1.7 Schematic representation of the functional principle of a lithium-ion battery 54

Figure 1.8 Degradation mechanisms in Li-ion cells 60

Figure 1.9 Changes and degradation processes at the anode/electrolyte interface 61

Figure 1.10 Representative discharge profiles from the first cycle of MoS_2 as active electrode material relative to Li^+/Li calculated from DFT energies by C. George et.al.....66

Figure 2.1 Schematic representation of the Bragg equation 72

Figure 2.2 BrukerD8 Advance Eco diffractometer in Inorganic Chemistry Laboratory building (Department of Chemistry, University of Oxford). 74

Figure 2.3 The structure and cross-section of a typical TEM.....76

Figure 2.4 Left: JEOL 3000F Field Emission Electron Microscope. Right: JEOL ARM200F Aberration-corrected high-resolution (scanning) transmission electron microscope. Both microscopes belong to the David Cockayne Centre for Electron Microscopy (Department of Materials, University of Oxford). 77

Figure 2.5 Schematic diagram of a typical STEM ptychography experimental set-up.....79

Figure 2.6 Schematic diagram of photoelectron emission stimulated by x-ray absorption ...80

Figure 2.7 Thermo Scientific K-Alfa XPS instrument equipped with a microfocused monochromated Al X-ray source in Oxford Materials Characterization Service centre (Begbroke Science Park, University of Oxford). 81

Figure 2.8 The Bruker AVIII 400 (solid state) NMR spectrometer in Chemistry Research Laboratory building (Department of Chemistry, University of Oxford). 83

Figure 2.9 TMP molecules targeting Lewis and Brønsted acid sites on sulphated TiO_2 catalyst 84

Figure 2.10 Schematic diagram of energy splitting of unpaired electron with stimulation of external magnetic field 85

Figure 2.11 The X-band CW EPR spectrometer in Inorganic Chemistry Laboratory building (Department of Chemistry, University of Oxford). 86

Figure 2.12 Micromeritics Tristar II Plus BET instrument at Surface Analysis Facility (Department of Chemistry, University of Oxford) 89

Figure 2.13 7890B Agilent Gas Chromatography System in Wolfson Catalysis Laboratory (Department of Chemistry, University of Oxford). 91

Figure 2.14 Constant Current (CC) and Constant Voltage (CV) control of the battery charging with voltage and current response 92

Figure 3.1 The system setup for TMP/TMPO adsorption on the surface of a solid acid catalyst. 105

Figure 4.1 Diffraction patterns of P25 TiO_2 and sulphated P25 TiO_2 showing impact of calcination temperature on crystallinity of the nanoparticles. Symbol A depicts anatase phase while symbol R shows pattern of the rutile phase at the corresponding facets. 116

Figure 4.2 Infra-red spectra of P25 TiO_2 and sulphated P25 TiO_2 calcined at different temperatures. 118

Figure 4.3 Sulphated P25 TiO_2 solid acid catalyst activity in esterification reaction of levulinic acid in ethanol and compared to commercial solid Brønsted acid catalyst Amberlyst-15...120
Figure 4.4 Diffraction patterns of a) as-prepared and b) sulphated TiO_2 anatase nanoparticles and impact of calcination on their crystal structure. 122
Figure 4.5 Raman spectra of a) as-prepared and b) sulphated TiO_2 anatase nanoparticles and impact of calcination on their crystal structure. 124
Figure 4.6 TEM images of sulphated TiO_2 anatase nanoparticles a-b) before c-d) after calcination at 450 ^oC 126
Figure 4.7 FT-IR spectra of TiO_2 nanoparticles and sulphate functionalised TiO_2 nanoparticles calcined at different temperatures.....127
Figure 4.8 TGA weight loss analysis of sulphated TiO_2 solid acids. 128
Figure 4.9 Illustration of the effect of interparticle forces, calcination and sonication on the particle size and distribution. 135
Figure 4.10 Deconvoluted ^{31}P NMR spectra of TMP probe molecules adsorbed on acid sites of both sulphated and non-sulphated TiO_2 nanoparticles and P25 TiO_2.....137
Figure 4.11 Deconvoluted ^{31}P NMR spectra of TMPO probe molecules adsorbed on TiO_2 nanoparticles 142
Figure 4.12 Sulphated TiO_2 nanoparticles solid acid catalyst activity in esterification reaction of levulinic acid in ethanol and compared to commercial solid Brønsted acid catalyst Amberlyst-15.....145
Figure 4.13 Rate of conversion of levulinic acid into ethyl levulinate as a matter of time using sulphated TiO_2 and commercial Amberlyst-15 solid acid catalysts.....146
Figure 4.14 Recyclability of the sulphated TiO_2 and commercial Amberlyst-15 solid acid catalysts in esterification reaction of levulinic acid in ethanol at 70 ^oC for 5 hours. 147

Figure 4.15 Probing Lewis acidity of the TiO_2 catalysts in a Lewis acid catalysed reaction of pyruvaldehyde to lactic acid 150
Figure 5.1 AC-TEM and DFTEM images of single-layer MoS_2 nanosheets. 165
Figure 5.2 Bright-field (top) and Dark-field (bottom) STEM images of restacked single-layer MoS_2 nanosheets. 166
Figure 5.3 STEM imaging and analysis of single Pd atom sites on the surface of single layer MoS_2 nanosheets 167
Figure 5.4 STEM images coupled with EDX analysis of Pd single atoms and nanoparticle sites on the surface of single-layer MoS_2 nanosheets calcined at 300°C under 5% H_2/Ar 168
Figure 5.5 Raman spectra shows phase retainment of Pd-doped bulk and single-layer MoS_2 upon heating. 171
Figure 5.6 PXRD patterns as-prepared and calcined Pd-doped bulk MoS_2 samples. 174
Figure 5.7 PXRD patterns as-prepared and calcined Pd-doped single-layer MoS_2 samples. 174
Figure 5.8 EPR spectra of Pd-doped MoS_2 nanosheet and Pd-doped bulk analogue materials. 176
Figure 5.9 Mo 3d and S 1s and 2p regions of XPS spectra of bulk and single-layer MoS_2. ...179
Figure 5.10 Pd 3d region of XPS spectra of as-prepared uncalcined Pd-doped bulk and single-layer MoS_2. 180
Figure 5.11 Pd 3d region of XPS spectra of 300°C calcined Pd-doped bulk and single-layer MoS_2. 181
Figure 5.12 Conversion and selectivity of Pd-doped MoS_2 and commercial Pd/C catalysts in the Heck coupling reaction of styrene and iodobenzene 192
Figure 5.13 Heck coupling reaction mechanism over Palladium nanoparticle catalyst. 195
Figure 5.14 Suzuki coupling reaction mechanism over Palladium nanoparticle catalyst. 195

Figure 5.15 Schematic diagram of hydrogenation mechanism of 1-pentyne using supported Pd heterogeneous catalyst. 198

Figure 6.1 XRD diffractogram showing crystalline arrangement pattern in different MoS_2 samples. 212

Figure 6.2 TEM images of a) bulk, b) few-layers and c) single-layer MoS_2 nanosheets. 213

Figure 6.3 Raman spectra showing different phases present in MoS_2 samples. 215

Figure 6.4 Mo 3d and S 1s and 2p regions of XPS spectra of bulk and single-layer MoS_2. ...217

Figure 6.5 EPR analysis of MoS_2 nanosheet and bulk materials. 218

Figure 6.6 SEM coupled with EDX images showing freshly prepared calendered electrodes a) bulk, b) few-layer, and c) single-layer MoS_2 active materials.....220

Figure 6.7 Galvanostatic rate performance of bulk, few-layer, and single-layer MoS_2 negative electrodes in Li-ion cells. Each electrode was cycled 5 times at applied currents of 50, 100, 200, 400 and again at 50 mA/g. 221

Figure 6.8 Voltage vs capacity curves of first three charge-discharge cycles at 50 mA/g current applied to bulk, few-layer, and single-layer MoS_2 electrodes. 224

Figure 6.9 Voltage vs capacity curves of each fifth cycle at different applied currents. These curves show retention of capacity and indicate lithium storage mechanism in each active material. 226

Figure 6.10 In-situ monitoring lithiation of MoS_2 active material during the first discharge cycle at 100 mA/g current.....227

Figure 6.11 ADF C_s-STEM coupled with EELS analysis shows large lithium content in lithiated single-layer MoS_2. 229

Figure 6.12 Ptychographic analysis performed on ADF C_s-STEM images of lithiated single-layer MoS_2.....230

Figure 6.13 The effect of loading and calender press onto the performance of single-layer MoS_2 negative electrodes. Galvanostatic rate performance of electrodes made of three different castings of the same single-layer MoS_2 ink. Thickness and loading of each electrode is denoted in the legend of the graph. Each electrode was cycled 5 times at applied currents of 50, 100, 200, 400 and again at 50 mA/g. 233

Figure 6.14 Galvanostatic rate performance of bulk, few-layer, and single-layer MoS_2 negative electrodes in Na-ion cells. Each electrode was cycled 5 times at applied currents of 50, 100, 200, 400 and again at 50 mA/g. 235

Figure 6.15 Voltage vs capacity curves of first three charge-discharge cycles at 50 mA/g current applied to bulk, few-layer, and single-layer MoS_2 electrodes in Na-ion cells. 238

Figure 6.16 Voltage vs capacity curves of each fifth cycle at different applied currents. These curves show retention of capacity and indicate lithium storage mechanism in each MoS_2 active material in Na-ion cells. 239

Figure 6.17 Temperature-programmed reduction (TPR) of Sn doped single-layer MoS_2. 241

Figure 6.18 XRD patterns as-prepared and calcined Sn doped single-layer MoS_2 samples. . 243

Figure 6.19 Raman spectra showing Sn-doped and undoped single-layer MoS_2 samples. ... 245

Figure 6.20 Sn 3d region of XPS spectra of Sn-doped single-layer MoS_2 samples. 245

Figure 6.21 STEM images and illustration of preferred stable sites of Sn single atoms on single-layer MoS_2 basal planes. Line profiles confirm the location and presence of Sn single-atom sites. 247

Figure 6.22 Galvanostatic rate performance of Sn-doped single-layer MoS_2 negative electrodes in Li-ion cells. Each electrode was cycled 5 times at applied currents of 50, 100, 200, 400 and again at 50 mA/g. 249

Figure 6.23 Voltage vs capacity curves of the first three charge-discharge cycles at 50 mA/g current applied to Sn-doped single-layer MoS_2 electrodes in Li-ion cells.....250

List of Tables

Table 4.1 World annual production of selected mineral acids published in 2014 by U.S. Environmental Protection Agency. 113

Table 4.2 BET analysis of sulphated TiO_2 anatase nanoparticles shows the impact of calcination temperature on surface area of the anatase nanoparticles..... 125

Table 4.3 TGA weight loss analysis of sulphated TiO_2 solid acids..... 129

Table 4.4 Summary of XPS peak fitting of the Ti 2p region for P25 TiO_2 and TiO_2 anatase nanoparticles. Each individual peak fitting can be found in the appendix..... 130

Table 4.5 Summary of XPS peak fitting of the O 1s region for P25 TiO_2 and TiO_2 anatase nanoparticles. Each individual peak fitting can be found in the appendix. The relative concentration of individual oxygen species is given in parenthesis..... 132

Table 4.6 Summary of XPS peak fitting of the S 2p region for sulphated P25 TiO_2 and TiO_2 anatase nanoparticles. Each individual peak fitting can be found in the appendix. 133

Table 4.7 XPS elemental analysis of sulphate content 134

Table 4.8 Summary of deconvoluted TMP ^{31}P NMR peak positions. Peaks were ascribed to relevant acid sites and chemical shift of these is related to their acidity strength..... 136

Table 4.9 Summary of deconvoluted TMP ^{31}P NMR peak integrated area, representing the amount of TMP adsorbed on each acid site and therefore the number of acid sites. 140

Table 4.10 Summary of deconvoluted TMPO ^{31}P NMR peak positions. Peaks were ascribed to relevant acid sites and chemical shift of these is related to their acidity strength..... 143

Table 4.11 Summary of deconvoluted TMPO ^{31}P NMR peak integrated area, representing the amount of TMPO adsorbed on each acid site and therefore the number of acid sites..... 143

Table 5.1 EPR analysis shows the effect of Pd doping on the electron delocalized charge on the surface of MoS_2. 177

Table 5.2 Activity of Pd-doped MoS_2 and commercial Pd/C catalysts (10 mg catalyst) in Suzuki coupling reaction of alkyl benzene derivatives (1 mmol) with phenylboronic acid (1.2 mmol) in isopropanol water (7:3) solvent mixture using K_2CO_3 (2.5 mmol) as a base at 60^oC after 1 hour of reaction time. 186

Table 5.3 Pd-doped MoS_2 catalyst stability and recyclability in Suzuki coupling reaction of iodobenzene (1 mmol) with phenylboronic acid (1.2 mmol) in isopropanol : water (7:3) solvent mixture over Pd-doped MoS_2 catalysts (10 mg) using K_2CO_3 (2.5 mmol) as a base.....187

Table 5.4 % Yield, TON and TOF of biphenyl in the Suzuki coupling reaction in different solvents using Pd-doped MoS_2 catalyst, compared to the commercial Pd/C catalyst 190

Table 5.5 Pd-doped MoS_2 catalyst stability and recyclability in Heck coupling reaction. 193

Table 5.6 Turnover number (TON) calculated from the yield given in Table 5.5 193

Table 5.7 Turnover frequency (TOF) calculated from the yield and turnover number in Tables 5.5 and 5.6. 194

Table 5.8 % Yields of 1-pentyne hydrogenation products at 25°C (top) and 75°C (bottom), including turnover frequency for partial and full hydrogenation of 1-pentyne.....200

Table 6.1 Comparison of BET surface area with EPR analysis of unpaired electrons in MoS_2 samples. 219

Table 6.2 Performance comparison of MoS_2 samples tested in this work with some of the best performing MoS_2 electrode materials in Li-ion batteries recently published in literature...254

Table 6.3 Performance comparison of MoS_2 samples tested in this work with some of the best performing MoS_2 electrode materials in Na-ion batteries recently published in literature. 255

List of Schemes

Scheme 4.1 Brønsted acid catalysed esterification reaction mechanism of levulinic acid with ethanol. 119

Scheme 4.2 Illustration for the interaction of TMP molecule with different acidic sites on bare and sulphated titania. 138

Scheme 4.3 Schematic illustration of bridging and corner attached sulphates on the surface of TiO_2 nanoparticles. Arrows indicate the withdrawing electron effect that the sulphate group has on the Ti and consequently on the acidic proton. 139

Scheme 5.1 Illustration of the top-down physical and chemical exfoliation sonochemical synthesis of few-layer and single-layer MoS_2 nanosheets from their bulk analogue 162

Scheme 5.2 Schematic diagram of Suzuki coupling reaction of iodo- or chloro-benzene derivatives with phenylboronic acid to yield biphenyl adducts 183

Scheme 5.3 Schematic diagram of Heck coupling reaction of iodobenzene with styrene over supported palladium heterogeneous catalyst to yield E- and Z-stilbene. 191

Scheme 5.4 Illustration of partial hydrogenation of alkynes to alkenes over Palladium nanoparticle catalyst. 197

Scheme 6.1 Illustration of the top-down physical and chemical exfoliation sonochemical synthesis of few-layer and single-layer MoS_2 nanosheets from their bulk analogue 211

Chapter 1 Introduction

1.1 Nanomaterials and nanotechnology

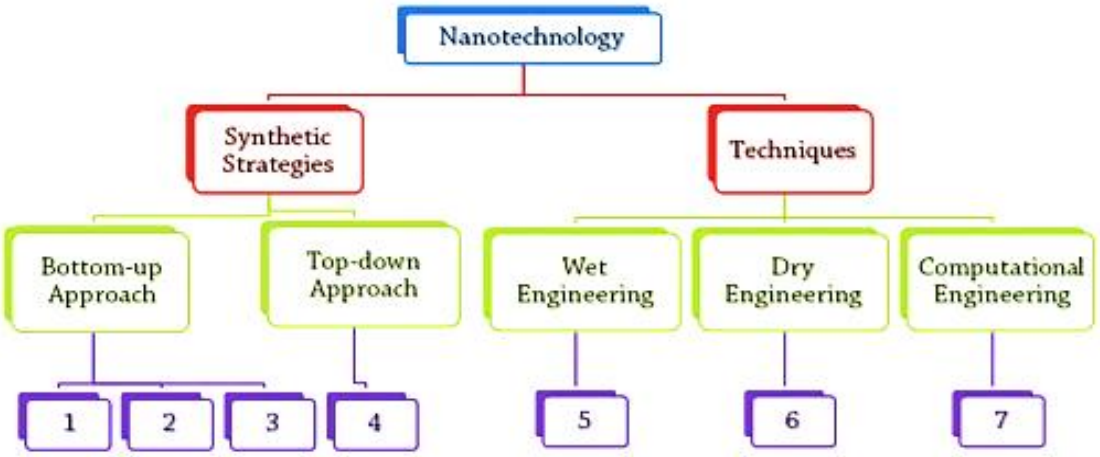
Nanomaterials are materials with at least one dimension in the nanoscale. The International Organization for Standardization defines nanomaterials as materials with any external dimension in the nanoscale region, of the length range approximately from 1 nm to 100 nm, or having internal structure or surface structure in the nanoscale. In the present world nanomaterials are rapidly becoming commercialized and beginning to emerge as new exciting commodities.[1,2] Applications include thin films or surface coatings, such as on computer chips, or as nanostructures for catalysis and energy storage applications.[3] By using nanostructures, products may be enhanced to include new physical and chemical properties.[4] The small structure of nanomaterials means that they have a greater relative surface area than other materials and this can improve properties such as strength and electrical characteristics or reactivity. These changes in physicochemical properties are connected to the number of atoms or molecules forming the material.[5] If only one dimension is restricted, a layered shape or a 2D material will be obtained.

Nanotechnology is a branch of research within the field of engineering of new materials, with a focus on the nanoscale level. There are multiple synthesising techniques and approaches for the production of nanomaterials and nanostructures, though in general they can be categorised into two groups.[6–11] Figure 1.1 shows a summary of the major synthesis strategies and techniques used within the field of nanotechnology.[12]

(a) The bottom-up approach involves the minituarisation of material components down to atomic level, to allow subsequent formation of nanostructures by self-assembly processes. These self-assembly processes are governed by physical forces in operation

at the nanoscale, which combine the basic atomic units into larger stable structures. This approach organises the basic components in hierarchical nanocomplexes. Examples of this are hydrothermal synthesis of nanoparticles or nanosheets, or nanoparticles formed from colloidal dispersion, and the sol-gel method.

(b) The top-down approach involves starting with macroscopic structures, and externally controlling the forces which govern nanostructure formation. This approach consists of adding or removing thin layers of bulk materials. Example methods includes exfolation of layer materials, ball milling, and mask etching, amongst others.



1	2	3	4
Physical *(Gas solid transformation)*	**Chemical** *(Liquid solid transformation)*	**Biological** *(Bioreduction)*	1. Bulk nanomachining 2. Fragmentation: Nanomilling, spark erosion, etc. 3. Lithography (Optical, ultraviolet, X-ray, electron beam, laser, etc.)
1. CVD and PVD 2. MBE 3. PLD 4. ALD 5. Ion-implantation 6. Spray pyrolysis	1. Co-precipitation 2. Sol-gel 3. Chemical reduction 4. Sono- and photochemical 5. Electrochemical 6. Microemulsion 7. Solvo-thermal (hydrothermal) 8. Template/surface derived method	1. By plants 2. By bacteria 3. By fungi 4. By yeast 5. By algae 6. By biomolecules 7. By agricultural and industrial wastes	

5	6	7
1. Biomimetic and tissue nanotechnology 2. Bioimaging, biosensing and bioanalytics 3. Nanodiagnostics 4. Nanotherapy 5. Pharmaceuticals 6. Cosmetics 7. Environment harvesting and remediation	1. Information processing, storage and transmission 2. Electronics, optoelectronics and photonics 3. Sensors, MEMs and energy devices 4. Food packaging and storage 5. Pigments, protective glasses, textiles	1. Ab-initio and semi empirical: a. Quantum or molecular mechanics b. Quantum or molecular dynamics of: *i. Nanostructures and interfaces* *ii. Assembly and growth* *iii. Biointeractions* 2. Optimisation and predictability

Figure 1.1 Synthetic strategies and engineering techniques used in nanotechnology; table reproduced from reference.[12]

1.2 Inorganic nanoparticles

Research focuses on nanoparticles as either agents of change of various phenomena and processes, or as basic units, or building blocks, of materials and devices with characteristics tailored to specific applications. Nanoparticles have many properties that can be advantageous for new materials due to characteristics specific to the nanoscale: confinement effects, larger surface to volume ratio, interactions at length scales where wave phenomena are comparable in features to the structural features, with the possibility to create new atomic and macromolecular structures.[7,9–11] The manufacture of nanoparticles is intrinsic to the nanotechnology field, where the aim is to realise properties specific to the nanoparticle, nanocrystal or nanolayer level, as assembly of precursor particles and related structures is the main route to forming nanostructured materials. Important applications that take advantage of the nanoscale-specific properties are the environment, biological systems, functional nanostructures, coatings and dispersions, and consolidated materials.[13]

There are three types of effects of which the manufacturing processes for nanoparticles, nanocrystal, and nanolayers take advantage and these are:[14]

(a) Scaling down of size can cause new physical, chemical, or biological properties. Smaller particle size defines a larger surface and interfacial area, increased numbers of molecules on particle interfaces, increased surface tension forces, quantum electromagnetic interactions, and size confinement effects (including electronic, optic, confined crystallisation and flow structures). Shape and volume variations on the nanoscale affect the wavelike properties of electrons inside matter. Quantum effects become significant within organised structures under 50 nm, with effects exhibited even at room temperature when the scale reduces below 10 nm.

(b) Reducing the size to these scales has another way of bringing about new phenomena – the size of the particle, crystal, or microstructure grain becomes comparable to the interaction length scales of physical, chemical and biological phenomena (such as the magnetic, laser, photonic, and heat radiation wavelengths). New phenomena can manifest in unusual optoelectronic and magnetic properties of nanostructured materials, placing artificial components inside biological cells, and suspension colour dependence on particle size.

(c) Particulate systems introduce a significant increase in degree of complexity and speed of processes. Time scales are altered due to smaller distances and an increased spectrum of forces with intrinsically short time scales (magnetic, electrostatic, electrophoresis, radiation pressure, amongst others).

There are multiple routes for the generation of new atomic, molecular and macromolecular structures of materials: chemistry, where the focus is on chemical self-assembly and three-dimensional macromolecular structures; nanofabrication, which focuses on manipulation of three-dimensional structures and fabricating nanostructures on their surfaces; and biotechnology, which concentrates on methods such as the evolutionary approach, bio-templating, and three-dimensional molecular folding.

New phenomena and properties of the nanoscale are yet to be fully understood, with much room for research into the resulting structures to be effectively controlled and manipulated for tailored applications. Only a small part of the novel properties that arise due to the small structure size and short time scales (mechanical, optical, electric, magnetic, thermal, chemical, and biological), when compared to the bulk material, have been fully identified and quantified.[3]

1.2.1 Inorganic nanoparticles in heterogeneous catalysis

There is rapidly growing requirement for environmental pollution control and heterogeneous catalysis is thought to be the key solution to this problem. Heterogeneous catalysis is defined as a catalysed chemical reaction or process where the phase of the catalyst differs from the phase of the reactants or products. Solid-state heterogeneous catalysts successfully employed in industrial processes are used mainly within hydrogenation reactions. Although heterogeneous catalysts are utilized in some industrial large-scale chemical processes, typically within petrochemical applications, most chemicals manufacturing processes (fine, speciality, pharmaceutical, etc.) still prefer the use of homogeneous reagents and catalysts. Most of the processes using homogeneous catalysts were developed over the past 100 years with the aim of increasing product yield, with little or no interest in reducing environmental impact of inorganic waste and toxic by-products formed during the reaction. The majority of waste is produced during the separation stage, when a water quench and neutralisation process generates large volumes of hazardous waste.[15,16] There are many associated costs for processes still using homogeneous catalysts such as waste disposal, environmental, and societal, in the form of an increasingly hostile public opinion towards chemical waste.[17,18]

Heterogeneous catalysts, especially in the form of solid-state catalysts, and reagents in either liquid or gas phase go a long way to achieve these goals. However, there are many requirements of these catalysts. They need to be competitive in their catalytic activity and their active sites also need to possess similar selectivity to that of homogeneous catalysts. Another critical factor for the solid-state heterogeneous catalysts to be attractive for industrial use is whether and how many times over they can be reused, which is dictated by their chemical stability, and reproducibility of their active sites within the frame of economical

viability.[19,20] Heterogeneously catalysed reactions further benefit from greater ease and efficiency of product isolation, as well as the ability to run under milder conditions with higher selectivity. The efficiency factor of reaction is increased by the stability of a single acid site during the reaction time. The employment of a heterogeneous catalyst can further simplify the catalytic process by removing unnecessary steps such as neutralisation, or extraction of the active catalytic species that are required for homogeneous catalysts. The lifetime of materials is another critical factor for employment of solid-state catalysts as the overall cost can be reduced by easy recycling of solid-state catalysts, and by a significant reduction of waste volume. There are several types of heterogeneous catalysts that have been designed and tailored to specific reactions, but their use is limited due to their structure: polymer-supported catalysts have been used in research and within process chemistry, although their polymeric structure is easily altered by thermal and chemical exposure; zeolites on the other hand have been successfully used in catalysing vapour phase chemistry, thanks in part to their excellent thermal and chemical stability, however, their small zeolitic pore size limits their use to very small molecules, and where liquid-phase reactions are restricted to diffusion control.[21–27] These limitations can be by-passed by engineering high surface area inorganic nanoparticles, either by creating unsaturated highly reactive sites on their surface, or by introducing large number of stable functional groups on their surface. All chemical reactions take place on the nanoparticle surface, therefore pore size and diffusion restrictions of zeolites can be circumvented, while relatively high thermal and chemical stability of the nanoparticles surpass the limitations of polymeric systems.[28–30]

1.2.2 Inorganic nanostructures in battery applications

Batteries have emerged as an essential energy storage system for renewable energy applications for future generations. Large-scale battery-based energy storage systems are paving the way to more practical and efficient utilisation of the intermittent availability of renewable energy sources such as solar, thermal, wind and water, subjected to irregular alternations throughout a short-term as well as longer term periods of time.[31,32] Li-ion batteries became the dominant power in the current energy storage market as they represent the most mature, advanced and efficient rechargeable technology, that revolutionized portable electronic devices.[31,33] However, rechargeable Li-ion batteries lack in rapid and efficient charging abilities leading to quick degradation of the electrode material and undesirable chemical reactions within the electrochemical system, particularly when high volumetric currents of fast charging and discharging are used.[31,34–38]

One of the main drawbacks limiting fast charging and causing irreversible degradation is linked to restricted movement of ions and electrons within the limited lattice space of the bulk electrode material resulting in a lot of strain at the entry points and slowing charge-discharge capabilities and overall energy storage capacity of the system.[32,36,39] The rate performance is further hindered by inefficient electronic conductivity of the electrode materials and often electron transfer additive substances have to be incorporated.[31,40]

Since the diffusion of Li ions in solid state electrode materials is considered as the rate-determining step in Li ion batteries, inorganic nanomaterials could hold the key to achieving higher power densities via stable rapid ion and electron transport, and high energy density via maximization of the charge storage capability.[31,35] Another desirable advantage is their high surface area allowing for an increased contact area with the electrolyte and leading to

an improved lithium-ion movement across the electrode material interface.[32] Therefore, nanomaterials have been under extensive investigation for their promising electrochemical properties such as excellent kinetics and cycling stability. However, application of nanomaterials also possesses several limiting disadvantages that have to be taken into consideration in any rational electrode design. These drawbacks are typically associated with the size of the nanomaterials such as limiting control and challenging and costly manufacturing on large scale, and electrolyte degradation and undesirable side reactions on their increased surface-electrolyte interface.[31,34,41]

Two-dimensional (2D) nanomaterials that are characterized as one to several atoms thick nanosheets are considered to be emerging and the most promising electrode materials. 2D nanomaterials allow for increased interlayer distances to decrease energy barriers for accelerated ion diffusion across the basal planes, thus enabling improved accessibility of the Li ions to reach the electrode material lattice sites, and leading closer to realization of the full power density and energy density capabilities of the material.[32,36–39,41] More detailed description and relevant context is given in Section 1.5.

1.3 Titania nanoparticles

Metal oxide nanoparticles have high density of corners and edges on their surface due to their limited size, resulting in unique chemical and physical properties.[7] Nanoparticle electronic structures can be of semiconductor, metallic, or insulator character. As nanoparticles scale down, the increase in the number of interfacial and surface atoms creates strain or stress, structural perturbations and size-related structural alterations cause changes in crystallographic cell parameters.[42]

Titania (TiO_2) belongs to the family of transition metal oxides. At present, metal oxide nanoparticle research is an area of intense scientific activity due to a variety of potential technological applications, playing a vital role in the fields of materials chemistry, medicine, agriculture, information technology, biomedical, optical, electronics, catalysis, environment, energy, and sensors.[12,43,44]

1.3.1 Properties of Titania

Three commonly known polymorphs of TiO_2 found in nature are rutile (tetragonal), anatase (tetragonal) and brookite (orthorhombic).[45] Anatase TiO_2 has a tetragonal structure with slightly larger distortion of the TiO_6 octahedron compared to that of rutile phase and is shown in Figure 1.2.[46,47] While the anatase phase converts to rutile at temperatures above 823 K, at very low temperatures near 0 K the anatase phase is the more stable phase. The anatase structure is generally more attractive over the other TiO_2 polymorphs for many applications due to its higher electron mobility, lower density and low dielectric constant, higher Fermi level, and higher degree of hydroxylation, all playing an important role in the surface chemistry of the material.[45,48–50]

Increased electron mobility, small crystallite size, and the threshold of crystallinity of the anatase TiO_2 are highly desirable prerequisites to develop a highly acidic solid acid catalyst. For this purpose, a sol-gel method can be used in the synthesis of anatase TiO_2 nanoparticles. The sol-gel process is a wet-chemical technique which can be defined as the conversion of a precursor solution to an inorganic solid, through a polymerization reaction induced by water molecules.[51] Essentially the hydrolysis process forms a dispersion of colloidal particles in a liquid media called a sol, and condensation of these colloidal particles – caused by changes in pH or temperature – leads to the formation of a gel. Tuning various parameters during the

sol-gel process influences the size and properties of the formed anatase TiO_2 nanoparticles, and can be used to introduce and control desirable physicochemical properties of these nanoparticles.[52] These parameters include the type and concentration of the precursor used, the water-precursor molar ratio, the type of solvent and the pH and the temperature during the reaction process.[53]

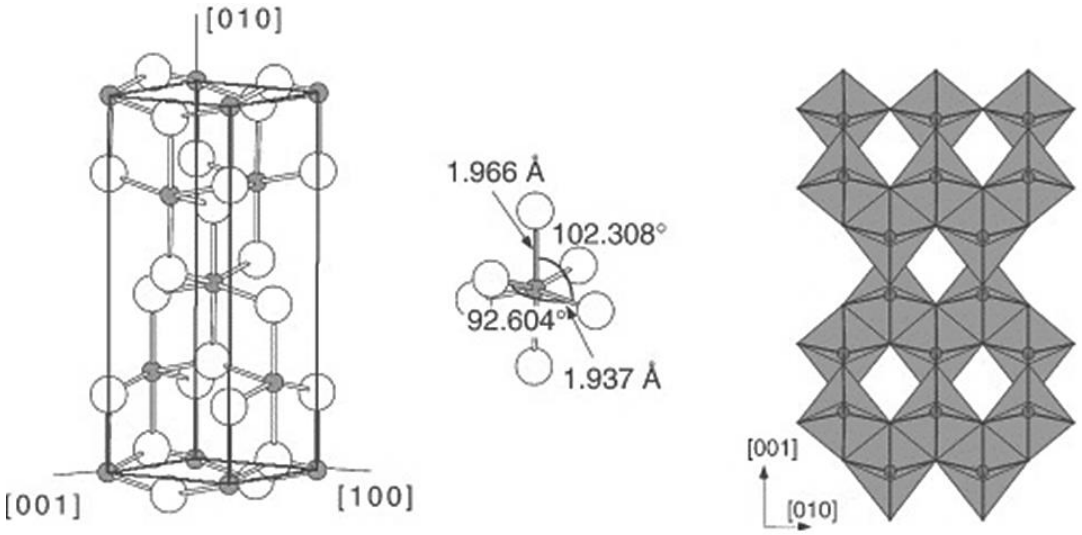


Figure 1.2 Structure of the anatase TiO_2 polymorph as reproduced from reference.[54] On the left is the tetragonal unit cell with cell dimensions of a = b = 3.782 Å and c = 9.502 Å. The basic building units are composed of slightly distorted octahedra with the bond lengths and angles of the octahedrally coordinated Ti atoms indicated in the middle. The stacking of the octahedra building units in the anatase TiO_2 structure is shown on the right.

1.3.2 Sulphated titania as a solid acid catalyst

Acid catalysis is one of the most important areas of catalysed industrial processes in all sectors of chemical manufacturing. However mineral acids as homogeneous catalysts are employed in these processes due to their high acidity strength, allowing for all the molecules or metal ions to be potential active sites.[55] Since the use of mineral acids happens in the same phase as the reaction there are associated difficulties with employment of hazardous liquid acids

such as toxicity, safety and environmental pollution.[56] The high acidity of reaction mixtures also means that they are largely corrosive to the equipment. Solid acids are solid state materials with acidic properties arising from their inherent surface structure.[57,58] These could be weakly bonded acidic protons (Brønsted acid) or electronically unsaturated sites (Lewis acid). Intricate tailoring of solid acid catalysts is required to replace mineral acids. This can be achieved by designing high surface area and unsaturated sites of metal oxide nanoparticles and engineering acidic functional groups on their surface. High product yield and selectivity generally depend on the acidic strength and number of acid sites and these can be tuned in form of direct structural properties of the material by deliberate introduction of structural properties into their morphology such as high surface area and porosity, or in form of stable functional groups purposely engineered on the surface of a solid acid catalyst. Innovative engineering of novel functionalised metal oxide nanoparticles can deliver highly sought-after greener alternatives to the large industrial use of mineral acids, and make many chemical processes in industry safer and more environmentally friendly.

Sulphated metal oxides have been under increasing investigation recently due to their high thermostability, strong acidity, and unique catalytic activities in many environmentally benign reactions. Interest in the field of metal oxide nanoparticles has been focused on sulphated zirconia, titania, tin oxide, and iron oxide as strong solid acids.[59–67]

Among the sulphated metal oxides, sulphated zirconia and sulphated titania are known to possess a strong acidity and exhibit superior activity to many acid-catalysed reactions. Sulphated titania has been successfully employed as an efficient catalyst in a number of industrially important reactions including isomerization and olefin oligomerisation, Friedel–Crafts acylation and alkylation reactions, esterification and transesterification, decomposition

of secondary alcohols and chlorofluorocarbons, condensation reactions, photocatalytic oxidation and selective catalytic reduction of NO_x.[29–48] The increasing demand for highly acidic, environmentally friendly, and active catalysts brings attention back to sophisticated engineering of titania nanoparticles, to reduce their size and to study their structural and physicochemical properties to deliver higher activity and a stability that is currently lacking.

1.3.3 Solid Acid Characterisation

A comprehensive understanding of solid acid catalysts is required to be able to design and develop these compounds for application in industrial processes. This understanding must cover detailed acid features, including acid types, concentrations, distributions, and strengths of acid sites. Brønsted acid (BA) sites are proton donors, associated with acidic hydroxyls (-OH groups). Lewis acid (LA) sites are electron-deficient and accept electron pairs, often associated with active metal centres on the surface of solid acid catalysts. [58,88,89]

Acidity of solid acids can be characterised by a variety of different analytical and spectroscopic techniques. Perhaps the most well-established of these is the Hammett method which uses a range of closely related UV-vis probes to generate the Hammett acidity. Diffuse reflectance ultraviolet-visible (UV-vis) spectroscopy can be used for qualitative analysis of metal centres in solid acid catalysts. Probe methods are used to indirectly detect Brønsted and Lewis acidity, where the adsorption of a desirable base probe molecule on the acidic proton (Brønsted) or electronically deficient empty orbital within the structure (Lewis) detects the type of acidity. Other indirect conventional acidity characterisation techniques are temperature-programmed desorption (TPD) of ammonia or alkylamines and FT-IR spectroscopy of pyridine and carbon monoxide, where heat of adsorption/desorption associated with a basic probe molecule and acid site are assessed, providing overall strength of acid sites through variable-

temperature measurements only.[90–96] Within the frame of these conventional methods, NH_3-TPD is possibly the most commonly used, where broad desorption peaks correlating to acidity strength can be observed. Though popular owing to its relatively easy application, this method is limited as it does not differentiate between Brønsted and Lewis acid sites well.[94] In addition, the method's reliability is highly dependent on the diffusivity of the adsorbate probe molecule, which is mediated by the pore structure of the solid acid adsorbent and possible formation of adsorption complex.[96]

In comparison with conventional Hammett acidity function and NH_3-TPD techniques, spectroscopic characterisation methods are generally agreed to give greater reliability for qualitative and quantitative analysis of acid sites. FT-IR spectroscopy is an example whose use has generally increased over several decades for direct detection of structural hydroxyl groups (-OH) on solid catalysts; the hydroxyl groups on the surface display characteristic bands over a stretch region of 3600 – 3750 cm^{-1}. Other than direct detection of surface hydroxyl groups, FT-IR studies with probe molecules are also used for acidity characterisation, where a base probe molecule, such as pyridine or 2,6-ditert-butylpyridine, is adsorbed on the surface of the catalyst. Specifically, the pyridine-IR (py-IR) method has been extensively used for analysis of the surface acidity of solid acids.[90] This method has the advantage of being able to identify Brønsted and Lewis acid sites simultaneously. IR adsorption bands at ca. 1545 and 1450 cm^{-1} are assigned to Brønsted and Lewis acid sites, respectively, while both types additionally contribute to a band at ca. 1490 cm^{-1}. However, this additional overlapping band renders determination of the extinction coefficient of pyridine adsorbed on BA and LA sites impossible, making quantitative measurements of acid concentration in solid acids impractical.[91,97]

1.3.3.1 NMR as a powerful characterisation tool for solid acids

Together with the former techniques, solid-state nuclear magnetic resonance spectroscopy (NMR) is a powerful technique for the characterisation of acid properties of solid catalysts. There is evidence to suggest that solid-state NMR is highly reliable for the probing of local structures of framework and extra-framework species.[98–103] One type of this technique is ^{1}H Magic Angle Spinning (MAS) NMR, which probes structures of various hydroxyl groups, such as acidic bridging hydroxyls and weakly acidic terminal hydroxyls which are commonly observed in aluminosilicates such as zeolites.[97,104–106] NMR spectroscopy has the capability to provide not only qualitative but also quantitative data analysis, therefore it has an advantage over most conventional acidity characterisation techniques.

Detailed acid features of solid acid types, such as acid type, location, concentration, strength, etc., can be investigated by the use of solid-state NMR. To further enhance the qualitative and quantitative data acquisition, a suitable probe molecule containing the desired NMR-sensitive nucleus (^{1}H, ^{13}C, ^{15}N, ^{31}P) can be chosen according to the sample to be probed. Solid state ^{1}H and ^{15}N NMR of pyridine, ^{1}H NMR of deuterated acetonitrile, ^{13}C NMR of acetone and mesityl, and ^{31}P NMR of trimethylphosphine (TMP) and trimethylphosphine oxide (TMPO) have been utilised in investigation of solid acid properties.[107–129] Additionally, ^{1}H NMR of deuterated pyridine is a well-used tool for probing surface acidic hydroxyls. In general, ^{1}H resonances that arise from adsorption of deuterated pyridine on nonacidic or weakly acidic terminal hydroxyls produce signals in the range of 2 – 10 ppm, due to the formation of hydrogen bonds between the surface hydroxyls and the probe molecule. Deuterated pyridine, adsorbed on BA sites, producing pyridinium ion, on the other hand, gives signals in the range 12 – 20 ppm.[130] Another method is to probe the guest-host interactions involving BA and LA sites by use of ^{15}N NMR of deuterated pyridine.[131] Another well-established method for

probing the relative acidic strength of BA sites in solid acids is characterisation by ^{13}C NMR of isotope-labelled 2-^{13}C-acetone, which relies on the measurement of the ^{13}C shift caused by the interaction of the acidic proton with the carbonyl oxygen.[127] Consequently, the hydrogen bond interaction results in a chemical shift of ^{13}C resonance towards downfield – a stronger Brønsted acidity gives a greater observed chemical shift.

Although ^{1}H-pyridine and ^{13}C NMR techniques are useful for determination of relative acidic strength of solid acid catalysts, they have limitations in their key NMR parameters. The chemical shift range of the proton nucleus (^{1}H with spin quantum number I = ½) is very narrow at a maximum of 20 ppm, giving inferior spectral resolution, while the ^{13}C nucleus (I = ½) has a better resolution due to larger chemical shift range of 300 ppm. Conversely, the proton nucleus has a very high natural abundance of 99.989%, compared to a low natural abundance of 1.07% of the ^{13}C nucleus, giving low to moderate sensitivity of detection. Hence, most ^{13}C NMR analyses require ^{13}C-enriched reagents, which can be expensive.[132]

Comparatively, the ^{31}P (I = ½) nucleus has advantages in both sensitivity and resolution of detected spectra of phosphorus containing reagents. Its natural abundance of 100 % and wider detection range of chemical shift of 650 ppm are the reasons for its superiority. Probes containing phosphorus, such as trimethylphosphine (TMP) and trimethylphosphine oxides (TMPO), have been developed for use as NMR probes for the characterisation of acid properties of solid catalysts in recent decades.[13,26–40] This has enabled detailed features of acid sites in solid acids to be assessed such as acid type, distribution, concentration and strength. Complementary theoretical studies have shown quantitative correlations between the observed ^{31}P chemical shift of the adsorbed probe molecule and acid strength, for both TMP and TMPO ^{31}P solid state NMR.[109,117,118,120–122]

It was Lunsford and co-workers that were the first to take advantage of TMP as a probe molecule for the ^{31}P solid state NMR characterisation of Brønsted and Lewis acidities of calcined H-Y zeolites.[128] A single peak in a range of -2 to -5 ppm is observed in ^{31}P NMR spectrum of TMP adsorbed on Brønsted acid sites, assigned to the formation of $[TMPH]^+$ complexes between TMP and the Brønsted acidic proton. Chemical shifts due to chemisorbed TMP on Lewis acid sites are observed in the range from -32 to -58 ppm. This level of distinction between the peak ranges of the two acid types has resulted in TMP ^{31}P NMR approach being recognised as a highly sensitive method for acid site type identification in solid acid catalysts. It has since been implemented for characterisation of acidity of many solid acid systems including amorphous silica-alumina, microporous and mesoporous zeolites, mixed metal oxides, sulphated metal oxides, and heteropolyacids.[36,45–54] Furthermore, the wide chemical shift range of -20 to -60 ppm of a TMP probe adsorbed on Lewis acid site means that the TMP ^{31}P NMR approach is highly sensitive for the determination of strength of Lewis acid sites. This is not the case for TMP probe bound at a Brønsted acid site, where differentiating the strength of these sites is less practical due to the narrow ^{31}P chemical shift resonance range of -2 to -5 ppm.[133,134,136–140,142,143] TMPO ^{31}P NMR provides the contrasting approach, as it is highly sensitive in determination of Brønsted acidic strengths.[21-29,31-33] Similarly to TMP, the ^{31}P NMR resonances of adsorbed TMPO probe molecules also span over a wide range of chemical shifts in the 40 to 100 ppm region. Chemical shifts of Lewis acid sites appear between 45 and 55 ppm and are typically less sensitive to differentiate acidic strength. In contrast to TMP, however, the distribution of acidic strengths arising from Brønsted acid sites results in a much wider chemical shift range of 55 to 98 ppm, making TMPO ^{31}P NMR an ideal probe to determine Brønsted acid strengths and to quantify their abundance in the solid acid catalyst.[144]

1.4 Palladium nanoparticles

1.4.1 Palladium chemistry

There is growing interest for metallic nanomaterials within the field of nanotechnology. This is due to the extraordinary properties of noble metals such as catalytic, electronic, magnetic, optical and mechanical properties, which makes the study of possible applications of nano-sized noble metal materials of great importance and value for the possible benefits they could offer within many fields.[145–148] Palladium is one such metal, as a rare and precious metal belonging to the platinum group elements.[127] The study of palladium-based materials is highly valuable as it is one of the most efficient metals within catalysis.[150,151]

Palladium sits within Group 10 of the periodic table, but the configuration of its outermost electron shells sets it apart from the other elements in the group. Palladium ($4d^{10}$ $5s^{0}$) has a totally empty fifth s-orbital shell, diverging from nickel ($3d^{8}$ $4s^{2}$), platinum ($5d^{9}$ $6s^{1}$) and darmstadtium ($6d^{9}$ $7s^{1}$ or $6d^{10}$ $7s^{2}$). This phenomenon means that its properties differ from the other Group 10 elements. It has the lowest melting point and the lowest density of all platinum group metals (Ru, Rh, Pd, Os, Ir, Pt). As an example, palladium dissolves slowly in concentrated nitric acid, in hot or concentrated sulphuric acid, and in hydrochloric acid if broken up finely.[152] It has multiple oxidation states, commonly 0, 1+, 2+, 4+, but even 3+ and 6+ states have been evidenced.[153–155] Compounds with the 3+ oxidation state of palladium have been suggested as intermediates in multiple palladium-catalysed cross-coupling reactions, though these compounds are rare. A limitation to wide use of palladium is its high material cost, nevertheless in the nanoscale, or its alloy nanoclusters, it has been extensively researched for industrial applications. Akira Suzuki, Richard F. Heck and Ei-ichi Negishi

received the Nobel Prize in Chemistry in 2010 for using palladium in combination with a wide variety of ligands for highly selective chemical transformations.[156,157]

Group 10 or platinum group elements are valuable for their intrinsic high catalytic ability under mild conditions, high selectivity towards specific products, high stability under various reaction conditions, and tolerance to catalyst poisoning, etc.[158] Platinum is the most commonly used Group 10 metal element in catalysis, but could soon be superseded by palladium due to the latter's wider availability and competitive catalytic properties. Palladium is mainly used as an active catalyst material in automotive catalytic converters, but has other applications in electronic, engineering, biomedical and jewellery industries.[148,149,159–162] Although homogeneous organometallic palladium catalysts exhibit fantastic activity, selectivity, together with a well-understood reaction mechanisms, their application in industry is difficult as they are expensive, usually non-recyclable, with challenging separation from the product mixture.[156,163–171] Palladium nanoparticles have the capability to be even more effective catalyst materials due to their high surface area to volume ratio and high surface energy.[172]

Palladium nanoparticles are known for their important catalytic, mechanical and optical properties which could be utilised within various industrial applications, especially for chemical applications.[173] Their catalytic viability is shown in their ability to dissociate molecular hydrogen into the atomic state within organic carbon-carbon coupling formation reactions, such as the Suzuki-Miyaura and Heck cross-coupling reactions, hydrogenations of unsaturated alkenes, and alcohol oxidations.[156,174–178] The catalytic viability has been utilised successfully to control hazardous exhaust emissions from automotive engines, to produce intermediates of pharmaceuticals and fine chemicals, and to process environmental

pollutants. Furthermore, palladium nanoparticles have shown to be excellent at degrading methylene blue, methyl orange and nitrophenyl dyes, and thus can be used to process effluents polluted by these compounds.[173] Another application for palladium nanoparticles is within electro-catalysis. Palladium's capability to absorb hydrogen enables palladium nanoparticles to be used in hydrogen storage applications as well as electrochemical reactions in fuel cells.[149,179,180] Another form that possesses excellent electro-catalytic properties is carbon microsphere-supported palladium nanoparticles, which have large potential in direct ethanol fuel cells.[181,182] Over the last 10 years, palladium nanostructures have also been shown to be of interest in many other applications such as sensors for analyte detection, or to be used in the production of electrical equipment.[183,184]

Palladium generally adopts a highly symmetric face-centred-cubic (FCC) crystal structure. Using mathematical calculations to determine the thermodynamic equilibrium shape of a FCC nanocrystal, the result is a truncated octahedron bound by six (100) and eight (111) planes.[185] A challenge for synthesis is to produce shapes that are different to these highly spherical polyhedral forms. Examples of non-spherical shapes that have been synthesised successfully include highly faceted polyhedral structures bound by (100) or (111) facets such as cubes, tetrahedra and icosahedra, one-dimensional rod-like, two-dimensional plate-like, and three-dimensional porous nanostructures with multiple branches. To synthesise nanoparticles in solution phase, a nucleation event is initiated, to be followed by a growth stage in which palladium solutes are consumed.[186,187] The desired nanoparticle morphology is controlled by dictating the initial nuclei shape and directing the growth of the nuclei and nanocrystals. Nuclei can assume a range of shapes sensitive to chemical potentials of the various crystallographic faces, which are dependent on reaction environment conditions (temperature, solute concentration, etc.).[188]

Modern transition metal nanoclusters are different from classical colloidal structures in advantageous ways: they are generally smaller (1 – 10 nm in diameter), with a narrower dispersion of size; their synthesis is reliable and reproducible with well-defined composition and clean surfaces; they can be isolated and re-dissolved in aqueous and/or organic solvents; they show higher reproducible catalytic activity with high selectivity; and they have great potential for recovery and reuse of the catalyst.[146,189–191] It is the aforementioned special nature of its fundamental electronic configuration, which can be strongly influenced by coordination environment, that gives palladium nanoparticles their intrinsic catalytic properties.[192] It is with the manipulation of this coordination environment and the electronic band structure, by alloying with a secondary element, anchoring to a support, or controlling particle size, etc., that makes palladium nanoparticles different from that of monometallic palladium.

1.4.2 Palladium nanoparticle synthesis

There are two main methods for the synthesis of palladium nanoparticles for catalytic applications: the metal salts reduction and the decomposition of organometallic complexes.[193–198] A key issue which is independent of the process chosen is the stabilisation of the nanoparticles during synthesis to avoid formation of bulk metal, which is achieved by protective agent. Stabilisation can be attained by two methods: electrostatic stabilisation by use of ionic compounds as protective agents, or by steric stabilisation using neutral molecules (polymers or other bulky molecules). Electrostatic stabilisation is mainly limited to aqueous media, whilst steric protection can be applied in organic and aqueous solvents. The agent used for steric stabilisation will influence the reactivity and stability of the synthesised nanoparticles. Usual candidates for stabilising agents are polymers, surfactants and ionic

liquids. To discuss an interesting contrasting method, immobilisation of colloidal palladium nanoparticles on a solid support enables the simple filtration of the catalyst for recycling. This can also reduce ion or atom leaching from the particles.

1.4.3 Palladium nanoparticles as catalysts in organic synthesis

It is due to their large surface area that metal nanoparticles are effective catalysts for chemical transformations. With reduction in size, relative surface increases, which in turn increases catalytic activity. It is therefore important to identify the correct stabilising agent for the desired size and surface stability (to minimise palladium leaching) of palladium nanoparticles. Once palladium nanoparticles are synthesised and isolated for use as catalysts, one should consider the risk of leaching and formation of catalytically active molecular species. Several proposed mechanisms are summarised in Figure 1.3. Palladium nanoparticles can be used as true heterogeneous catalysts, or to provide a reservoir for homogeneous molecular palladium species. In the latter situation, one of two processes may occur: either naked palladium atoms could leach from the nanoparticles, or the oxidative addition first step of the reaction could occur at the nanoparticle surface, followed by leaching of the [Pd(Ar)X] species, initiating a homogeneous catalytic cycle. It has been suggested that leaching is a reversible process in that palladium nanoparticles can be formed during reactions from metal complexes, and in reverse, the palladium nanoparticles act as a reservoir of molecular species.[150,199–202]

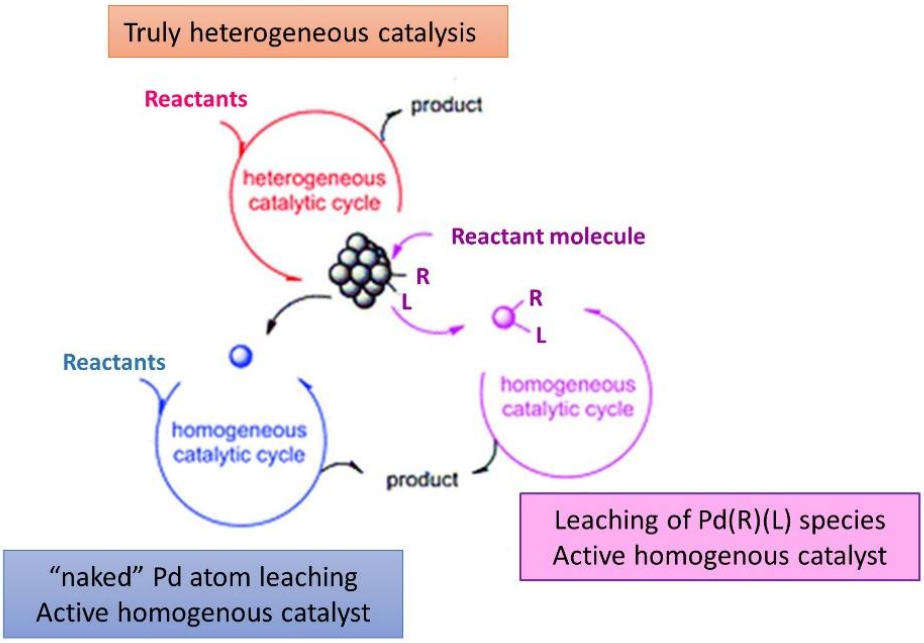


Figure 1.3 Possible reaction mechanisms of palladium nanoparticles discussed in literature. Figure was adapted from reference.[203]

1.4.3.1 Palladium and cross-coupling reactions

Amongst the most adaptable and useful tools for organic synthesis across academia and industry are cross-coupling and related reactions, which include the Heck reaction, the Buchwald-Hartwig reaction, the Suzuki-Miyaura and Sonogashira reactions (both of which are direct arylation reactions).[204] The methods are a relatively mature technology, whose foundations were laid as far back as the 1970's by those who gave them their names. In the 1990's, these methods were discovered to achieve an extraordinary improvement in activity of metal complexes, with large, strongly σ-donating ligands. This kickstarted the development and widespread application of these reactions in industrial production plants. In cross-coupling and related reactions, palladium salts or complexes, which can be either formed prior to or in situ on addition of the ligand, are generally used as sources of palladium. It is usually palladium (II) species which is selected as a starting material due to their superior stability. Compounds such as these species are reduced in situ to palladium (0) species, which

then enter into the catalytic cycle. These mechanisms are organometallic in nature and take place in the coordination sphere of the metal.

Figure 1.4 shows the most recognised mechanism for the catalytic cycle of cross-coupling reactions. It starts with the oxidative addition of an organic or pseudo- halide to the catalytically active species, assumed to be $L_nPd(0)$, where L_n is the number (n) of ligands (L) coordinated to Pd. In some of the coupling reactions (Negishi, Suzuki-Miyaura, and related reactions) the next step is transmetalation with an organometallic reagent, followed by reductive elimination, which delivers the required product. In the Heck coupling on the other hand, what follows is the migratory insertion of an alkene, followed by a β-hydride elimination/base-assisted H–X elimination sequence, to give the desired product. The substituents on the alkene, as well as the nature of the ligand, can be specifically chosen to control the formation of linear or branched products, or a mixture of both.

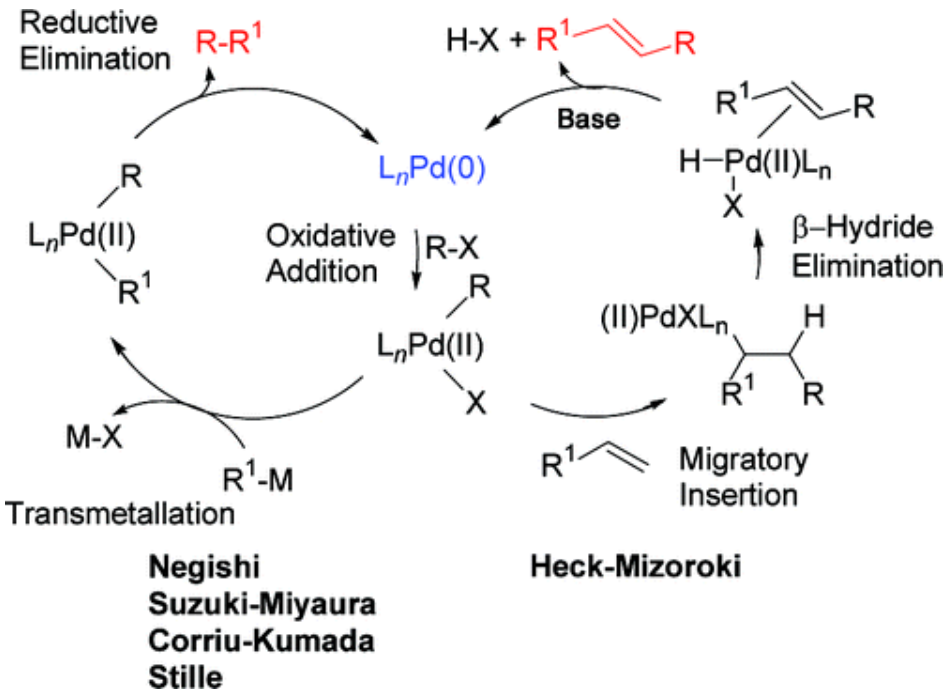


Figure 1.4 General Mechanism of Cross-Coupling Reactions as pictured in reference.[205]

It has been shown that palladium nanoclusters and colloidally-stable palladium nanoparticle dispersion solutions can deem comparative effectiveness and attractiveness as industrial catalysts for organic coupling reactions in organic solvents similar to homogeneous palladium catalysts.[206] Yet to be fully understood, however, is the reaction mechanism of heterogeneous palladium catalysts, which is believed either a leaching mechanism, or, more likely, due to the high energy surface chemistry of the nanoparticles. In recent years, highly dispersed nanosized palladium metal on a solid support has been predicted to provide comparatively good catalytic performance in organic coupling reactions, with the significant economic advantage of ease of recovery and recycling.[207–211]

1.4.3.2 Palladium and hydrogenation reactions

Palladium catalysts are not only interesting for organic coupling reactions but also for hydrogenation of unsaturated hydrocarbons. Materials that absorb hydrogen can be employed in hydrogen storage, purification, and hydrogenation catalytic processes, therefore acting as clean energy carriers. It is becoming increasingly important to achieve high product yield in a way that does not compromise on energy use and environmentally damaging methods, whilst still being economical. Sustainable catalysts for selective hydrogenation are being developed by this principle, with palladium at the heart as the best known metal for permeating hydrogen gas selectively.[212] With the exception of palladium, the majority of metals require an input of energy to surpass the activation barrier of reaction, thus requiring high hydrogen pressure or high temperature. Chemisorption of the hydrogen molecule to the palladium surface by collision is the first step in hydrogen storage. This chemisorbed hydrogen atom then diffuses below the surface, to several nanometres depth. Palladium is remarkable as at room temperature and atmospheric pressure, it is able to absorb large volumetric quantities of hydrogen, and subsequently forming palladium hydride (PdH_x). It is palladium's

exceptional dissociative properties that allow its use as a catalyst to facilitate hydrogen absorption and desorption in other metal hydrides.[213] Furthermore, palladium's intrinsic hydrogen selectivity, fast sorption kinetics, and reversibility of formation of hydrides, enable palladium-based alloy membranes to achieve high hydrogen gas purity. An example of palladium's applications in this area is for industrial scale feedstock in petrochemical processes, where palladium membranes with high mechanical strengths are sought.[214,215] Another example is as hydrogen sensors that rely on the changes in properties of palladium on exposure to hydrogen.[216] As well as brilliant selectivity towards the permeation of hydrogen, palladium nanomaterials have been shown recently to have a good stability in repeated treatments of hydrogen absorption.[217] All of these properties combine to evidence palladium-based materials as amongst the best metals for catalytic reactions involving hydrogen, such as the hydrogenation of unsaturated organic molecules.

An important process for the purification of alkenes produced in industrial applications is selective hydrogenation of alkynes.[218–220] The method of achieving a high purity of alkenes goes hand in hand with increasing the efficiency of conversion of the alkyne (or an alkadiene) but is compromised by the further hydrogenation of alkenes to alkanes. Selective hydrogenation is a solution that has two common approaches through tailoring of heterogeneous catalysts. The first approach involves providing ensemble control and electronic contributions to adsorb reactants and products by constructing multi-metallic nanomaterials; an example is palladium-silver alloy and palladium-silver core-shell nanoparticles on γ-alumina support. The second approach uses modification of the metal nanoparticle surface to regulate metal-organic interactions; an example is the catalyst still largely used in industry, the Lindlar catalyst (5 wt. % Pd on calcium carbonate poisoned by lead promoter and quinoline).[221–224] Even though these approaches have been used for many

years both in academia and industry, the relationship between structure and activity has not yet been properly established due to additive complexity, varied surface properties, and as yet not-understood interface structure, and there are associated safety hazards due to the presence of toxic lead additives.[224–229]

In the case of the palladium-silver alloy or core-shell nanoparticles of the same metallic alloy supported on low surface area γ-alumina, the palladium performs the part of the active component, whilst it is the silver that has been added as a structural modifier which improves selectivity towards alkenes through limitation of formation of hydrides (or carbides which are believed to affect selectivity over monometallic palladium catalysts) as shown in Figure 1.5.[229–234] Even in optimised conditions, an extra measure taken is the addition of carbon monoxide to limit the over-hydrogenation, as it adsorbs more strongly than the alkene but less than the alkyne. This is not an ideal situation though, as constant regulation of the amount of carbon monoxide is required to avoid "alkyne slip" and changes over the lifetime of the catalyst. Over recent years, a substantial amount of research has been reported surrounding the development of novel catalysts for selective alkyne hydrogenation. Many varying approaches have been attempted for enhancing the selectivity of palladium catalysts including alloying with metals alternative to silver, adsorption of organic modifiers, or even using novel supports.[235–254] There are even a small number of catalysts that do not include palladium and have been identified as intrinsically more selective. These, however, require more extreme temperature conditions as dissociation of hydrogen is easier with increased temperatures.[255–262] This requirement of higher temperature can be avoided by addition of dopants or a second metal which eases the dissociation of hydrogen.[263–269]

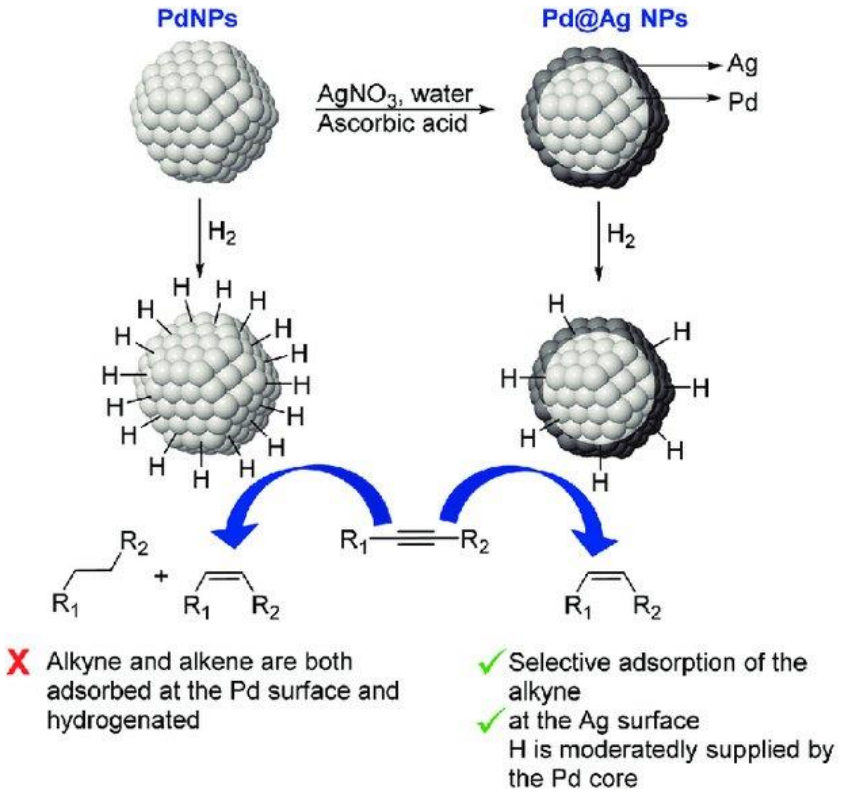


Figure 1.5 Synthesis of palladium core and silver shell nanoparticles and their role in selective hydrogenation of alkynes in comparison to pure palladium nanoparticles as reproduced from reference.[270]

Palladium sulphides (Pd_4S) have also been identified and explored for their promising high selectivity as catalysts for the hydrogenation of alkynes (acetylene and methyl acetylene) and alkadienes (propadiene and butadiene).[271–274] High temperatures (200 – 250 ˚C) are required to optimise selectivity for partial hydrogenation of alkynes to alkenes, however, under these conditions, an unusually low rate of alkane formation was observed.[275] It is theorised that the modification by sulphide stimulates similar behaviour to the effect of silver and lead in the industrial catalysts. The sulphide introduces steric and electronic changes which do not allow the full hydrogenation of alkene intermediates during the hydrogenation of alkynes, thus creating a modified palladium surface with a high catalytic selectivity towards alkenes.[276] Unfortunately, comparably to palladium metal nanoparticles, these Pd_4S nanoclusters are

generally not suitably stable under these reaction conditions, are relatively soluble in water, and are tricky to separate and recycle.

Many scientists launched an investigation to provide a solution to these issues and have researched palladium nanoparticles and their deposition onto solid supports. However, catalytic activity of these supported catalysts was found to be relatively low at room temperature, therefore leading back to the requirement of higher temperature conditions. A method for increasing activity at lower temperatures could be to merge catalytically active palladium nanostructures with transition metal dichalcogenides as their supporting structure. The metal and sulphides contained within this support create a similar effect on the activity of palladium nanoparticle catalyst that could be acquired by modification of their structure or by alloying with another metal. Another benefit of the transition metal dichalcogenides is their stability and intoxicity which alleviate the problems of separation and recyclability, higher costs and safety uncertainties when it comes to using these chemicals in products for human or animal consumption, cosmetics, and manufacture of medical products.

1.5 Two-dimensional nanomaterials in lithium-ion batteries

1.5.1 Global climate change and societal need for energy solutions

Some of the hottest topics today surround climate change, energy production and energy storage. We are becoming increasingly aware that our behaviour towards the planet and the processes that we use in mass scales are unsustainable and inefficient in our pursuit of cleaner energy usage. Depleting fossil-fuel resources and our ever-increasing energy needs work as one to force the pursuit of sustainable energy alternatives, which includes both renewable energy sources and efficient storage technologies. These technologies are still far from the efficiency we need to achieve a sustainable system, therefore it is important for us to rally

scientific resource to focus on these tasks, especially the transition from fossil fuels to sustainable energy sources. The other item that massively impacts our energy usage is our ever-growing global population. To put this into perspective we need to cope with the concurrent energy demands and our present rate of energy production must be doubled by 2050.[277] Several renewable energy resources that have been established are by definition intermittent as their stability relies on external factors: wind, solar, tidal, biomass and geothermal. The locations of these sources are also generally dispersed in relation to the remote large-scale facilities that currently provide the bulk of electrical energy. Therefore, before we can successfully shift from being reliant on fossil-fuels to getting the majority of our energy from renewable technologies, we must significantly improve on our ability to store energy. It is therefore fundamental that in designing new electrochemical storage systems, material abundance, eco efficient synthetic processes and lifecycle analysis are considered. Currently there are technologies that focus on these issues, however in each example there remain difficulties to resolve. Figure 1.6 shows a comparison between energy and power density of various types of energy conversion and storage devices.[278]

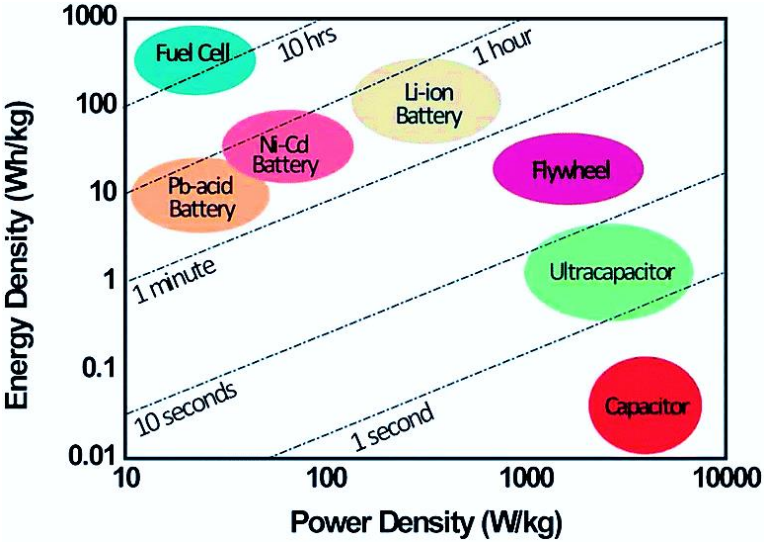


Figure 1.6 Ragone plot for different energy storage technologies reproduced from reference.[278]

1.5.2 Lithium-ion batteries

Lithium-ion batteries are used by millions of people in their day-to-day lives – laptops and mobile phones, hybrid electric cars, to name the most common uses. The technology's many advantages are the reason for its incorporation into all these products, these include high energy density, light weight, and ability to recharge. A lithium-ion battery is made up of two electrodes, a (negative) anode and a (positive) cathode, a separator, electrolyte, and two current collectors (positive and negative). It is the anode and cathode that store the lithium. During operation, lithium ions move from the anode to the cathode, as well as in reverse, via the electrolyte through the separator. The electrodes are structures made up of a combination of active materials, additives, and binders. The main role of the active ingredients is the safe long-term storage of lithium. In modern lithium-ion batteries, metal oxides are common active ingredients for cathodes, whilst different types of carbon are used for anodes. Additives are used to increase electronic conductivity in the composite electrode, these are usually carbon materials. The role of the binder is to ensure the active materials remain in physical contact with each other as well as with the current collector. The redox voltage of the electrode material must sit within the range of stable operating voltages of the electrolyte. The cathode material should present a low lithium chemical potential, whilst the anode material should present a high lithium chemical potential, in order to realise the highest cell operating voltage. The separator is made of a permeable membrane that is also a good insulator. Its role is to facilitate the exchange of lithium ions from one side of the membrane to the other, whilst preventing electrical short circuits. Figure 1.7 shows a schematic of a standard lithium-ion battery and its components. The operation principle is also illustrated. During applicational use of the battery – during this stage the battery is

discharging and supplying an electrical current – lithium ions move from the anode to the cathode, causing electrons to flow from one side to the other. During charging of the battery, when it is plugged to an external electricity source and the opposite occurs, lithium ions move from the cathode to the anode.

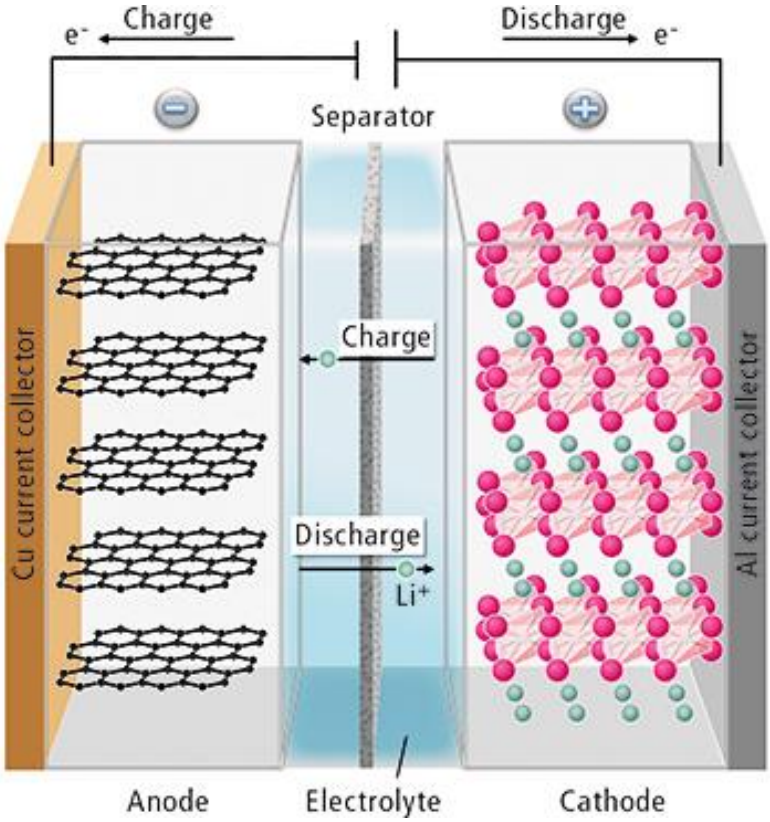


Figure 1.7 Schematic representation of the functional principle of a lithium-ion battery reproduced from reference.[279]

1.5.3 Advantages and drawbacks of using lithium-ion batteries

Energy density and power density are the two most common and vital concepts related to lithium-ion batteries. Energy density defines the amount of storable energy a battery can hold relative to its mass, measured in Watt-hours per kilogram (Wh/kg). Power density defines the amount of power relative to its mass that a battery can produce, measured in Watts per kilogram (W/kg). To calculate the energy stored in a battery, the discharge power (measured

in Watts) is multiplied by the discharge time (measured in hours). The energy capacity of a battery decreases over time with cycling, dependent on parameters used including charge/discharge rate and operation temperature. The cell voltage depends on the potential difference of the electrodes, the kinetics of the reaction, as well as the cell resistance. The decreases in power and efficiency of energy conversion are brought about by the enhanced voltage plateaus seen in charging and reduced voltage plateaus in discharging, which are caused partly by a rise in cell impedance. Therefore, it is a rise in impedance and drop in capacity that define the life cycle of a battery.

Research and development of lithium-ion batteries continues to be at the forefront of the industry, as lithium-ion is seen to be a promising energy storage technology. This is due to its high energy density, low self-discharge feature, almost zero-memory effect, high open circuit voltage, high coulombic efficiency, as well as long lifespan.[280–283] These batteries are already widely used as power sources for a large variety of applications due to the properties above, as well as a range of possible chemical potentials with diverse electrode designs. In the last ten years, there has been a push towards high charge capacities/power densities for next generation of lithium-ion batteries to be used in electric vehicles, hybrid electric vehicles, aerospace applications, and autonomous electric devices, such as hybrid solar batteries.[283–286] Recently, it is within this industry of electric and hybrid electric vehicles that high-energy density Li-ion batteries are believed to be the best power source.

It is due to this versatility that lithium-ion battery technologies are seen to have such high potential. They provide solutions for a vast range of applications that span many Watt-hours (in portable electronic devices), many *kilo*-Watt-hours (within electric vehicles), and tens of *mega*-Watt-hours (for grid applications), with capability to design autonomy and power

requirements.[283,287] This does not mean that to develop lithium-ion batteries suitable for transport and to cope with society's unstable energy requirements is anywhere close to a simple task, especially when materials development is considered. At present, lithium-ion batteries are costly for some applications (such as transport and grid), and the availability of lithium and certain transition metals currently used for these technologies is increasingly becoming an issue into the future.[288] Even considering this, lithium-ion batteries have intrinsic advantages over other energy technologies. To start from fundamental chemistry, lithium has the lowest reduction potential of any element, which allows lithium-ion batteries to have the highest possible cell potential; it is also the third lightest element, and has one of the smallest ionic radii of any singly charged ion. It is these properties that allow batteries based on lithium to have high power density, gravimetric capacity, and volumetric capacity. Although it would seem beneficial to have multivalent cations due to the associated higher charge capacity per ion, this additional charge would significantly reduce their mobility. It is commonly the ionic diffusion in solid electrodes that is the rate-limiting step for battery power performance, therefore this factor of decreased ionic mobility creates a large barrier for development of alternative chemistries to overcome. In developing better energy storage systems, it is not enough to look only at the classical factors of specific energy and power, lifetime, cost and safety; abundance of materials and energy cost of battery manufacture and recycling must be taken into account.[277,280,281,283] Hence, lithium-ion batteries remain at the forefront as the energy storage technology with the highest potential for the transfer within the energy sector from the burning of fossil fuels to more sustainable energy production methods, that is within current availability. Lithium-ion batteries are currently the go-to electrochemical energy storage technology for portable items; by improving their performance whilst decreasing

costs their use can be expanded to a wider range of applications, and even allow development of new technologies requiring energy storage.

One dangerous assumption to avoid, however, is that by selection of environmentally friendly, green, cheap and available elements, the final material or energy storage system will in turn be green and cheap. Raw materials must be extracted and processed, the electrolyte and electrode materials must be synthesized, energy storage devices have to be manufactured, on top of the requirement for all components to be recyclable. Over years of development aiming for high energy density storage systems, aqueous electrolytes (for example lead-acid and nickel-based batteries) have led to non-aqueous based electrolytes (such as in lithium-ion based batteries), which enable considerably higher operating voltages. An advantage to lithium-ion batteries, in converse to the lead-acid and nickel-cadmium and nickel-metal hydride batteries, is their flexibility in choice for positive and negative electrode materials. This opens many options for design of new high-performance electrodes based on low-cost elements. Development into new positive electrodes is split into two areas of research: the improvement of layered oxides and design of new polyanionic compounds. Lithium iron phosphate and layered lithium cobalt have been the benchmark materials for a considerable time, but are being made redundant by nickel cobalt aluminium oxides (NCA), nickel manganese cobalt oxides (NMC), or Johnson Matthey's next generation high nickel cathode material eLNO®.[283,289–291] Development of negative electrodes is more varied and less focused, but just as important for developing high power, high capacity batteries. Graphite and graphene, hard carbon, lithium titanate, tin-based, and silicon based materials are amongst the most commonly used materials for production of the anode.[270–281]

1.5.4 Selection of anode materials for lithium-ion batteries

The negative electrode (anode) in a lithium-ion (Li-ion) battery consists of a lithium intercalation compound casted into a thin layer on the current collector. It is important for the active materials to be in thin uniform coatings for cells with organic electrolytes. The final coating quality is dependent on the processes involved within the mixing and coating of anode materials, which can severely affect the rate capability, cell capacity and general cell aging behaviour. Malfunctions such as cell thermal runaway and cell failure can be caused by defects in the coating of the negative electrode. Lithium could be an option for the anode material of Li-ion batteries, but lithium is prone to plating during charge and discharge cycles, and along with the ensuing dendrites there is a risk of short-circuit occurring within the cell. It is due to this that alternatives such as carbonaceous materials with high capacity storage for lithium are chosen for Li-ion battery anodes. A current prominent example of material used for anode material is graphite. Carbonaceous anodes present industrially viable lithium intercalation and deintercalation rates, which are known as charge/discharge rates – or C-rates – of a battery. Unfortunately, cell performance is limited due to the formation of solid electrolyte interphase (SEI) when the electrolyte decomposes during cell cycling.

There are three categories into which Li-ion battery anode materials can be grouped – intercalation, conversion, and alloying.[303–305] Each of the three categories has its own characteristic features. Intercalation materials are commonly identified by a low working potential with small but stable specific capacity. As an example, graphite with specific capacity of 372 $mA{\cdot}h{\cdot}g^{-1}$ is the most effective intercalation anode material to be used in industrial Li-ion batteries. Conversion materials often offer a much higher reversible capacity, commonly within the range of 500 - 1100 $mA{\cdot}h{\cdot}g^{-1}$, but is limited by large polarisation and a sloping

voltage profile of the charge/discharge cycle that diminishes practicality of use in industrial applications. Materials based on alloying have the highest practical reversible capacity of 800 – 1800 mA·h·g^{-1}, which is significantly higher than that of the traditional graphite anode, along with low working potential, relatively good rate capability and cycling performance.[306] However, although conversion and alloying materials would appear to be ideal, the associated large volume expansion is a feature that induces material fracture and is the major source of the materials' fast fading capacity. Another negative point to consider when using these materials is the significant loss of lithium to the anode during the first charge, wherein the anode is lithiated. There are many substantial issues with conversion-reaction anodes; these consist of large volume changes of up to 400 % during the charge/discharge cycle (when using a silicon-based anode), pulverisation of particles, constant solid electrolyte interphase formation, and the resulting capture of active lithium from the cathode within the anode solid electrolyte interphase.[307–312]

1.5.5 Li-ion battery aging mechanisms

Solid electrolyte interphase (SEI) has a major effect on battery performance. The SEI layer is formed after the first cycle when organic and inorganic compounds decompose, subsequently acting as a barrier layer against solvent co-intercalation which causes the exfoliation of the electrode surface. However, an unnecessarily large amount of SEI formation is detrimental as it captures lithium ions, as well as reduces the active material surface area. Accordingly, a considerable increase in formation of SEI decreases irreversible volumetric energy density and battery performance.

Battery aging can be described as a reduction in lifespan, performance, and reliability of a battery system. It can be a factor in either or both of capacity and power fading.[279] All

components in any system are subject to aging, and as batteries are made up of an assembly of aging parts, there is much interdependence of deteriorating performance and part-to-part effects of operational conditions and subsequent expedited entire systematic aging. Figure 1.8 shows a summary of mechanisms of degradation and their interdependence, demonstrating the complexity of degradation in Li-ion batteries.

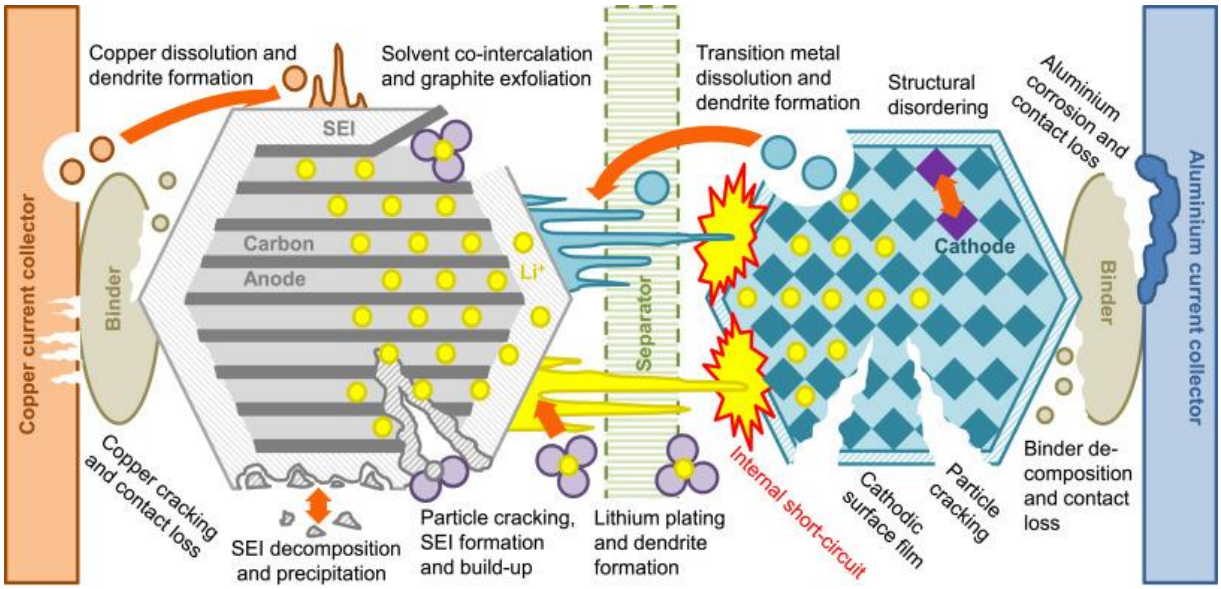


Figure 1.8 Degradation mechanisms in Li-ion cells as adopted from reference.[279]

There exist multiple aging mechanisms due to the interactions of the subcomponents, of both mechanical and chemical origins, which are all closely interrelated. Chemical degradation mechanisms are due to SEI formation, electrolyte reduction and decomposition, binder decomposition, solvent co-intercalation, active material dissolution, gas evolution, and lithium loss.[313,314] Reduction of the electrolyte could occur through the lithiated anode within a range of low potential, otherwise oxidation could occur through the de-lithiated cathode in a high potential range. Impurities in the electrolyte could act as catalysts for side reactions.[315–317] Side reaction kinetics are strongly reliant on variables such as temperature and cell voltage, whilst the redox reactions at the electrodes with the electrolyte contributes to SEI layer

formation, causing an increase in impedance and fade in capacity. Figure 1.9 portrays degradation processes occurring on the graphite negative electrode.[278]

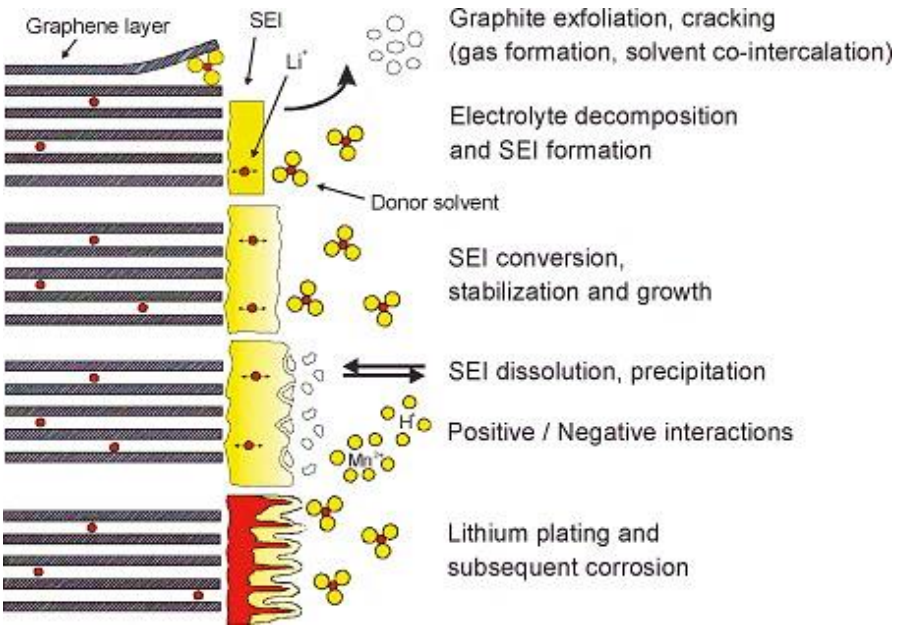


Figure 1.9 Changes and degradation processes at the anode/electrolyte interface reproduced from reference.[278]

Commercial carbon-based anodes exhibit an intercalation reaction mechanism, examples of materials are graphite and hard carbon. Anodes of these materials possess reasonable and reversible lithium ion storage capacity, with graphite being a common base material for anodes in commercial Li-ion batteries.[318,319] However, anodes could certainly have and would benefit from a higher storage capacity of lithium ions, and in addition these materials suffer with a slow loss of capacity. Furthermore, graphite anodes require specific solvents that do not encourage graphite exfoliation, whilst allowing reversible lithium intercalation: there are few carbonate-based solvents that allow this.[320,321] Development for new Li-ion battery anodes has revolved around the wish to replace graphite as the material of choice. There are certain requirements that must be satisfied in order to produce a material that will succeed graphite; (a) the material must comprise of elements or compounds of low atomic weights,

be of low density, and contain a high ratio of lithium per formula unit; (b) the material must possess high stability and cyclability in order to generate capacities that are large, retainable and reversible; (c) the material must have a potential similar to that of lithium metal, which, in combination with a cathode material of high voltage, would enable a high operating voltage of the battery; (d) the material cannot be soluble in the electrolytic solvents, and must be chemically inert to the electrolytic solvent or salts; (e) the material must be commercially viable in that the anode must be economical, environmentally green, safe, and have a high electrical and Li-ion conductivity.

Research on electrode materials has had successful development in the field of nanomaterials with high capacities at high current densities, particularly for anode materials.[322–324] Currently, anode materials generally demonstrate lower operating voltages, but higher capacity than cathode materials. Therefore, the goal of achieving Li-ion battery cells of sufficiently high energy density, power density, and high operating voltages should be possible to achieve by a combination of these anodes and cathodes. Nanostructured materials exist in the wide range of zero to three dimensions, creating capacity for tailoring structures to specific requirements. Li-ion diffusion paths are generally short in zero-dimensional electrodes, this stops the material being able to accommodate the stresses of lithium intercalation and de-intercalation.[325–327] Nanostructures of one-dimension generate a straight path along the growth direction for efficient charge transport.[328,329] Materials comprising of one-dimensional nanostructures show improved electrode kinetics and higher rate capability but suffer from a number of disadvantages. These nanostructures have low mechanical and structural stability owing to aggregation, possess poor surface properties, detrimental cyclic stabilities, and low electrical and electronic conductivities.[326,330,331] Improved structural stability, rate performance and cyclic stability is gained by moving to two-

and three-dimensional nanostructured materials.[332–334] Two-dimensional nanosheets or monolayers have gained a large attention within scientific and engineering community due to reports of the use of graphene and its composites, as well as metal dichalcogenides.[335,336] These atomic or several molecule thick nanostructures show extraordinary physicochemical properties compared to their bulk analogue, characterized by strong in-plane bonds and weak van der Waals coupling between the layers. The two-dimensional nanomaterial graphene has been largely researched, separately to graphite, as an ideal material for carbon-based electrodes due to the unique physicochemical properties it possesses.[318] Graphene has high electrical conductivity, high surface area, is light and chemically stable, hence it is ideal for high capacity energy storage. It allows far higher efficiency of lithium intercalation due to its structure, and can therefore significantly reduce charging times.[338] As a material, it exhibits additional properties such as the bipolar field-effect, ferromagnetism, quantum hall effect, high electron mobility and superconductivity.[338] Unfortunately, graphene can still not directly compete with and replace graphite as an anode material, as it has a rather low coulombic efficiency, high platform for charge and discharge and relatively low capacity for lithium storage.[339] In addition, issues with scaling up graphene productions impedes its wide implementation in Li-ion battery systems.

1.5.6 Molybdenum disulphide as an alternative to graphite/graphene

Commercially available graphite anodes many drawbacks associated with the non-ideal safety aspects and low capacities they exhibit. Large-scale applications requiring safe and reliable electrode materials capable of high energy densities and power densities provide the need for the search for graphite's replacement.[282,340,341] Molybdenum disulphide (MoS_2) is a two-dimensional transition metal dichalcogenide that, due to its unique layered structure, has

shown great promise as a next-generation anode material. It comprises of a molybdenum layer sandwiched between two layers of sulphur, and exhibits high theoretical capacity and low cost.[342–344] Another advantage to MoS_2 as an anodic material over graphite is its ability to increase the lifetime of the Li-ion battery cell by use of higher lithium ion intercalation voltage as well as impeding lithium metal dendrite formation.

MoS_2 is a semiconductor with trigonal (2H) structure; where the sulphur atoms align in the lattice positions of a hexagonal close-packed (hcp) structure. Molybdenum atoms are arranged in a plane and sit between two layers of atomic sulphur, wherein every molybdenum atom is coordinated to six sulphur atoms in trigonal prismatic geometry. Another polytype of MoS_2 with tetragonal symmetry is the octahedral phase (1T) which comprises of individual MoS_2 layers made of MoS_6 octahedron sharing edge with each other, and one MoS_2 layer per repeating unit. The unique structure of the S-Mo-S layers and the weak van der Waals interactions between these layers allows easy favourable lithium ion intercalation and de-intercalation kinetics. This is believed to occur because of a low volume expansion during conversion reaction, in comparison to other metals.[326] The unique structure also induces transformation from the semiconducting 2H phase to metallic 1T phase during lithium ion intercalation.[328] This 1T phase is considered to be unstable under ambient conditions and will transform back to the 2H phase, which has higher thermodynamic stability, or possibly to a further two metastable polymorphs of distorted 1T structure: 1T' and 1T".[348–351] It is possible that the three 1T phases could be stabilised by electron donation through ion intercalation, whilst all three 1T phases and the 2H phase can co-exist together in the same MoS_2 nanosheet.[352,353] Hydration of MoS_2 generally results in the formation of 1T" when oxidation occurs after water reaction with the intercalated compound. These processes of hydration and intercalation provide additional electrons which support the formation of a distorted

octahedral structure. Later oxidation processes remove these extra electrons and the octahedral structure is preserved with a distortion.[354,355]

Bulk MoS_2 multi-layered particles suffer from fundamentally low electronic conductivity and degradation of layer structure, causing poor retention of capacity over long charge/discharge cycling.[345,356] There are other inherent disadvantages of MoS_2 anodes, such as large volume change of the active material and an instability of the solid electrolyte interphase.[342,345] It is therefore highly desirable to study the lithiation mechanism of MoS_2. The pristine MoS_2 phase's conversion into lithium sulphides and metallic molybdenum phases is proposed as the probable mechanism by experts in the field, but a full understanding and widely accepted conclusion is yet to be achieved.

In the first lithiation process, it has been observed that MoS_2 is transformed into metallic nanoparticles which are dispersed in a matrix of lithium sulphides and polysulphides. This provides a theoretical capacity at nearly double the capacity of a commercial graphite anode, at 669 $mAh \cdot g^{-1}$.[357] The first step in this process is a phase transition from 2H-MoS_2 to 1T-Li_xMoS_2 phases (from trigonal prismatic to octahedral), taking place from around 1.1 V versus Li^+/Li and further, and being a result of the lithium ions starting to react with sulphur atoms. Following this phase transition, at around 0.5 V versus Li^+/Li the intensity of conversion reactions increases, leading 1T-Li_xMoS_2 to disintegrate and fragment into amorphous lithium sulphides and molybdenum metal particles.[358,359] After this, fast volume expansion and generation of unstable solid electrolyte interphase occur, consuming active lithium whilst decreasing the electronic conductivity of the electrode.[360,361] The described overall reaction results in a low capacity with poor Coulombic efficiency. This is due to the fact that after reactions with lithium ions, MoS_2 electrodes are enriched with the undesirable reaction

products of polysulphide species, and also become partially dissolved within the electrolyte. When standard conductive additives are used (for example, particles of carbon at around 50 - 200 nm in diameter), there is the specific issue of low electron conductivity, as these are likely to lose electrical contact with the active particles at some point during the conversion reactions. A typical discharge profile of MoS_2 active material during lithiation process is shown in figure 1.10, and compared to density functional theory (DFT) calculations.[362]

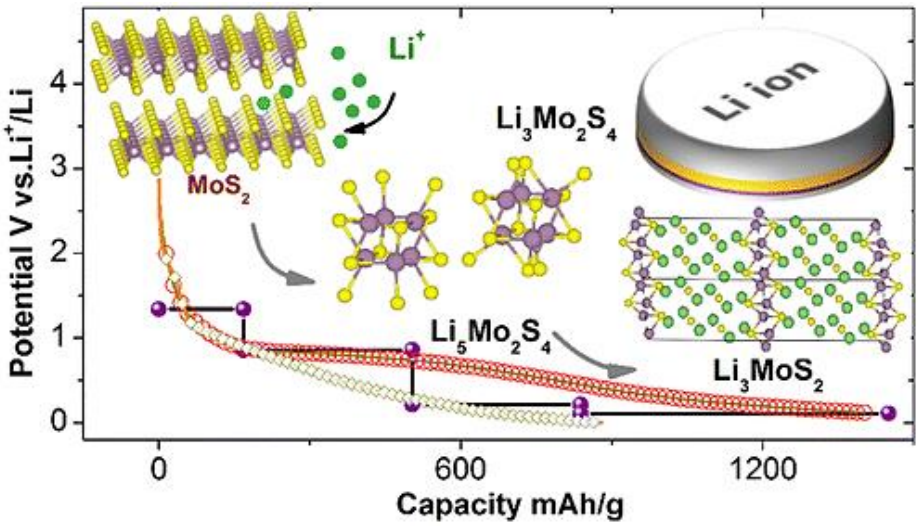


Figure 1.10 Representative discharge profiles from the first cycle of MoS_2 as active electrode material relative to Li^+/Li calculated from DFT energies by C. George et.al. and reproduced from reference.[362]

This is rather surprising when compared to MoS_2 nanostructures and nanocomposite materials, which exhibit improved performance of lithium storage likely owing to their large surface area, short path of diffusion, and morphology that can be tuned.[355,363–370] The MoS_2 layers allow intercalation of lithium ions into their interstitial structures, forming the intermediate phase of Li-Mo-S before a conversion reaction can occur. The fact that the lithium is accepted into the MoS_2 in a two-step process indicates that the structural tension applied in the lithiation process can in part be reduced. This is evidence for the reports of

competing processes lithium intercalation and partial conversion, but the effect of this on the mechanism of lithium reaction in nanostructures in comparison to bulk MoS_2 continues to be unsolved.

The conversion reaction accommodates a significant volumetric expansion, the stress of this must be alleviated to impede fast fading of capacity and to achieve cycling stability. A trend that has lately been validated many times shows that nanostructured analogues for negative electrode materials regularly surpass their bulk equivalents within the variables of capacity and cycle life. With this in mind, there is a wide range of emerging nanostructured electrode materials making a highly competitive Li-ion battery field with regards to electrochemical performance. In comparison to the rest of the field, MoS_2 performs well in experimental reversible specific capacity, with values up to 1290 $mA{\cdot}h{\cdot}g^{-1}$ reported in the literature for MoS_2 nanocomposite electrodes.[371] MoS_2 with increased interlayer distances is expected to supply a larger space for lithium intercalation and its diffusion. By increasing this interlayer distance, the diffusion energy barrier for ion intercalation is decreased, improving intralayer conductivity, which would be beneficial in electrochemical energy storage devices based on ion intercalation processes. Ion intercalation energy has been showed to be lowered by increasing the interlayer spacing in MoS_2 using density functional theory (DFT) simulations with van der Waals corrections. Optimum interlayer expansion for intercalation of lithium ions has been calculated as 11 % and 23 % for sodium ion intercalation compared to in the bulk MoS_2.[372] This suggested mechanism of improved lithiation and cycling ability of nanostructured MoS_2 electrodes seems reasonably likely to be correct. However, the widely accepted mechanism for conversion of MoS_2 fails to align with reports of improvements in stability and cycling ability of these electrodes.

Decades of research and inherent fundamental scientific advantages have brought the Li-ion battery to its current state of high energy density, high cycle life, high efficiency. Yet there are still more boundaries to push and barriers to overcome with regards to cost, energy density, power density, cycle life, and safety.[340] There are many promising electrode materials developed, but most still have not yet achieved optimum electrical conductivity, speed of lithium transport, inertness to unfavourable interactions with the electrolyte, thermal stability, mechanical stability or resistance to high volume expansion. As research continues, new materials and processes of producing them will enable these barriers to be pushed ever further, enabling Li-ion batteries to have yet higher bearing in our lives in the future.

1.6 The Objective of the Thesis

The aim of this thesis is to develop new inorganic based nanoparticles by using nano-engineering tools in solving some of the current major chemical industrial challenges. Three experimental works (Chapter 2, 4-6) are presented in this thesis with reference to the above literature.

Acid catalysis is one of the most important areas of catalysed industrial processes across all sectors of chemical manufacturing. Innovative engineering of novel functionalised metal oxide nanoparticles can deliver highly sought-after greener alternatives to the large industrial use of mineral acids, and make many chemical processes in industry safer and more environmentally friendly. Highly active solid acid catalysts can be achieved by introducing high surface area metal oxide nanoparticles with unsaturated sites and engineering highly acidic functional groups on their surface. Sulphate functional groups on metal oxide nanoparticles can provide high thermostability, strong acidity, and unique catalytic activities in many environmentally benign reactions. In this regard, Chapter 4 will present the preparation of

very small, high surface area TiO_2 nanoparticles, their in-depth characterisation using highly sensitive probe solid state ^{31}P NMR to investigate their remarkable acidity and catalytic application in the biomass esterification reaction of levulinic acid, and in the Cannizaro reaction to produce lactic acid on account of their dual functionality in terms of Brønsted and Lewis acidity.

Palladium catalysts have found a wide use of applications spanning from pharmaceutical industry to chemical manufacturing and catalytic converters in automobile exhausts. However, the rare abundance of palladium ore deposits mean that the catalysts are often very expensive and are not cost efficient. In order to increase the cost efficiency of these catalysts, an improvement in activity and reduction in expensive metal mass is needed. Although palladium is a very well performing catalyst, an enhancement in activity and reduction in cost can be achieved by employing catalytically active stable single atoms or very small nanoparticles while maintaining the close contact of the active metal with an electron rich support. Chapter 5 will address these challenges by creating large and stable doping sites for Palladium atoms on exfoliated MoS_2 nanosheets.

Batteries have emerged as an essential energy storage system for renewable energy applications for future generations. However, rechargeable Li-ion batteries lack in rapid and efficient charging abilities leading to quick degradation of the electrode material and undesirable chemical reactions within the electrochemical system, particularly when high volumetric currents of fast charging and discharging is used. Inorganic nanomaterials have been under extensive investigation for their promising electrochemical properties to solve these issues via their excellent kinetics and cycling stability, stable rapid ion and electron transport, increased contact area with the electrolyte and an improved lithium-ion access

within electrode material. However, application of nanomaterials also comprises several limiting disadvantages that have to be tackled in any rational electrode design such as costly manufacturing on large scale, electrolyte degradation and undesirable side reactions, and uncontrolled solid-electrolyte interface growth. Chapter 6 presents an attempt to develop Li new battery materials by using single/thin layers of transition metal chalcogenides.

Chapter 2 Analytical techniques

2.1 Introduction

Characterisation and analytical techniques are methods widely used in the development of nanomaterials for applications in catalysis, semiconductors, and energy storage systems. Many analytical techniques have been used for the work presented in this thesis; ranging from microscopy, which provides understanding of metal particle size, dispersion and shape; to spectroscopy, which examines adsorbates at the material surface alongside providing information about electronic properties of inorganic materials. There is no single analytical technique that superposes the others – a combination of complementary methods is essential to gaining true understanding of the properties of nanomaterials.

Analytical characterisation techniques are methods used to identify, quantify or isolate materials, and to characterise their physical properties. Techniques include microscopy, light or radiation scattering, diffraction, spectroscopy, calorimetry, chromatography, thermal methods and the probing of molecules adsorbed on the material surface; which all provide information regarding the geometry and composition of inorganic nanomaterials, as well as their electronic properties. The majority of characterisation methods can be split into two regimes – probing the surface of the material in the nanoscale (0 – 3 nm), or investigating the whole material in its bulk form. Generally, for the characterisation of nanosized materials where particle sizes are often small enough to sit within the order of 10 nm, surface techniques prevail.

2.2 Powder x-ray diffraction

To generate x-rays in a laboratory scale diffractometer, such as the one in Oxford's Inorganic Chemistry Laboratory, a Cu source is bombarded with high energy electrons. As a result of this bombardment, electrons in the core levels of the Cu are ejected, leaving holes for the higher energy electrons to drop down into. As the high energy electrons become more stable, they release their energy in the form of x-rays with a wide spectrum of wavelengths. To produce a beam of single wavelength, the x-rays are then passed through a collimator and monochromator. When these x-rays hit the crystalline sample, they are elastically scattered by the electrons in its atoms, diffracting and undergoing constructive and destructive interference. The angles at which constructive interference occurs are specific to the material and are defined by Braggs Law:

$$2d \sin\theta = n\lambda \tag{1}$$

Where d is the interlayer spacing of the crystallographic planes, θ is the angle of incidence of x-rays to the crystallographic places, n is an integer, and λ is the wavelength of the incoming x-rays.

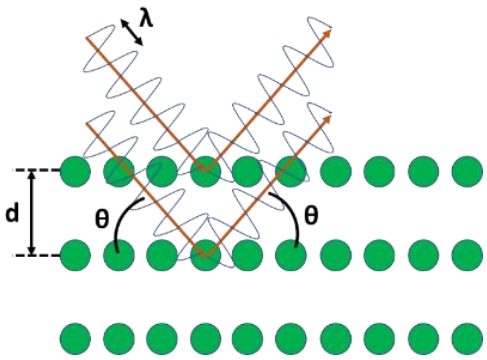


Figure 2.1 Schematic representation of the Bragg equation

Where Braggs Law is satisfied and the angle of incidence produces constructive interference, a reflection peak in the profile is observed. Crystal lattice type, unit cell parameters and

wavelength of incident x-rays determine the specific positions of these reflections. Intensity of reflections is dependent on the relative locations and the type of atoms scattering the x-ray beam.[373] The pattern produced can be identified by comparison with an existing database containing over 50,000 unique powder x-ray diffraction patterns.[374]

Where the angle of incidence produces destructive interference, reflections cancel each other out and no peaks are observed in the profile. Figure 2.1 shows an example where destructive interference is observed; the two incident rays are in phase before reflection, and are out of phase after reflection. Constructive interference can occur at other angles of incidence.

Where constructive interference is observed, Braggs Law is used to calculate the interlayer spacing of the crystallographic planes. Further to this, equation 2 is used to calculate the lattice parameter for crystalline materials with a cubic lattice:

$$\frac{1}{d^2} = \frac{h^2+k^2+l^2}{a^2} \tag{2}$$

where d is the interlayer spacing; h, k, and l, are Miller indices and a is the lattice parameter. Small shifts in the diffraction angle can identify a change in the lattice parameter, and can be used to confirm a compression or expansion of the crystalline lattice.

For extended crystals with long-range order, the only angle at which reflections are seen is the diffraction angle, as destructive interference is inhibiting at all other angles. This creates sharp peaks only at the diffraction angles. Nanomaterials have no long-range order, resulting in a less pronounced difference in constructive and destructive interference, leading to peak broadening. The mean crystallite size can be correlated with this peak broadening by the Scherrer equation, equation 3:

$$L = \frac{K\lambda}{\beta \cos\theta} \tag{3}$$

Where L is the average crystalline size, K is the shape factor (usually 1), λ is the wavelength of the incident x-rays, β is the full-width-half-maximum (FWHM) and θ is the diffraction angle. The FWHM is calculated as the width of a peak at half of its maximum height, and is used as a measure of extent of peak broadening.

The Scherrer equation can be used as a guide to estimate particle size. Most commonly, it provides a lower limit for particle size, as there are other factors unaccounted for in the equation that can induce peak broadening. Examples of other factors include strains and imperfections in lattices, twinning of particles and effects of instruments used. To obtain a reliable determination of particle size, a combination of XRD and other methods such as electron microscopy and dynamic light scattering are used.



Figure 2.2 Bruker D8 Advance Eco diffractometer in the Inorganic Chemistry Laboratory building (Department of Chemistry, University of Oxford).

2.3 Transmission electron microscopy

Transmission electron microscopy (TEM) is a very useful analytical tool for studying nanoscale morphologies of materials. TEM provides information regarding the size and shape of

nanomaterials, as well as very fine details of their internal structure.[375] The TEM method is similar in principle to that of an ordinary optical microscope; TEM differs in two main ways; in source – electrons instead of photons; and lenses – electromagnetic instead of optical – to focus the beam. Figure 2.3. shows the structure and cross-section of a typical TEM. Tungsten filaments, LaB_6 crystals or field emission guns are used as the electron source. The electrons are then accelerated to achieve an energy with wavelength smaller than typical interatomic spacing and focused at the sample by a series of magnetic lenses.[376] Samples must be thinner than 100 nm, otherwise the electrons cannot penetrate the specimen. To achieve this maximum thickness, the sample can be dispersed in a volatile solvent prior to loading onto the TEM grid. The electron beam that transmits through the sample is refocused by a set of further lenses to project onto a phosphor screen. A charge coupled device camera is used to capture the image of the sample. Resolution of a TEM image is dependent on the electron wavelength, therefore, to achieve a resolution of 0.3 nm, the typical operating voltage will range from 100 – 200 keV (λ = 2.5 to 3.7 pm) under 10^{-6} mbar vacuum.

Typical optical microscopes offer a resolution of the order of the wavelength of visible light, at 1 μm. This is large in comparison to the structures that we wish to probe when working with nanoscale materials. TEM, by using an electron beam with wavelength below 0.1 nm, can offer a resolution down to 0.1 nm. This secures TEM as one of the most powerful characterisation tools as it permits the observation of structural features, dispersion across supports and particle morphologies in the nanoscale. In contrast to the x-ray techniques discussed in this section, the power to focus electron beams means TEM provides qualitative information of only the small area probed, rather than from the whole sample.

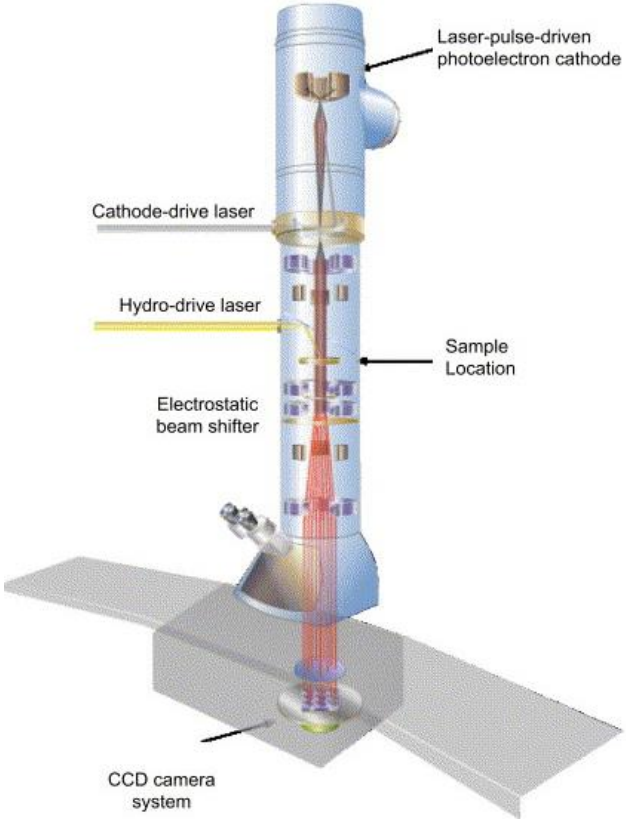


Figure 2.3 The structure and cross-section of a typical TEM.[377]

A current, higher than the work function of the cathode material, is passed through the cathode filament (LaB_6) to induce emission of electrons. These electrons are focussed through multiple magnetic lenses onto the sample. Without an objective aperture, there would be very little contrast contained in the image. Whether diffracted or non-diffracted electrons pass through the objective aperture depends on the point on the back focal plane at which it is opened. In bright field TEM, the objective aperture allows non-diffracted electrons through to create an image where the atomic structure is within the shadows of the bright field image. Conversely, in dark field TEM, the objective aperture allows only the diffracted electrons to pass through, creating a dark field image where the atomic positions are shown by the focal locations of the electrons within the image. This diffraction contrast is used to observe the main crystalline features of the sample.



Figure 2.4 Left: JEOL 3000F Field Emission Electron Microscope. Right: JEOL ARM200F Aberration-corrected high-resolution (scanning) transmission electron microscope. Both microscopes belong to the David Cockayne Centre for Electron Microscopy (Department of Materials, University of Oxford).

2.4 Scanning transmission electron microscopy and ptychography

Scanning transmission electron microscopy (STEM) is a type of transmission electron microscopy.[378] STEM follows the same method of image formation of TEM. However, in STEM, the electron beam is focused to a fine spot with typical spot size of 0.05 – 0.2 nm, wherein this focal spot is raster scanned over the sample in an illumination system constructed to ensure the beam remains parallel to the optical axis.[379] The method of raster-scanning the beam across the sample makes STEM suitable for analytical techniques such as spectroscopic mapping by energy dispersive x-ray (EDX) spectroscopy, Z-contrast annular dark field imaging,

or electron energy loss spectroscopy (EELS). These signals are obtained simultaneously, providing direct correlation of images with spectroscopic data.

Ptychography is a computational method of microscopic imaging, based on a 2D multiplicative approximation, to model the interaction of the specimen and the probe, a method originally suggested by Hoppe.[380,381] It generates images through the processing of multiple coherent interference patters scattered from the object of interest. The interference patterns are generated by a field of illumination, or an aperture stop moving laterally by a known amount with respect to the specimen or a wave field, which fall under the title of translational invariance, the distinguishing feature of the model. The interference patterns occur some distance out from the field of illumination or wave field, in order that the scattered waves spread out and fold into one another, as shown in Figure 2.5. One important benefit of this model is that it does not rely on the object absorbing radiation, as it is sensitive to the phase of the radiation that has passed through the specimen, thus allowing transparent objects to be seen with clarity.

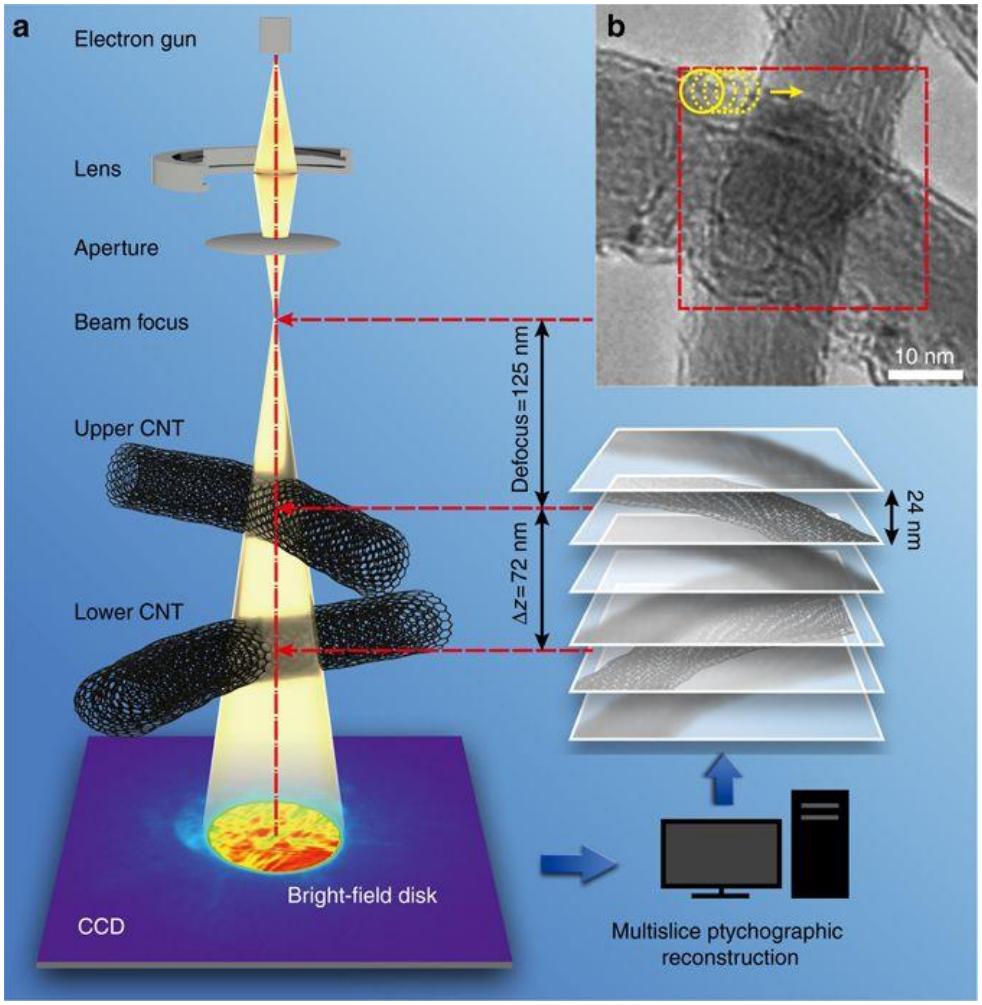


Figure 2.5 Schematic diagram of a typical STEM ptychography experimental set-up adapted from reference.[382]

2.5 X-ray photoelectron spectroscopy

X-ray photoelectron spectroscopy (XPS) is the most sensitive technique when it comes to probing the sample surface for information about element composition and corresponding oxidation state. The surface is irradiated with x-rays of known energy, causing valence or core electrons of the targeted atom to be ejected from the nucleus with kinetic energy E_k, as shown in Figure 2.6.

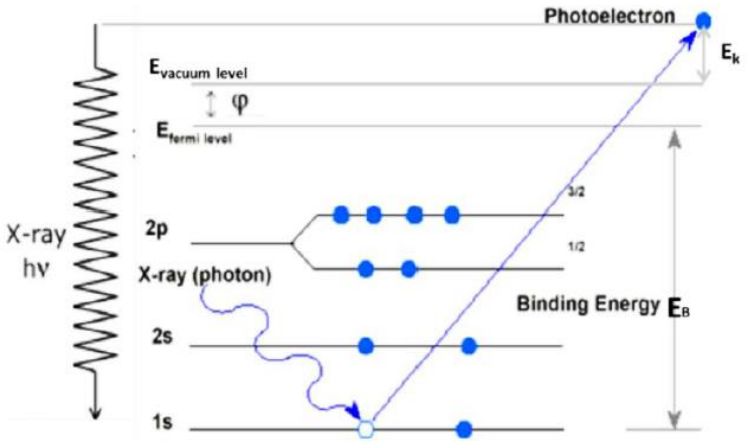


Figure 2.6 Schematic diagram of photoelectron emission stimulated by x-ray absorption.[383]

The binding energy of the electron (E_B) provides information regarding its host element as well as corresponding oxidation state. This binding energy of the electron is directly related to the detectable kinetic energy of the ejected electron (E_k), thus allowing the determination of the binding energy of the electron by Equation 4:

$$E_B = h\upsilon - E_k - \phi \quad (4)$$

where E_k is the kinetic energy of the ejected electron; h is Planck's constant; υ is the frequency of the incident X-ray; E_B is the binding energy of the ejected electron; ϕ is the work function of the spectrometer.

Generally, XPS is used for quantitative analysis of the surface chemical composition that can be achieved by integration of the area below the peaks in the signal generated. XPS as a technique is interesting for use with nanomaterials: as whilst x-rays can penetrate deeply into a non-nanoscale samples, only a small fraction of surface photoelectrons – within a small distance from the surface – can escape the material to be detected by the spectrometer; whereas with nanoscale materials, the entire material's thickness can be in the order of the region from which all ejected electrons can feasibly escape the material. Therefore,

quantitative analysis of XPS signal, when used with nanoscale materials, can give fairly accurate data as to the proportional composition and corresponding oxidation states of the entire bulk sample, not limited to surface probing.

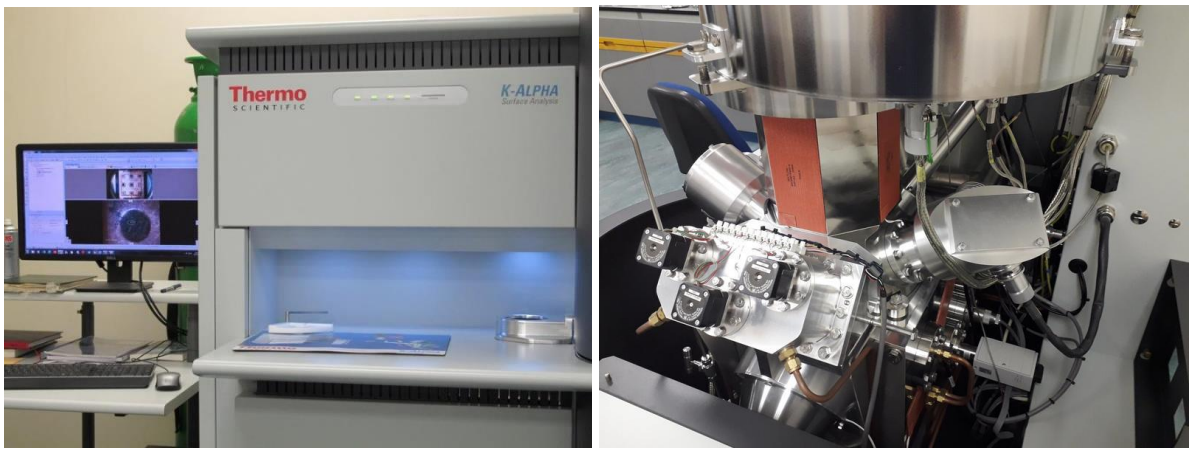


Figure 2.7 Thermo Scientific K-Alfa XPS instrument equipped with a microfocused monochromated Al X-ray source in the Oxford Materials Characterization Service Centre (Begbroke Science Park, University of Oxford).

2.6 Energy-dispersive x-ray spectroscopy

Energy dispersive x-ray spectroscopy (EDX) is another useful technique for identifying elemental composition. EDX is commonly used with TEM, therefore the sample is probed in a localised method across the microscopy image.[379] TEM's high-energy electron beam can be used in a similar method to XPS to probe electronic states of atoms. XPS analyses the whole sample surface up to a depth of 3 nm, where TEM probes only a small segment.

An incoming beam of electrons causes excitation of a core electron, creating a core hole. A higher energy electron undergoes relaxation and fills this core hole, emitting an x-ray characteristic of the element. The detected x-ray emissions are used to quantify the concentrations of these elements in the sample region probed. The sample spot focus is scanned across the sample to create two-dimensional qualitative maps of elemental

composition, as well as one-dimensional linear scans and individual point analysis in regions of interest.

2.7 Magic angle spinning nuclear magnetic resonance

Nuclear magnetic resonance spectroscopy (NMR) measures a molecule's chemical shift to determine chemical, physical, electronic, and structural information. Analysis of a sample is not restricted to its surface, as it is a bulk technique. It is also highly element specific, and can therefore be used to probe individual elements in the sample with a high degree of resolution.

When an NMR active nucleus with a permanent magnetic dipole (i.e. a non-zero nuclear spin) is placed in an external magnetic field, its spin will align in a direction which is either parallel or anti-parallel to the external field. Radio frequency (RF) pulses are directed at the sample, which absorbs the radiation at the frequency required to reverse the alignment of the spin in the external field.[384]

The RF value at which each NMR active nucleus will resonate is specific to its chemical, structural, and electronic environment. Small changes in the environment of each nucleus will shift the RF value slightly. A more electron rich environment will shield the nucleus from the magnetic field, with less energy required to reverse the spin, resulting in a lower RF value for the transition, and a peak of lower chemical shift value. A less electron rich environment will deshield the nucleus, with more energy required to reverse the spin, leading to a higher chemical shift value.[385]

In the solid state, due to limited vibrational and rotational movement of molecules, each atom will be in a slightly different electronic environment, causing broad peaks in the NMR spectrum. This is because many of the spin interactions that affect RF value of transition are

anisotropic, and therefore, without continuous movement of the sample, extensive atomic-level molecular structural information is difficult to obtain. A method to reduce peak broadening is Magic Angle Spinning (MAS), where the sample is spun at an angle of 54°74'. This reduces the interaction of the adjacent molecules, reducing the effect of peak broadening.[386] This method can be limited by restrictions in mobility in the molecule, therefore not allowing the reduction in peak broadening.



Figure 2.8 The Bruker AVIII 400 (solid state) NMR spectrometer in the Chemistry Research Laboratory building (Department of Chemistry, University of Oxford).

2.8 Trimethylphosphine (TMP) adsorbed probe for ^{13}P MAS NMR

Lunsford and co-workers were the first to adopt the method of using trimethylphosphine (TMP) probe and solid state ^{31}P MAS NMR for the characterisation of different solid acid sites to study the acidity of zeolites by means of the NMR ppm shifts in 1994. [387] ^{31}P MAS NMR

measurements with NMR TMP probe can be used for detailed characterization of different acid sites and their strength in TiO_2 solid acid catalysts. The strength of interaction of the adsorbed TMP molecule with each acid site, Lewis acid or Brønsted acid, can be differentiated by the ^{31}P chemical shift of adsorbed TMP. Typically, -2 to -6 ppm is associated with the $TMPH^+$ ionic complex formed by the reaction of TMP molecules with Brønsted acid protons (proton donor) of the solid acid, while TMP chemisorbed at Lewis acid (electron acceptor) sites spans over a wider range of -20 to -58 ppm. The wide range makes it easy to differentiate the strength of the Lewis acid, with a less negative ppm value indicating a stronger Lewis acidity. Furthermore, quantitative analysis of the deconvoluted ^{31}P NMR peaks can be used to account for the amount of acid sites of each acid type.

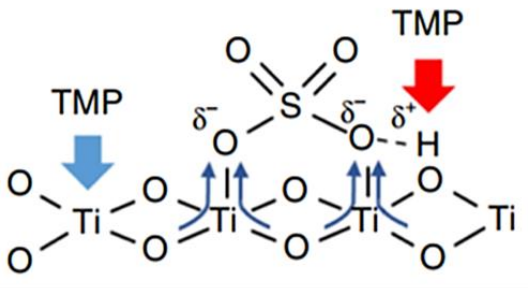


Figure 2.9 TMP molecules interacting with Lewis and Brønsted acid sites on sulphated TiO_2 catalyst.[383]

2.9 Electron paramagnetic resonance

Electron Paramagnetic Resonance (EPR) is a technique used for studying materials with unpaired electrons. Electrons have magnetic moment and spin quantum number, s = ½, with magnetic components m_s = + ½ and m_s = -½. Without an external magnetic field, electrons in the two separated energy levels are degenerated and follow the Boltzmann distribution. With the application of an external magnetic field of strength B_0, the electron's magnetic moment

aligns itself parallel (m_s = + ½) or antiparallel (m_s = - ½) to the field, governing the splitting of the energy level. Each alignment has a specific energy due to the Zeeman effect:

$$E = m_s g_e \mu_B B_0 \quad (5)$$

where *E* is the energy level of the unpaired electron, B_0 is the strength of magnetic field, μ_B is the Bohr magneton, g_e is the electron's "g-factor" (g_e = 2.0023 for the free electron).[388] Equation 5 implies that the gap between the two states for unpaired free electrons is proportional to the strength of the magnetic field (I.e. $\Delta E = g_e \mu_B B_0$) (Figure 2.10).

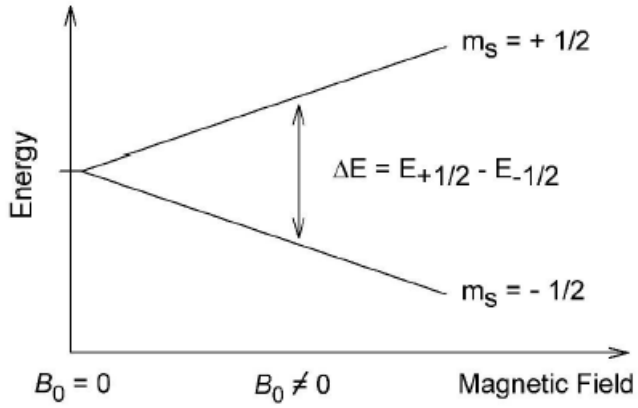


Figure 2.10 Schematic diagram of energy splitting of unpaired electron with the stimulation an of external magnetic field.[383]

Unpaired electrons can be excited from lower to higher energy levels by exposing them to microwaves with energy equal to ΔE. G-factor can be calculated using the frequency of the absorption signal. For an unpaired electron sitting on a radical or defect, the effective field strength (B_{eff}) it experiences is affected by the surrounding atoms:

$$B_{eff} = (1 - \sigma) B_0 \quad (6)$$

where σ is the total effect of all the surrounding atoms. The EPR signal should be observed at:

$$h\vartheta = g_e \mu_B B_0 (1 - \sigma) \quad (7)$$

The change of the chemical environment of the unpaired electron is indicated by a shift in the g_e value. This means that EPR is a sensitive technique for detection and identification of free radicals or paramagnetic centers.



Figure 2.11 The X-band CW EPR spectrometer in the Inorganic Chemistry Laboratory building (Department of Chemistry, University of Oxford).

2.10 Inductively coupled plasma-atomic emission spectroscopy (ICP-AES)

Inductively Coupled Plasma-Atomic Emission Spectroscopy (ICP-AES) is a type of emission spectroscopic technique used for the detection of metal elements in materials. Inductively coupled plasma is used to produce excited atoms and ions that emit electromagnetic radiation at characteristic wavelengths of a particular element. Atomic emission spectroscopy consequently measures the characteristic electromagnetic radiation emitted from decaying

atoms and ions, and provides elemental identification and quantitative analysis, where the intensity of the emission shows the concentration of the corresponding element.[389,390]

Solid samples of known weight are digested in concentrated acidic media and subsequently diluted to the required concentration for the ICP-AES detector to avoid any oversaturation. The sample solution is injected into the ICP-AES instrument where it is atomized and thermally excited by the inductive coupled plasma in the stream of argon gas at temperatures close to 7000°C. The relaxation of these outer-shell excited electrons as they return to the ground state is accompanied by the emission of photons with a specific energy characteristic of each element in the sample.[391] The quantification of each element requires the use of a known wavelength for excitation of the outer-shell electrons. The intensity of the emitted photons is then proportional to the concentration of the analysed element. In this project, the ICP-AES data of solid samples were measured in collaboration with Johnson Matthey Technology Centre, Sonning Common, United Kingdom.

2.11 Raman spectroscopy

Raman Spectroscopy is a non-destructive spectroscopic analysis technique used to provide detailed information about chemical structure, phase and polymorphism, crystallinity or molecular interactions. The method's typical use is for the determination of vibrational modes of molecules, although other lower-frequency modes of systems such as rotational modes may also be observed.[392]

The method is based on the interaction of light with the chemical bonds of the sample: a molecule scatters light incident from a high intensity laser source. Most of the light scattered off the molecule is of the same wavelength as the source and does not provide useful information – this is called Rayleigh Scattering. A minimal amount of light is scattered at

different wavelengths, dependent on the chemical structure of the sample – this is called Raman scattering. Raman scattering results in a spectrum of a number of peaks, indicating the intensity and wavelength of the Raman scattered light. Each peak provides information as to a specific molecular feature such as bond vibrations, including individual and groups of bonds, polymer chain vibrations or lattice modes. The Raman spectrum profile provides a unique chemical fingerprint for identification of the material. For ease of chemical identification, comprehensive libraries of Raman spectra exist for comparison.

2.12 Thermogravimetric analysis (TGA)

Thermogravimetric Analysis (TGA) is an analysis technique that measures change in sample mass as a function of time or temperature. Changes in mass – when a material is heated, cooled, or temperature is kept constant – can be indicative of a material's physical and chemical properties, shown by physicochemical changes such as solvent loss, desorption, vaporization, oxidation and decomposition.[393]

A small mass of the sample is loaded into a Pt or Al_2O_3 pan and sealed into a measurement furnace purged with an inert or reactive gas. The weight of the pan is monitored by a microbalance throughout the experiment, over the period of the temperature ramp or isothermal time, and compared to the tared pan. Small changes in mass can be observed, and are attributed to volatile solvents, desorption of adsorbates, or decomposition of polymers and supports.

2.13 BET isotherm - surface area measurement

The Brunauer-Emmett-Teller (BET) isotherm is an important analysis technique for the measurement of the specific surface area of a sample.[394] The theory is an extension of the

Langmuir theory, which is a theory for monolayer adsorption to multilayer adsorption; with the assumption that layers with exposed surface area are in equilibrium with the adsorbate species.[395] The BET isotherm is described by the following:

$$\frac{P}{V(P_0-P)} = \frac{1}{V_m C} + \frac{(C-1)P}{V_m C P_0} \quad (8)$$

where V is the absorbed gas quantity at pressure P, V_m is the monolayer adsorbed gas quantity, P_0 is the saturated vapour pressure of adsorbate at the temperature of adsorption, C is the BET constant, a function of the heat of adsorption.

A t-plot analysis of the adsorption branch of the isotherm is used to determine the microporous surface area and volume. Pore size distributions of samples are analysed from the desorption branch of the isotherm by the BJH method.[396]



Figure 2.12 Micromeritics Tristar II Plus BET instrument at the Surface Analysis Facility (Department of Chemistry, University of Oxford)

2.14 Temperature programmed reduction (TPR)

Temperature programmed reduction (TPR) is a technique for determining the quantity of reducible species in a sample and the temperature of reduction. TPR can be used to detect

the induced reduction of a secondary metal at the temperature of reduction of the primary metal. When the primary metal reaches reduction temperature, there may be a coupled reduction with adjacent metals, forming reduced metal species on the primary metal surface.

Hydrogen gas is passed through a fixed bed of the sample that is packed into a quartz reactor tube, which sits within a temperature programmed furnace. The gas output is passed through a TCD detector which monitors change in hydrogen concentration relative to the input gas. Reduction occurring in the sample leads to a lower concentration of hydrogen in the output gas, showing a positive peak. A higher concentration of hydrogen, caused by expulsion of hydrogen from the sample, shows a negative peak. The reactor tube can be submitted to a programmed temperature ramp, allowing study of reduction over a temperature range. A method to improve accuracy of measurement is to remove surface contaminants that could affect the data by heating samples to a specific temperature under an inert gas or vacuum prior to BET measurement.

2.15 Gas chromatography-mass spectrometry (GC-MS)

Gas chromatography-mass spectrometry (GC-MS) is a tool comprised of two techniques, GC and MS, for conclusive chemical identification, although it is not without limitations. The individual techniques alone are insufficient for reliable identification of chemical compounds. GC, as shown in Figure 2.13, is used for the separation of molecules from a mixture by the use of a capillary column, and depends on the molecular difference in interaction with the stationary phase of the column. The difference in interaction is observed by different retention times before elution of the various molecules within the capillary, resulting in separation of the components. The difference in vapour pressure between the mobile phase (e.g. helium as an inert carrier gas) and the gaseous analyte separates the components in the

sample mixture. This elute is fed into the MS for separate identification of each of the different molecules. MS ionises and breaks the sample molecules into smaller ionised fragments, which are accelerated and subjected to an electric or magnetic field which deflects the fragments according to their charge-to-mass ratio. The resulting spectra is used to identify the sample by correlating to known masses or characteristic fragmentation patterns.



Figure 2.13 The 7890B Agilent Gas Chromatography System in the Wolfson Catalysis Laboratory (Department of Chemistry, University of Oxford).

2.16 Electrochemical cycling

Electrochemical cycling, or charge-discharge cycling, is a technique wherein electric current is controlled and potential is measured. This electrochemical technique is widely used for research into rechargeable batteries. The method typically applies a current between the positive and negative electrodes of a battery, with direction of current determining charge or discharge of the battery. The applied current is expressed with the nomenclature of 'C-rate' within the battery industry, to enable normalisation against battery capacity which varies

between batteries. C-rate is a measure of the rate of discharge of a battery relative to its maximum achievable capacity. For example, a 1 C rate means that the battery will discharge within 1 hour at the galvanostatic discharge current applied: a 100 mAh battery discharged at a 1 C rate will deliver a current of 100 mA for 1 hour; a 3 C rate for the same battery would deliver 300 mA for 20 minutes; and a 1/5 C rate would delivery 20 mA for 5 hours.

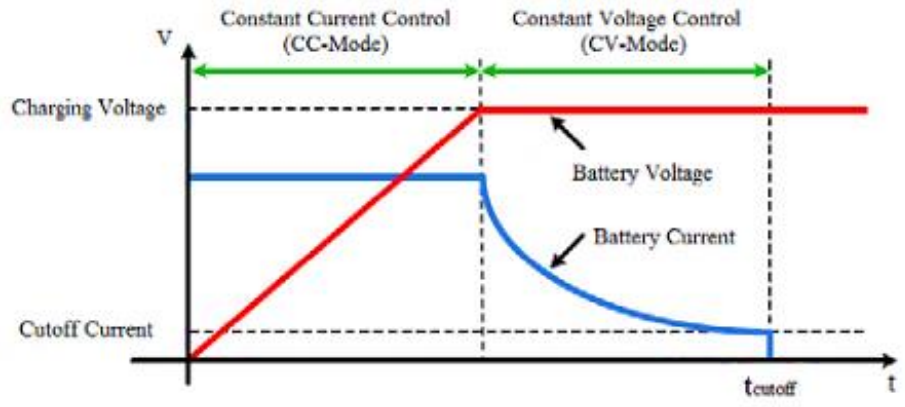


Figure 2.14 Constant Current (CC) and Constant Voltage (CV) control of the battery charging with voltage and current response. Image reproduced from reference.[397]

There are a number of methods for charge-discharge cycling of rechargeable batteries. Typical cycling protocols within rechargeable lithium battery research include constant current cycling and constant current-constant voltage (CC-CV) cycling. The CC-CV charging protocol is most often used for lithium-ion battery charging, see Figure 2.14. It involves two steps for charging – initially, a constant current is applied across the battery until the upper limit of the cycling voltage window is reached; then the charger is switched into constant voltage mode, where the voltage is kept at the upper voltage limit, whilst the current decreases exponentially with time. When the current drops below a specified level, e.g. 3 % of the initial current in the constant step, the charging is terminated. The constant voltage step in the CC-CV cycling method is a saturation charge which boosts the cell/electrode capacity. However, this can stress the electrode material due to the high voltage.

Other examples of battery charging protocols are: float charging, trickle charging, taper charging and pulsed charging.

Chapter 3 Experimental Methods

3.1 Liquid exfoliation of MoS_2 via n-butyllithium intercalation

Single layer 1T crystal phase molybdenum disulphide (MoS_2) nanosheets were prepared by a standard chemical exfoliation method. Typically, 0.5 g of bulk MoS_2 crystalline powder was soaked in 8 mL of 1.6 M n-butyllithium in hexanes solution and stirred for 72 hours under inert atmosphere. 8 mL of degassed hexane solvent was added, and the diluted mixture was carefully filtered over a cellulose acetate membrane. The lithium intercalated MoS_2 powder, denoted as Li_xMoS_2, was washed 5 times with hexane to remove excess butyllithium and other organics, and then dried under vacuum for 24 hours. 0.5g of dried Li_xMoS_2 was immersed into 500 mL of H_2O and the resulting suspension was homogenized in an ultrasonic bath for 2 hours. The ultrasonic waves provide physical means to exfoliate the MoS_2 sheets and the exfoliation process is assisted by chemical reaction between lithium and water molecules resulting in LiOH and evolution of hydrogen gas in between the MoS_2 layers. The suspension was centrifuged at 5000 rpm for 20 minutes to remove unexfoliated multilayer material and supernatant was collected. In order to obtain mostly single layers, the supernatant was centrifuged another 2 times and any sediments were separated from the suspension. The supernatant suspension was basic due to defects in MoS_2 single layers and the presence of LiOH and was neutralized by dropwise addition of 1 M hydrochloric acid solution. Disruption of the delocalised negative charge on the single layer nanosheets resulted in slow flocculation of the suspended single layer MoS_2 material. The flocculates were collected using polycarbonate membrane over a suction filtration, and washed several times to remove LiOH and other contaminants, then dried under vacuum for 24 hours.

3.2 Liquid exfoliation of MoS_2 via physical exfoliation assisted by hydrazine decomposition

Few layer MoS_2 nanosheets were prepared by standard method of physical exfoliation assisted by hydrazine decomposition. In a typical experiment, 6 g of bulk MoS_2 was suspended in 400 mL of isopropanol/water (ratio 3:7). 8 mL of hydrazine monohydrate was added in a fume hood and the suspension was sonicated for 12 hours. The extended time of sonication and ultrasonic waves provide physical means to exfoliate the MoS_2 sheets and the exfoliation process is assisted by hydrazine decomposition into nitrogen and hydrogen gases, resulting in higher yields of exfoliated few-layer thick nanosheets. Dispersed few-layer MoS_2 nanosheets were centrifuged at 3000 rpm for 60 minutes and the resulting supernatant was collected and neutralized to pH 7 with 1 M hydrochloric acid solution. Disrupting the negative charge on basal planes of the dispersed nanosheets resulted in slow flocculation of the few-layer MoS_2 material. The flocculates were collected using suction filtration and a polycarbonate membrane, washed several times to remove any contaminants and dried under vacuum for 24 hours.

3.3 Tetrabutylammonium (TBA) functionalisation of exfoliated MoS_2

1 mL of 40 w% TBAOH in H_2O solution was added to aqueous suspension of about 1g of exfoliated single-layer MoS_2 nanosheets and stirred for 48 hours. TBA^+ cations are attracted to the dislocated minus charge on the exfoliated layered material and neutralises this charge misbalance. When TBA^+ establishes ionic bonds the TBA sandwiched in MoS_2 started to flocculate and sediment. The remaining TBA^+ was removed by reaction with 0.1M hydrochloric acid. The final product was obtained by vacuum filtering, washing several times with water and drying under vacuum for 12 hours.

3.4 Palladium deposition on exfoliated MoS_2

200 mg of MoS_2 nanosheets were resuspended in 2000 mL of deionised water using an ultrasonic homogenizer bath (with a power output of 35W and an operating frequency at 37kHz). 95 µL of 15.18 % $Pd(NO_3)_2$ aqueous solution was added dropwise from a pipette while being stirred vigorously. The suspension of MoS_2 with Pd precursor was stirred for 1 hour to allow Pd^{2+} species to target dislocated negative charge across the planes and on the edges of the MoS_2 nanosheets. Thereafter 76 mg of sodium borohydride (1 mM) was carefully added to the vigorously stirred solution to reduce Pd^{2+} species to Pd^0 and the solution was stirred overnight. 1 M hydrochloric acid solution was added dropwise to neutralize the suspension and initiate flocculation of Pd-doped MoS_2 nanosheets. The flocculates were collected using polycarbonate membrane over a suction filtration, and shaken and washed with copious amounts of deionised water, then rinsed 3 times with ethanol and dried at 70 °C under vacuum for 24 hours.

3.5 Silicon deposition on exfoliated MoS_2

200 mg of MoS_2 nanosheets were resuspended in 2000 mL of deionised water using ultrasonic homogenizer bath (with a power output of 35W and an operating frequency at 37kHz). 27 µL of 97 % triisopropylsilyl chloride was added dropwise to the suspension of MoS_2 using a pipette while stirred vigorously. The suspension of MoS_2 with Si precursor was stirred for 1 hour to allow Si species to target dislocated negative charge on the planes and edges of the MoS_2 nanosheets. Thereafter 76 mg of sodium borohydride (1 mM) was carefully added to the vigorously stirred solution to reduce $(i\text{-}Pr)_3Si^+$ species to Si^0 and the solution was stirred overnight. 1 M hydrochloric acid solution was added dropwise to neutralize the suspension and initiate flocculation of Si-doped MoS_2 nanosheets. The flocculates were collected using

polycarbonate membrane over a suction filtration, and shaken and washed with copious amounts of deionised water, then rinsed 3 times with ethanol and dried at 70 °C under vacuum for 24 hours.

3.6 Tin deposition on exfoliated MoS_2

200 mg of MoS_2 nanosheets were resuspended in 2000 mL of deionised water using ultrasonic homogenizer bath (with a power output of 35W and an operating frequency at 37kHz). 29.6 mg of tin (II) acetate was dissolved in a small volume of dilute hydrochloric acid and then added dropwise to the MoS_2 nanosheets suspension by pipette while stirred vigorously. Immediately thereafter 76 mg of sodium borohydride (1 mM) was carefully added to the vigorously stirred solution to reduce Sn^{2+} species to Sn^0 and the suspension was stirred overnight. 1 M hydrochloric acid solution was added dropwise to neutralize the suspension and initiate flocculation of Sn-doped MoS_2 nanosheets. The flocculates were collected using polycarbonate membrane over a suction filtration, and shaken and washed with copious amounts of deionised water, then rinsed 3 times with ethanol and dried at 70 °C under vacuum for 24 hours.

3.7 Heat reduction of doped MoS_2 nanosheets

As prepared doped MoS_2 nanosheets were spread out into a quartz glass boat crucible and placed into a quartz furnace tube. The tube was inserted into furnace oven and connected to 60 mL/min 5% H_2 95% Ar flow. The sample was heated at a rate of 5 °C per minute until desired calcination reduction temperature was reached, then constant temperature was kept for 2 hours before the sample was cooled down to room temperature. Calcined samples were named according to their maximum calcination temperature.

3.8 Electrode preparation for Li-ion battery testing

MoS_2 samples were mixed with C65 carbon and Kynarflex280 with a weight ratio of 8:1:1 in a N-methyl-2-pyrrolidone (NMP) mixture according to standard industrial procedure. Specifically, the ink slurry was made by sequential mixing. First the binding agent is mixed with a small amount of NMP, followed by the addition of carbon C65 and another small amount of NMP. Finally MoS_2 material was added with the remaining amount of NMP and mixed until the ink was homogeneous thick liquid with no agglomerates. The prepared slurry was cast onto a clean and ironed Cu foil, dried at 120 °C, calendered to the mass density and thickness of interest, and cut to 14mm diameter disc electrodes. Each electrode was measured for its weight, thickness and loadings were calculated. Such prepared electrodes were assembled in a Li-ion and Na-ion battery coin cells inside an argon filled glovebox and sealed for testing. A typical 2032 coin cell consisted of 80 µl of electrolyte solution (for Li-ion: lithium hexafluorophosphate in propylene carbonate and dimethylcarbonate 1:1 w/w (LP30)), lithium/sodium metal as cathode, glassfiber separator, spacer and the prepared MoS_2 anodes.

3.9 Electrochemical cycling

The electrochemical performance of the active electrode material was tested by subjecting the assembled coin cells to galvanostatic cycling measurements using a Maccor multifunction 4000 series battery tester. The cycling conditions were set within 3.0 V and 0.1 V cut-off limits. The cycling rate test involved five sets of charge/discharge cycles at current rates in the following order: 50 $mA \cdot g^{-1}$, 100 $mA \cdot g^{-1}$, 200 $mA \cdot g^{-1}$, 400 $mA \cdot g^{-1}$, and to verify the capacity retention again at 50 $mA \cdot g^{-1}$. Battery ageing test involved 500 charge/discharge cycles at a single current rate of 100 $mA \cdot g^{-1}$. The current density at the various rates for each coin cell

was calculated from the mass of the active material on the electrode. Throughout the research work, all potentials are reported with respect to the metallic lithium voltage (Li/Li^+).

3.10 Suzuki coupling reaction

The reaction was carried out in a sealed Pyrex glass batch reactor coupled to a condenser. In a typical reaction method, 1.2 mmol of aryl boronic acid, 2.5 mmol of potassium carbonate and 5.3 mg of Pd catalyst were placed in the Pyrex glass and 5 mL of solvent was added. The reaction mixture was vigorously stirred and heated to the reaction temperature of 60 °C. The addition of 1 mmol of aryl halide to the mixture was considered as the beginning of the reaction time. Each reaction was carried out for 60 minutes in a sealed environment under air. As the reaction reached the set time limit, the reaction mixture was removed, and the catalyst was filtered off. The catalyst was washed 2 times with water and 2 times with ethanol and dried at 70 °C under vacuum before it was reused for next reaction. The filtrate was extracted three times with ethyl acetate and the combined organic layer was analysed by GC-MS to determine the products and the yield. A known amount of 2-isopropylphenol internal standard was added to the organic mixture, and the ratio of integrated areas of aryl halide reactant to the reaction product with respect to the internal standard was used to calculate the reaction yield and conversion rates.

3.11 Heck coupling reaction

The reaction was carried out in a sealed Pyrex glass batch reactor coupled to a condenser. In a typical reaction method, 2.5 mmol of potassium carbonate and 1.5 mol% equivalent of Pd catalyst were placed in the Pyrex glass and 5 mL of dimethylformamide solvent was added. The reaction mixture was vigorously stirred and heated to the reaction temperature of 80 °C. The addition of 1 mmol of aryl halide and 1.2 mmol of styrene to the mixture was considered

as the beginning of the reaction time. Each reaction was carried out for 300 minutes in a sealed environment under air. As the reaction reached the set time limit, the reaction mixture was removed, and the catalyst was filtered off. The catalyst was washed 2 times with water and 2 times with ethanol and dried at 70 °C under vacuum before it was reused for next reaction. The filtrate was extracted three times with ethyl acetate and water and the combined organic layer was analysed by GC-MS to determine the products and the yield. A known amount of 2-isopropylphenol internal standard was added to the organic mixture, and the ratio of integrated areas of aryl halide reactant to the reaction products with respect to the internal standard was used to calculate the reaction yield and conversion rates.

3.12 Vapour-phase hydrogenation of 1-pentyne

The selective hydrogenation of 1-pentyne was performed using a fixed bed reactor. A typical reaction setup involved the use of 10 mg of Pd catalyst that was inserted between two plugs of quartz wool and placed into a furnace. The reaction conditions were set at 200 mL/min gas flowrate on an air calibrated mass flow controller using 40% H_2/He as hydrogenation reactant gas. 1 M pentyne solution with 1 M 2-methylpentane as an internal standard in n-hexane solvent was used as the reactant feed. Once flushing was complete, the fixed bed reactor was heated to 250 °C at a rate of 2 °C/min. Analysis was performed at different temperatures using online Gas Chromatography.

3.13 Synthesis of titania anatase nanoparticles

Anatase titanium dioxide (TiO_2) nanoparticles were synthesized using titanium tetrachloride ($TiCl_4$) as a precursor. 1 M sulphuric acid solution was cooled down to near 0 °C in an ice bath. 1 mL of Titanium tetrachloride was added dropwise to the solution while stirring vigorously. After 30 mins, the solution was slowly brought to 30 °C and stirred until transparent. The

transparent solution was stirred for further 60 minutes to ensure titanium hydroxide has been formed and 30 % ammonium hydroxide assay was slowly added drop by drop while vigorously stirring until the solution became neutral and TiO_2 precipitates started forming. This mixture was left to gel for 1 hour and white precipitates were collected by filtration. TiO_2 precipitates were washed by redispersing in deionised water and collected by centrifugation. This process was repeated 5 times and checked for pH of the filtrate to be neutral. White precipitates were dried at 60 °C under vacuum overnight.

3.14 Functionalization of solid acid catalysts with sulphuric acid

The sulphated TiO_2 nanoparticles were synthesized by dispersion of 2 g of previously synthesized TiO_2 nanoparticles, or commercial P25 nanoparticles, in 40 mL of 0.5 M sulphuric acid solution for 2 hours under vigorous stirring. The sulphate-functionalized nanoparticles were collected by centrifugation, washed with water and dried at 60 °C under vacuum overnight.

Dry sulphated anatase TiO_2 nanoparticles, sulphated P25 titania nanoparticles as well as dry non-sulphated TiO_2 nanoparticles as a reference material were calcined at different temperatures under the same conditions. First, as prepared TiO_2 nanopowder was spread out into a quartz glass boat crucible and placed into a quartz furnace tube. The tube was inserted into a furnace and connected to a 60 mL/min air flow. The sample was heated at a rate of 5 °C per minute until desired calcination temperature was reached, then constant temperature was kept for 3 hours before the sample was cooled down to room temperature. Calcined samples were named according to their maximum calcination temperature.

3.15 Cannizzaro reaction of pyruvaldehyde to lactic acid

The Lewis acidity of solid acids catalyst was tested using the Lewis acid catalysed reaction of pyruvaldehyde with water. The formation of lactic acid proceeds via an intramolecular hydride transfer under mild conditions. Typically, 50 mg of the catalyst was placed in a Pyrex tube and 2 mL of 0.1 M pyruvaldehyde solution was added. The reaction mixture was sealed, brought to 110 °C and maintained for 2 hours. The catalyst was removed from the pyruvaldehyde solution and the solution was analysed using high performance liquid chromatography (HPLC).

3.16 Esterification reaction of levulinic acid to ethyl levulinate

The reaction was carried out in a sealed Pyrex glass batch reactor coupled to a stirrer and a condenser. In a typical reaction method, 1.2 g of levulinic acid was mixed with 3 mL of ethanol and brought to 70 °C. The addition of 30 mg of a catalyst to the mixture was considered as the beginning of the reaction time. The reaction mixture was stirred for 5 hours at 700 rpm under reflux at 70 °C. As the reaction reached the set time limit, the reaction mixture was removed, and the catalyst was filtered off. The catalyst was thoroughly washed 3 times with ethanol and dried at 70 °C under vacuum before it was reused for next reaction. The filtrate of the reaction was analysed by GC-MS to determine the products and the yield. A known amount of 2-isopropylphenol internal standard was added to the reaction mixture, and the ratio of integrated areas of levulinic acid reactant to the reaction product of ethyl levulinate with respect to the internal standard was used to calculate the reaction yield and conversion rates.

3.17 Continuous-wave electron paramagnetic resonance

All measurements were carried out at 20 °C. The continuous-wave electron paramagnetic resonance (CW-EPR) X-band measurements were obtained on a Bruker BioSpin EMXmicro spectrometer with a Bruker SHQE-W cylindrical TE011-mode resonator. Sample powder was weighed and loaded into EPR tube for quantitative analysis. The signal intensity versus electron spin number was obtained from the double integral of the spectrum based on a reference powder of Cu(II)TPP with 1 spin per molecule. All X-Band spectra were collected over a 300 Gauss field range and 15 scans were adopted for each measurement. The microwave frequency range was 9.87-9.82 GHz with field modulation frequency of 100 kHz, modulation amplitude 6 G, microwave power 4 mW, and a sweep of 41 s over 80 mT. The quantitative result can be obtained from the signal intensity versus electron-spin numbers by calculating the double integral of a defined peak range of the spectra. Acquired data were analysed and plotted using Origin software package.

3.18 Powder X-ray diffraction (XRD)

Finely ground powder samples were pressed into a fixed depth well on a glass slide, using a flat glass slide to form an even thickness and smooth surface, and loaded onto a plastic sample holder for XRD characterisation. Powder x-ray diffraction was performed using a Bruker D8 Advance Eco diffractometer, with the generator operating at 40 kV and 40 mA with Cu $K\alpha_1$ radiation (λ = 1.54056 Å). The samples were rotated at 50 rpm and the scans were collected with angles between 5° and 90°, an opening degree of 1, a step size of 0.0217° and a step time of 1 second.

3.19 Trimethylphosphine (TMP) / trimethylphosphine oxide (TMPO) adsorbed sample for ^{31}P MAS NMR

In a typical experiment, 150 mg of TiO_2 sample was placed in a home-made glass tube and activated at 150 °C for 2 hours under vacuum (10^{-1} Pa) to achieve maximum adsorption of TMP molecules, then brought to room temperature. 1 mmol of TMP per gram of catalyst was introduced into this system and vapourised until constant pressure, as a result of the equilibrium between the TMP and the catalyst surface, was reached. To promote TMP adsorption, the sample tube was immersed in liquid nitrogen for the duration of the adsorption process. Excess of unadsorbed TMP molecules was removed by mild evacuation of the reaction tube and the whole process was repeated three times to ensure only fully adsorbed TMP molecules were present on the catalyst surface. Finally, the sample tube was flame sealed and transferred to Bruker 4 mm ZrO_2 rotor with a Kel-F endcap in a glove box under nitrogen atmosphere in preparation for the NMR measurement.

Avance III 400 WB spectrometer was used at room temperature following well established procedure.[383] To remove the effect of proton spins on ^{31}P spectra, a strong radio frequency field can be applied in a pulsed way at the resonance frequency of the non-observed abundant spins which contribute to the coupling of both spin species. This is to decrease the spin-spin interactions of the protons and bring the excess peak broadening effectively to zero. The high power decoupling (HPDEC) could then be used for the quantitative ^{31}P spectral peak analysis. Considering the long relaxation time of ^{31}P nuclei in NMR experiment, 30° pulse with the width of 1.20 µs, 15 s delay time was used. 800 scans were recorded with the radiofrequency for decoupling set to 59 kHz and the spectral width set to 400 ppm, from 200

to −200 ppm. The ^{31}P chemical shifts were correlated toan 85% aqueous solution of H_3PO_4, with $NH_4H_2PO_4$ as a secondary standard.

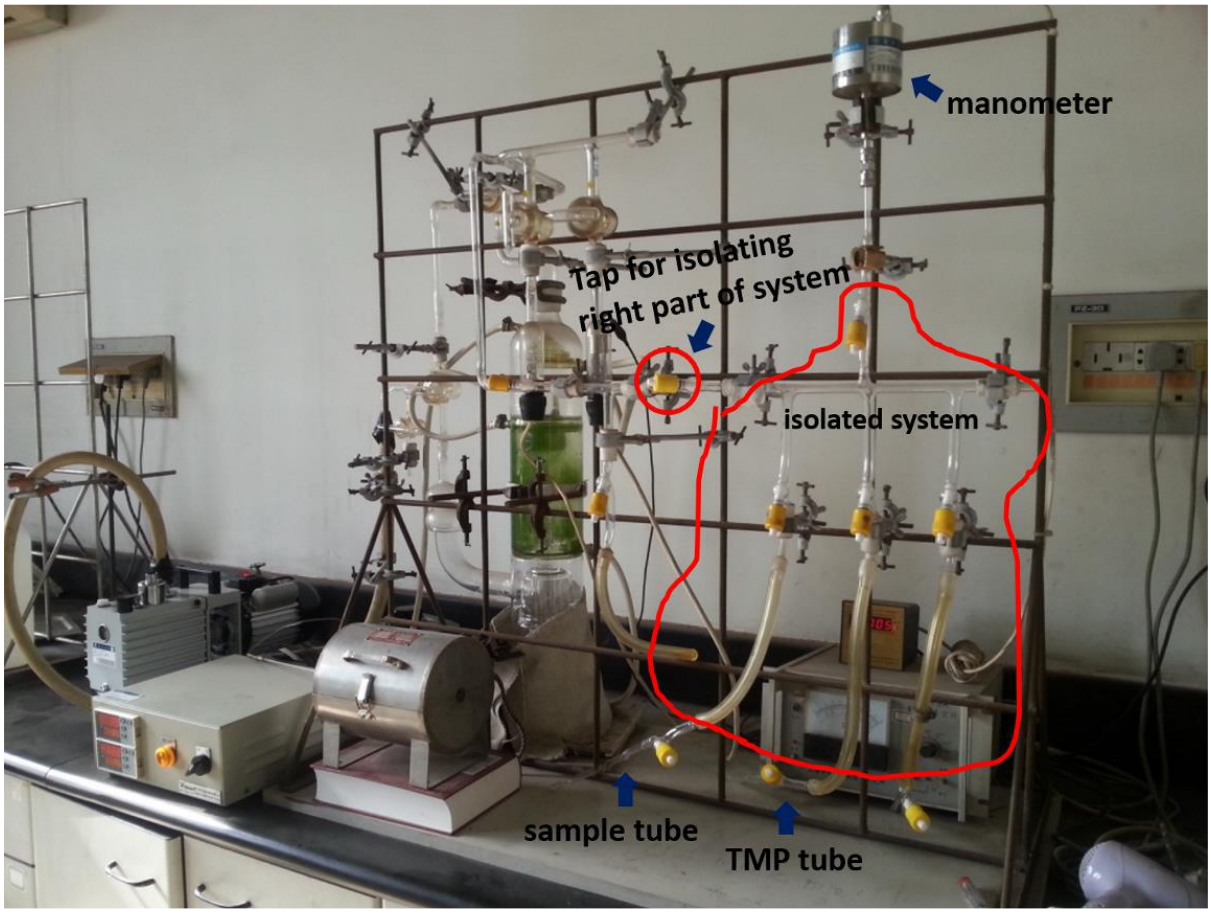


Figure 3.1 The system setup for TMP/TMPO adsorption on the surface of a solid acid catalyst.

Solid state magic angle spinning (MAS) NMR experiments were carried out using a Bruker

3.20 NMR spectrum deconvolution

The original TMP and TMPO NMR spectra were deconvoluted using the OriginPro software and the multiple peak fitting analyser tool. The overlapping peaks were quantified for each acid site type that is present in the analysed sample. Calibration runs using standard samples with known amount of various adsorbed TMP concentrations were undertaken to perform the quantitative analysis of adsorbed TMP molecules on the TiO_2 samples. Deconvolution

results of this quantitative analysis for TiO_2 catalysts are displayed in Tables 4.8, 4.9, 4.10 and 4.11.

3.21 High-angle annular dark field scanning transition electron microscopy (HAADF-STEM)

Finely ground samples were placed onto the holey carbon coated Cu-TEM grids for analysis. The analysis was performed using a JEOL-JEM2100 Aberration-Corrected Transmission Electron Microscope. An electron beam with a voltage of 60 kV was applied for the imaging to avoid beam excitation and reduce sample damage. To minimise degradation of the MoS_2 nanosheets under the electron beam, the samples were exposed to a relatively short irradiation time and were subjected to random mapping of a large irradiation area. An off-axis annular detector imaging was used for Dark-field (Z-contrast) imaging and atomic resolution imaging. Compositional analysis by X-ray emission detection was recorded with a Bruker 5030 SDD detector with a window area of $30mm^2$. All results were processed with Esprit 2.0 software.

3.22 Electron ptychographic phase imaging

Wigner-distribution deconvolution electron ptychography for atomic resolution imaging was performed for lithiated MoS_2 crystalline specimens to make use of its high sensitivity for imaging light elements. The focus probe ptychography experiment was performed using a pnCCD STEM camera, a direct electron radiation-hard fast pixelated detector mounted on a JEOL ARM200CF aberration corrected microscope. The pnCCD STEM camera delivers a readout speed of 1000 full frames per second with a full frame of 264 × 264 detector pixels. 4D dataset consisting of 66 × 264 pixel diffraction patterns for each probe position was recorded by STEM scanning consisting of 256 × 256 real space probe positions. The camera's

dynamic wide range enables to record both the bright field and dark field signals with single electron sensitivity. Ptychography experiments were optimised to have the largest number of pixels for the bright field signal, while the dark field signal was recorded simultaneously using an annular dark field (ADF) detector to form a simultaneous incoherent Z-contrast image. Sets of as-recorded STEM images were submitted for fast non-iterative ptychographic method called Wigner-distribution deconvolution. Wigner-distribution deconvolution is a full reconstruction of collected images that considers the non-linear terms through a deconvolution approach. This experiment followed the work described by Yang, Martinez and Nellist.[398,399]

3.23 Gas chromatography mass spectrometry

Gas chromatography mass spectrometry (GC-MS) analysis was carried out using an Agilent gas chromatograph equipped with a high polarity Agilent HP-INNOWax 19091N-133 column, 30 m × 250 µm × 0.25 µm and connected online to mass spectrometer. The GC oven was programmed to keep initial temperature of 40 °C for 5 minutes, then start ramping the temperature at 10 °C/min to 260 °C and hold at 260 °C for another 5 minutes. 2-isopropylphenol was added to all samples as the internal standard. The peaks were analysed by comparing the corresponding spectra with those of the NIST 2011 MS library.

3.24 High performance liquid chromatography (HPLC)

HPLC analysis was carried out using a Laserchrom Sykam S 1125 HPLC pump system equipped with a differential refractive index Laserchrom Sykam S 3585 detector, Laserchrom Sykam S 5250 sample injector, and Laserchrom Sykam S 4120 column oven with an Aminex HPX-87H column. The flow rate was set to 0.5 mL min^{-1}, with eluent 0.025 M H_2SO_4.

3.25 Brunauer-Emmett-Teller (BET) surface analysis

Specific surface areas were analysed using a Micromeritics Tristar II Plus instrument using the Brunauer-Emmett-Teller (BET) surface analysis method. Finely ground samples were placed in quartz tubes and precisely weighed, and in-situ degassed overnight at 110 °C for 12 h before each measurement. The samples were measured for the N_2 adsorption and desorption at 77 K.

3.26 X-ray photoelectron spectroscopy

XPS surface analysis measurements were recorded on a Thermo Scientific K-Alfa XPS instrument equipped with a microfocused monochromated Al X-ray source and a 180° double focussing hemispherical analyser-128-channel detector. The source was operated at 12 keV, and a 400 µm spot size was used. The instrument was operated at constant analyser energy of 200 eV for survey scans and 50 eV for detailed scans. Charge neutralization was applied using a combination of the focused low energy electron beam and the large area ion flux from a single source. The data acquisition and analysis were conducted with CasaXPS (Casa Software Ltd.). The peak position was referenced to the C 1s peak of the carbon tape at 285.00 eV.

3.27 Transmission electron microscopy (TEM) with energy-dispersive x-ray spectroscopy (EDX)

TEM EDX analysis was performed using a number of instruments. Lower resolution imaging was performed on a JEOL 3000F microscope, which was operated at 300 kV. Higher resolution TEM was performed at Johnson Matthey on a JEM 2800 microscope operated at 200 kV, with dark field imaging in scanning mode using an off-axis annular detector and EDX analysis also

in scanning mode. The attainable spatial resolution of the microscope is 78 pm with a probe spherical-aberration corrector, the illumination semi-angle of 25 mrad and probe current of 100 pA. The collection angles were fixed at 12–25 mrad. EDX analysis was performed to locate elemental distribution with an SDD-type EDX detector. The attainable energy-resolution of the EDX detector is 130 eV. A higher beam current of 300 pA was used with a longer dwell time of 0.1 ms per pixel repeated for 200 times. Spatial drift was corrected with a simultaneous image collector. Sample inks were prepared by dispersing approximately 1 mg of sample in approximately 1 mL of ethanol and sonicating for 30 minutes. One drop of this dispersion was cast onto a holey carbon copper grid (400 mesh) and the solvent was allowed to evaporate in air before analysis.

3.28 Temperature programmed reduction (TPR)

TPR measurements were undertaken using a Quantachrome Instruments ChemBET Pulsar TPR/TPD Automated Chemisorption Analyser. Standard analysis was performed by packing 20 mg of sample inside the quartz reactor U-tube, fixed with quartz wool at both ends of the reactor bed. Each sample was pre-treated in helium for 30 minutes at 100 °C and cooled to room temperature before analysis. TPR was performed in a H_2 flow of 100 mL/min, with a temperature programme from 40 °C to 800 °C and a ramp rate of 10 °C/min. The TCD detector was set at 150 mA with an attenuation of 2.

3.29 Thermogravimetric analysis (TGA)

TGA measurements were undertaken using a TA instruments TGA 50, with a gas flow of air at 100 ml/min inside the furnace. A sample powder was placed in a sample pan which was loaded into the furnace. The sample pan mass was accurately measured using a microbalance and compared to the tared pan. The sample was held at isothermal conditions for 10 minutes,

then the temperature was ramped at 10 °C/min to 900 °C. The sample mass was measured over time throughout the temperature ramp.

3.30 Inductive coupled plasma – atomic emission spectroscopy

ICP-AES was performed on an IRIS Intrepid II XSP spectrometer. The samples were digested in aqua regia and then heavily diluted with deionized water. The final concentration of the elements of interest was brought to the range of 10-100 ppm.

3.31 Raman spectroscopy

The samples were dried at 60 °C under vacuum before the measurements. Raman spectra were collected on a PerkinElmer 400F Raman spectrometer using a laser excitation wavelength of 532 nm. Eight scans of 10 s exposure time were applied for each sample.

Chapter 4 Functionalised anatase titania nanoparticles as a highly efficient solid acid catalyst

4.1 Introduction

Due to the global aim of reducing petroleum use and the search for alternative sources for sustainable production of chemicals and fuels, the method of conversion of cellulosic biomass has recently received mass attention. Cellulosic biomass is the most abundant renewable resource available, and is viewed as the feedstock for the green chemistry of the future.[400] Biomass conversion potentially has many environmentally friendly applications, including production of biofuels, chemicals, and polymeric materials.[401] Esters of levulinic acid belong to the biomass-derived platform of chemicals that are used on a large scale in industry as blend components in diesel formulations, and manufacturing of fragrances.[402,403] Derivatives of levulinate esters are used in production of cancer therapeutics, herbicides and resins.[403–405] Levulinate esters are typically obtained from biomass resources via three synthetic routes: conversion of furfurals and their derivatives; direct acid-catalysed alcoholysis of biomass; and esterification of biomass-derived levulinic acid.[406–411] Among levulinate esters, ethyl levulinate is a versatile chemical feedstock for industrial applications in the flavouring and fragrance industries and up to 5 wt.% as a direct miscible additive to diesel biofuel. The addition of ethyl levulinate to biofuels leads to cleaner burning of the diesel, higher lubricity and flashpoint stability, as well as improved cold flow properties and lower sulphur content.[402,412,413]

Ethyl levulinate is typically obtained by a two-step reaction from cellulosic biomass.[159,406,413–415] The first step involves acid hydrolysis of the biomass media to levulinic acid and its purification.[416] This is followed by esterification of levulinic acid with ethanol in the presence

of a Brønsted acid catalyst. The two-step method is typically employed by industry as it provides high purity product with high yields. Heterogeneous catalysts offer many advantages such as little or no catalyst deactivation and reduction of waste by-products, all of which provide cost-effective pure products.[417–419] Heterogeneous catalysts can also provide a direct single-step synthetic route from biomass to levulinate esters.

Acid catalysis is by far the most important area of catalysis employed by industries in all sectors of chemical manufacturing. Many industrial processes use mineral acids as homogeneous catalysts due to their high acidity strength, allowing for all the molecules or metal ions to be potential active sites.[55] The United States Environmental Protection Agency's data of annual production of mineral acids are shown in Table 4.1. However, when used as catalysts, these are in the same phase as the reaction and are difficult to separate, leading to equipment corrosion, toxicity and environmental pollution.[56] Large safety and environmental concerns of these hazardous liquid acids led to consideration of other, greener and safer alternatives. Heterogeneous solid acid catalysts are high surface area solids that offer easy separation and a high purity product, easy catalyst removal and recyclability, tailored active sites, as well as selectivity towards desired products.[420,58] Examples of solid acids that have been successfully employed as acid replacements, and are under intense investigation at present, are zeolites (HZSM-5, TS-1, H-Y) functionalized or modified metal oxides (sulphated TiO_2/ ZrO_2/ZnO, acidic niobates), functionalized or modified silica (silica sulphuric acid), sulfonic acid-functionalized carbon materials, functionalized polymers (Amberlyst-15 H^+ resin) and heteropolyacids ($H_3PW_{12}O_{40}$).[89,387,421–425]

Table 4.1 World annual production of selected mineral acids published in 2014 by U.S. Environmental Protection Agency.

Sulphuric acid	200,000,000 tonnes
Nitric acid	60,000,000 tonnes
Phosphoric acid	38,000,000 tonnes
Hydrochloric acid	20,000,000 tonnes

Only some solid acids remain active and insoluble and their acidic sites remain stable during reactions that involve water, either in form of a reactant or product. These reactions include hydrolysis, hydration and esterification reactions. The difficulty in employing solid acids as a catalyst in water-based reactions is the severe poisoning of their acid sites by water molecules, resulting in loss of catalytic activity.[418] Therefore, significant attention is focused on developing new water-tolerant solid acids that would bring a major breakthrough in industrial applications of solid acids in aqueous solutions.

The catalytic activity of metal oxide nanoparticles has been intensively studied.[426] They possess high surface area, and the structural composition of their facets combined with their surface energy and stability lead to different catalytic activity when compared to larger particles. Among them, titania is a very attractive material for being non-toxic, abundant, and relatively inexpensive. The activity of titania nanoparticles, however, depends highly on particle size, crystalline structure, and morphology. In their pure dry form, nanoparticles only possess Lewis acid sites at exposed metal centres at edges and corners of crystals. When exposed to an acidic medium, functional species attach to the crystal surface and may tune the crystal properties via the electron-withdrawing effect. This can be used when very small

nanoparticles are heated in air to promote higher crystallinity and as such improve their acidic properties.

Introducing further functionalization with acidic functional groups on their surfaces creates additional Lewis or Brønsted acid sites with a synergistic effect between the metal core and the functional group, whilst also stabilizing reactive high energy surface sites. For instance, a strong electronic-withdrawing effect imposed by sulphates results in high Lewis acidity of the neighbouring exposed metal atom, while two additional Brønsted acid sites are created, one on the neighbouring oxygen atom and another with a proton on the sulphate group. These two acid types are catalyst features that affect the reaction pathway while concentration and distribution of acid sites on the catalyst surface and their strength dictate the activity and selectivity of the catalysed reaction.

The major focus of this project is centred around synthesis and characterization of titanium oxide nanoparticles, all of which possess large surface area with a high proportion of potential active sites and large structural flexibility. This nano-sized form of titanium dioxide functionalized with sulphate groups and acidic protons offers high acidity and moderate reusability in both aqueous and organic media in the model Brønsted acid catalysed biomass esterification reaction of levulinic acid into ethyl levulinate, and Lewis acid catalysed Cannizzaro reaction of pyruvaldehyde to lactic acid.[415,427]

4.2 Results and discussion

A superacid is a medium defined as having stronger acidity than that of 100% pure sulphuric acid. According to more up to date definition, a superacid is described as a substance with chemical potential of the proton higher than that of pure sulphuric acid.[428] Superacids are typically made by mixing of a strong Brønsted acid with a strong Lewis acid. Functionalization

of metal oxides belongs to the most promising and the most studied group of solid superacids. Miniaturisation of metal oxide particles into nanoparticles and other nanostructures leads to increased surface to volume ratio and therefore larger proportion of acidic sites per unit of volume as well as unit of weight. In addition, nanostructures possess higher surface energy as a result of their small size, and this can further contribute to the higher acidity of the functional acidic species.

Further improvement is therefore seen in synthesizing metal oxide nanoparticles with very high surface to volume ratio that would provide a scope for dense deposition of acidic sulphates on their surface. It is important to note that acid catalysed reactions are not necessarily linked to the surface area of the catalyst but its total acidity, therefore it is important to create large number of strong but stable acid sites on the surface of metal oxide nanoparticles. One of the most studied and best understood metal oxides, that has been shown to couple well with sulphates, and that has been demonstrated as a highly Brønsted acidic as well as Lewis acidic catalyst, is nanoparticulate titania.[17]

Surface stability and reactivity of titania nanoparticles are closely associated with their surface morphology. The most reactive nanoparticles are dominated with high surface energy which in turn dictates their stability. It is known that sulphated metal oxides sometimes suffer from rapid deactivation and short catalytic life due to the loss of the sulphate species on their surface. Stabilizing acidity and sulphate species on the surface of metal oxide nanoparticles, therefore, is highly required.

4.2.1 Sulphated P25 TiO_2 Nanoparticles as Solid Acid Catalysts

In order to establish a stability and activity trend, acidic sulphate functional species were deposited on the commercial P25 titania nanoparticles, containing anatase and rutile phases

in 3:1 ratio.[429] These nanoparticles are generally 21-25 nm large, although it has been reported that anatase nanoparticles can aggregate to 85 nm large nanoparticles.[430] The phase mixture of two different polymorphs is also known to have synergistic effects in catalysis, in particular, an increased activity was demonstrated in photocatalysis.[431]

Sulphate treated commercial P25 TiO_2 nanoparticles were calcined under air with a range of different temperatures and examined for structural changes and presence of sulphate species. PXRD diffractograms of these samples, depicted in Figure 4.1, show diffraction patterns corresponding to both rutile and anatase phases. These nanoparticles have a well-defined crystalline structure and both sulphation and calcination at different temperature had no impact on their crystallinity or their particle size.

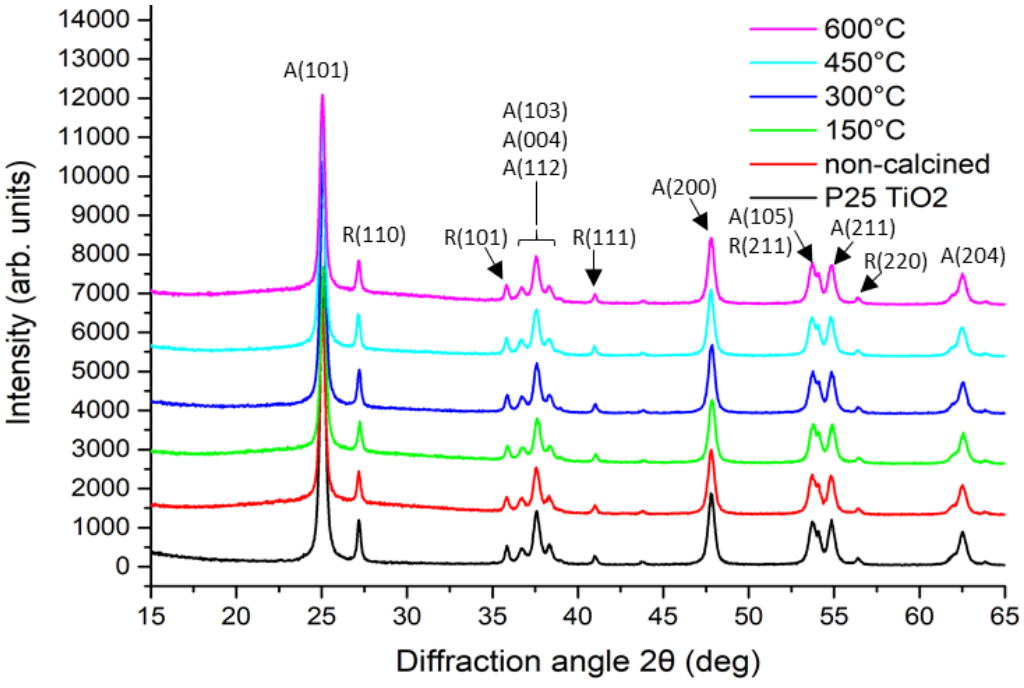


Figure 4.1 Diffraction patterns of P25 TiO_2 and sulphated P25 TiO_2 showing the impact of calcination temperature on crystallinity of the nanoparticles. Symbol A depicts anatase phase while symbol R shows pattern of the rutile phase.

Fourier-Transform Infrared Spectroscopy (FT-IR) was used to confirm the presence of sulphate species and to elucidate different binding modes on P25 titania surface. The FT-IR spectrum of the prepared sulphated titania nanocatalysts (Figure 4.2) showed five extra vibration bands at 1263, 1157, 1122, 1048, 976 cm^{-1} in comparison to the spectrum of P25 TiO_2 nanoparticles, suggesting the incorporation of sulphate groups on TiO_2 surface. The former two are typically associated with asymmetric stretches of S=O of a chelating bidentate sulphate, while the latter are typically associated with symmetric stretches of sulphate species.[432,433] 1263 and 1122 cm^{-1} stretches were associated with bidentate sulphate to a corner single titanium atom, while 1157 and 1048 cm^{-1} stretches were ascribed to bridging bidentate sulphate species to two titanium surface atoms.[81] The peak at 976 cm^{-1} can be assigned to weakly bound sulphate to a corner single titanium atom.[81] The intensity of IR bands decreases as sulphated P25 titania nanoparticles are calcined at higher temperatures which suggest detachment of sulphate groups from the surface.

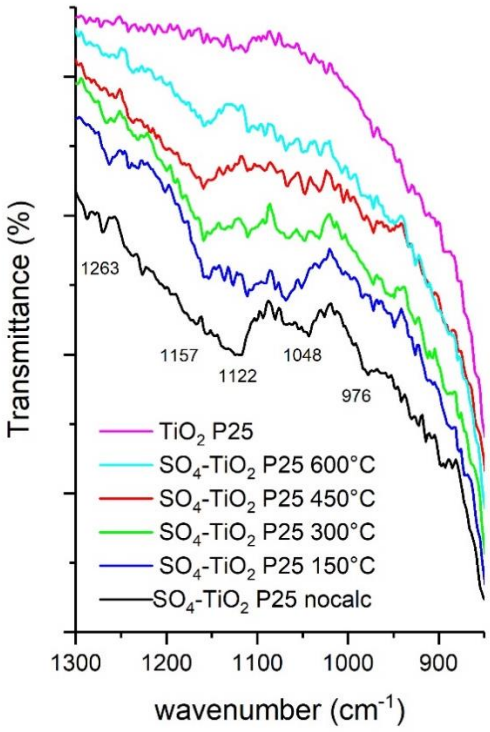
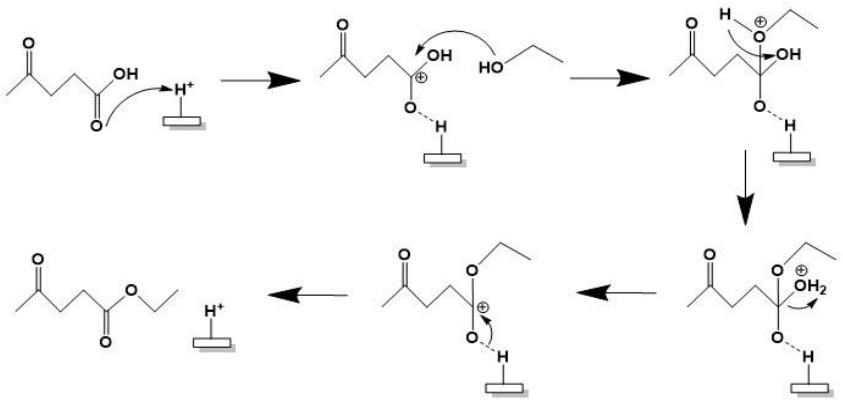


Figure 4.2 Infra-red spectra of P25 TiO_2 and sulphated P25 TiO_2 calcined at different temperatures.

After confirming the presence of sulphate groups on P25, the samples were tested as solid oxide catalysts in the esterification reaction of levulinic acid to ethyl levulinate with ethanol. The esterification reaction between levulinic acid and ethanol catalysed by protonic Brønsted acid sites is proposed elsewhere, which follows a typical nucleophilic substitution process based on a bimolecular process (Scheme 4.1).[434] First, the lone pair electrons on oxygen atoms of carboxyl group attacks to the proton on the catalyst surface which increases the electrophilicity of carbonyl carbon. This is followed by the attack of nucleophilic ethanolic oxygen to the electrophilic carbonyl carbon to form the oxonium ion. Then the intermediate molecule goes to a rearrangement in which the hydrogen atom is transferred onto hydroxyl group attached to carbonyl carbon atom, and forms a new oxonium ion. Finally, the loss of water and successive deprotonation lead to the formation of ethyl levulinate. The acid sites of the catalyst are being regenerated from the deprotonation step.



Scheme 4.1 The Brønsted acid catalysed esterification reaction mechanism of levulinic acid with ethanol.

Figure 4.3 shows the performance of P25 TiO_2 solid acid catalysts with and without sulphate functionalisation in comparison with a commercial Amberlyst-15 catalyst in ethanol at 70 °C after 5 hours of reaction. In the absence of a catalyst, the reaction proceeds at a very slow rate and the measured conversion rate was only 2.9%. When P25 TiO_2 was added in the reaction mixture, the activity increased by more than 3 times. Although the addition of sulphate functionalisation to the surface of P25 nanoparticles reduced the catalytic activity substantially, the activity started to increase in correlation with increasing calcination temperature and peaked at 450 ^oC (24.5% conversion). Further increase of calcination temperature to 600 ^oC resulted in a drop of catalytic activity to similar level as P25 TiO_2 without functional surface groups. These results indicate that 450 ^oC is the optimum calcination temperature for sulphate functionalised P25 TiO_2 nanoparticles to be a good solid acid catalyst. Although SO_4-P25 TiO_2 nanoparticles calcined at 450 ^oC showed the best activity among all P25 TiO_2 catalysts with and without sulphate functionalisation, their catalytic activity remained an order of magnitude lower than the popular commercial Brønsted solid acid catalyst – polymeric resin Amberlyst-15. The highly acidic protonic moieties of Amberlyst-15 lead to 39.8% conversion under the same reaction conditions.

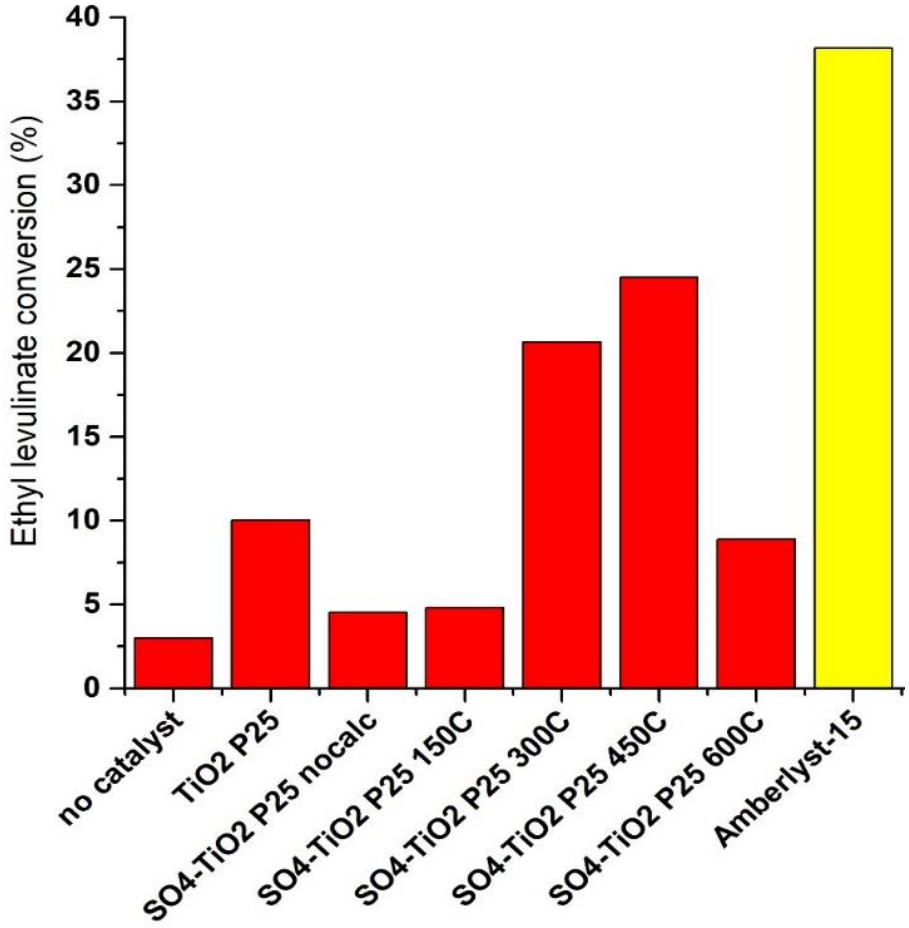


Figure 4.3 Sulphated P25 TiO_2 solid acid catalyst activity in esterification reaction of levulinic acid in ethanol and compared to commercial solid Brønsted acid catalyst Amberlyst-15.

4.2.2 Preparation, Characterisation and Catalytic Testing of High Surface Area Anatase Titania Nanostructures

As discussed earlier, the catalytic activity of superacids can be increased by decreasing the particle size because of higher surface to volume ratio which would offer sites for dense deposition of acidic sulphates. In this regard, very small anatase titania nanoparticles were successfully synthesized by complete hydrolysis of a titanium chloride precursor in an acidic medium and subsequent neutralization by addition of aqueous ammonia solution. Influence of treatment of diluted sulphuric acid as well as the impact of washing and heating of

sulphated metal oxides on the morphology of titania nanostructures have been investigated. Important step in this procedure is to find the threshold for concentration and length of acid treatment and preserve the particles in their most active state. Therefore, a range of calcination steps were explored, and as-prepared titania nanoparticles were characterized and catalytically tested.

4.2.2.1 Morphological, Structural and Physicochemical Properties

The particle size and crystallinity of TiO_2 nanoparticles before and after sulphate functionalization were studied by PXRD. Figure 4.4a. depicts the XRD patterns of TiO_2 nanoparticles before and after calcination at various temperatures. It is apparent that as-prepared TiO_2 nanoparticles exhibit an amorphous nature. When submitted to mild to moderate calcination temperatures under flow of oxygen, particle sintering and increase in crystallinity is expected to appear. This can be seen at 450 ^oC and more profoundly at 600 ^oC, when the material starts to give a clear crystalline patter. The Bragg reflections were analysed to be corresponding to a pure anatase TiO_2 phase (Anatase XRD JCPDS Card no. 78-2486).[435] The twelve visible peaks with 2θ angles at 25.12°, 36.70°, 37.70°, 38.35°, 47.88°, 53.79°, 54.29°, 62.59°, 68.67°, 70.15°, 75.00°, 82.70° were assigned to (101), (103), (004), (112), (200), (105), (211), (204), (116), (220), (215), and (224) crystal planes of the tetragonal phase of TiO_2, space group I41/amd, respectively. It is worth noting that the same XRD trend has been observed for both sulphated and untreated anatase TiO_2 nanoparticles alike (Figure 4.4b). This result indicates that the surface functionalisation of TiO_2 with sulphate species has little to no influence on the final crystal structure of the nanoparticles.

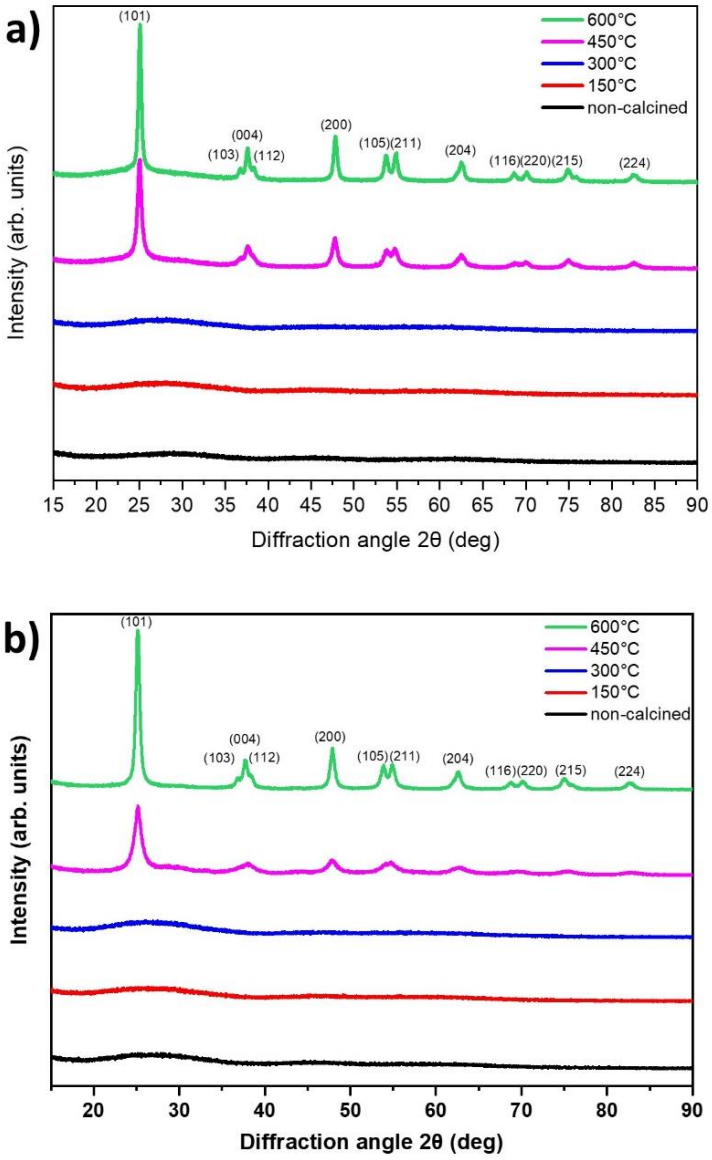


Figure 4.4 Diffraction patterns of a) as-prepared and b) sulphated TiO_2 anatase nanoparticles and impact of calcination on their crystal structure.

Furthermore, the mean size of crystalline sulphated anatase TiO_2 nanoparticles was estimated using the full width at half maximum (FWHM) of Bragg peak at 25.12°, corresponding to (101) plane and Scherrer formula as follows:

$D=0.9\lambda /B\cos\theta$

where, 0.9 is the shape factor, λ is the X-ray wavelength, B is the line broadening at half of the maximum intensity (FWHM) in radians, and θ is the Bragg angle (in degrees).

The mean sizes of sulphated TiO_2 nanoparticles calcined at 450 and 600 ^oC were determined as 8.8 and 17.8 nm, respectively.

Raman spectroscopy (Figure 4.5) further confirmed this trend in crystallinity following the slow appearance of five distinct TiO_2 peaks as a function of increasing temperature treatment at 450°C and 600°C. It is well known that the anatase phase of TiO_2 has six Raman active modes, starting with a strong band followed by weak and moderate bands, at 144 cm^{-1} (E_g), 197 cm^{-1} (E_g), 397 (B_{1g}), 513 (A_{1g}), 519 (B_{1g}) and 637 (E_g) cm^{-1}.[436,437] In this study, the bands located at 513 and 519 cm^{-1} overlap and only one broad peak centred at 517 cm^{-1} can be observed. Raman spectra of TiO_2 nanoparticles before and after functionalization with sulphate functional group agree with PXRD data, and thus confirm the formation of high purity TiO_2 anatase phase upon thermal treatment above 450 ^oC and non-destructive inclusion of sulphates to titania structure.

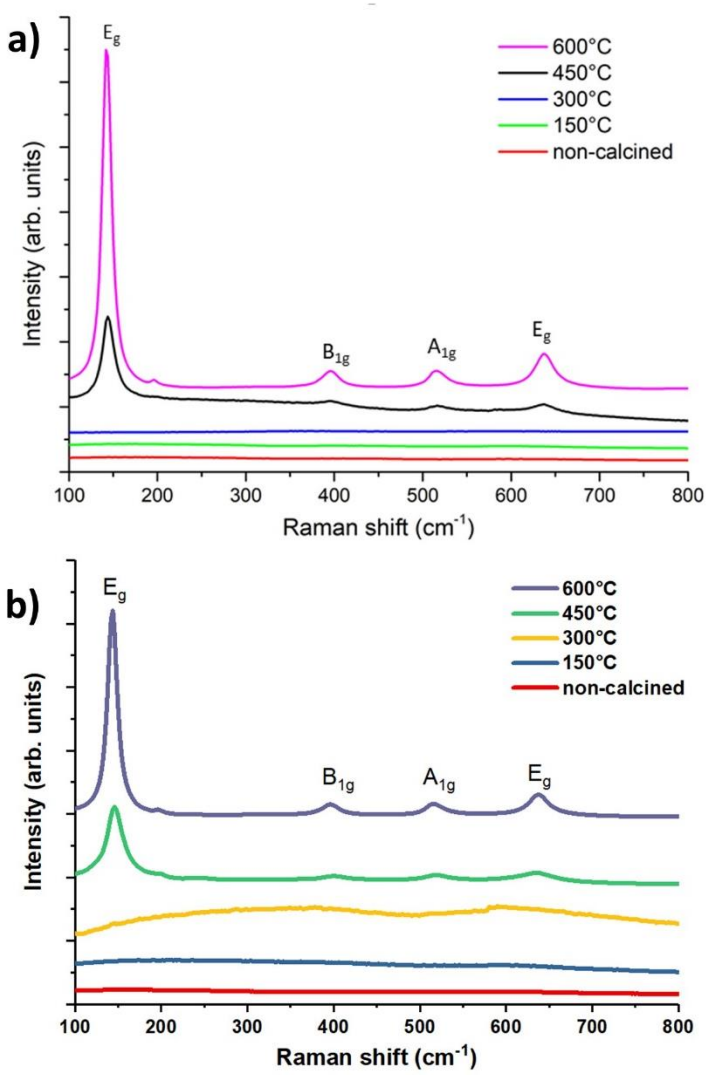


Figure 4.5 Raman spectra of a) as-prepared and b) sulphated TiO_2 anatase nanoparticles and the impact of calcination on their crystal structure.

The surface area of as-prepared and sulphated TiO_2 nanoparticles were analysed using nitrogen adsorption-desorption isotherms and Brunauer–Emmett–Teller theory. As given in Table 4.2, the as-prepared TiO_2 nanoparticles exhibited a very high surface area, especially in comparison with the commercial Degussa P25 titania, which has been reported in literature to have a surface area of 45-50 m^2/g.[438,439] However, the very high surface area of the anatase nanoparticles reduced dramatically upon functionalization with sulphate functional groups upon their surface. This could be due to agglomeration of nanoparticles at elevated temperatures and/or sulphates and hydrogen bonding of water molecules on the surface of

nanoparticles resulting in a gas probe molecules being partially restricted from effective adsorption. The slight increase in the surface area of sulphated titania calcined at 450 ^{o}C, when compared to non-calcined sulphated titania, may be due to the emergence of more accessible TiO_2 surface upon partial removal of weekly bound SO_4^{2-} and H_2O molecular networks from TiO_2 surface.

Table 4.2 BET analysis of sulphated TiO_2 anatase nanoparticles shows the impact of calcination temperature on the surface area of the anatase nanoparticles.

Catalyst	Surface area (m^2 g^{-1})
SO_4-TiO_2 non-calcined	**142**
SO_4-TiO_2 300°C	**139**
SO_4-TiO_2 450°C	**178**
SO_4-TiO_2 600°C	**26**
TiO_2 nanoparticles	**354**

In order to explore the morphology of the sulphated TiO_2 nanostructures before and after calcination, TEM images were collected. As depicted in Figure 4.6 a and b, sulphated TiO_2 anatase nanoparticles before calcination adopt a morphology similar to that of large two-dimensional nanosheets instead of the commonly known truncated octahedra. The lateral dimension of these nanostructures is in the micrometer range. Paying a closer look with high resolution TEM (HRTEM) showed that these superstructures are formed by stacking of many small interlinked hydrated TiO_2 nanograins via their hydroxyl groups, which are mainly amorphous in nature. This observation is in agreement with PXRD results. Interestingly, after calcination, the agglomerated superstructures fragmented into smaller nanoparticles of random shapes (Figure 4.6 c and d). HRTEM images of these small nanostructures revealed

that the newly formed nanoparticles are crystalline in nature with measured lattice spacing of 0.36 nm. This coincides with the (101) facets of the anatase TiO_2 phase.

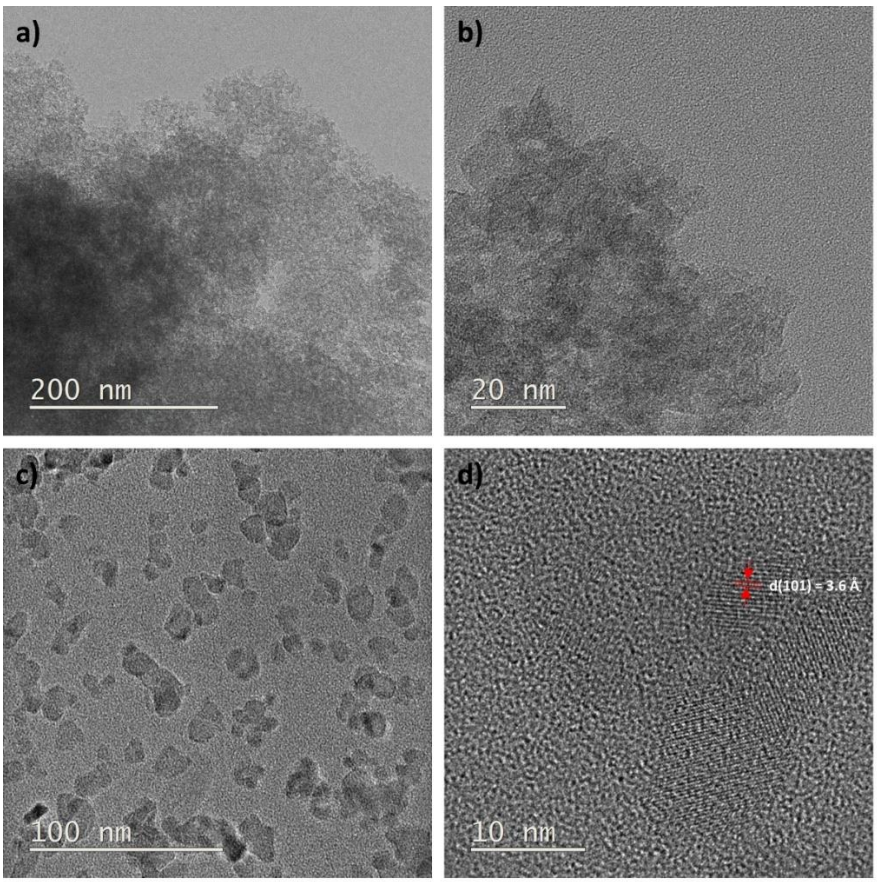


Figure 4.6 TEM images of sulphated TiO_2 anatase nanoparticles a-b) before c-d) after calcination at 450 ^oC

PXRD, Raman, BET and TEM analyses provided insights about the structure, crystallinity, and size of TiO_2 nanoparticles; but no information has been gained in relation to the nature of sulphate species and their quantities within the samples. Therefore, FT-IR, TGA and XPS analyses were employed to further investigate insights into the role of these highly acidic species.

FT-IR spectra of SO_4-TiO_2 nanoparticles in the range of 800-1300 cm^{-1} are shown in Figure 4.7. These IR stretching bands were similar to the ones observed with SO_4-P25 TiO_2. As expected, TiO_2 nanoparticles did not show any IR vibrations bands between 800-1300 cm^{-1}. However,

sulphate functionalisation resulted in observation of five additional vibration bands at 1263, 1157, 1122, 1048, 976 cm^{-1} corresponding to asymmetric and symmetric stretches of S-O of the chelating bidentate sulphate. FT-IR spectra evidence that sulphate species are strongly coordinated on TiO_2 surface and remain intact until 500-600 ^oC temperature region. It is a known fact that sulphate species become unstable at higher temperatures and detach from the surface of nanoparticles.[440] Indeed, they were found to be mostly detached from the surface for the 600 ^oC calcined sample.

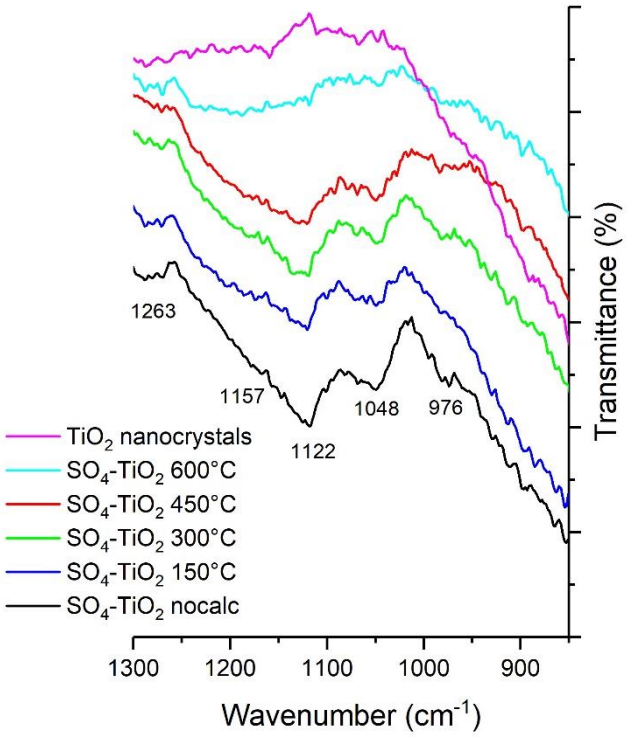


Figure 4.7 FT-IR spectra of TiO_2 nanoparticles and sulphate functionalised TiO_2 nanoparticles calcined at different temperatures.

After qualitative analysis of the presence of sulphate species on TiO_2 nanoparticles provided by FT-IR spectroscopy, TGA and XPS analytical methods were employed to quantify the amount of sulphate groups on TiO_2 nanoparticles as a means of the calcination temperature treatment.

Figure 4.8 represents the thermal evolution of untreated and sulphated titanium oxides. Three main thermal events were noted in all TGA curves. The first mass loss can be observed in the range between the start of the run at room temperature and 180 ^{o}C, and is attributed to the elimination of physisorbed water and traces of ammonium chloride, remnants of the material's synthesis. The second stage of weight loss located between 180 and 450 °C could be assigned to a partial dehydroxylation of $Ti(OH)_4$, which would result into a transformation from the amorphous phase to the crystalline structure of TiO_2.[441] The amount of weight loss between 25-450 ^{o}C gradually decreases as samples are calcined at higher temperatures because partial amount of water and hydroxyl groups are already lost during calcination process. The final weight loss in the range of 450-750 ^{o}C is associated with the elimination of sulphate ions, and information on the amount of sulphate species can be obtained. The weight loss of pure TiO_2 nanoparticles in the temperature range of 450-750 ^{o}C is very shallow, accounting for <2% of the total mass. On the other hand, the desorption of sulphate species from the surface of sulphated TiO_2 nanoparticles yields a very distinct curve for sulphated TiO_2 nanostructures.

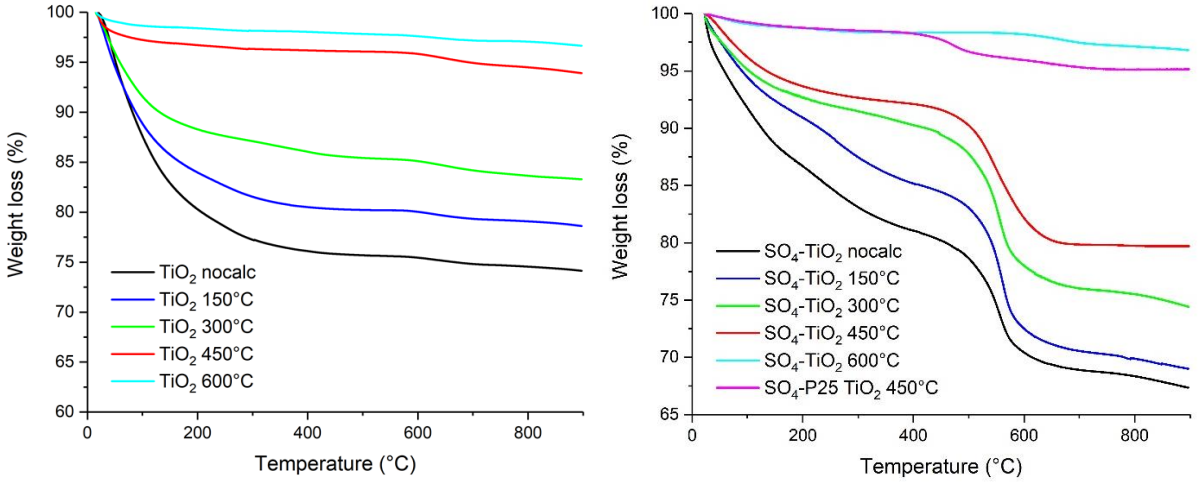


Figure 4.8 TGA weight loss analysis of sulphated TiO_2 solid acids.

By calculating the weight difference between 450 and 750 °C, SO_4 content in samples can be determined easily. Table 4.3. summarizes the SO_4 weight percentages of sulphated TiO_2 nanoparticles. Initial sulphate content does not change upon calcination at 150 °C. This is expected as chemisorbed sulphate species start to come off around 400 °C. As the calcination temperature increases, the sulphate amount is decreasing slowly but once the temperature is over 500 °C, a steep sulphate loss is observable. It is clear that 600 °C is enough to eliminate almost all sulphate groups from the surface.

For comparison, TGA of sulphated P25 TiO_2 calcined at 450 °C was also measured. The sulphate amount on commercial P25 TiO_2 was found to be 3.3-fold lower than the sulphate content found in anatase TiO_2 nanoparticles prepared in-house, despite both catalysts calcined at the same temperature. The decrease in sulphate content is in good correlation with the decrease in BET surface area (148 vs 45 m^2/g for TiO_2 and P25 TiO_2 respectively), suggesting that surface area and sulphate content might have linear relationship.

Table 4.3 TGA weight loss analysis of sulphated TiO_2 solid acids

Solid acid catalyst	***SO_4 weight %***
SO_4-TiO_2 non-calcined	14.81
SO_4-TiO_2 150°C	14.38
SO_4-TiO_2 300°C	12.44
SO_4-TiO_2 450°C	11.07
SO_4-TiO_2 600°C	1.10
SO_4-P25 TiO_2 450°C	3.34

To identify the effects of calcination temperature on the surface properties of SO_4^{2-}/TiO_2, XPS studies with regards to S 2p, Ti 2p, and O 1s binding energy regions were carried out. All deconvoluted XPS spectra are presented in Appendix Figures A4.1, A4.2 and A4.3.

Table 4.4 summarizes the positions of deconvoluted Ti 2p XPS peaks. The binding energy values of Ti $2p_{1/2}$ and Ti $2p_{3/2}$ for different oxidation states of titanium are reported elsewhere as being 454.1 and 460.2 eV for Ti^0 , 454.9 and 460.8 eV for Ti^{+2}, 456.9 and 462.6 eV for Ti^{+3}, and 458.9 and 464.6 eV for Ti^{+4}.[442–446] For pure titania, the binding energy of Ti $2p_{3/2}$ in +4 oxidation state was found to be 458.8 eV but for sulphate functionalised titania, this value shifted to higher energies (around 459.2 eV). This might be because of electron withdrawing effect of sulphate group coordinated to surface titanium through oxygen atoms and increasing the positive polarity on the titanium atom. Except for TiO_2 nanoparticles, Ti $2p_{3/2}$ and $2p_{1/2}$ peaks of all other catalysts could be fitted as a single peak at ~459 and 465 eV respectively, which indicates Ti atoms in an octahedral environment and coordinated to oxygen. For as-prepared TiO_2 nanoparticles, an additional titanium feature was observed. The lower binding energies of Ti $2p_{3/2}$ and $2p_{1/2}$ observed at 457.2 and 462.9 eV respectively are attributed to Ti ions in +3 oxidation state. Ti^{3+} defect sites on the catalyst surface are commonly observed in layered structures and in small nanoparticles, particularly at the edges of the nanostructures due to unsaturated coordination. Upon sulphate functionalisation, these defect sites are occupied by SO_4^{2-} ions.

Table 4.4 Summary of XPS peak fitting of the Ti 2p region for P25 TiO_2 and TiO_2 anatase nanoparticles. Each individual peak fitting can be found in the appendix.

catalyst	Ti $2p_{3/2}$ (Ti IV) (eV)	Ti $2p_{3/2}$ (Ti III) (eV)	Ti $2p_{1/2}$ (Ti IV) (eV)	Ti $2p_{1/2}$ (Ti III) (eV)
SO_4 - TiO_2 nocalc	459.22	-	464.94	-
SO_4 - TiO_2 150°C	459.14	-	464.86	-
SO_4 - TiO_2 300°C	459.29	-	465.01	-
SO_4 - TiO_2 450°C	459.29	-	465.01	-
SO_4 - TiO_2 600°C	459.27	-	464.99	-
SO_4 – P25 TiO_2 nocalc	459.24	-	464.96	-
SO_4 – P25 TiO_2 450°C	459.16	-	464.88	-
TiO_2 nanoparticles	458.89	457.19	464.61	462.91
P25 TiO_2	458.96	-	464.68	-

XPS spectra of the O 1s region of TiO_2 nanoparticles with and without sulphate functionalisation are shown in Appendix Figure A4.2. The curve-fitting results show that there are four different environments of oxygen species: lattice oxygen (Ti-O), oxygen in sulphate species, surface hydroxyl groups (Ti-OH) and hydroxyl groups at the defect sites on the catalyst surface. The peak positions and relative percentages of each species are given in Table 4.5. TiO_2 nanoparticles are the only sample where oxygen bonded to Ti^{3+} defect sites was detected as discussed in the previous paragraph. The treatment of these nanostructures with H_2SO_4 results in occupation of entire defect sites by sulphate ions while the hydroxyl amount on the catalyst surface does not seem to change. Subsequently, no drastic change is observed in either the position or the content of lattice and sulphate oxygens of the samples when they are calcined until 450 ^oC. However, the amount of Ti-OH group decreases progressively with increase in temperature, which is presumably due to partial dehydroxylation of the surface at these temperatures. When the calcination temperature is increased to 600 ^oC, sulphate group starts detaching from the surface; therefore, a decrease in the amount of sulphate group is observed by XPS peak deconvolution analysis. Meanwhile, the rise in the concentration of lattice oxygen by 14% is evident which is attributed to higher crystallinity of titania nanoparticles gained at elevated calcination temperatures. These results agree well with TGA and XRD observations. Compared to TiO_2 nanoparticles, P25 TiO_2 has much larger lattice oxygen and does not show any defect sites owing to its well crystalline nature. Similarly, when SO_4-P25 TiO_2 is calcined at 450 ^oC, the amount of lattice oxygen and surface hydroxyl reduces due to the decomposition of functional groups.

Table 4.5 Summary of XPS peak fitting of the O 1s region for P25 TiO_2 and TiO_2 anatase nanoparticles. Each individual peak fitting can be found in the appendix. The relative concentration of individual oxygen species is given in parenthesis.

catalyst	O 1s - Ti-O lattice (eV)	O 1s – Ti-OH (eV)	O 1s – sulphates (eV)	O 1s – TiOOH (defects) (eV)
SO_4 - TiO_2 nocalc	530.52 (69.16%)	531.82 (13.14%)	532.38 (17.7%)	-
SO_4 - TiO_2 150°C	530.59 (65.48%)	531.89 (14.27%)	532.30 (20.25%)	-
SO_4 - TiO_2 300°C	530.53 (68.02%)	531.83 (9.34%)	532.11 (22.63%)	-
SO_4 - TiO_2 450°C	530.52 (69.8%)	531.82 (6.34%)	532.11 (23.86%)	-
SO_4 - TiO_2 600°C	530.47 (79.68%)	531.77 (10.11%)	532.12 (10.21%)	-
SO_4 – P25 TiO_2 nocalc	530.43 (75.8%)	531.73 (7.40%)	532.12 (16.79%)	-
SO_4 – P25 TiO_2 450°C	530.36 (78.07%)	531.66 (9.19%)	532.10 (12.74%)	-
TiO_2 nanoparticles	530.28 (53.43%)	531.58 (13.58%)	-	528.69 (32.99%)
P25 TiO_2	530.19 (89.66%)	531.49 (10.34%)	-	-

Appendix Figure A4.3 depicts the XPS spectra and Table 4.6 summarizes XPS peak fitting of the S 2p region for sulphated P25 TiO_2 and TiO_2 anatase nanoparticles. The broad peak at 169 eV may be assigned to S 2p with the S atom in the (VI) oxidation state and in the form of SO_4^{2-} ions, based on the reported data in the literature.[443,447] It has been reported that the peaks at the binding energies of 163.5 and 167.5 eV are due the formation of TiS and SO_3^{2-} species respectively. The absence of these peaks in the XPS spectra of sulphated titania samples suggest that neither TiS nor SO_3^{2-} species had formed during sulphate functionalisation and calcination processes. These results indicate that the present sulphate species entirely consist of SO_4^{2-} and are coordinated to TiO_2 surface through oxygen atoms. It is worth noting that the

probability of the presence of free sulphate ions in the sample is low as the samples were thoroughly washed.

Table 4.6 Summary of XPS peak fitting of the S 2p region for sulphated P25 TiO_2 and TiO_2 anatase nanoparticles. Each individual peak fitting can be found in the appendix.

catalyst	S 2p 3/2	S 2p 1/2
SO_4 - TiO_2 nocalc	169.01	170.19
SO_4 - TiO_2 150°C	169.04	170.22
SO_4 - TiO_2 300°C	169.15	170.33
SO_4 - TiO_2 450°C	169.12	170.30
SO_4 - TiO_2 600°C	169.10	170.28
SO_4 – P25 TiO_2 nocalc	168.98	170.16
SO_4 – P25 TiO_2 450°C	168.97	170.15
TiO_2 nanoparticles	-	-
P25 TiO_2	-	-

Finally, the relative composition of sulphate species on titania nanoparticles were calculated by integrating the peak intensities of all elements from XPS survey spectra and divided by sensitivity factors of the corresponding peak. The results obtained are presented in Table 4.7. As seen, the sulphate content determined by XPS differs from the one obtained from TGA analysis. It is because TGA is a bulk technique and reflects the results from entire sample; however, XPS is a near surface sensitive technique and provides detailed information from the top layer of solid samples. The results indicate that not all sulphate species are located and accessible on the catalyst surface for SO_4-TiO_2 samples that are calcined until 450 ^oC. In these samples, some sulphate groups might be located in between the nanolayers which could be missed out by X-ray beam as it can penetrate up to a certain depth. In contrast, the percentage of sulphate on P25 TiO_2 samples was found to be larger than the amounts calculated from TGA results. More likely, sulphate species are located only on the surface of

P25 TiO_2 nanoparticles; therefore, their relative concentration was found to be larger by XPS analysis.

Table 4.7 XPS elemental analysis of sulphate content

catalyst	*SO_4 weight %*
SO_4-TiO_2 150°C	**9.11**
SO_4-TiO_2 300°C	**10.55**
SO_4-TiO_2 450°C	**11.21**
SO_4-TiO_2 600°C	**4.73**
SO_4-TiO_2 nocalc	**8.06**
SO_4-P25 TiO_2	**7.64**
SO_4-P25 TiO_2 450°C	**5.96**

To sum up, the aforementioned characterization techniques indicate that layered TiO_2 with high surface area can be synthesized by slow hydrolysis of titanium tetrachloride under mild conditions. Stirring these TiO_2 nanolayers in dilute sulphuric acid leads to chemisorption of sulphate species on the surface of TiO_2 nanoparticles. The sulphate functionalisation of the nanoparticles surface induces strong interparticle interaction due to H-bonding between sulphate and water molecules, resulting in coalescence of nanolayers into superstructures. Upon calcination above 300 ^oC, this strong interparticle physical bonding is disrupted by complete dehydration and partial removal of sulphate species. Subsequently, these loosely bonded nanolayered structures can be re-dispersed by ultrasound sonication. This phenomenon is illustrated in Figure 4.9 for better visualisation. The observation of fragmented nanolayers in TEM images after calcination is more likely due to breakage of

physical bonding between nanoparticles by ultrasound during sample preparation for microscopy imaging.

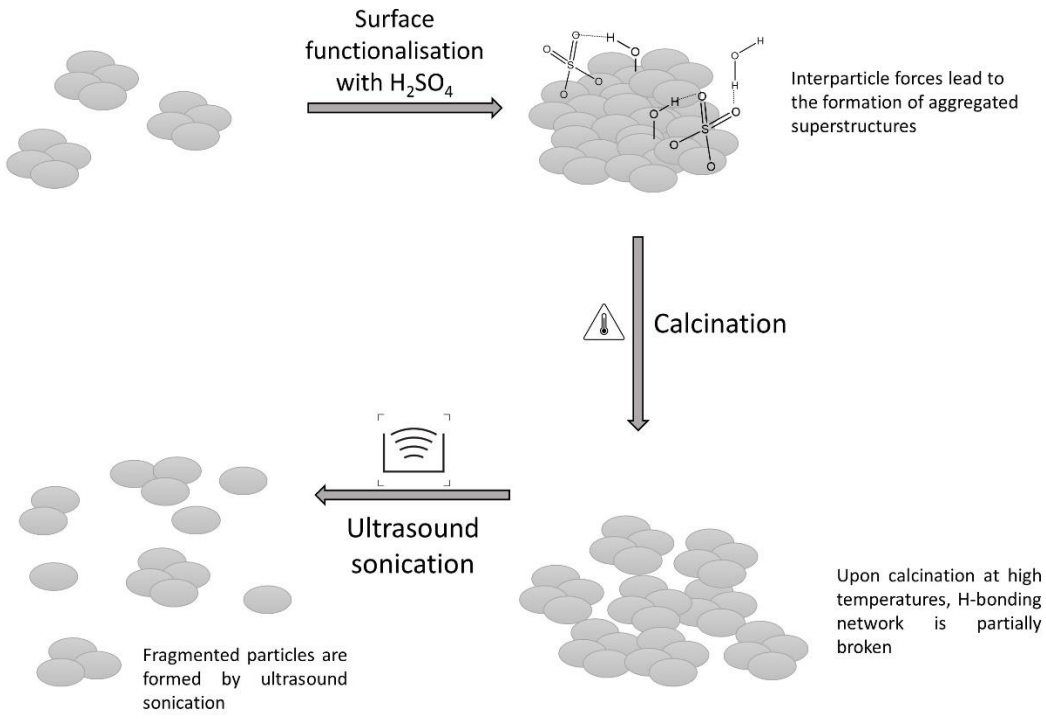


Figure 4.9 Illustration of the effect of interparticle forces, calcination and sonication on the particle size and distribution.

4.2.2.2 Investigation of Acidic Properties of Sulphated Titania Nanoparticles

^{31}P MAS NMR measurements using trimethylphosphine (TMP) and trimethylphosphine oxide (TMPO) as NMR probe molecules were performed for detailed characterization of different acid sites and their strength in TiO_2 solid acid catalysts. The strength of Lewis and Brønsted acid sites can be differentiated by the ^{31}P chemical shift of adsorbed TMP and TMPO molecules, which provide complementary information. TMP ^{31}P NMR technique is highly sensitive to Lewis acid strength as the chemical shift window has a very broad range of -20 to -55 ppm. In contrast, Brønsted acidity is related to a rather small region of -2 to -5 ppm but serves as an accurate quantitative tool to account for the number of Brønsted acid sites to

couple up with analysis using TMPO probe. In contrast to the TMP probe, TMPO is a more sensitive analytical tool towards Brønsted acid sites as there is much wider chemical shift range in ^{31}P NMR spectra – typically between -60 and -85 ppm, while peaks in the range of -50 to -59 ppm can be generally associated with Lewis acid sites, and peaks below -50 ppm typically relates to physisorbed TMPO species on the surface of the probed material.

Figure 4.10 shows deconvoluted ^{31}P NMR spectra of TMP probe molecules adsorbed on acid sites of both sulphated and non-sulphated TiO_2 nanoparticles as well as P25 TiO_2. Typically, -2 to -6 ppm is associated with the $TMPH^+$ ionic complex formed by reacting of the TMP molecules with Brønsted acid proton (proton donor) of the solid acid while TMP chemisorbed to Lewis acid sites (electron acceptor) spans over a wider range of -20 to -58 ppm. The wide range makes it easy to differentiate the strength of the Lewis acid sites with less negative ppm value indicating the stronger Lewis acidity. Table 4.8 summarizes the positions of deconvoluted TMP ^{31}P NMR peaks.

Table 4.8 Summary of deconvoluted TMP ^{31}P NMR peak positions. Peaks were ascribed to relevant acid sites and chemical shift of these is related to their acidity strength.

NMR chemical shift of TMP (ppm)	peak 1	peak 2	peak 3	peak 4	peak 5
P25 TiO_2	-	-27.64	-34.81	-	-
SO_4 - P25 TiO_2 450°C	-4.00	-27.41	-34.17	-	-
TiO_2 nanoparticles	-4.31	-26.05	-32.45	-48.52	-56.59
SO_4-TiO_2 non-calcined	-3.98	-25.17	-33.13	-	-
SO_4-TiO_2 300°C	-4.20	-25.89	-34.11	-	-
SO_4-TiO_2 450°C	-3.98	-26.81	-34.01	-	-
SO_4-TiO_2 600°C	-4.63	-27.06	-35.69	-	-

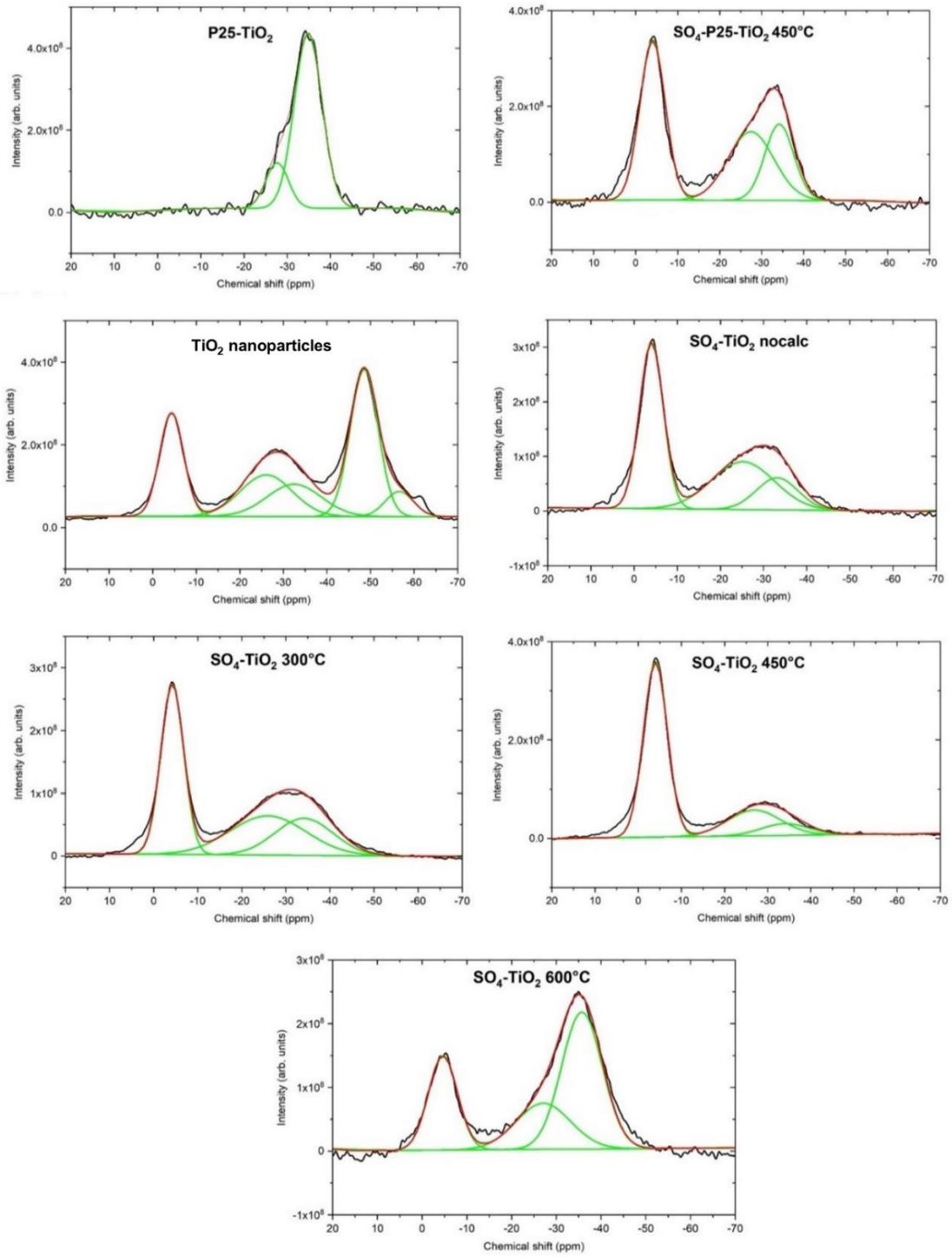
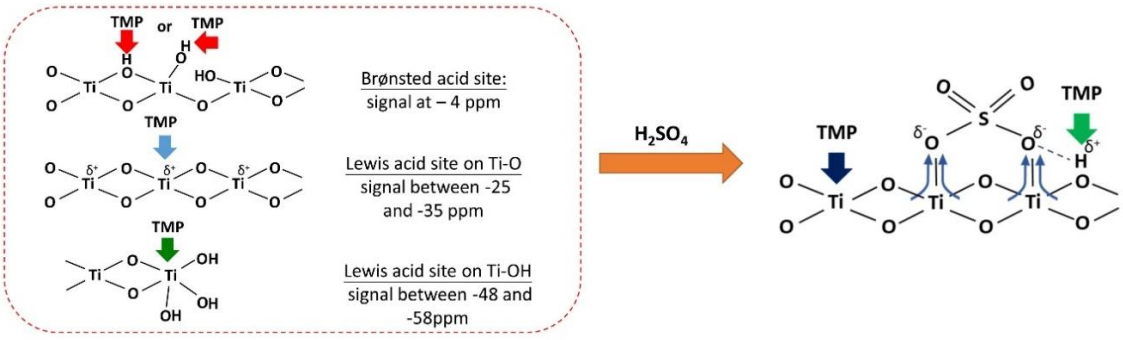


Figure 4.10 Deconvoluted ^{31}P NMR spectra of TMP probe molecules adsorbed on acid sites of both sulphated and non-sulphated TiO_2 nanoparticles and P25 TiO_2.

The existence of an NMR peak at -4 ppm indicates that commercial P25 TiO_2 does not have acidic protons (Brønsted acid sites) on its surface. This is expected as commercial P25 titania is exposed to extensive washing and high temperature calcination prior to sales. However, a

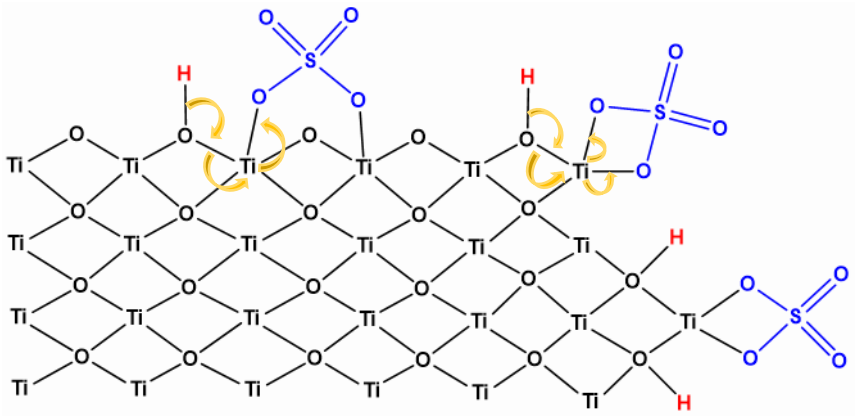
broad peak with a shoulder, spanning between -20 and -50 ppm and corresponding to Lewis acid sites could be clearly observed. These Lewis acid sites are presumably formed at the defect sites or at the edges where an oxygen vacancy is formed next to Ti atoms. As expected, sulphuric acid treatment with a subsequent calcination at 450 ^{o}C, protonates the surface of TiO_2 and forms Brønsted acid sites, which is observed as an intense NMR peak at -4 ppm. Unlike P25, as-prepared TiO_2 nanoparticles exhibit a complex ^{31}P NMR spectrum. 3 distinct NMR peaks centered at -4.31, -28 and – 50 ppm correspond to TMP interacting with H atom on Ti-OH (Brønsted acid site) and TMP interacting with Ti atom on Ti-O and Ti-OH (Lewis acid sites) respectively. The NMR results agree with the XPS data where two titanium species were also observed (TiO_2 and TiOOH). The observation of an extra big peak at -50 ppm is due to the incomplete condensation of –OH groups because as-prepared TiO_2 nanoparticles were dried but not calcined at the time of NMR measurements. Scheme 4.2 illustrates TMP interaction with different acidic sites and their corresponding chemical shift in ^{31}P NMR for better visualisation.



Scheme 4.2 Illustration for the interaction of TMP molecule with different acidic sites on bare and sulphated titania.

The careful deconvolution process unveils the presence of two more peaks within the envelop of these 3 distinct peaks. Interestingly, NMR peaks corresponding to Lewis acidic sites of as-prepared TiO_2 shifted downwards (deshielded) with respect to NMR peaks of P25 TiO_2 which

gives the evidence that the strength of Lewis acidic sites on as-prepared TiO_2 nanoparticles is higher than that of P25. Upon functionalisation of the surface with sulphuric acid, the peaks at -48 and -56 ppm disappear which might be due to the preferential chelating of SO_4^{2-} to Ti-OH or due to acid-base treatment leading to surface dehydroxylation. In addition, the remaining peaks shift further downfield, suggesting increase in acid strength. This is not surprising as the electron withdrawing effect of sulphate increases the positive charge on protons and Ti atoms (Scheme 4.3). Finally, calcining the sulphated TiO_2 nanoparticles at elevated temperatures does not change the position of the peaks significantly but their relative intensity is changed.



Scheme 4.3 Schematic illustration of bridging and corner attached sulphates on the surface of the TiO_2 nanoparticles. The arrows indicate the withdrawing electron effect that the sulphate group has on the Ti and consequently on the acidic proton.

Furthermore, quantitative analysis of the deconvoluted ^{31}P NMR peaks was used to account for the amount of acid sites of each acid type. The results are given in Table 4.9. Among measured catalysts, as-prepared TiO_2 nanoparticles revealed highest amount of acidity; however, 43% of its total acidity is coming from weak Lewis acid site that are hydrated species within the nanoparticles which do not contribute much to acidic properties of the material. The strongest Lewis acidity was observed for P25-TiO_2 nanoparticles without any functional

groups. Similar Lewis acid shift with smaller NMR peak, meaning same acid strength but smaller number of Lewis acid sites, was observed in 450°C calcined sulphated P25-TiO_2. This was linked to the lost Lewis acid sites that are occupied with sulphate species. In contrast, sulphated titania nanoparticles exhibited smaller and weaker Lewis acidity.

Table 4.9 Summary of deconvoluted TMP ^{31}P NMR peak integrated area, representing the amount of TMP adsorbed on each acid site and therefore the number of acid sites.

Density of adsorbed TMP ($\mu mol/g_{catalyst}$)	Brønsted Acid	Lewis Acid			Total Lewis Acid	Total
	Peak 1	Peak 2	Peak 3	Peaks 4 & 5		
P25 TiO_2	-	2.300	10.715	-	13.015	13.015
SO_4 - P25 TiO_2 450°C	7.896	6.124	4.279	-	10.403	18.299
TiO_2 nanoparticles	5.382	4.716	3.812	10.460	18.988	24.371
SO_4-TiO_2 non-calcined	6.569	4.981	2.213	-	7.194	13.763
SO_4-TiO_2 300°C	5.490	4.222	3.026	-	7.248	12.738
SO_4-TiO_2 450°C	7.706	2.522	1.028	-	3.73	11.256
SO_4-TiO_2 600°C	3.769	3.448	7.651	-	11.099	14.868

TMPO probe was used as a more sensitive analytical tool towards Brønsted acid sites as there is much wider chemical shift range in ^{31}P NMR spectra – typically between 60 and 85 ppm, while peaks in the range of 50 to 59 ppm can be generally associated with Lewis acid sites, and peaks below 50 ppm typically relate to physisorbed TMPO species on the surface of the probed material. Figure 4.11 shows deconvoluted NMR peaks and Tables 4.10 and 4.11 summarize the peak positions and TMPO content in each peak location respectively. Broad NMR peaks within Brønsted acidity region were obtained for all sulphated samples. Deconvolution of the broad NMR peaks had to be performed with utmost care and in conjunction with other qualitative and quantitative results such as TMP ^{31}P NMR for the number of Brønsted acid sides, while concentration of sulphate species present on the surface

was cross-checked with TGA-SDT analysis and XPS elemental analysis. XPS analysis peak deconvolution in particular provided an indispensable tool to understand the content and environment of sulphate species on the surface of titania nanoparticles.

As expected, and in agreement with TMP ^{31}P NMR experimental results, P25 titania nanoparticles showed mostly physisorbed TMPO and a small peak for Lewis acid sites, while 450°C calcined sulphated-P25 titania nanoparticles showed very distinct peak in the Brønsted acid region. A high content of Brønsted acid sites was observed in as-prepared sulphated titania nanoparticles as well as sulphated titania nanoparticles calcined at 300 °C. Peak deconvolution showed this is a result of a large content of less strongly bound sulphate functional moieties. These species are highly acidic but their weaker bonding to the titania surface resulted in decreased stability and as a consequence, their catalytic acidic activity (see Catalytic Testing section below). Calcination process showed that these sulphate species create stronger bonding to the titania surface and despite overall acid strength as measured by NMR shift slightly decreased, the number of stable acidic sites available on the nanoparticle surface increased which is highlighted by larger detected content and broader NMR peak in the Brønsted acid region. 600°C calcined sample showed small content of very stable acid sites and very similar NMR shift as the 450°C sulphated P25 titania, confirming the trend in acidity and stability.

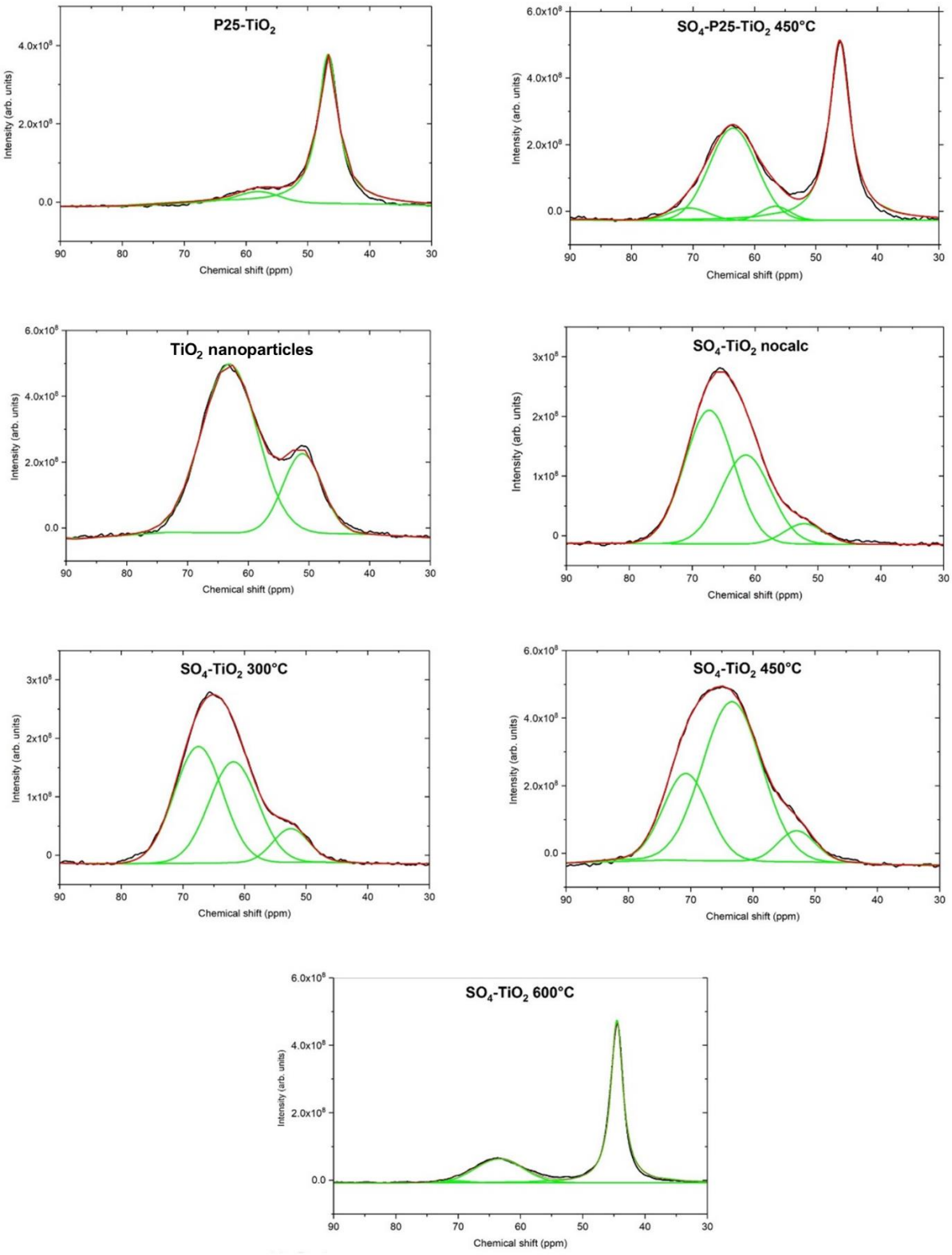


Figure 4.11 Deconvoluted ^{31}P NMR spectra of TMPO probe molecules adsorbed on TiO_2 nanoparticles

Table 4.10 Summary of deconvoluted TMPO ^{31}P NMR peak positions. Peaks were ascribed to relevant acid sites and chemical shift of these is related to their acidity strength.

Chemical Shift (ppm)	Peak 1	Peak 2	Peak 3	Peak 4
P25 TiO_2	-	-	57.96	46.74
SO_4 - P25 TiO_2 450°C	70.69	63.52	56.60	46.14
TiO_2 nanoparticles	-	63.13	51.08	-
SO_4-TiO_2 nocalc	67.29	61.47	52.21	-
SO_4-TiO_2 300°C	67.49	61.81	52.51	-
SO_4-TiO_2 450°C	70.78	63.37	52.97	-
SO_4-TiO_2 600°C	70.53	63.42	-	44.53

Table 4.11 Summary of deconvoluted TMPO ^{31}P NMR peak integrated area, representing the amount of TMPO adsorbed on each acid site and therefore the number of acid sites.

Density of adsorbed TMPO ($\mu mol/g_{catalyst}$)	Brønsted Acid		Lewis Acid		Physisorbed TMPO	Total Brønsted Acid
	peak 1	peak 2	peak 3		peak 4	
P25 TiO_2	-	-	0.704	7.270	-	7.974
SO_4 - P25 TiO_2 450°C	0.922	8.332	0.804	10.397	9.254	20.454
TiO_2 nanoparticles	-	18.389	6.100	-	18.389	24.489
SO_4-TiO_2 nocalc	6.900	4.603	0.839	-	11.503	12.342
SO_4-TiO_2 300°C	6.134	5.340	1.327	-	11.474	12.801
SO_4-TiO_2 450°C	7.336	17.563	2.152	-	24.899	27.050
SO_4-TiO_2 600°C	0.108	2.145	-	5.549	2.253	7.802

4.2.2.3 Catalytic Testing

Initially, the catalytic performance of TiO_2 solid acids was examined for the production of ethyl levulinate from the esterification reaction of levulinic acid and ethanol at 70 °C for 5 hours. Figure 4.12 exhibits the conversion rates of various solid acid catalysts under the same reaction conditions. In the absence of a catalyst, the conversion was only about 2.9%. The conversion rate slightly increased to 4% when as-prepared small anatase TiO_2 nanoparticles were used. Upon surface functionalisation of anatase TiO_2 nanoparticles with sulphuric acid, the catalytic activity was further increased by 4-fold. Calcination of sulphate functionalised

TiO_2 nanoparticles improved the activity further. The catalytic activity of calcined samples followed a volcano trend with increasing calcination temperatures, peaking at 450°C, which is the same activity trend observed with sulphated P25 catalysts as exhibited in Figure 4.3 and discussed previously. It is vital to point out that the large increase started happening only when crystalline phase started being introduced by calcination under flow of air. 450°C was found to be the optimum calcination temperature at which particles are crystalline, the surface is covered with sufficient amount of stable and accessible hydroxyl and sulphate groups with optimum acidic strength. It is known that sulphate species become unstable at around 550°C and start coming off from the surface which results in agglomerated nanoparticles with reduced acidic sites. However, it is worth noting that that the particle size is not only the factor that drives the overall acidity, and catalytic activity of esterification reaction, but all the amount, strength, stability and accessibility of active Brønsted acidic sites are equally important. In comparison to SO_4-P25-TiO_2 450^oC catalyst (the catalytic performance of which was presented in Figure 4.3), SO_4-anatase TiO_2 450^oC doubled the conversion rate owing to their small size and higher amount of Brønsted acidic sites. SO_4-anatase TiO_2 calcined at 450 ^oC also exhibited superior catalytic activity compared to commercial Amberlyst-15 catalyst which makes it a promising candidate for acid catalysed reactions.

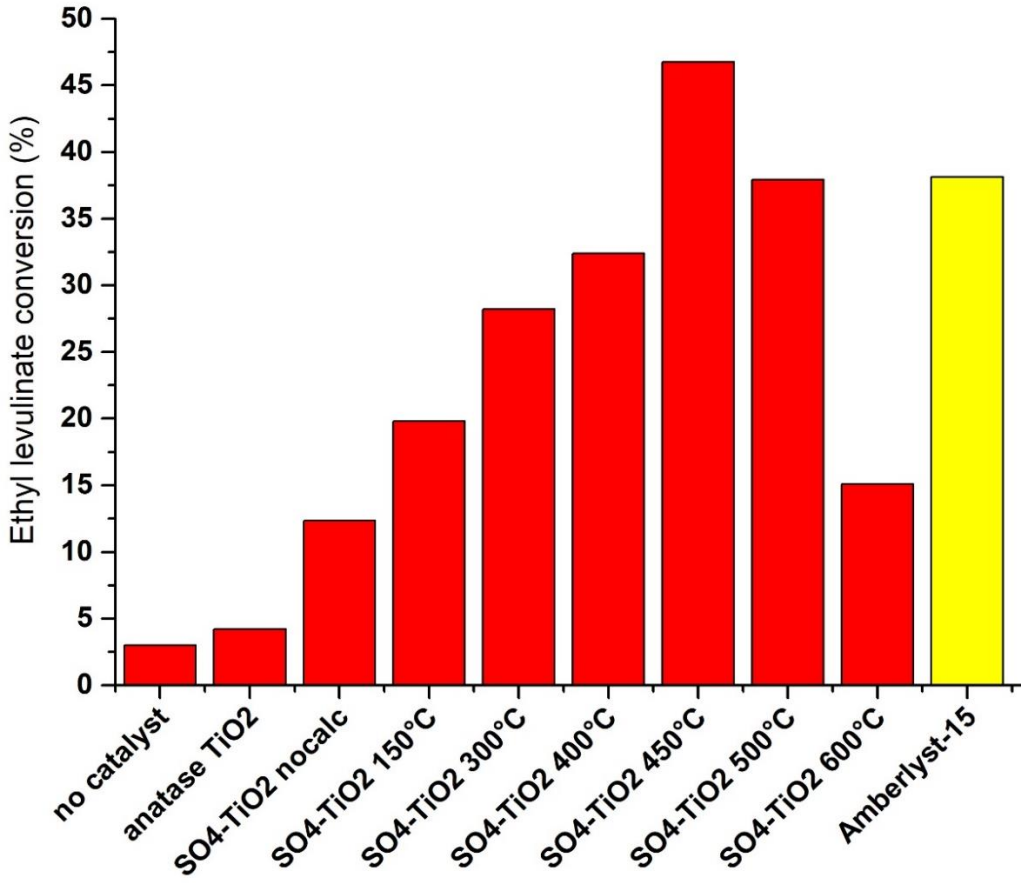


Figure 4.12 Sulphated TiO_2 nanoparticles solid acid catalyst activity in esterification reaction of levulinic acid in ethanol and compared to commercial solid Brønsted acid catalyst Amberlyst-15.

The reaction rate over time was also monitored to have a closer look to the performance of catalysts. As displayed in Figure 4.13, the conversion of ethyl levulinate increases linearly with time for all catalysts. Indicated by a small slope, the conversion rate was rather slow with SO_4-P25-TiO_2 450 ^oC catalyst. Although, both SO_4-TiO_2 450 ^oC and Amberlyst-15 catalysts appeared to give similar conversion percentages (around 10%) at the beginning of the reaction (first 60 minutes), SO_4-TiO_2 450 ^oC started to outperform Amberlyst-15 in the successive reaction time.

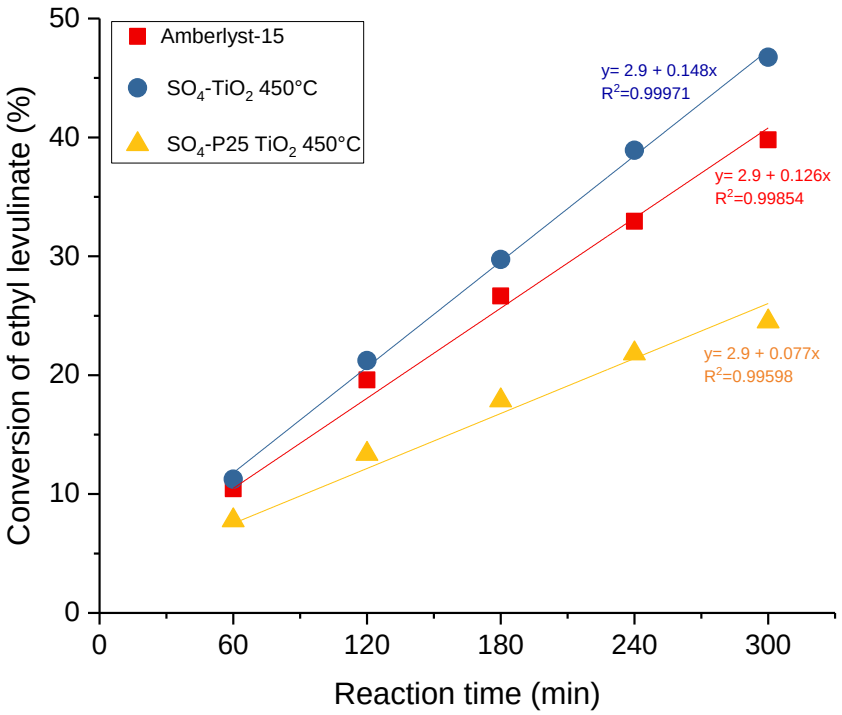


Figure 4.13 Rate of conversion of levulinic acid into ethyl levulinate as a matter of time using sulphated TiO_2 and commercial Amberlyst-15 solid acid catalysts.

Finally, the stability was conducted under the same reaction conditions by the recycling experiments. The catalysts were recovered from the first reaction, properly washed several times, collected, and dried overnight, and then reused in the next reaction without any post-treatment. The catalytic results are shown in Figure 4.14. On the basis of the results, none of the catalysts exhibit durability for prolonged period of time. Each catalyst gradually lost a portion of its activity in each subsequent run; however, the speed of deactivation varied between catalysts. SO_4-TiO_2 catalysts lost their activity faster than Amberlyst-15. After the 5th run, their activities reached to a plateau where only 6-8% conversion was observed. Although the activity of Amberlyst-15 was initially lower than that of SO_4-TiO_2 450 ^oC, it performed better than other two SO_4-TiO_2 catalysts after 2nd run, owing to its intrinsic properties of polymeric chains and their stability to chain-breaking in the reaction mixture, rather than desorption of protonic moieties. In contrast, activity of the weaker-bound

sulphate species drops when they detach from the metal oxide surface. Although the reason of deactivation under our experimental conditions is not known unambiguously, the loss (leaching) of active components, surface poisoning by coordination of substrates or agglomeration of particles are all plausible causes of catalyst deactivation. Recently, Liu *et. al.* published a review paper regarding the strategies to follow for increasing the stability of solid acid catalysts.[448] As a future work, SO_4-TiO_2 solid acid catalysts can be modified by introducing a surface protecting group or by addition of a co-catalyst to hinder leaching and sintering problems during catalysis.

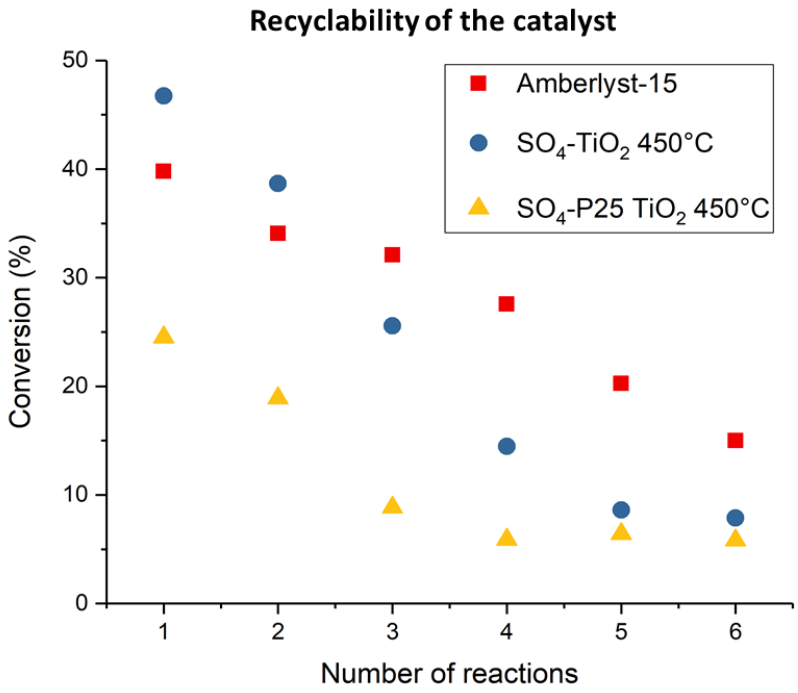


Figure 4.14 Recyclability of the sulphated TiO_2 and commercial Amberlyst-15 solid acid catalysts in the esterification reaction of levulinic acid in ethanol at 70 ^oC for 5 hours.

Given the fact that the as-prepared TiO_2 solid acid catalysts also show Lewis acidic character in addition to Brønsted acidity, these were also tested in catalysis of pyruvaldehyde to lactic acid which proceeds strictly via Lewis acidic sites to expand the scope of application.[449] Figure

4.15 summarizes the results of pyruvaldehyde Cannizzaro reaction to lactic acid over solid catalysts performed in water in a sealed Pyrex tube at 110 ^{o}C for 2 hours.

At a first glance, it has been found that the catalytic results are not directly related (or could not be correlated) with the amount and strength of the Lewis acid sites of the solid catalysts measured by ^{31}P NMR using TMP as a probe molecule, as one might have expected. This is presumably because TMP is a small molecule and its adsorption was measured in the gaseous phase where all acidic sites were accessible, whereas pyruvaldehyde is a large molecule and not all acidic sites could be accessible in the presence of a solvent as it may also interact electronically with the surface species. Nevertheless, clear trends within the group of catalysts were distinctly identified. Among various catalysts tested, as-prepared TiO_2 nanoparticles exhibited the highest catalytic activity (97% yield towards lactic acid), referring to its high surface area and Lewis acid content. Calcination of TiO_2 nanoparticles led to a decrease in activity progressively with the increase of calcination temperature. The decline in activity might be correlated with the decrease in defect sites and their surface area. PXRD results (see Figure 4.4) show that the crystallinity and particle size of TiO_2 nanoparticles increase as the calcination temperature is raised, resulting in reduced amount of accessible Ti defect sites for effective catalysis. Sulphate functionalisation of TiO_2 nanoparticles also reduces the activity slightly which likely because sulphate molecules occupy catalytically active, Lewis acidic Ti defect sites. Similar to the observations made with TiO_2 nanoparticles, the catalytic activity of sulphate functionalised TiO_2 nanoparticles decreases slowly as the calcination temperature increases. However, SO_4-TiO_2 calcined at 450 ^{o}C is an outliner in this trend. As discussed previously in BET and XPS sections, 450 ^{o}C is the optimum calcination temperature at which TiO_2 nanoparticles become crystalline and partial removal of -SO_4 and -OH groups expose more accessible acidic sites on the surface. Further increasing the

calcination temperature to 600 ^{o}C leads to removal of almost all sulphate functional groups and causes severe agglomeration which reduces the active surface area, thus the catalytic activity. Overall, these catalytic results indicate that the catalytic activity of solid acid catalysts does not only depend on number and strength of acidic sites but also to morphology and surface area of the nanostructures. Both the acid sites and surface area of the catalyst influence the catalytic performance of these solid acid catalysts.

Commercial Amberlyst-15 and P25 TiO_2 with and without sulphate functionalisation have also been tested for comparison. As expected the use of Amberlyst-15 catalyst resulted in only 4% pyruvaldehyde conversion to lactic acid largely due to the absence of Lewis acidic sites. P25 TiO_2 possessed comparable catalytic activity (87% conversion) to that of non-calcined SO_4-TiO_2. Similar to TiO_2 nanoparticle catalysts, sulphate functionalisation of P25 reduced the catalytic activity by 7%. Upon calcination at 450 ^{o}C, some of the catalytic activity could be regained due the partial removal of sulphate group leaving unsaturated Ti atoms as Lewis acidic sites on the surface. Moreover, the control experiment performed in the absence of catalyst showed no catalytic activity and confirmed that reaction proceeds only in the presence of a Lewis acid catalyst.

In summary, it has been demonstrated that high surface area, small TiO_2 nanoparticles (with or without sulphate functionalisation) prepared in this study are versatile and promising solid acid catalysts that can provide higher catalytic activity and better stability both in Brønsted and Lewis acid catalysed reactions compared to commercial solid acid catalysts.

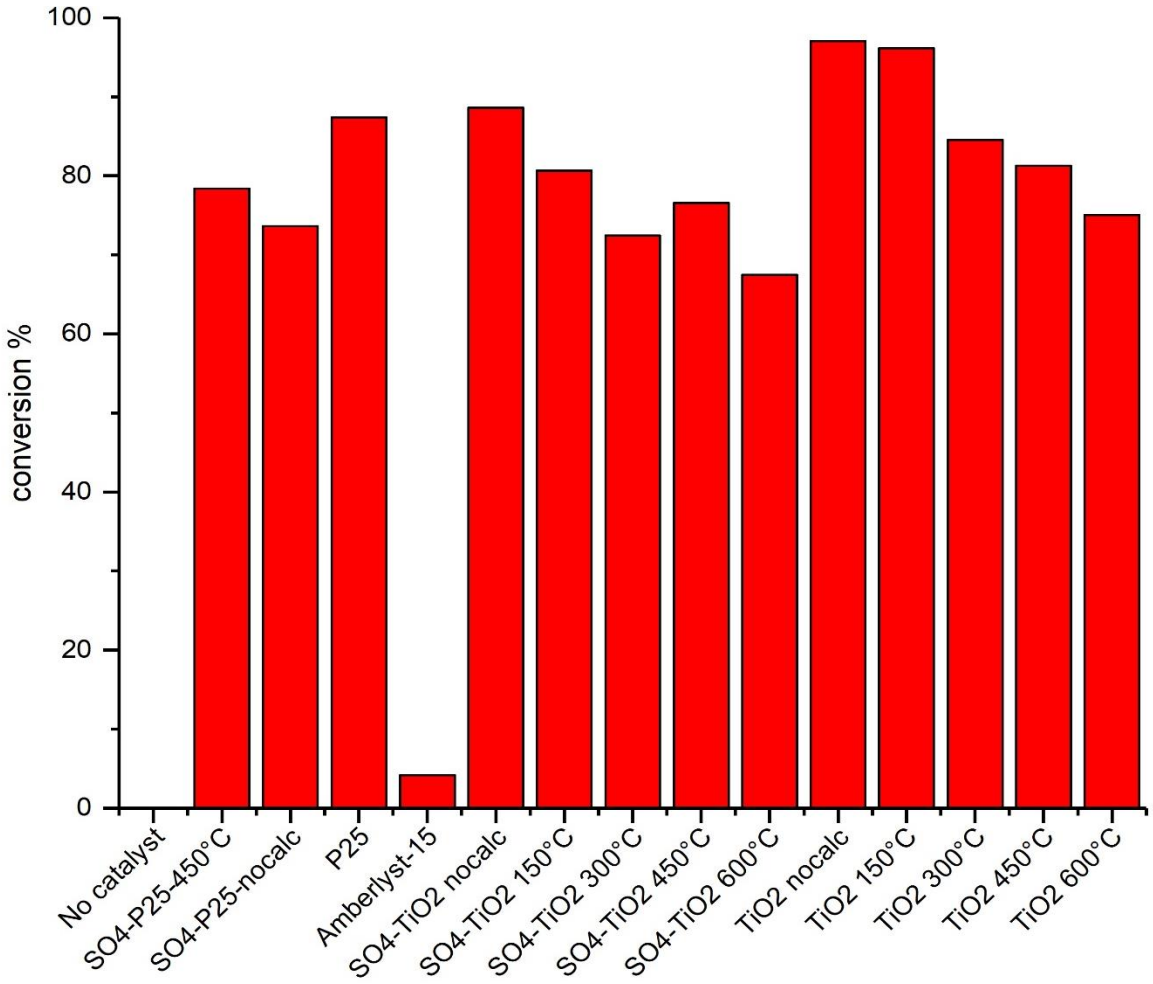


Figure 4.15 Probing Lewis acidity of the TiO_2 catalysts in a Lewis acid catalysed reaction of pyruvaldehyde to lactic acid. Commercial P25 TiO_2 and Amberlyst-15 were also tested as a reference.

4.3 Conclusion

This work has scoped the properties of titania nanoparticles as a promising heterogeneous solid phase candidate for acid catalysed reactions. The catalytic activity was determined and compared to commercially available P25 titania, 21-25nm large crystalline nanoparticles, as well as widely-used highly acidic commercial polymeric resin type of Brønsted solid acid catalyst Amberlyst-15.

Very small titania nanoparticles were successfully synthesized from titanium. These nanoparticles were analysed with PXRD and Raman as a means of calcination temperature to

attribute particle size and associate their crystalline structure. Surface functionalisation with sulphate species was performed to introduce highly acidic moieties on the surface of as-prepared TiO_2 nanoparticles as well as commercial P25 titania, and these were characterized, analysed and tested as a means of the calcination temperature providing additional stability to sulphate species.

PXRD analysis of both P25 and as-prepared TiO_2 nanoparticles confirmed there were no structural changes induced to the titania nanoparticles upon functionalization with sulphates. TEM imaging indicated formation of agglomerates nanograin superstructures which started to fragment into smaller nanoparticles with increasing calcination temperature. FT-IR spectroscopy was used to account for the presence and natural environment of the adsorbed sulphate species. It confirmed asymmetric stretches of S=O chelating bidentate sulphate as well as symmetric stretches of sulphate species and weakly bound sulphates to the corner surface titanium atom. Surface analysis with BET revealed very high surface area of as-prepared anatase nanoparticles which dramatically reduced upon calcination and functionalization with sulphates. However, as sulphates become bonded more strongly, a slight increase in surface area was observed.

In order to address the acidity content, type and strength, highly sensitive analytical tool to bring light into the performance of sulphated titania nanoparticles, trimethylphospine (TMP) and trimethylphospine oxide (TMPO) probe adsorbates that easily bind to acid sites and are applicable to the ^{31}P NMR technique were employed. The strength of the TMP/TMPO bond resulted in a peak shift in NMR spectra and these were consequently associated with TiO_2 surface acidity for detailed characterization of different acid sites and their strength.

Integrating the peaks accounted for quantity of each acid type and was linked to the type and stability of sulphate species on the TiO_2 surface.

The TMP ^{31}P NMR technique was used to probe Lewis acidity of titania nanoparticles as the chemical shift window is highly sensitive for Lewis acid strength, while the Brønsted acidity is defined by a rather small ppm region and served as an accurate quantitative tool to account for the number of Brønsted acid sites. As expected, the strongest Lewis acidity was observed for P25-TiO_2 nanoparticles without any functional groups. NMR peaks corresponding to Lewis acidic sites of as-prepared TiO_2 shows the strength of Lewis acidic sites is higher than that of P25. Upon functionalisation of the surface with sulphates, preferential chelating of SO_4^{2-} to Ti-OH is proposed leading to the electron withdrawing effect of sulphates increasing the positive charge on protons and Ti species. Interestingly, calcining the sulphated TiO_2 nanoparticles at elevated temperatures did not change the position of the peaks but resulted in a change of their relative intensities. Quantitative analysis of the deconvoluted ^{31}P NMR peaks was used to account for the amount of acid sites of each acid type. For as-prepared TiO_2 nanoparticles revealed 43% of its total acidity originated from weak Lewis acid sites of their hydrated species within the nanoparticles. While the strongest Lewis acidity was observed for P25-TiO_2 nanoparticles without any functional groups, a similar Lewis acid chemical shift with smaller NMR peak, meaning smaller number of Lewis acid sites, was observed in 450°C calcined sulphated P25-TiO_2. This was linked to the lost Lewis acid sites that are occupied with sulphate species. In contrast, sulphated titania nanoparticles exhibited smaller and weaker Lewis acidity.

The TMPO probe was used to analyse acidity strength of Brønsted acid sites providing a tool with wider chemical shift range in ^{31}P NMR leading to broad NMR peaks within the Brønsted

acidity region. Deconvolution of the broad NMR peaks was performed in conjunction with other qualitative and quantitative results such as TMP ^{31}P NMR for the number of Brønsted acid sides, while the concentration of sulphate species present on the surface was cross-checked with TGA-SDT analysis and XPS elemental analysis. XPS analysis in particular provided an indispensable tool to understand the content and environment of sulphate species in the near surface region of different titania nanoparticles. High content of Brønsted acid sites was shown for as-prepared sulphated titania nanoparticles as well as calcined sulphated titania nanoparticles and sulphated P25 TiO_2 samples. Peak deconvolution of sulphated TiO_2 samples calcined at 300°C or lower temperature showed a large content of less strongly bound sulphate functional moieties. These species are highly acidic but their weaker bonding to the titania surface resulted in decreased stability and as a consequence, their catalytic acidic activity. Calcination at 450°C creates stronger bonding to the titania surface for the sulphate species and despite the observation that the overall acidity as measured by the NMR shift is slightly decreased, the number of stable acidic sites available on the nanoparticle surface increased which is highlighted by larger detected content and broader NMR peaks in the Brønsted acid region. In contrast, 600°C calcined TiO_2 nanoparticles showed small content of very stable acid sites and very similar NMR shift to the 450°C sulphated P25 titania, confirming the trend in acidity and stability.

Testing of sulphated titania nanoparticles in the Bronsted acid catalysed esterification reaction of levulinic acid showed highest activity at both 450°C calcined sulphated titania samples which reiterates the significance of the calcination temperature on the performance of functional sulphate groups to remain active and stable. The trend of calcined nanoparticles gave a volcano activity plot with largest conversions observed for 450°C calcined sulphated titania nanoparticles. However, when compared to the catalyst activity of the larger

commercial P25 titania nanoparticles functionalised via the same method, a significantly lower acidic activity was achieved. Most importantly, SO_4-anatase TiO_2 calcined at 450 ^oC owing to the high surface area with a large number of exposed corner titanium atoms and has led to unprecedented acidic activity, outperforming a widely used commercial polymeric resin Amberlyst-15, which makes it a promising candidate for solid acid catalysed reactions.

Since TiO_2 solid acid catalysts also show Lewis acidic character in addition to strong Brønsted acidity and to expand the scope of application of these novel solid acid catalysts, catalytic activity in a reaction of pyruvaldehyde to lactic acid which proceeds strictly via Lewis acidic sites was studied. A couple of clear trends within the group of catalysts were identified. As-prepared anatase TiO_2 nanoparticles possessed the highest catalytic activity, resulting from the very high surface area and number of available Lewis acid sites. Calcination of TiO_2 nanoparticles led to decrease in their surface area and the number of defect sites affecting the activity with the increase of calcination temperature. In contrast, sulphate functionalisation of TiO_2 nanoparticles reduced activity was observed and linked to sulphate molecules occupying catalytically active, Lewis acidic Ti defect sites. Similar to the observations made with TiO_2 nanoparticles, the catalytic activity of sulphate functionalised TiO_2 nanoparticles decreased with increasing calcination temperature.

In summary, successful synthesis of novel highly acidic solid acid sulphated titania nanoparticles has been achieved via sophisticated chemical engineering process and their outstanding physicochemical properties were studied in detail with a series of highly sensitive analytical characterisation tools to bring full understanding of the improved performance of this material. Highly promising potential was successfully demonstrated in comparison against other solid acid commercially used materials.

Chapter 5 Pd-doped 1T-Phase Single Layer Molybdenum Disulphide Nanosheets and Their Catalytic Activity in Organic Reactions

5.1 Introduction

Today, green chemistry is of the utmost importance, with much of society's conversation tending towards how to reduce pollution and increase environmental efficiency. Increasing efficiency of reactions whilst also ensuring low environmental impact follows societal need for sustainability and green chemistry processes. Catalysts are used to speed up reactions, but historically these have been developed to improve the economic yield, overlooking environmental effects. Palladium metal and palladium metal compounds are used as catalysts across multiple reactions including hydrogenations, oxidations, and cross-couplings.[450–458] Homogeneous catalysis using these metals has advantages of high product yield and high efficiency, however, low catalyst recovery and residual catalyst in the synthesised molecules remain an issue.[459–462] Therefore, expanding to mass-scale becomes problematic due to poor product quality and fast depletion of toxic catalyst material, which are a matter for both economic and environmental concern. A solution is to confine the palladium-based catalysts onto various heterogeneous supports, such as organic-inorganic fluorinated hybrid materials, polymers, glass-polymer composites, ionic liquids, *etc.*[451,463–471] By binding these molecules to supports, efficiency is increased due to easy separation from the product, convenient handling, non-leaching/toxic nature, and ability to be reused.[472]

Suzuki and Heck are cross-coupling reactions that are significant in the synthesis of natural products and fine chemicals.[473–475] They are used across a wide range of industries such as pharmaceuticals, biologically active molecules, and material science, in which they are used as a powerful and straightforward tool for carbon-carbon bond formation.[476–478] Synthesis of

biaryls is made more effective by the Suzuki cross-coupling reactions of arylboronic acids and aryl halides, while substitution of alkenes is facilitated by the Heck coupling reactions between aryl halides and alkenes. Both biaryls and alkenes are an important class of organic compounds as they are useful precursors to pharmaceuticals, polymers, liquid crystals, and ligands.[156,479] Palladium-based catalysts have been shown to outperform many metallic catalysts studied for Suzuki and Heck reactions.[480–483] Soluble homogeneous Pd metal complexes with coordinating phosphine ligands in organic solvents are traditionally used to catalyse Suzuki and Heck coupling reactions resulting in tedious catalyst separation and recovery as well as causing high levels of palladium contamination in the final product.[484,485,486] Therefore, heterogeneous Pd catalysts are being extensively studied to improve upon issues with homogeneous Pd catalysts and replace them as the preferred catalyst form of choice.

The large surface area of transition metal nanoparticles enables effective catalytic nature for chemical transformations.[204] Metal particles are typically prepared by reduction of metal ions in the presence of surfactant and polymer stabilisers. Palladium nanoclusters and colloidally-stable palladium nanoparticles/nanoclusters dispersed in solution have been reported to be effective catalysts for several Suzuki and Heck coupling reactions in organic solvents.[206] Recent research has focused on highly dispersed/nanosized Pd metal on solid support as catalysts, that can provide a very good catalytic performance for organic coupling reactions, as well as being recoverable and recyclable, all of which leads to increasing economic viability.[207–211]

Many materials can be used to support Pd nanomaterials, including carbon materials, polymers, and inorganic materials.[487–493] Palladium supported on activated carbon (Pd/C) is

the most commonly used in heterogeneous Pd-catalysed coupling reactions due to its efficiency and commercial availability.[494–496] Pd/C is stable in air, water, acids and bases, and generally does not need reactions to be performed in an inert atmosphere. As Pd/C is stable in such environments, Pd/C-catalysed Suzuki and Heck cross-coupling reactions have been performed in organic media, aqueous media, and under microwave conditions.[58–69] Pd/C catalysis has good to excellent yield for a large variety of substrates, and is recoverable and recyclable over a large number of cycles.[494–496,509] However, palladium nanoparticles are generally observed to be more catalytically active when not on a solid support. A compromise of this higher catalytic activity and the easy recovery of supported palladium nanomaterials must be accomplished to achieve an improved system. Most Pd heterogeneous catalysts also perform well only at elevated temperatures compared to that of homogeneous catalysts. However, obtaining higher activity at low reaction temperatures is a key to making these environmentally friendly heterogeneous catalysts more attractive for implementation in industry. A better understanding of the interaction between the palladium nanoparticle and the support is required to design an efficient heterogeneous catalyst for organic cross-coupling reactions.

Palladium catalysts are not only interesting for organic coupling reactions but also for hydrogenation of alkynes to alkenes and alkanes. Alkenes in particular are important in the fine chemical, petrochemical and polymer industries, with the lower molecular weight alkenes generated in the petrochemical industry and higher molecular weight alkenes synthesised via derivatives of the same industry as well as by employing additional synthetic methods.[510,511,512] The processes used in these industries that produce alkenes include thermal treatment, dehydrogenation, catalytic cracking, and hydrogenation.[511,513,514] These processes produce not only the desired products but also undesirable products, such as

alkanes, alkynes, and other unsaturated by-products.[249,515] A high yield of the desired alkene is required in an economical, energy-saving and environmentally-green method. Increasing focus has been put on the development of sustainable catalysts for selective hydrogenation of alkynes to the targeted alkene in order to reduce waste by-products and increase product yield, overall process cost, and to reduce negative impact on the environment. This selective hydrogenation of a variety of substrates is an important technology in the bulk and fine chemical industries, where the key property of reaction is the selectivity to the desired product.[516] Selectivity to the desired product improves economic viability by reducing loss of reagent to formation of undesired products, as well as improving downstream processes by easing by-product separation.[517] An especially difficult and challenging reaction is the selective hydrogenation of monosubstituted alkynes to the corresponding monosubstituted alkenes.[518–524] An understanding and control over the synthesis of the active site, as well as the method of attachment of the active site to the catalyst support is required to create an optimised catalyst for this reaction.

The benefits that palladium brings to hydrogenation reactions is its high hydrogenating capacity, as well as activity and selectivity at low temperatures.[525–527] The benefits of heterogeneous palladium catalysts over their homogeneous counterparts are related to their stability under atmospheric conditions, easy separation properties without palladium leaching from the catalyst into reaction mixture, and their reusability, all contributing to the green chemistry idea of an environmentally friendly industrial catalyst. One of the key industrial hydrogenation processes of monosubstituted alkynes is the vapour-phase 1-pentyne hydrogenation reaction using palladium catalyst. Palladium supported on γ-alumina or palladium on carbon supports (Pd/C) are generally used for full hydrogenation of 1-pentyne to pentane, and are generally employed or under investigation in chemical industry. Of

particular interest is the activity of Pd/C catalyst that make use of incorporating carbon as well as hydrogen into the palladium's surface, controlling hydrogenation events at this surface, however, this also leads to the deactivation and degradation of the palladium catalyst over time.[528–531]

A classical catalyst widely employed in partial hydrogenation of internal alkynes to corresponding alkenes for its effectiveness is the Lindlar catalyst. [532–538] A typical Lindlar catalyst generally consists of 5 wt. % Pd supported on calcium carbonate ($CaCO_3$) poisoned with a lead promoter. However, the Lindlar catalyst also possesses several drawbacks such as low reactivity at mild reaction temperatures, difficulties with separation and consequent recycling of the catalyst, very high toxicity of the lead promoter associated with its instability and leaching in the reaction mixture, and high cost due to its high metal loadings that cannot be easily and cheaply recovered. The toxicity of lead has caused the restriction of use of the catalyst in a number of important industrial processes, namely the manufacture of food, cosmetics, and medicine. Therefore, it is highly desirable and challenging to address these issues when designing a new, greener catalyst, while retaining or further improving the activity and selectivity of the Lindlar catalyst, particularly towards partial hydrogenation of medium and large molecular weight alkynes.

Palladium sulphides have been observed to be selective in use as heterogeneous catalysts for partial hydrogenation of alkynes (acetylene and methyl acetylene) and alkadienes (propadiene and butadiene) as well as Suzuki coupling reactions.[271–274] Palladium sulphides were found to have optimised selectivity for partial hydrogenation of alkynes to alkenes at the relatively high temperature range of 200 – 250 °C.[275] The sulphide content purportedly has an impact in both the steric and electronic effects preventing the full hydrogenation of

alkene intermediates during the hydrogenation reaction of alkynes, thus bestowing upon the modified Pd surface a high catalytic selectivity towards the preferred alkenes.[276] However, similarly to Pd metal nanoparticles, the palladium sulphide nanoclusters can be unstable under these reaction conditions, difficult to separate and recycle, and have been found to be moderately soluble in water.

Two-dimensional crystals and nanomaterials have been found to have exceptional electronic, optical, and mechanical properties, and attracted an increased attention from scientists and engineers over the last decade.[336,539–541] Although graphene is the most well-known example of two-dimensional nanomaterials, attention has skewed towards metal dichalcogenides due to their unique properties and various applications across a multitude of sectors; in energy storage, sensing, electronic devices and photo- and electro-catalysis.[542–548] Among transition metal dichalcogenides, molybdenum disulphide (MoS_2) nanosheets are one of the most promising materials as catalyst support materials for heterogeneous palladium catalysts.[548–550] Two-dimensional MoS_2 nanosheets, commonly produced by exfoliating bulk MoS_2, are inorganic analogues of graphene that possess exciting electronic, optical and catalytic properties, often profound or significantly enhanced when compared to those of the bulk material.[349,551,552] This not only opens up the surface area of the support to be utilised for Pd active sites, but the use of electron-rich MoS_2 nanosheets in addition, which acts as a charge transfer platform for active Pd catalysts, and is thought to facilitate and improve their overall catalytic performance via efficient electron transfer between palladium species and the MoS_2 support, resulting in carbon-hydrogen bond activation in alkyne hydrogenation and carbon-carbon bond activation in organic coupling reactions at low operating temperatures. In addition, most palladium nanoparticles and nanostructures undergo constant aggregation during reaction and the recycling process due to their high surface energy, which in turn leads

to a dramatic decrease in catalytic activity. MoS_2 nanosheets have been demonstrated to stabilize transition metal nanoclusters and single metal atoms on its base planes and edges, while preserving catalytic activity of the active sites.[551,553,554]

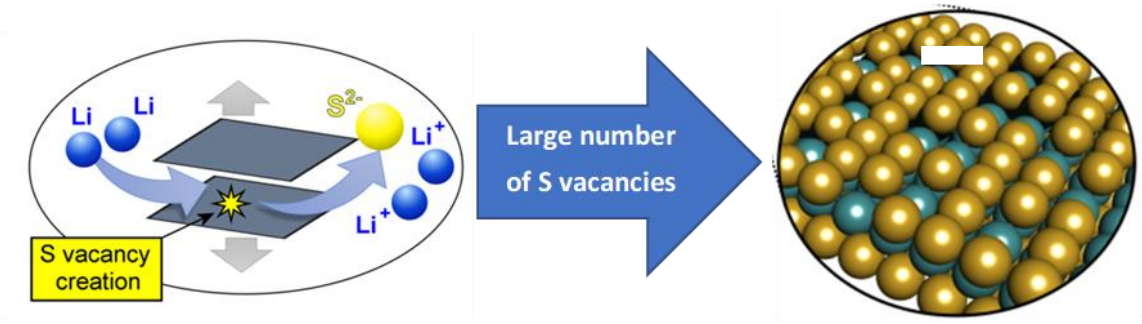
Furthermore, two different phases of exfoliated MoS_2 nanosheets can be used as supports. Semiconducting trigonal-prismatic 2H phase is the most stable and naturally abundant phase, however, much more interesting from the perspective of catalyst support, is the metallic octahedral 1T phase.[555,556] It offers modified electronic properties as a result of structural changes and has also been found to be more catalytically active compared to the 2H phase.[551] The metallic-like character of the 1T phase can readily provide electrons to the Pd catalyst atoms and nanoparticles and enhance their catalytic activity.[557–561] However, the 1T phase is generally considered as a metastable phase. Recently, it was shown that the metallic 1T character can indeed be preserved when structural defects on MoS_2 basal planes are doped, and hence made more stable with other transition metal atoms and nanoparticles.[553,554,562,563] Additionally, the flat nature of the nanosheets and abundance of sulphur atoms can help maintain the improved steric and electronic effect on the active Pd species, similar to palladium sulphides, and mitigate the issues with solubility and stability of the active Pd species.

The primary aim of this chapter is to investigate the synthesis, characterisation, and catalytic application of Pd-doped single layer MoS_2 nanosheets with exposed 1T phase as a sophisticated and versatile Pd heterogeneous catalyst. The aims of the synthetic architecture of the Pd catalyst is to produce well integrated Pd into single layer nanosheets of metallic 1T phase of MoS_2 as a platform for easy electron transfer between the two entities to promote higher catalytic activity of deposited Pd nanostructures. The use of $Pd(NO_3)_2$ aqueous solution

as a Pd precursor with continuous addition and vigorous dispersion into single layer MoS_2 suspension mixture is intended to allow for homogeneous deposition across the single layer nanosheets. Subsequent addition of the strong reducing agent sodium borohydride is to target oxidised Pd species into reduction to their metallic phase. The structural and morphological characteristics of Pd-doped MoS_2 materials were investigated by a combination of characterisation techniques including TEM, Raman, PXRD, EPR and XPS and structural and electronic changes of the catalyst material were depicted and correlated to their catalytic performance evaluated in a series of industrially sought-after processes of C-C cross coupling and alkyne hydrogenation reactions.

5.2 Results and discussion

Organolithium chemistry was used to intercalate lithium into the planes of bulk MoS_2 layered structure. Sonic wave assisted top-down chemical exfoliation method was utilised by introducing lithiated MoS_2 to water media, where exfoliated monolayers get suspended. Removal of the unexfoliated parts led to the synthesis of monolayer MoS_2 under ambient conditions. The synthesis method of single-layer MoS_2 nanosheets is illustrated in scheme 5.1.



Scheme 5.1 Illustration of the top-down physical and chemical exfoliation sonochemical synthesis of few-layer and single-layer MoS_2 nanosheets from their bulk analogue. Adapted from a study on Co-doped MoS_2 monolayer catalysts by Liu, Tsang et.al. [554]

During the sonochemical exfoliation of MoS_2 layers, large numbers of sulphur vacancies and unpaired electrons are formed on the basal planes of MoS_2 which can be targeted by electron deficient positively charged species. Therefore, these defect sites can be utilised for functionalization or doping of the MoS_2 material. When the impregnating solution is diluted enough, further nucleation to metal nanoparticles can be surpressed. It is also expected that the larger number of exposed sulphur vacancies and other defect sites would allow further uptake and stabilisation of dopant species and their reduction into single atoms, which in turn can lead to higher catalytic activity of the exfoliated single-layer material. In this regard, single atom doping on single-layer MoS_2 nanosheets was successfully demonstrated by Liu and co-workers, who employed Co-doped single-layer MoS_2 as highly performing catalyst in hydrodeoxygenation reaction.[554] However, these were predominantly 2H phase monolayers.

One of the aspects of doping is to adsorb catalytically active metal species on the surface of the MoS_2 substrate. It is important to note that adsorbed precursor metal species are often in their oxidized form. To promote reduction of the metal species to their metallic state, sodium borohydride ($NaBH_4$) is used as a reducing agent. However, this often is not enough and further reduction under a flow of reducing gas and elevated temperatures is needed. In the present work, MoS_2 nanosheets were prepared by sonochemical exfoliation method, then Pd^{2+} species were introduced. Pd^{2+} species were reduced to Pd^0 with $NaBH_4$ at room temperature followed by calcination at 300 ^oC under 5%H_2 in Ar gas flow, chosen based on TPR results (See Appendix for further information).

5.2.1 Structural and Morphological Characterisation of the Catalysts

In order to confirm the exfoliated nature of the MoS_2 nanosheets, and the exfoliation efficiency from their bulk analogue, electron microscopy images were recorded and examined.

Aberration-corrected transmission electron microscopy (AC-TEM) Images (Figure 5.1) revealed a large number of very thin nanosheets across the examined sample. The predominance of single layers is obvious upon inspection with few bilayers also being present. However, it is easier examining the thickness of the edges of the nanosheets using dark field mode TEM (DFTEM). DFTEM confirmed that the majority of nanosheets were indeed monolayers. In addition, it also showed that many of the nanosheets appearing as bilayers had an increased gap between the two monolayers, with extended interlayer spacing of 9.2-9.3 Å compared to non-expanded MoS_2 with interlayer spacing of 6.2 Å. The measured indicating these were two monolayers formerly exfoliated that were restacked back together. It is well documented that if foreign species are present in the dispersion of freestanding MoS_2 monolayers during the restacking process, the foreign species are possibly trapped in the gaps of restacked MoS_2 monolayers. In our synthesis method, Li is expected to intercalate into the interlayer gaps of MoS_2. Upon exposure to atmosphere, the intercalated alkali metal reacts with moisture to expand interlayer spacing of the MoS_2 by 3.2 Å.[372]

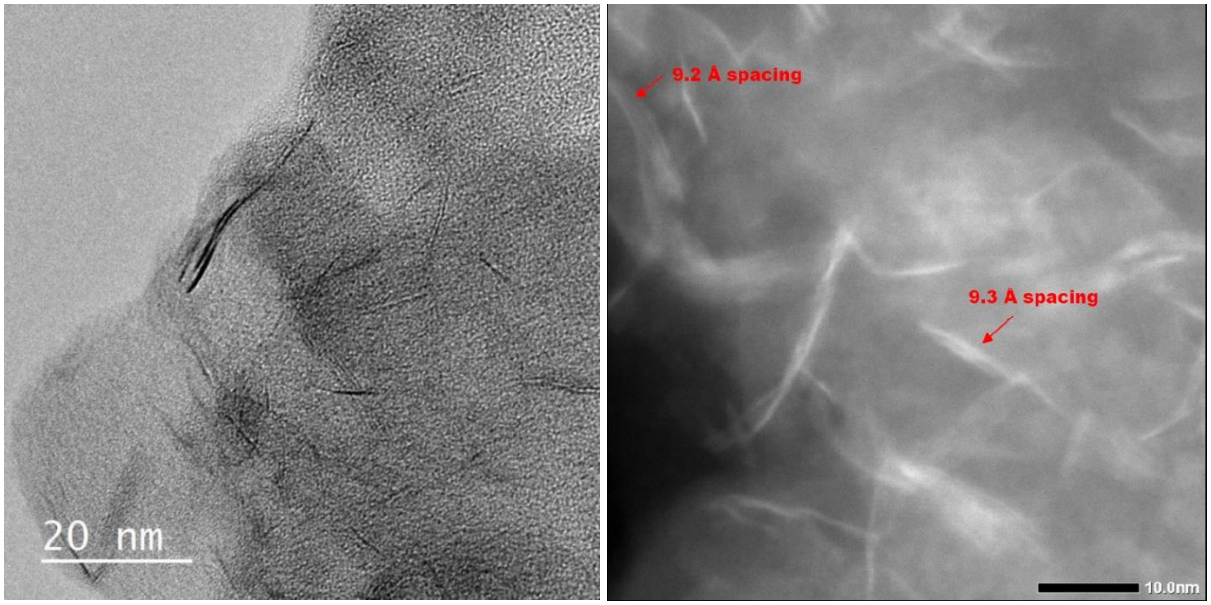


Figure 5.1 AC-TEM and DFTEM images of single-layer MoS_2 nanosheets.

A scanning transmission electron microscope (STEM) enables high resolution electron imaging capable to depict individual atoms and molecules, thus, making it a highly attractive tool to study materials' elemental structure. Bright-field imaging in scanning mode using an on-axis detector is capable of atomic resolution imaging. High Angle Annular Dark-field (Z-contrast) imaging in scanning mode using an annular detector is also capable of atomic-resolution imaging. Using these two scanning modes makes this highly sophisticated analytical technique an ideal probe for studying individual MoS_2 nanosheets, as well as for unveiling the structural phase across their basal planes. Figure 5.2 portrays Bright-field and Dark-field STEM images of restacked single-layer MoS_2 nanosheets. Inspection of these images revealed that individual layers are indeed restacked monolayers. The layers largely exist as the 1T-phase, however, there are few areas where 2H-phase is also observed.

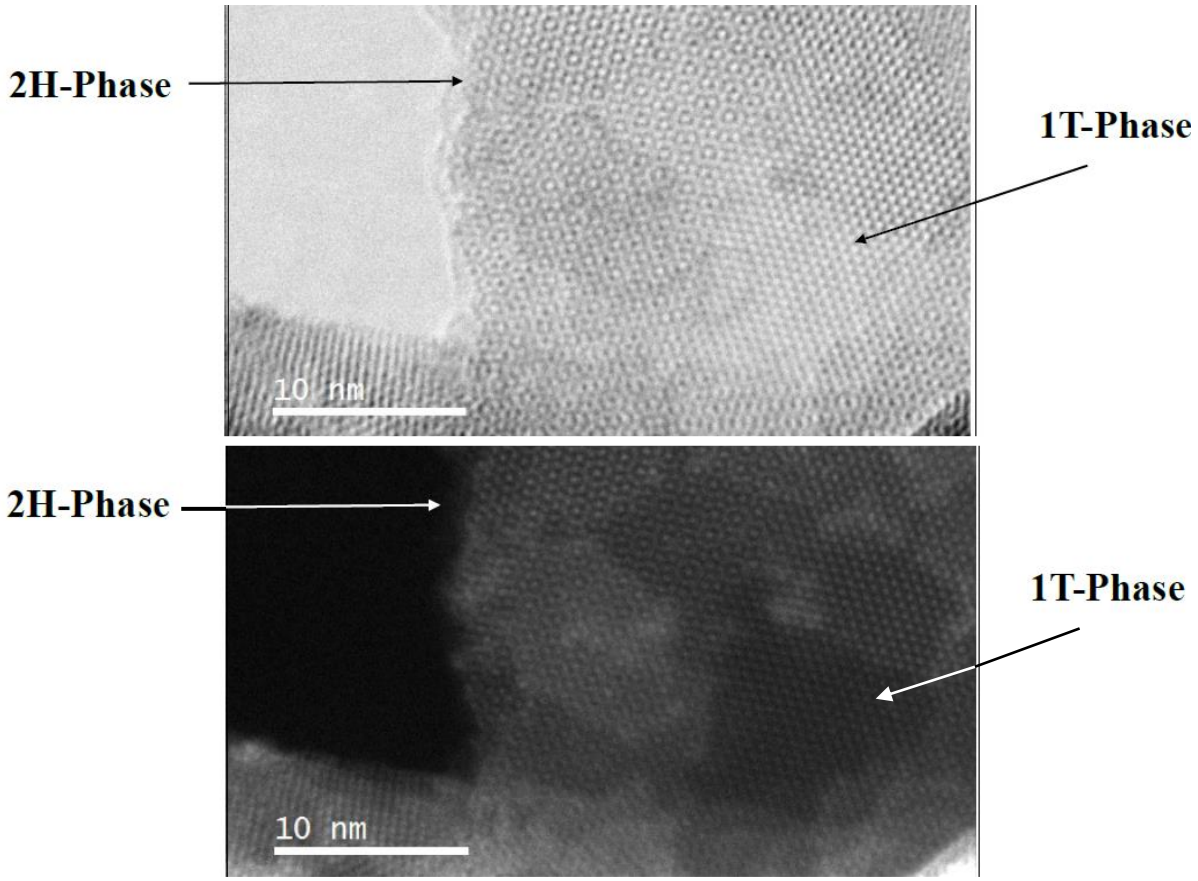


Figure 5.2 Bright-field (top) and Dark-field (bottom) STEM images of restacked single-layer MoS_2 nanosheets.

Figure 5.3 right shows High-Resolution STEM imaging of the as-prepared Pd-doped MoS_2 nanosheets. It seems that doping Pd via impregnation method did not change the morphology or the crystallinity of the MoS_2 nanosheets. Single atoms located on the basal planes are clearly observed on STEM images, and their brightness signifies they are larger metallic atoms. It has been previously demonstrated that Pd single atoms can be stabilised on basal planes of MoS_2 either as a sulphur site substitute atom or in Mo atop site.[564] Illustration of such atomic arrangement from the top view perspective is shown Figure 5.3 left. This is indeed observed in this sample prepared by impregnation method of depositing Pd species on MoS_2 nanosheets, and their consequent reduction into single atoms and small nanoclusters with sodium borohydride.

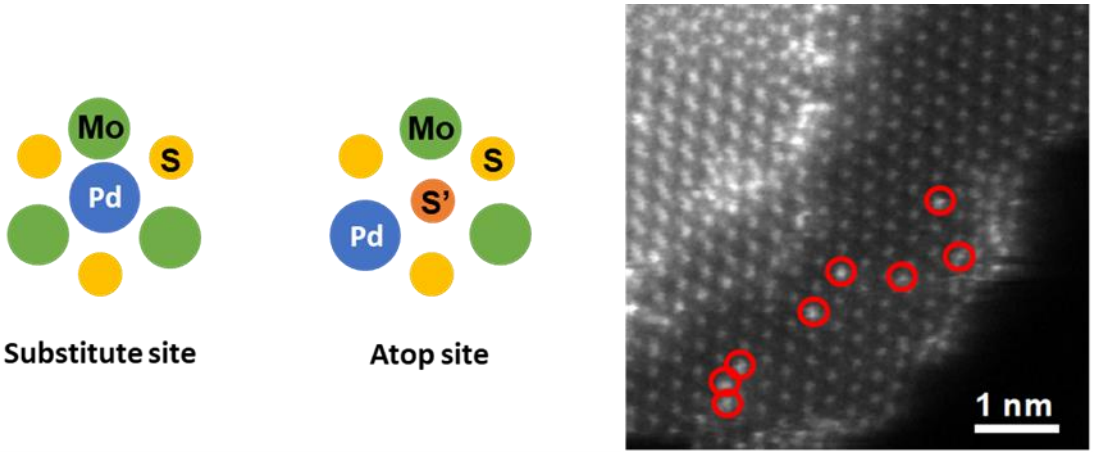


Figure 5.3 STEM imaging and analysis of single Pd atom sites on the surface of single layer MoS_2 nanosheets. Top view perspective of the atomic arrangement of the Pd occupied sites on the nanosheet basal plane.

When STEM imaging is coupled with Energy-Dispersive X-ray Spectroscopy (EDX), individual elements that the sample is composed of, and their precise location can be identified. EDX is an analytical technique used for elemental characterization, displaying a unique set of peaks for each element in the electromagnetic emission spectrum. This highly sophisticated analytical technique makes an ideal probe for detecting individual Pd structures and single atoms on the MoS_2 surface, identifying individual nanosheets, as well as for unveiling the phase of MoS_2 nanosheets across their basal planes. Figure 5.4 presents STEM images coupled with EDX analysis rendering information about the changes to Pd-doped single-layer MoS_2 upon calcination at 300°C under reducing conditions of 5% H_2/Ar. The top left image depicts a larger area of the sample with two highlighted areas that represents well the observations of the sample. These two areas were assigned with numbers 1 and 2. Area 1 shows Pd nanoparticle with a measured diameter of 20 nm. This is the largest nanoparticle observed by STEM imaging. Corresponding EDX analysis confirms that this is indeed a Pd nanoparticle as very high Pd content is recorded for this area.

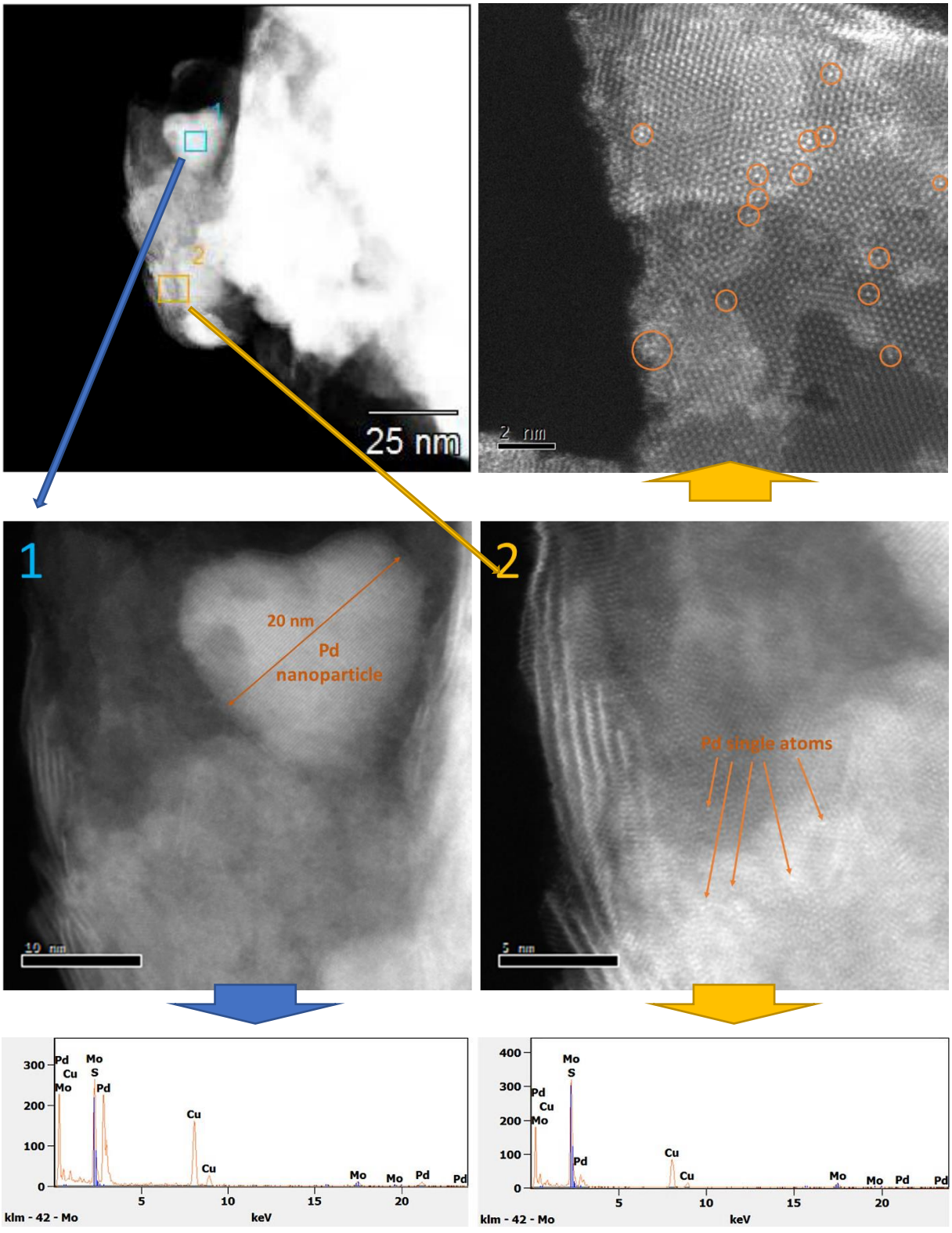


Figure 5.4 STEM images coupled with EDX analysis of Pd single atoms and nanoparticle sites on the surface of single-layer MoS_2 nanosheets calcined at 300°C under 5% H_2/Ar. (The presence of Cu in EDX spectra is due to the usage of copper based TEM grid)

In contrast, area 2 displays part of the single-layer MoS_2 where only Pd single atoms are likely to be observed. These are highlighted in the zoom in top right corner. There are multiple areas where bright single atomic units can be seen, and some of the most obvious were highlighted by orange circles. In order to be able to confirm their presence, an EDX scan of the area was recorded and analysed. The EDX spectra revealed much lower Pd content compared to the area with Pd nanoparticle, but confirmed presence of a good amount of Pd. However, there are no Pd nanoparticles observed, and the Pd content can be entirely ascribed to the presence of Pd single atoms. It is important to note that these single atoms were able to withstand the calcination heat and remained stable. It can be postulated that these are the single atomic units firmly attached on the MoS_2 structural defects and remained stable during the calcination process.

Overall, electron microscopy analyses show that sonochemical treatment of bulk MoS_2 led to successful exfoliation of layers. The lithium exfoliated sample characterized by TEM revealed that majority of the flakes are monolayers and few appeared as two or three layers. The expanded interlayer spacing of multi-layer MoS_2 nanosheets indicated that their existence is not due to unsuccessful exfoliation of bulk MoS_2 but mainly due to re-stacking of formerly exfoliated monolayers. Interestingly the exfoliated MoS_2 layers mainly adopt 1T phase over the more thermodynamically stable 2H phase of its precursor and impregnation of Pd, followed by $NaBH_4$ reduction, did not cause any change in the morphology or the crystallinity of the MoS_2 template. However, restacking was more severe and formation of both Pd single atoms and nanoclusters was evident in Pd-doped samples. It should be noted that the dispersion of single molecular layer sample from colloid solution to solid form for characterization is highly dependent on the nature of sample preparation method. It has been observed that the TEM sample prepared by placing a droplet of dispersed aqueous single layer

MoS_2 ($^{SL}MoS_2$) containing solution on a copper grid sample holder followed by fast evaporation, would lead to some degree of aggregation. Considering that the dispersion of non-doped and Pd-doped $^{SL}MoS_2$ in aqueous solution was excellent, which formed stable black colloid solution, the aggregation of MoS_2 nanosheets observed in the TEM might also be due to the artefact in the sample preparation. Thermal treatment of Pd-doped $^{SL}MoS_2$ increased the size of Pd nanoparticles to 20 nm but the presence of single atom dispersed Pd at the basal plane of MoS_2 could still be observed visually by TEM and confirmed by EDX analysis.

To further confirm the phase identity of the bare and doped MoS_2 samples, Raman, powder X-ray diffraction (PXRD), Electron paramagnetic resonance (EPR) and X-ray photoelectron spectroscopy (XPS) techniques were applied.

Raman spectroscopy is known as a powerful non-destructive technique for the characterization of crystalline structures of single-layer nanosheets and bulk MoS_2. As presented in Figure 5.5, two most significant vibrational modes of 2H phase MoS_2 are E_{2g} and A_{1g}. E_{2g} arises from in-plane vibrations of two sulphur atoms with respect to the molybdenum, while A_{1g} which corresponds to the out-of-plane vibrations of S atoms in opposite directions.[565] The origin of the 2LA(M) peak is ascribed to a second-order longitudinal acoustic phonon peak, however, it has been proposed that it can overlap with additional peak referring to the first-order optical phonon vibration denoted as A_{2u}.[566,567]

Upon exfoliation of the MoS_2 nanosheets, structural changes to the MoS_2 basal planes from 2H phase to 1T phase take place. The 1T phase has relatively lower in-plane symmetry, leading to loss of long-range structural features that could be depicted by powder diffraction. 1T phase for single layer MoS_2 nanosheets with characteristic Raman modes of E_{1g}, and low-

frequency phonon modes J_1, J_2 and J_3 are clearly observed. The appearances of these characteristic peaks for 1T phase are attributed to the longitudinal acoustic phonon modes. A_{1g} mode characteristic for out of plane stretches in semiconducting 2H phase and 2LA(M) longitudinal acoustic phonon mode are lost.[568,569]

The influences of Pd-doping and reduction calcination temperature on the phase of MoS_2 were also studied using Raman spectroscopy. The profile lines of Pd-doped samples are identical with their undoped $^{SL}MoS_2$ counterparts, indicating that no structural changes were inflicted by Pd-doping and the calcination at 300°C under reducing conditions. The drop in peak intensities is ascribed to large Pd doping that in turn would result in lower peak signals, but the ratio of these that remained are as expected.

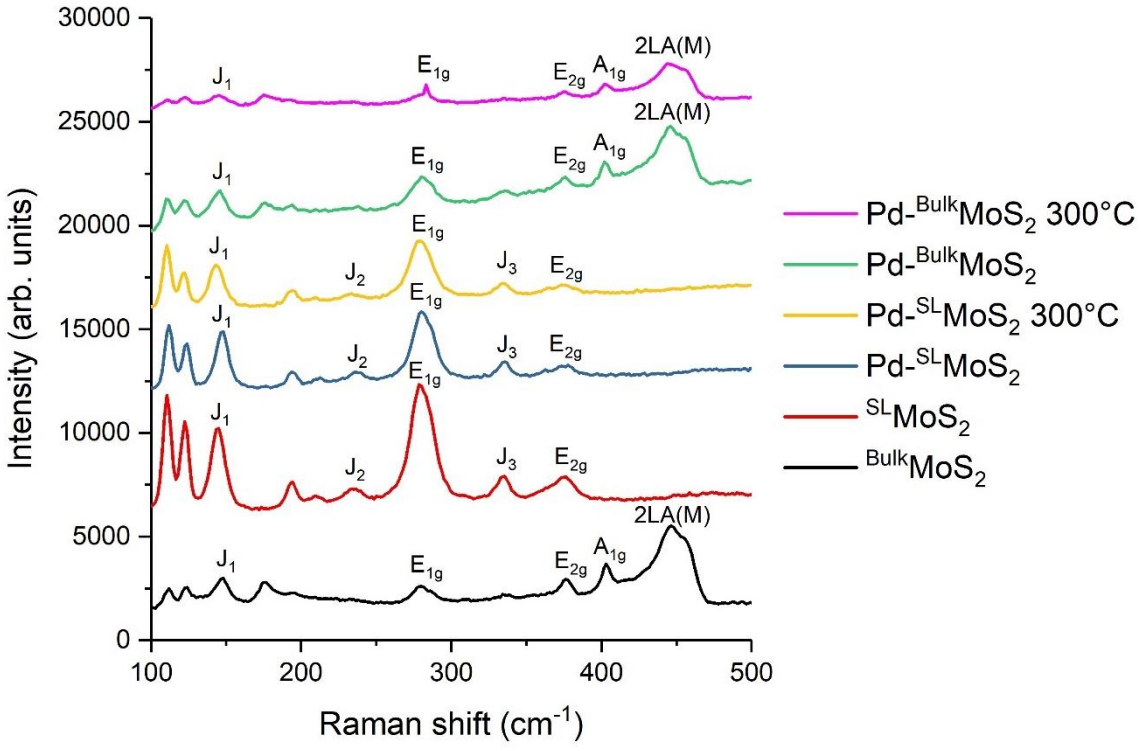


Figure 5.5 Raman spectra showing phase retainment of Pd-doped bulk and single-layer MoS_2 upon heating.

Powder X-ray diffraction (PXRD) was used to determine crystallinity of the synthesized MoS_2 nanosheets and to examine their crystalline structure. PXRD diffractograms showing crystalline arrangement pattern in different MoS_2 and Pd-doped MoS_2 samples are presented in Figures 5.6 and 5.7. Undoped bulk MoS_2 shows a typical pattern for 2H trigonal prismatic phase, and high sharp intense peaks indicate high crystallinity throughout the sample. In contrast, chemically exfoliated single-layer MoS_2 using organolithium species typically result in large number of monolayers as shown by analysis of HRTEM imaging. In addition, phase change from semiconducting 2H phase to metallic 1T phase is expected due to structural changes as a result of the lithium intercalation during exfoliation process. Changes in structure lead to loss of a long-range repetitive pattern and the diffraction peaks nearly vanish. In general, to identify a reduced number of layers, the (002) diffraction peak represents repetitive pattern across the basal planes of nanosheets and is perpendicular to the basal planes of MoS_2, and therefore can be a good indicator of the reduced number sheets in exfoliated MoS_2 flakes, as well as restacking of the exfoliated material. It was previously reported that single-layer nanosheets get restacked and may return from 1T to 2H phase, however, this was not observed and 1T phase of exfoliated MoS_2 monolayers remained stable upon restacking.[570–572] The lack of other peaks shows that the material lacks long range crystallinity, and this is expected for 2D materials.

Pd deposition on MoS_2 surface should reflect any larger nanoparticles and their nature, although if single-atom doping takes place, this will likely not be observable. The PXRD pattern of uncalcined Pd-doped bulk MoS_2 showed only metallic palladium species. This confirms that the aim of using reducing agent sodium borohydride was successful. The broad nature of the diffraction patterns indicates small particle size. In addition, no reduced molybdenum species or phase change of the bulk MoS_2 were observed. Pd-doped bulk MoS_2 calcined at 300°C

revealed mostly Pd^0 species with larger particle size evident by sharper and narrower nature of Pd diffraction peaks; however, new very small peaks attributed to PdH_x species can be observed. These results agree with TPR measurement (see Appendix Figure A5.1) of Pd-doped bulk MoS_2, which reveals no hydrogen consumption peak below 300°C, the temperature regime that oxidized Pd species are expected to be reduced. A weak hydrogen uptake peak is observed only around 300°C which is ascribed to slow and steady uptake of hydrogen to form palladium hydride within Pd^0 deposited on bulk MoS_2.

On the other hand, Pd-doped single-layer MoS_2 showed only 4 very small peaks that can be attributed to Pd species. Peaks at 41°, 47° and 68° 2θ diffraction angles were ascribed to the presence of very small metallic Pd^0 nanoparticles, while a peak at 36° 2θ would indicate unreduced PdO being present in the sample. The very small peaks also indicate that large part of palladium deposited on the exfoliated nanosheets did not form nanoparticles, and would exist on the surface of MoS_2 nanosheets as either oxidised species not reduced by $NaBH_4$, or reduced metallic Pd^0 single atoms and few atom-clusters. Heating of the sample under reducing gas is expected to result in both reduction of the oxidized species such as PdO, uptake hydrogen to form PdH_x alloy nanoparticles, but also sintering of some of the Pd single atoms into nanoparticles. This is particularly obvious in the PXRD pattern of Pd-doped single-layer MoS_2 sample calcined at 300°C under 5 % hydrogen gas, where sharp peaks related to Pd^0 nanoparticles as well as PdH_x alloy nanoparticles are observed. Furthermore, no reduction or structural change of the metallic 1T MoS_2 phase was observed. This shows the stability of the 1T phase at high temperatures or under reduction conditions. These results are in alignment with TEM observations which revealed the presence of mainly single atoms and few of small Pd nanoclusters on dominant 1T phase before calcination, but formation of larger nanoparticles was observed after thermal treatment without any phase change.

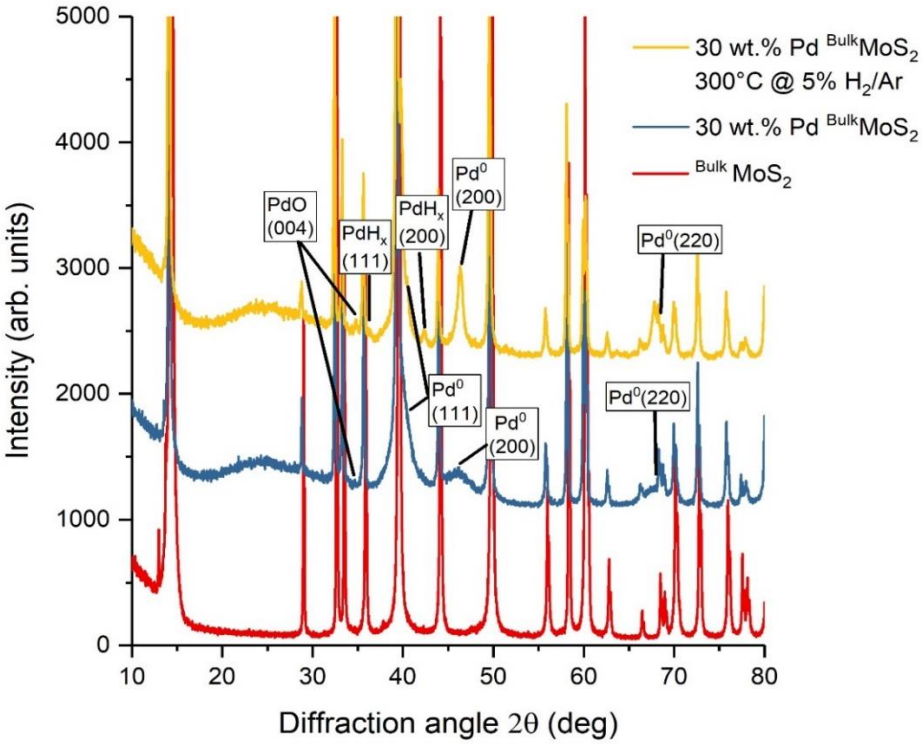


Figure 5.6 PXRD patterns as-prepared and calcined Pd-doped bulk MoS_2 samples.

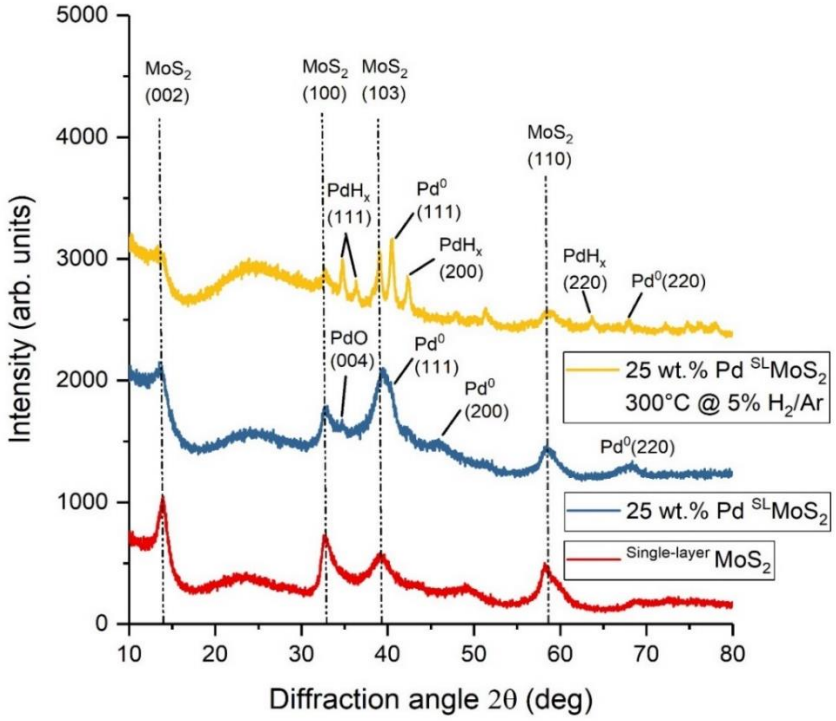


Figure 5.7 PXRD patterns as-prepared and calcined Pd-doped single-layer MoS_2 samples.

Electron paramagnetic resonance (EPR) is a characterisation technique for accounting of unpaired electrons where quantitative, structural, and dynamic information can be inferred.

Thus, it can reflect the phase nature of the MoS_2 nanosheets across their basal planes, edges and on unsaturated defective sites. The metallic 1T phase of the exfoliated MoS_2 nanosheets, often resulting from sulphur vacancies on or other structural interference caused to basal planes in the material layered structure, leads to increased number of delocalised electrons. This is in contrast with the semiconducting 2H phase of the bulk material that possess a limited number of unpaired electrons at the basal plane edges and structural defects. It is important to mention that structural defects usually result in local change of 2H to 1T phase, and therefore the extent of 1T phase present in the sample can be extracted from EPR spectra of MoS_2 nanosheets. Unpaired electrons at basal planes and edges make ideal stabilisation sites for positively charged species, and thus are the primary target sites for functionalization or doping of the MoS_2 material.

Liu and co-workers used single atom doping into sulphur vacancies of single-layer MoS_2 nanosheets as a successful tool to deposit and stabilise catalytically active metal single atoms, and they used EPR spectra to demonstrate the use of the unpaired electrons in this process.[554] In order to study this effect on Pd doping of MoS_2 samples, EPR spectra of both undoped and Pd-doped samples were recorded and analysed (g factor of 2.0), and are displayed in Figure 5.8, and summarized in Table 5.1. A surprising amount of unpaired electrons is observed in bulk MoS_2 sample (4.73×10^{15} g^{-1}) given its relatively small surface area as obtained from Brunauer–Emmett–Teller surface analysis technique (8.4 $m^2 \cdot g^{-1}$). These are predicted to be mostly located at multilayer flake edges and defective crystallite interfaces. On the other hand, restacked single-layer MoS_2 nanosheets showed 3.9 fold increase in unpaired electrons (18.36×10^{15} g^{-1}) while the BET surface area revealed 3.6 fold increase in surface area (30.5 $m^2 \cdot g^{-1}$). The increase in unpaired electrons can be directly related to the basal plane structural perturbation resulting in presence of unpaired electrons of the metallic 1T phase.

Thus, the trend of transformation of the semiconducting trigonal prismatic 2H phase into octahedral 1T phase upon chemical exfoliation of bulk MoS_2 into monolayers can be observed. It also demonstrates that organochemical lithiation of the bulk material results in structural perturbation of the constituent layers. This had an impact on the phase transition that remained stable after delithiation and restacking of individual nanosheets.

Analysis of the non-calcined Pd-doped MoS_2 samples revealed that the deposition of Pd onto the surface of MoS_2 essentially wiped off the unpaired electrons present on both of the MoS_2 materials. Pd species are attracted by the electron rich sites and get energetically stabilized. Therefore, it is theoretically possible to deposit a high amount of stable metal single-atom if the reaction conditions are set exactly right.

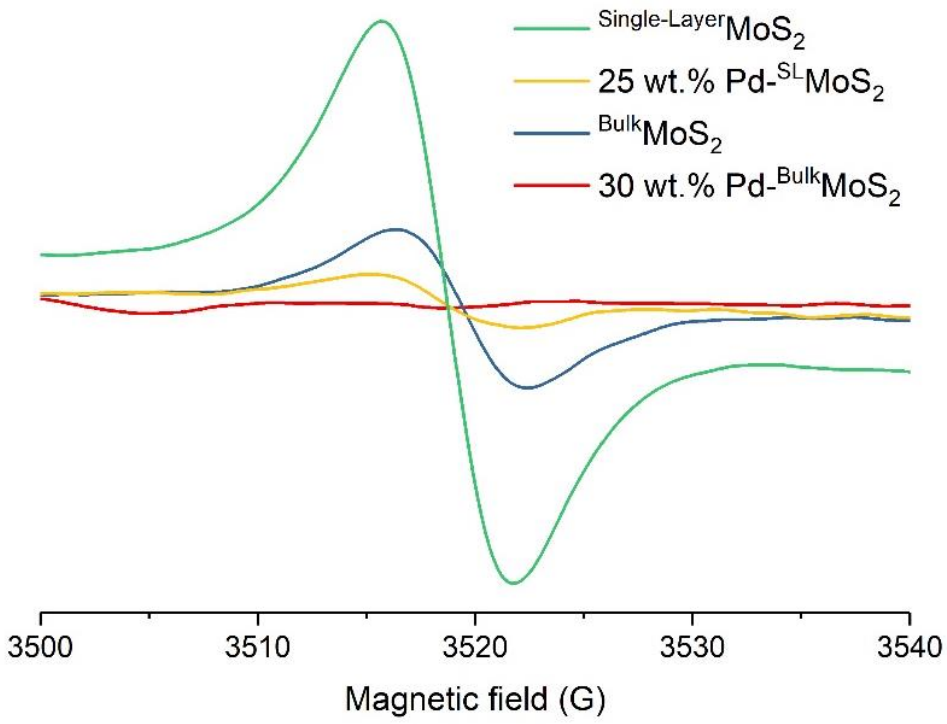


Figure 5.8 EPR spectra of Pd-doped MoS_2 nanosheet and Pd-doped bulk analogue materials.

Table 5.1 EPR analysis shows the effect of Pd doping on the electron delocalized charge on the surface of MoS_2.

sample	EPR [V_s] at g = 2.0 spin counts / g
Bulk MoS_2	4.73×10^{15}
30 wt.% Pd - $^{Bulk}MoS_2$	0
Single-layer MoS_2	18.36×10^{15}
25 wt.% Pd - $^{SL}MoS_2$	4.24×10^{15}

X-ray photoelectron spectroscopy (XPS) of bulk and single-layer MoS_2 nanosheets was used to identify the structural composition of the two polymorphs and chemical state of Mo and S in the material. Intensities were normalised and binding energy scales were corrected by taking C1s at 285eV as a reference. XPS is a widely accepted surface-sensitive quantitative spectroscopic analysis technique to monitor elemental composition of the material, and their chemical state as well as the overall electronic structure. The binding energies of the MoS_2 samples can distinguish between the semiconducting 2H trigonal prismatic phase and the metallic 1T octahedral phase as both Mo 3d region and S 2p regions of the 1T phase appear at binding energy 0.8 eV lower than for the 2H polymorph.[573] This was indeed the case as Figure 5.9 shows. The Mo 3d and S 2p regions specifically show the shift in binding energy between the metallic 1T phase of single-layer MoS_2 and the semiconducting 2H phase of bulk MoS_2. 2H phase bulk MoS_2 characteristic peaks of Mo $3d_{3/2}$ and $3d_{5/2}$ appeared at 232.5 eV and 229.1 eV, respectively. Corresponding characteristic peaks of the 1T phase of single-layer MoS_2 were shifted to lower binding energy by 0.8 eV, appearing at 231.7 eV and 228.3 eV for Mo $3d_{3/2}$ and $3d_{5/2}$ regions, respectively. In addition, the symmetry of the peaks in both regions indicate that both samples exist predominantly in their corresponding phase. It was

previously reported that liquid exfoliation of the MoS_2 nanosheets may result in the formation of MoO_3 and indeed a trace amount of Mo^{6+} species have been detected.[574,575] There is a very small peak observed in the Mo 3d region at 235.6 eV (bulk) and 234.8 eV (single-layer) that indicate a presence of small amount of Mo^{6+} species. However, this small peak is observed in both of the samples. It is hypothesized that it refers to sulphur enriched MoS_3 species.[576] S 2p region further supports these observations as a shift in binding energy of the 1T phase single-layer MoS_2 to lower binding energy values compared to 2H phase of the bulk MoS_2. The XPS scan of 1T phase showed 2 distinct sulphur $2p_{1/2}$ and $2p_{3/2}$ peaks at 162.6 eV and 161.4 eV, respectively, and 1s peak at 225 eV. A difference of 0.8 eV of the corresponding S $2p_{1/2}$ and $2p_{3/2}$ peaks of the 2H phase. A detailed peak fitting and deconvolution analyses were not performed, however, the symmetry of the peaks of each phase with respect to the other is additional evidence to Raman spectra phase analysis. S 2p region indicate there may be a very small content of what might correspond to sulphate species in the bulk MoS_2 sample, however, no apparent sulphate species were observed in 1T single-layer MoS_2 spectrum.

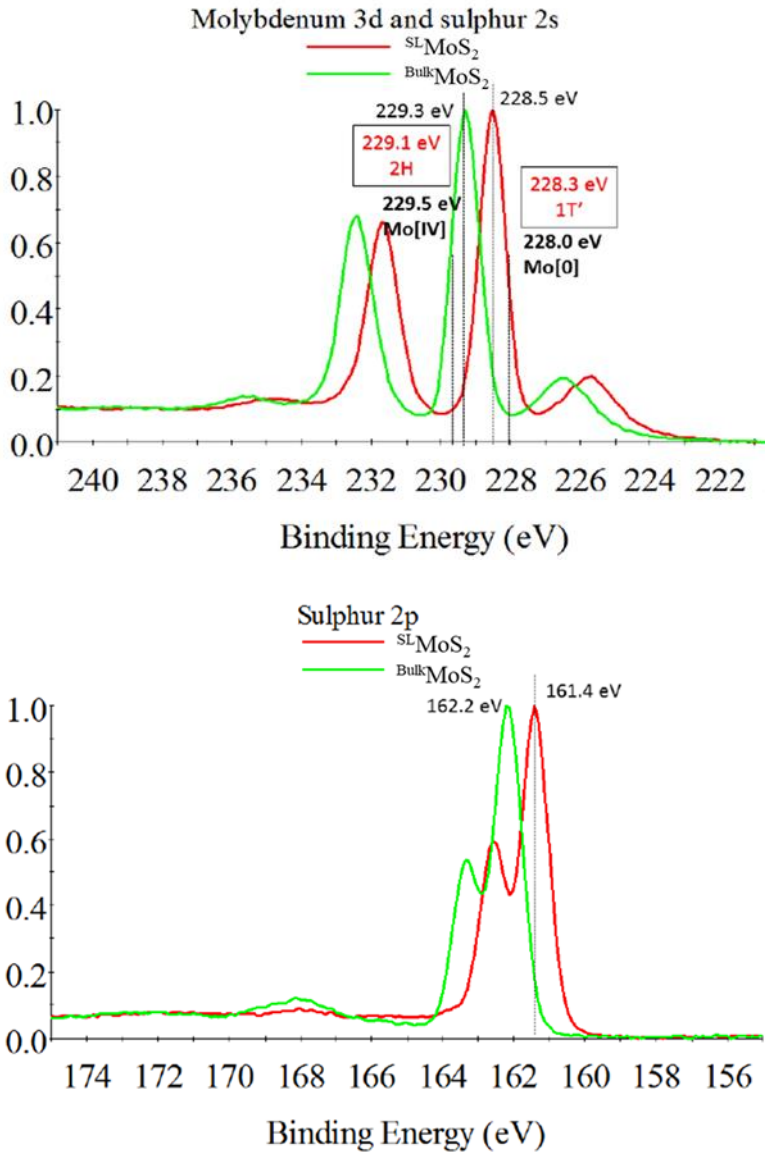


Figure 5.9 Mo 3d and S 1s and 2p regions of XPS spectra of bulk and single-layer MoS_2.

Pd 3d XPS spectra of Pd-doped bulk and single-layer MoS_2 samples before calcination, and their surface electron configurations, are shown in Figure 5.10. As before, intensities were normalised, and binding energy scales were corrected. The binding energy of Pd 3d peaks related to Pd^{2+} species and metallic Pd^0 have been identified and highlighted in the Pd $3d_{5/2}$ region. By inspection it can be deduced that the vast majority of Pd in both samples has been reduced to its metallic state with the use of reducing agent during the Pd deposition and

remained stable. There is a shoulder peak indicating presence of Pd^{2+} species in both samples, although their presence in Pd-doped bulk MoS_2 is evidently a lot smaller. These results correspond to PXRD analysis where distinct peaks indicating presence of PdO nanoparticles were clearly observed in both Pd-doped MoS_2 samples. Their relative intensity in the PXRD diffractogram is very small, however, being recorded on the same instrument in a matter of minutes of each other, would make a suitable comparison and lead to conclusion that PdO peak is larger in the single-layer Pd-doped MoS_2. This is now fully obvious in the XPS spectra when the two samples are compared. In contrast, Pd^0 species were identified only marginally in both samples by PXRD, but XPS is highly sensitive elemental analysis technique and showed predominance of Pd^0. As Pd^0 nanoparticles have a very distinct PXRD pattern it can be deduced that these species are most-likely in large number of single atom units.

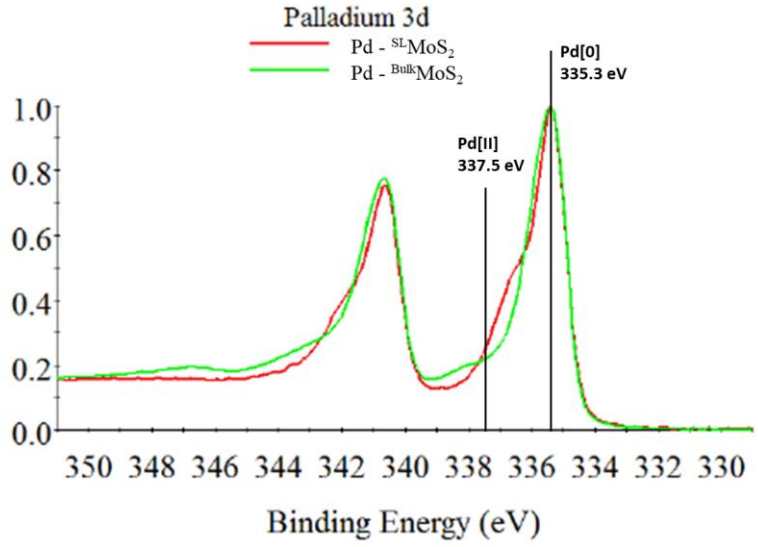


Figure 5.10 Pd 3d region of XPS spectra of as-prepared uncalcined Pd-doped bulk and single-layer MoS_2.

Calcination of Pd-doped bulk and single-layer MoS_2 samples at 300°C under 5 % hydrogen gas should lead to reduction of the oxidized Pd species, but may also result in aggregation, so called sintering, into larger nanoparticles, and as revealed by PXRD it also leads to uptake and

alloying of hydrogen with metallic palladium. XPS spectra of such calcined Pd-doped MoS_2 is displayed in Figure 5.11. Interestingly, XPS spectra of calcined Pd-doped bulk MoS_2 indicated that there was an increase in Pd^{2+} species rather than their reduction. This observation is also supported by PXRD result with a slight increase of (004) peak corresponding to PdO species. On the other hand, the Pd 3d region the XPS spectra of reduction of Pd-doped single-layer MoS_2 at 300°C under 5 % hydrogen indicated a large decrease of the Pd^{2+} species and their successful reduction to metallic Pd^0. This is also supported by PXRD observations which indicated a degree of aggregation of single atom Pd into larger Pd nanoclusters and nanoparticles. No other Pd species were observed in both calcined and non-calcined MoS_2 samples.

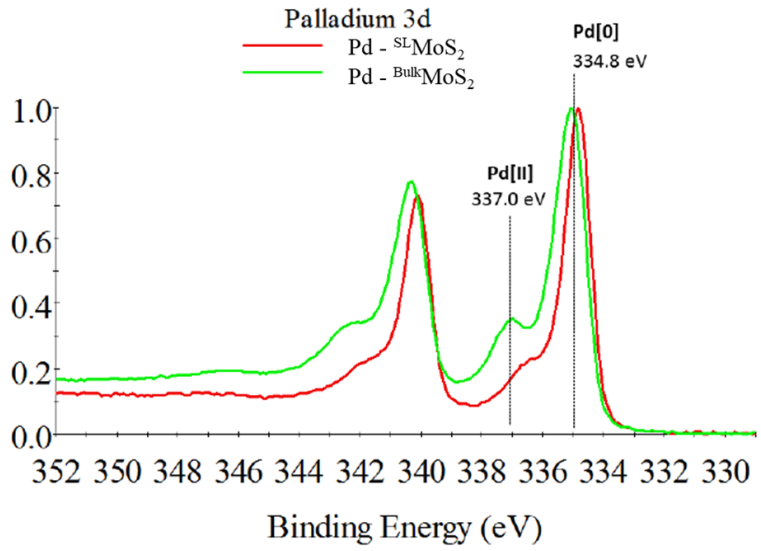


Figure 5.11 Pd 3d region of XPS spectra of 300°C calcined Pd-doped bulk and single-layer MoS_2.

XPS elemental analysis also revealed Mo to Pd ratios of 2.7 in Pd-doped single-layer MoS_2, and 1.2 in Pd-doped bulk MoS_2. However, it is important to remember that XPS is highly sensitive but also a surface analysis technique. Therefore, in order to quantify the actual loadings of Pd species in each sample, induced coupled plasma elemental analysis was

performed. ICP-AES confirmed the Pd loadings on bulk and single-layer MoS_2 to be 30 wt.% and 25 wt.% respectively (see Appendix). Mo to Pd molar ratios were also calculated as 2.98 and 1.13 for Pd-doped single-layer and bulk MoS_2 respectively, which are very similar to the results obtained by XPS analysis.

5.2.2 Catalytic Activity of Pd-doped MoS_2 Samples

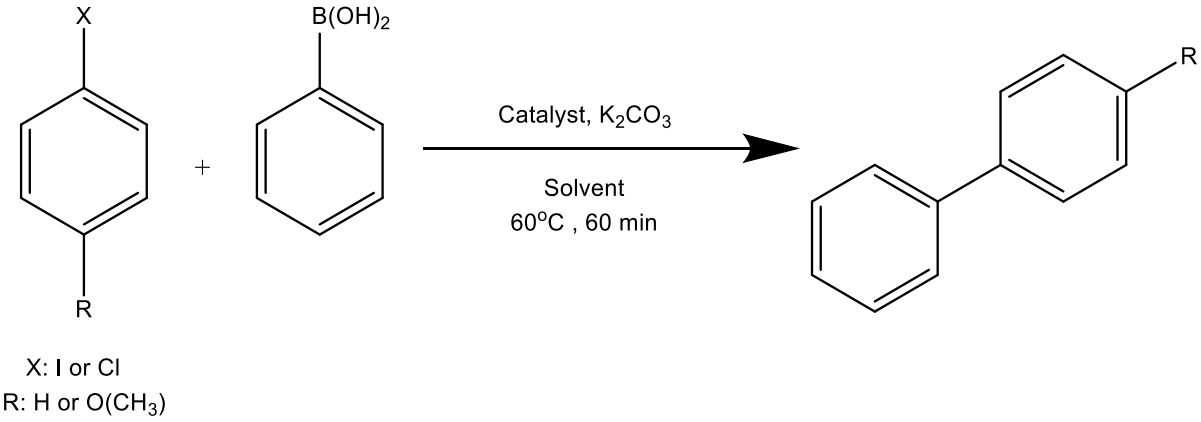
Palladium is one of the most exploited transition metals in catalysis due to its unique and versatile ability to stimulate various organic transformations, both under laboratory and industrial conditions. In many cases palladium-catalyzed reactions proceed under mild conditions, tolerate a wide range of functional groups and provide high chemo- regio- and diastereo-selectivity which make them very attractive for a variety of organic transformations.[577–579] As such, the use of palladium catalysts in cross-coupling and hydrogenation reactions has been the focus of a considerable amount of research.[580–586] The following sections evaluate the catalytic performance of as-prepared Pd-doped MoS_2 catalysts in Heck and Suzuki coupling reactions as well as alkyne hydrogenation.

5.2.2.1 Pd-doped MoS2 as Catalysts for Coupling Reactions

The importance of carbon–carbon bond forming reactions is well documented in the literature.[509,581,587] Today, Suzuki (C−C), Heck (C=C), and Sonogashira (C≡C) cross-coupling reactions along with numerous others have widely been applied in industrial applications. These reactions are typically catalysed by a ligand coordinated (phosphine or *N*-heterocyclic) palladium based homogeneous systems which have shown to yield high turnover frequency (TOFs) values. As a result, separation of these catalysts from the reaction media has presented the utmost challenge in this field because the catalyst incorporation into the final product results in the loss of precious catalyst and devalues the product especially since these

reactions are at the forefront of production in the pharmaceutical industry. Successful separation of these homogeneous catalysts from the product solution requires the use of expensive nanofiltration membranes or extensive and usually destructive column chromatography separation. The drawbacks experienced with homogeneous catalyst systems have prompted the development of recoverable and reusable heterogeneous counterparts to lessen product contamination and mitigate the loss of catalyst.

Herein, the performance of Pd-doped MoS_2 samples was first evaluated as heterogeneous catalysts in the Suzuki coupling reaction using arylhalide and phenylboronic acid substrates with potassium carbonate base (Scheme 5.2).



Scheme 5.2 Schematic diagram of the Suzuki coupling reaction of iodo- or chloro-benzene derivatives with phenylboronic acid to yield biphenyl adducts

In order to test the ability of Pd/MoS_2 as heterogeneous catalysts, the Suzuki reaction between iodobenzene and phenylboronic acid in IPA/water mixture using potassium carbonate as a base is chosen as a model reaction. The results obtained after 1 hour reaction time are summarized in Table 5.2. Compared to commercial Pd/C catalyst, poor product yield was observed with Pd/MoS_2 catalysts despite their higher Pd content which is presumably due to the difference observed in BET surface area between Pd/C and Pd/MoS_2 (890 vs 18

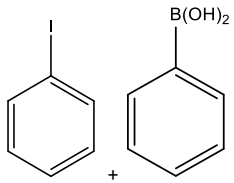
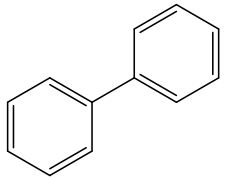
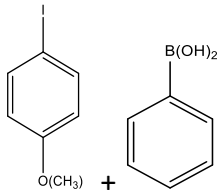
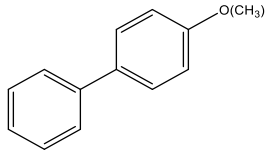
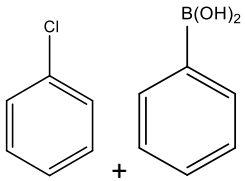
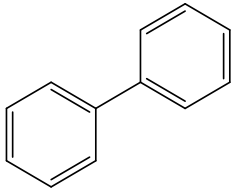
m^2/g respectively).[588] When the catalytic activity was normalized to number of active sites (total amount of Pd in moles), the difference in catalytic activity between Pd/C and Pd/MoS_2 catalysts was more prominent. However, interestingly the decrease in catalytic activity does not follow the same magnitude of decline in surface area. If it was, one would expect to observe a 49-fold higher catalytic activity with Pd/C compared to Pd/MoS_2 catalysts. This result indicates that Pd/MoS_2 catalysts have more exposed Pd active sites on the surface which agrees with the TEM observations where the majority of Pd was found to be atomically dispersed on MoS_2, especially before thermal treatment. Therefore, Pd-doped MoS_2 single layer materials are very promising as atom-efficient catalysts, if the poor morphology due to serious platelet aggregation by ab-face stacking upon drying could be avoided, and the exposed surface area could be increased. One way of increasing the surface area is to coat the surface of 'catalytically inert' porous inorganic nanostructures with catalytically active layered materials. Recently, O'Hare and co-workers developed a method that can produce a layered-double-hydroxide platelet arrangement with an open hierarchical structure. With this methodology, the group managed to coat the external surface of several inorganic nanostructures such as SiO_2 and zeolites to synthesize core-shell hybrids which avoided the *ab*-face aggregation of layered-double hydroxides, thus increasing the surface area of the materials dramatically.[589,590]

To discover the applicability and limitations of the current method, reactions of chlorobenzene and iodoanisole with phenylboronic acid were studied under the same reaction conditions (Table 5.2). It was found that the rate of the Suzuki reaction depended upon the nature of aryl substituents. When an iodo-group on benzene ring is replaced by chloro-, the product yield decreased dramatically. This is attributed to the strength of the aryl halide (Ar–X) bond, which increases on the group as I < Br < Cl (65, 81 and 96 kcal mol^{-1}

respectively) and makes the oxidative addition step progressively more difficult. Addition of an electron donating methoxy group to iodobenzene did not change the activity of the Pd/C commercial catalyst significantly but enhanced the reactivity of all Pd/MoS_2 catalysts by about 10-15%, except for calcined Pd/$^{SL}MoS_2$ with which the activity was found to be 2.5 times higher. This is particularly interesting as generally electron withdrawing groups on the aryl halide facilitate oxidative addition while electron donating groups make it more challenging.[591] Although the reason of this phenomenon is not known unambiguously, the 1T phase of MoS_2 is of metallic character and this could provide a platform for efficient electron delocalisation thus resulting in an increase of the reactivity of substituted aryl halide and boronic acid derivatives.[592–597] The unprecedent activity of calcined Pd/$^{SL}MoS_2$ can be attributed to PdH_x alloy formation. The hydrogen atoms located at the interstitial sites of Pd crystals can lead to geometric and electronic modifications of the host structure to give significant improvement in catalytic conversion and selectivity.[598] Moreover, H atoms at the interstitial sites are generally in hydridic character making Pd surface slightly positive. Therefore, the presence of an electron donating group on the substrate may facilitate the adsorption and reaction kinetics.

It is also worthwhile to mention that oxygen may promote the undesired homocoupling of arylboronic acid, especially in the presence of an aqueous base at elevated temperatures.[599,600]Therefore, Suzuki coupling reactions are sometimes performed under an inert atmosphere. In our study, 4-methoxybiphenyl (Table 5.2 middle row) was observed as the sole product despite performing the reaction under aerobic conditions. The absence of biphenyl when iodoanisole was used as a substrate indicates that homocoupling of arylboronic acid is not facilitated under the chosen reaction conditions.

Table 5.2 Activity of Pd-doped MoS_2 and commercial Pd/C catalysts (10 mg catalyst) in Suzuki coupling reaction of alkyl benzene derivatives (1 mmol) with phenylboronic acid (1.2 mmol) in isopropanol water (7:3) solvent mixture using K_2CO_3 (2.5 mmol) as a base at 60°C after 1 hour of reaction time.

Catalyst	***Yield***	***TON***	***TOF(min^{-1})***	***Reactants***	***Product***
5 wt% Pd/C	70.75	150.58	2.51	 Iodobenzene + Phenylboronic acid	 Biphenyl
30 wt.% Pd-^{bulk}MoS₂ uncalc	38.32	13.59	0.23		
30 wt.% Pd-^{bulk}MoS₂ 300°C	34.68	12.30	0.21		
25 wt.% Pd-^{SL}MoS₂ uncalc	51.24	21.81	0.36		
25 wt.% Pd-^{SL}MoS₂ 300°C	9.38	3.99	0.07		
5 wt% Pd/C	69.14	147.16	2.45	 Iodoanisole + phenylboronic acid	 4-Methoxybiphenyl
30 wt.% Pd-^{bulk}MoS₂ uncalc	43.76	15.52	0.26		
30 wt.% Pd-^{bulk}MoS₂ 300°C	42.53	15.09	0.25		
25 wt.% Pd-^{SL}MoS₂ uncalc	56.43	24.02	0.40		
25 wt.% Pd-^{SL}MoS₂ 300°C	24.24	10.32	0.17		
5 wt% Pd/C	3.51	7.47	0.12	 Chlorobenzene + Phenylboronic acid	 Biphenyl
30 wt.% Pd-^{bulk}MoS₂ uncalc	3.65	1.29	0.02		
30 wt.% Pd-^{bulk}MoS₂ 300°C	3.21	1.14	0.02		
25 wt.% Pd-^{SL}MoS₂ uncalc	4.25	1.81	0.03		
25 wt.% Pd-^{SL}MoS₂ 300°C	1.94	0.83	0.01		

One apparent advantage of heterogeneous catalysts compared to homogeneous counterparts is their easy separation from reaction medium and reusability. Table 5.3 shows the recyclability of Pd/MoS_2 catalysts in the Suzuki coupling reaction of iodobenzene and phenylboronic acid. As seen from the results, Pd-decorated MoS_2 catalysts, with or without annealing, showed similar catalytic activity in three successive reactions which highlights the excellent recyclability potential of these catalysts.

Table 5.3 Pd-doped MoS_2 catalyst stability and recyclability in the Suzuki coupling reaction of iodobenzene (1 mmol) with phenylboronic acid (1.2 mmol) in isopropanol : water (7:3) solvent mixture over Pd-doped MoS_2 catalysts (10 mg) using K_2CO_3 (2.5 mmol) as a base.

Catalyst	*TON*			*TOF* **(min^{-1})**		
	1st Reaction	**2nd Reaction**	**3rd Reaction**	**1st Reaction**	**2nd Reaction**	**3rd Reaction**
30 wt.% Pd-^{bulk}MoS$_2$ uncalc	13.59	14.11	13.03	0.23	0.24	0.22
30 wt.% Pd-^{bulk}MoS$_2$ 300°C	12.30	12.17	12.93	0.21	0.20	0.22
25 wt.% Pd-^{SL}MoS$_2$ uncalc	21.81	20.96	20.68	0.36	0.35	0.34
25 wt.% Pd-^{SL}MoS$_2$ 300°C	3.99	4.22	4.17	0.07	0.07	0.07

A cross-coupling reaction involves the interaction of several dissimilar substances. The reaction medium needs to dissolve a full range of solute types such as lipophilic reactants, catalysts (if homogeneous), bases *etc.* Solvents can also play an important role to activate or stabilize catalysts and reagents by coordination, modulate the reactivity of boronic acids and bases, thus influence the reaction selectivity and rate, and participate in separation of products and by-products.[601,602] Therefore, it is important, though challenging, to find the right solvent for effective catalysis. To determine the influence of solvent on the conversion

of coupling reaction between 1-iodobenzene and phenylboronic acid using Pd-doped MoS_2 catalysts, ethanol (EtOH), iso-propyl alcohol (IPA), N,N-dimethylformamide (DMF) and alcohol-water mixtures at a volumetric ratio of 7:3 were chosen as they are commonly used as solvents in Suzuki cross-coupling reactions in the literature.[550] All the reactions were carried out under air at 60 ^oC using potassium carbonate as a base (Table 5.4). Commercial Pd/C catalyst was also tested as a benchmark to evaluate the performance of Pd/MoS_2 catalysts prepared in this work.

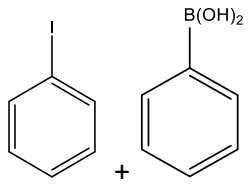
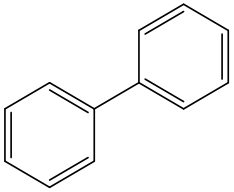
As seen in Table 5.4, the reactivity of the catalysts enhances as the polar protic character of the solvent increases. The polar nature of the solvent together with hydrogen bonding ability is not only important to dissolve all reagents but also to stabilise the reactants in transition states. The protic solvents can H-bond to the halide and activate the R-X bond; thus facilitating the oxidative addition of aryl halides to the metal surface while the polarity of the solvent can facilitate the formation of salt by-products (i.e. NaI and $KB(OH)_2CO_3$), The catalytic activity difference observed between ethanol and iso-propanol is attributed to their viscosity difference. The mass transfer between phases can influence the kinetics of reactions catalyzed by heterogeneous catalysts. The viscosity of the solvent is therefore a crucial parameter.[599] In this study, ethanol has a lower dynamic viscosity compared to iso-propyl alcohol (0.583 and 0.811mPa*s at 60 °C, respectively); therefore, more active in catalysis.[603,604] Furthermore, in agreement with the literature findings where in some cases the performance of Suzuki cross-coupling was found to be better in solvent mixtures than in only one solvent, water/alcohol miscible solvent mixture was found to be more effective for higher biphenyl yields in our model Suzuki coupling reaction, presumably due to more efficient dissolution of K_2CO_3 base in water.[601] This is exciting as the use of water as a solvent

is particularly attractive because it is a cheap, non-flammable, non-toxic and abundantly available.

Lastly, despite the reactivity of all catalysts dropped in an order of magnitude with the use of DMF as a solvent, Pd/MoS_2 catalysts were found to be much more active than Pd/C commercial counterparts which shows the versatile capability of these catalysts. DMF is known to act as a coordinating ligand to the metal centre. Metal nanoparticles, stabilized with DMF molecules through interaction of amido groups of DMF with metal surfaces are well documented in the literature.[605] Therefore, the decrease in catalytic activity of Pd catalysts in DMF media is thought to be due to hindrance of active metal sites by DMF coordination. This effect is less severe with Pd/MoS_2 catalysts compared to Pd/C catalyst, presumably, because delocalised negative charge on 1T phase of MoS_2 repels the lone pair electrons on amido group, thus prevents the coordination of DMF on Pd atoms at Pd-MoS_2 interface.

Table 5.4 % Yield, TON and TOF of biphenyl in the Suzuki coupling reaction in different solvents using Pd-doped MoS_2 catalyst, compared to the commercial Pd/C catalyst

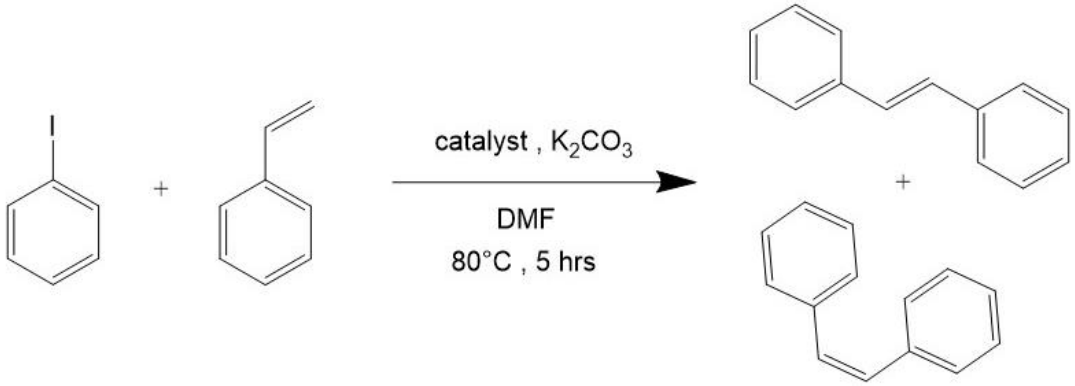
Catalyst *% Yield* *Reactants* *Product*

	IPA : H_2O (7 : 3)	**EtOH : H_2O (7 : 3)**	**IPA**	**EtOH**	**DMF**		
5 wt% Pd/C	70.75	95.20	17.92	87.07	2.66		
30 wt.% Pd-$^{bulk}MoS_2$ uncalc	38.32	81.29	21.39	81.60	24.33		
30 wt.% Pd-$^{bulk}MoS_2$ 300°C	34.68	72.38	18.62	73.17	20.91		
25 wt.% Pd-$^{SL}MoS_2$ uncalc	51.24	91.85	23.82	91.55	27.23		
25 wt.% Pd-$^{SL}MoS_2$ 300°C	9.38	42.12	7.83	40.99	10.36	Iodobenzene + Phenylboronic acid	Biphenyl

Catalyst *TON* *TOF*

	IPA : water (7 : 3)	**EtOH : water (7 : 3)**	**IPA**	**EtOH**	**DMF**	**IPA : water (7 : 3)**	**EtOH : water (7 : 3)**	**IPA**	**EtOH**	**DMF**
5 wt% Pd/C	150.58	202.62	38.14	185.32	5.66	2.51	3.38	0.64	3.09	0.09
30 wt.% Pd-$^{bulk}MoS_2$ uncalc	13.59	28.84	7.59	28.95	8.63	0.23	0.48	0.13	0.48	0.14
30 wt.% Pd-$^{bulk}MoS_2$ 300°C	12.30	25.68	6.61	25.96	7.42	0.21	0.43	0.11	0.43	0.12
25 wt.% Pd-$^{SL}MoS_2$ uncalc	21.81	39.10	10.14	38.97	11.59	0.36	0.65	0.17	0.65	0.19
25 wt.% Pd-$^{SL}MoS_2$ 300°C	3.99	17.93	3.33	17.45	4.41	0.07	0.30	0.06	0.29	0.07

Analogously, the catalytic activity of Pd-doped MoS_2 catalysts was evaluated for the Mizoroki–Heck reaction, which constructs C-C bond formation of aryl or alkyl halides with olefins. The Heck coupling reaction of iodobenzene with styrene (Scheme 5.3) was chosen as a model to evaluate the catalytic performance of Pd-doped MoS_2 samples with respect to a commercial Pd/C catalyst. The coupled product, i.e. stilbene, may form two isomers: E- and Z-stilbene where phenyl groups are in cis- or trans- positions respectively.



Scheme 5.3 Schematic diagram of the Heck coupling reaction of iodobenzene with styrene over supported palladium heterogeneous catalyst to yield E- and Z-stilbene.

E-stilbene, with a selectivity of at least 90%, was observed as the main product in all cases (Figure 5.12). The conversion, on the other hand, varied significantly. While only 9% conversion could be achieved with a commercial Pd/C catalyst, the activity of Pd-doped MoS_2 catalysts was found to be 3.2-fold higher at the minimum. The activity difference seen between Pd/MoS_2 catalysts and commercial Pd/C catalyst might be related with DMF being the solvent for the reaction medium. As discussed in the previous sections, coordinating nature of DMF might hinder the active sites on the metal which then leads to lower catalytic activity. DMF coordination on Pd/MoS_2 catalysts is expected to be less due to negative charge on MoS_2 nanosheets repelling the lone pair electrons on DMF molecule.

Among Pd-doped MoS_2 catalysts, uncalcined Pd/$^{SL}MoS_2$ outperformed the others with 52% conversion and 93% selectivity towards E-stilbene. The remarkable catalytic activity of uncalcined Pd/$^{SL}MoS_2$ among other Pd/MoS_2 catalysts can be attributed to the highly dispersed nature of Pd species.

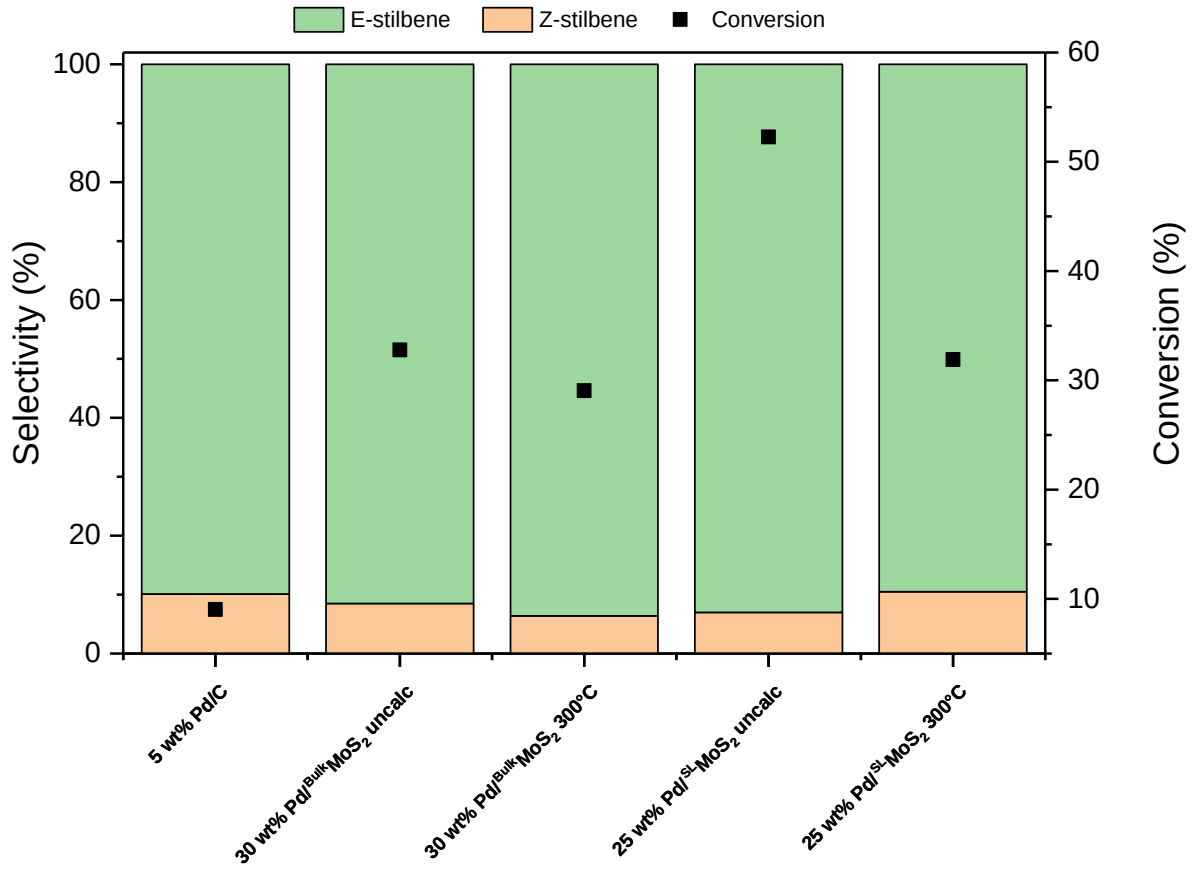


Figure 5.12 Conversion and selectivity of Pd-doped MoS_2 and commercial Pd/C catalysts in the Heck coupling reaction of styrene and iodobenzene. Reaction conditions: 1 mmol of aryl halide, 1.2 mmol of styrene, 2.5 mmol of K_2CO_3, 1.5 mol% equivalent of Pd catalyst (compared to aryl halide), 80^oC, 5 hours.

Tables 5.5, 5.6 and 5.7 reveal the reusability of Pd/MoS_2 catalysts in the Heck coupling reaction of iodobenzene and styrene as % Yield, TON and TOF respectively. Like recyclability results observed in the Suzuki coupling reaction, Pd-doped MoS_2 catalysts, with or without

annealing, showed no activity loss in three successive reactions which confirms the reusability potential of these catalysts in various C-C coupling reactions.

Table 5.5 Pd-doped MoS_2 catalyst stability and recyclability in Heck coupling reaction.

Yield (%)	**1st reaction**		**2nd reaction**		**3rd reaction**	
catalyst	**Z-stilbene**	**E-stilbene**	**Z-stilbene**	**E-stilbene**	**Z-stilbene**	**E-stilbene**
30 wt.% Pd-$^{bulk}MoS_2$ uncalcined	2.8	30.0	2.7	30.5	2.4	29.7
30 wt.% Pd/-$^{bulk}MoS_2$ 300°C	1.9	27.2	1.6	28.7	1.7	25.8
25 wt.% Pd-$^{SL}MoS_2$ uncalcined	3.6	48.7	3.6	44.9	3.8	48.2
25 wt.% Pd-$^{SL}MoS_2$ 300°C	3.3	28.6	2.7	29.9	2.5	26.0

Table 5.6 Turnover number (TON) calculated from the yield given in Table 5.5

TON	**1st reaction**		**2nd reaction**		**3rd reaction**	
catalyst	**Z-stilbene**	**E-stilbene**	**Z-stilbene**	**E-stilbene**	**Z-stilbene**	**E-stilbene**
30 wt.% Pd-$^{bulk}MoS_2$ uncalcined	1.85	20.01	1.79	20.32	1.60	19.77
30 wt.% Pd/-$^{bulk}MoS_2$ 300°C	1.25	18.12	1.04	19.11	1.11	17.17
25 wt.% Pd-$^{SL}MoS_2$ uncalcined	2.41	32.44	2.39	29.95	2.52	32.11
25 wt.% Pd-$^{SL}MoS_2$ 300°C	2.23	19.04	1.77	19.94	1.66	17.30

Table 5.7 Turnover frequency (TOF) calculated from the yield and turnover number in Tables 5.5 and 5.6.

TOF (h^{-1})	**1st reaction**		**2nd reaction**		**3rd reaction**	
catalyst	**Z-stilbene**	**E-stilbene**	**Z-stilbene**	**E-stilbene**	**Z-stilbene**	**E-stilbene**
30 wt.% Pd-$^{bulk}MoS_2$ uncalcined	0.37	4.00	0.36	4.06	0.32	3.95
30 wt.% Pd/-$^{bulk}MoS_2$ 300°C	0.25	3.62	0.21	3.82	0.22	3.43
25 wt.% Pd-$^{SL}MoS_2$ uncalcined	0.48	6.49	0.48	5.99	0.50	6.42
25 wt.% Pd-$^{SL}MoS_2$ 300°C	0.45	3.81	0.35	3.99	0.33	3.46

The main challenge in the development of heterogeneous catalytic systems for C–C cross coupling reactions has been in identifying the nature of the active catalyst species. While the reaction mechanism is well understood and documented for homogeneous systems in the literature, it is still a highly debated subject for heterogeneous catalysts. The literature is divided on this matter. Some researchers support the idea that the Pd doped solid catalyst is a pre-catalyst consisting a 'reservoir' of soluble, catalytically active palladium species which might be in molecular or nanoparticle form, thus the oxidative addition of the aryl halide (Ar–X) occurs on leached metal atoms under homogeneous environment.[606] Others, on the other hand, claim the catalysis takes place on the surface of the solid, insoluble palladium based heterogeneous catalyst.[207,607–609]

The detailed mechanistic study was out of scope of the present work. However, the widely accepted Heck and Suzuki coupling reaction cycles based on the experimental conditions presented herein are illustrated in Figures 5.13 and Figures 5.14. although it should be noted

that an anionic version of these catalytic cycles under homogeneous conditions was also proposed by Amatore and Jutant.[610] The first step of the catalytic cycle is an oxidative addition of the aryl halide to the Pd^0 to yield an aryl halide palladium(II) complex (ArPdX). The second step involves a nucleophilic attack on ArPdX, either a syn-addition (Heck reaction) or a transmetalation (cross-coupling reaction). The final product is then generated by either β-hydride elimination (Heck) or reductive elimination (cross-coupling).

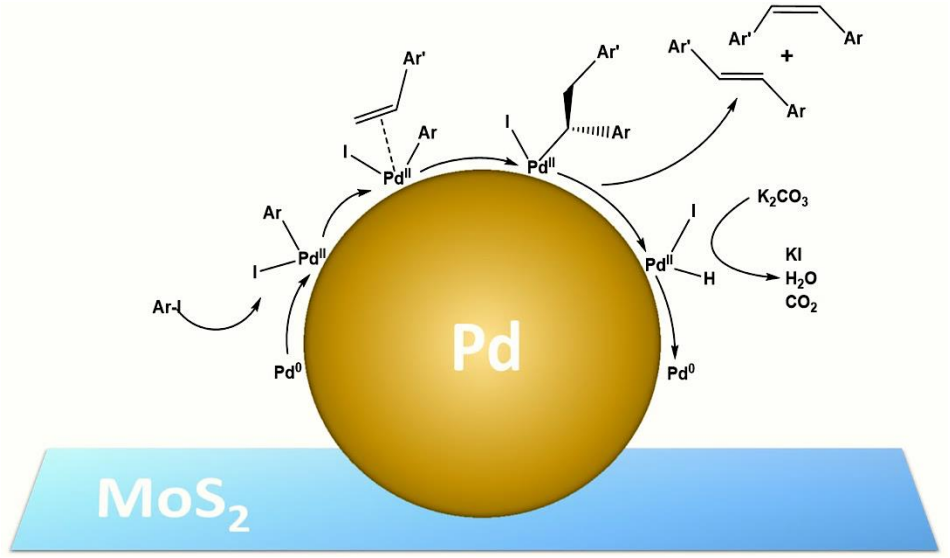


Figure 5.13 Heck coupling reaction mechanism over palladium nanoparticle catalyst.

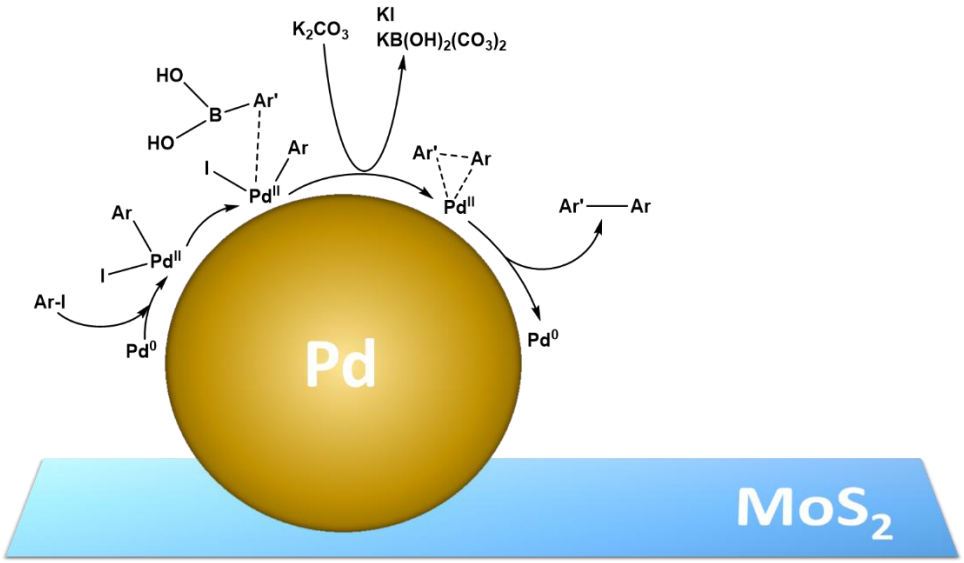
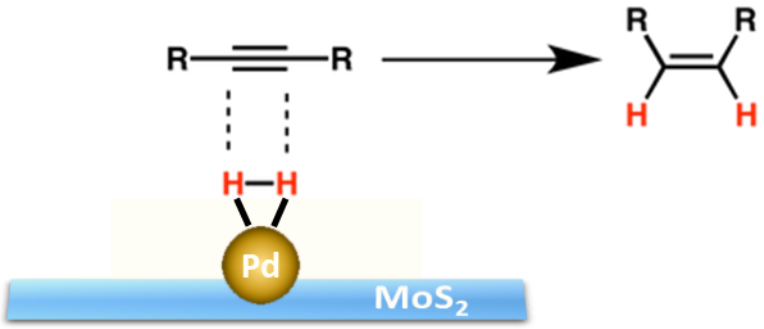


Figure 5.14 Suzuki coupling reaction mechanism over palladium nanoparticle catalyst.

5.2.2.2 Pd-doped MoS_2 as Highly Selective Catalysts in 1-Pentyne Hydrogenation

Selective hydrogenation is widely employed not only in academia but also in industry such as for manufacturing of polymer-grade ethylene, fine chemicals, agrochemicals, and pharmaceuticals. In both contexts, selectivity to the desired product is usually a key attribute because loss of reagent to the formation of undesired products is economically undesirable and can lead to challenges in separation downstream. The partial hydrogenation of alkynes to the corresponding alkenes is one of the most challenging reactions in selective hydrogenation as it usually suffers from low alkene selectivity, especially at high conversion. Palladium-based Lindlar catalyst (5 wt. % Pd on calcium carbonate poisoned by lead promoter and quinoline) has always been used as a benchmark catalyst for this catalytic process. However, the associated safety hazards due to the presence of toxic lead additives and poor metal utilization severely limit the application of the Lindlar catalyst in industry. As a result, the development of a novel and sustainable catalyst for partial hydrogenation of alkynes has become a desirable target.

In this study, the catalytic performance of Pd/MoS_2 samples was evaluated in the selective partial hydrogenation of 1-pentyne (Scheme 5.4), chosen as a model reaction for the selective hydrogenation of alkyne due to the high demand in industry and significantly less information in the literature about gas-phase hydrogenation involving longer-chain alkynes. The performance of Pd/MoS_2 catalysts along with several other Pd-based commercial catalysts (Pd/C, Pd/Graphite, $Pd(Pb)/CaCO_3$) in the selective hydrogenation of 1-pentyne were tested in a quartz microreactor using the laboratory facilities of Johnson-Matthey in Sonning Common. 1-pentyne vapor and a hydrogen–helium gas mixture were flowed through a catalyst bed while the temperature was increased from ambient to 250°C. Full details of the catalytic testing methodology are presented in Chapter 3.12.



Scheme 5.4 Illustration of the partial hydrogenation of alkynes to alkenes over palladium nanoparticle catalyst.

Table 5.8 and Figures A5.2 in the Appendix present the catalytic performance of the nine samples in 1-pentyne hydrogenation when tested at equivalent catalyst content (10 mg) at various temperatures. Except single-layer MoS_2 supported Pd catalysts, none of the catalysts showed significant selectivity towards desired partial hydrogenation product, 1-pentene, at 25 °C. In fact, pentane was observed as the main product for most of the catalysts. Uncalcined Pd/$^{SL}MoS_2$ was found to be the most selective catalyst amongst all tested catalytic systems, giving a remarkable selectivity of 88.7 towards 1-pentene at only 25 °C. When the same catalyst was annealed at 300 °C, the catalytic activity dropped significantly, mainly due to the agglomeration of Pd particles, leading to reduced active surface area.

The superior 1-pentene selectivity of Pd/$^{SL}MoS_2$ compared to Pd/$^{Bulk}MoS_2$ is attributed to its unique 1T phase and smaller Pd particle size. Hydrogen molecular diffusion on the 1T phase monolayer is retarded by a high energy barrier which avoids further hydrogenation. In addition, the binding energies of the pentenes are reported to be lower on the smaller nanoclusters, meaning that these molecules are expected to desorb more easily from the catalyst surface. Hence, the small clusters could display better selectivity, towards partial hydrogenation to 1-pentene compared with large clusters.[611]

Comparatively, common heterogeneous palladium catalysts based on supported nanoparticles, such as Pd/C, Pd/graphite or even strongly modified Lindlar-type Pd–Pb/ $CaCO_3$ failed to achieve high yields towards 1-pentene at low temperature, instead, the major product was saturated hydrocarbon: pentane.

When the reaction temperature was increased to 75 ^oC, the full conversion of 1-pentyne to hydrogenation products was obtained with all Pd-based catalysts. %Yields of products as well as TOF numbers are summarised in Table 5.8. Except for Pd/$^{SL}MoS_2$ and Pd/C catalysts, the pentane yield dropped slightly while isomers of pentene emerged (Figure 5.15). This indicates that the desorption of pentene from Pd surface is more favourable at 75 ^oC compared to 25 ^oC regardless of the particle size.

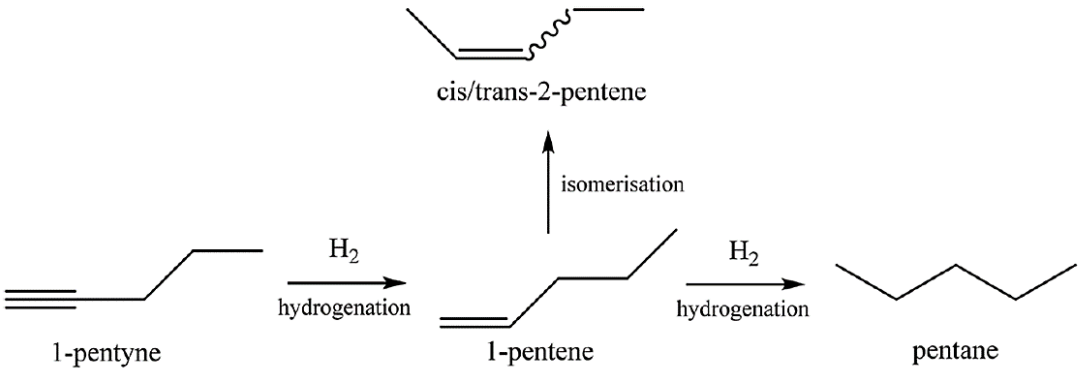


Figure 5.15 Schematic diagram of hydrogenation mechanism of 1-pentyne using supported Pd heterogeneous catalyst.

In summary, the most active catalysts studied were Pd/$^{SL}MoS_2$. The catalytic results of these catalysts obtained at low temperature match the activity (TOF) of the commercial Lindlar catalyst, despite having 5-fold higher Pd content. However, their selectivity towards 1-pentene and the very low degree of isomerization at low temperatures outperformed the

commercial catalysts. These results are very encouraging for the exploitation of Pd/$^{SL}MoS_2$ catalysts in industry.

Lastly, the control experiments using bulk and single-layer MoS_2 in the absence of palladium showed no product formation at any of the temperatures, indicating that palladium is indeed the active metal thriving the activation of hydrogen atoms and subsequent hydrogenation of 1-pentyne.

Table 5.8 % Yields of 1-pentyne hydrogenation products at 25°C (top) and 75°C (bottom), including turnover frequency for partial and full hydrogenation of 1-pentyne

Catalyst	%Yield at 25°C				TOF (1-pentene) / min^{-1}	TOF (pentane) / min^{-1}
	1-pentene	pentane	t-2-pentene	c-2-pentene		
Bulk MoS_2	0.00	0.00	0.00	0.00	0	0
Single-layer MoS_2	0.02	0.00	0.00	0.00	0	0
30wt% Pd - $^{Bulk}MoS_2$ uncalcined	0.07	99.00	0.00	0.80	4.74	6599.93
30wt% Pd - $^{Bulk}MoS_2$300°C	4.40	92.73	0.00	2.87	293.60	6182.04
25wt% Pd - $^{SL}MoS_2$ uncalcined	77.93	8.79	0.00	1.13	6234.16	703.49
25wt% Pd - $^{SL}MoS_2$ 300°C	17.58	0.73	0.00	0.00	1406.05	58.61
5 wt% Pd (Pb)- $CaCO_3$ (Lindlar)	18.66	70.92	0.00	8.32	6219.19	23638.74
5 wt% Pd - C	10.31	7.76	0.00	0.19	17175.42	12930.03
5 wt% Pd - graphite	0.12	98.76	0.00	1.08	15.95	13167.61
Catalyst	% Yield at 75°C				TOF (1-pentene) / min^{-1}	TOF (pentane) / min^{-1}
	1-pentene	pentane	t-2-pentene	c-2-pentene		
Bulk MoS_2	0.00	0.00	0.00	0.00	0	0
Single-layer MoS_2	0.00	0.00	0.00	0.00	0	0
30wt% Pd - $^{Bulk}MoS_2$ uncalcined	1.27	77.94	15.33	5.47	84.67	5196.00
30wt% Pd - $^{Bulk}MoS_2$300°C	1.15	79.16	15.06	4.63	76.67	5277.33
25wt% Pd - $^{SL}MoS_2$ uncalcined	73.55	13.01	7.74	5.47	5884.00	1040.80
25wt% Pd - $^{SL}MoS_2$ 300°C	81.60	7.94	5.93	4.53	6528.00	635.20
5 wt% Pd (Pb)- $CaCO_3$ (Lindlar)	20.47	44.70	24.40	10.44	6823.33	14900.00
5 wt% Pd - C	0.00	93.59	4.91	1.50	0.00	155983.33
5 wt% Pd - graphite	0.08	84.55	8.18	2.68	10.67	11273.33

5.3 Conclusion

The aim of the work described within this chapter was to synthesise, characterise and analyse the performance of Pd doped MoS_2 nanosheets for application as catalysts for the C-C coupling reactions of alkenes and aryls, C-C coupling Suzuki reactions of aryl iodides, and partial hydrogenation reaction of 1-pentyne to 1-pentene. Chemically exfoliated 1T-phase MoS_2 nanosheets dispersed in aqueous solution were successfully doped with Pd using the gradual addition of $Pd(NO_3)_2$ precursor and $NaBH_4$ as a reducing agent. XPS analysis showed a large content of Pd(II) species located predominantly in sulphur vacancies, or atop on S atoms and Mo atoms. Additionally, STEM imaging of Pd-$^{SL}MoS_2$ samples showed Pd nanoparticles up to 20 nm in diameter. Pd-decorated MoS_2 catalysts were shown to exhibit superior activity in C-C coupling reactions of alkenes and aryls, as well as excelled recyclability, outperforming other Pd-doped heterogeneous catalysts. Pd-decorated MoS_2 catalysts exhibited good activity in C-C coupling Suzuki reactions of aryl iodides, particularly in ethanol and ethanolic water mixtures, of which 1T phase Pd-doped $^{SL}MoS_2$ nanosheets without any heat treatment showed the highest activity. Pd doped $^{SL}MoS_2$ profiles as highly-active and remarkably selective heterogeneous catalyst in partial hydrogenation reaction of 1-pentyne to 1-pentene at low temperatures.

All samples used in this work were synthesized and thoroughly characterized using HRTEM, BET, EPR, and XPS methods. An increase of dopant concentration resulted in an 8-fold increase of Pd loading as confirmed by ICP and XPS. A decrease in EPR activity showed Pd atoms get stabilized by the electron density on MoS_2 nanosheets. Raman spectra indicated $^{SL}MoS_2$ nanosheets remain in the 1T phase after Pd deposition and annealing at 300 ^{o}C. PXRD showed the presence of Pd^0 and PdO nanoparticles after the sodium borohydride reduction

in solution, whilst annealing at 300 ^{o}C reduced PdO content in $^{SL}MoS_2$. Pd^{2+} was found due to incomplete reduction or surface re-oxidation as the sample was handled in air. The presence of an alloy of Pd^0 with metallic hydrogen (PdH_x) was indicated by the PXRD of annealed samples. XPS showed predominantly Pd^0 species with small content of Pd^{2+} species (PdO). However, the Pd^0 peak presents higher asymmetry, and Pd^0 content can be underestimated compared with Pd^{2+}. It was found that the 1T phase of the $^{SL}MoS_2$ was stable after annealing at 300 ºC and did not transform back to the 2H phase of $^{Bulk}MoS_2$. Nanoparticles of Pd up to 20 nm in diameter were observed on Pd-$^{SL}MoS_2$ samples using STEM imaging. Although difficult, stable Pd single atoms were also identified within the sample. Tested Pd-doped $^{SL}MoS_2$ samples were found to be largely 1T phase nanosheets with a few areas also showing presence of the 2H phase.

For the catalysis of the C-C coupling reactions of alkenes and aryls, Pd-decorated MoS_2 catalysts were found to exhibit superior activity and excellent recyclability – Pd atoms and nanoparticles were very stable on the MoS_2 support. They outperformed other largely inactive Pd-doped heterogeneous catalysts, of which 5 wt.% Pd/C showed the highest activity. 1T phase Pd-doped single-layer MoS_2 nanosheets without any heat treatment showed the highest activity and high selectivity to E-stilbene. However, annealing at 300ºC under 5% H_2/Ar reduced this catalyst activity to almost half, likely due to the sintering of Pd atoms into larger nanoparticles (observations made using PXRD and STEM methods support this theory). In contrast, both Pd-doped 2H phase bulk MoS_2 catalysts showed similar activity and selectivity to 300ºC annealed Pd-$^{SL}MoS_2$ and indicated small to no impact on Pd by thermal treatment.

C-C coupling Suzuki reactions of aryl iodides catalysed by Pd-decorated MoS_2 catalysts were shown to exhibit a reasonably good activity. Despite the fact that isopropanol-water mixtures are typically used, ethanol and ethanolic water mixtures showed the highest activity for all heterogeneous Pd catalysts. 4-iodoanisole showed lower conversion rates but confirmed good activity of Pd-MoS_2 catalysts in this reaction. Unsurprisingly, aryl chlorides showed very low activity in all solvents used due to a stronger electron withdrawing properties of chlorine. 1T phase Pd-doped $^{SL}MoS_2$ nanosheets without any heat treatment showed the highest activity. Annealing at 300 ^oC under 5% H_2/Ar reduced activity rapidly, likely due to sintering of Pd into larger nanoparticles. Both Pd-doped 2H phase bulk MoS_2 catalysts showed slightly lower activity than unannealed Pd-doped $^{SL}MoS_2$, and only minimal loss of activity was observed after annealing at 300 ^oC under 5% H_2/Ar. Pd-decorated MoS_2 catalysts were observed to have excellent recyclability – Pd is very stable on both MoS_2 supports before as well as after annealing. Commercial heterogeneous Pd/C showed higher activity than all Pd-MoS_2 catalysts in all reactions with exception of reactions in DMF solvent where Pd-MoS_2 catalysts performed slightly better. However, DMF is a toxic organic solvent with a high boiling point and therefore it is not a solvent of choice for this type of reaction.

Within partial hydrogenation reactions of 1-pentyne to 1-pentene at low temperatures, Pd doped $^{SL}MoS_2$ profiled as a highly-active and remarkably selective heterogeneous catalyst. Non-annealed Pd-$^{SL}MoS_2$ showed high 1-pentene yield (73-78%) at both 25 ^oC and 75 ^oC with very small isomerization. 300 ^oC annealed Pd-$^{SL}MoS_2$ showed even higher 1-pentene yield (82%) at 75 ^oC and smaller isomerization, while at 25 ^oC there was no isomerization but lower conversion (18%). These results match the activity (TOF) of the commercial Lindlar catalyst, however, the selectivity towards 1-pentene and the very low degree of isomerization at low temperatures outperformed the Lindlar catalyst. In comparison, both Pd on $^{Bulk}MoS_2$ catalysts

showed propensity to full hydrogenation of 1-pentyne to pentane and high conversion rates at 25 °C (99% & 93%). % Pentane yield was reduced to 78% at 75 °C, replacing its place to isomers of pentene. Good activity and high selectivity to pentane of Pd-$^{Bulk}MoS_2$ catalyst go in strong contrast to Pd-$^{SL}MoS_2$ results and can be explained by the high energy barrier of hydrogen molecular diffusion on the 1T phase monolayer.

5.4 Future Outlook

Overall, Pd-$^{SL}MoS_2$ catalysts proved to be a very promising heterogeneous catalyst for a range of organic transformation and coupling reactions under mild reaction conditions. However further improvements could be made through the optimization of the palladium deposition process to reduce the Pd nanoparticle size and engineer a larger number of single Pd atom sites. Targeting single Pd atoms deposited on the metallic 1T phase of MoS_2 would further improve the desirable catalytic activity of Pd species (only Pd atoms available on the surface of a nanoparticle would participate in the catalytic activity) to facilitate electron transfer directly between the two. It is assumed that engineering such system would likely result in more active catalyst at a cheaper cost since smaller amount of an expensive Pd is required. The scope of introducing other substrates could be extended to study these organic hydrogenation reactions and other organic coupling reactions. Since palladium catalysts are a widely desirable commodity in many other catalytic processes, testing the suitability of application of the Pd-$^{SL}MoS_2$ catalysts in these processes could also prove successful.

Chapter 6 Molybdenum disulfide nanosheets for high performance energy storage

6.1 Introduction

Due to the world's increasing energy challenges and the need to shift from burning fossil fuels to using sustainable energy sources, development of novel and advanced batteries for renewable energy storage is one of the most important challenges of modern electro-chemistry.[612,613] However, efficient energy storage is a long-standing technological and scientific issue limiting businesses and communities all around the world.[614] Due to continuous rise of demand for powerful energy sources for portable, automotive and stationary energy storage systems, high energy density and high efficiency rechargeable batteries are under intense development. The requirements of progressively smaller scale and larger capacity for a wide range of applications continue to be a strong driving force for the development of advanced alkali metal ion batteries.[615,616] Currently, lithium-ion batteries and sodium-ion batteries provide an unmatchable combination of high energy density and high power density.[617] The lithium-ion battery is one of the most important rechargeable energy storage devices in the present world and is considered as the solution for powering the next generation of automotive vehicles.[618] However, an improved higher energy density electrode material is required to make this transformation economically viable. Inorganic nanomaterials are considered to make this transition possible and have been extensively studied for their properties as electrode materials for rechargeable batteries in recent years.[619,620]

Two-dimensional (2D) materials represent a largely unexplored area of nanotechnology and have been under intense investigation since the isolation of graphene in 2004.[621] These

atomic or several molecule thick nanostructures show extraordinary physicochemical properties compared to their bulk analogue, characterized by strong in-plane bonds and weak van der Waals coupling between the layers.[355] Molybdenum disulphide (MoS_2) represents a good example of a layered material with strong intra-layer but weak inter-layer bonding, that is relatively cheap, safe, and has up to 3-fold lithium (or sodium) theoretical storage capacity than commercial graphite electrodes.[622,623] With recent development and study of 2D materials, MoS_2 has become of utmost interest again for various energy, electrical and electro-chemical applications due to its vastly different properties compared to the bulk material.[555,624,625] The attractiveness of MoS_2 as an electrode material comes with relatively high capacity retention and good rate capability when compared to other prospective forthcoming anode materials with high lithium storage capacity such as tin oxide and metallic tin. Nanostructured MoS_2-based anodes are considered to become even more exciting as the electrochemical properties outperform the bulk material.[626–630] However, low conductivity and capacity fading continue to be the main disadvantages of MoS_2-based electrodes that prevent its wider commercialisation.[631,632] The present lack of understanding of the structural dynamics induced by electrochemical intercalation of lithium or sodium ions into MoS_2 layers impedes its implementation in high energy-density batteries.[19,20]

MoS_2 can form several polymorphs, with semiconducting trigonal prism 2H and metallic octahedral 1T phases being the most commonly studied.[11-13] Weak van der Waals forces link individual MoS_2 sheets with interlayer spacing of 6.15-6.5Å.[14] MoS_2 is a semiconductor with indirect band gap and trigonal (2H) structure; the S atoms align in the lattice positions of a hexagonal close-packed (hcp) structure. Molybdenum atoms arranged in a plane sit between two layers of atomic sulphur, wherein every molybdenum atom is coordinated to six sulphur atoms in trigonal prismatic geometry. Another polytype of MoS_2 with tetragonal symmetry is

the octahedral phase (1T) which comprises of one MoS_2 layer per repeating unit where one of the sulphur atomic layers is translated with respect to the molybdenum atomic layer, which results in an octahedral coordination around the molybdenum atoms compared to the trigonal-prismatic coordination of the 2H phase monolayer.[622,635] The 1T phase is of metallic character with conductivity properties 10^7 times higher than the semiconducting 2H phase.[573] The unique structure of the S-Mo-S layers and the weak van der Waals interactions between these layers allows agreeable lithium ion intercalation and de-intercalation kinetics, which occurs due to a low volume expansion during the conversion reaction in comparison to other materials.[345] The unique structure also induces transformation from the semiconducting 2H phase to metallic 1T phase during lithium ion intercalation.[342,347] This 1T phase is widely understood to be unstable under ambient conditions and considered to transform back to the 2H phase of higher thermodynamic stability, or to a further two metastable polymorphs of distorted 1T structure: 1T' and 1T".[348–351] Researchers theorise that the three 1T phases can be stabilised by electron donation through ion intercalation, whilst all three 1T phases and the 2H phase can co-exist together within the same MoS_2 nanosheet.[353,618] Hydration of MoS_2 generally results in the formation of 1T" after water molecules react with the intercalated compound and oxidation occurs. These intercalation and hydration steps can provide additional electrons which support the formation of a distorted octahedral structure, which remains preserved even after further oxidation processes remove the extra electrons.[354,355]

Intercalation of lithium ions into MoS_2 occurs within the voltage range from 3.0 – 0.0 V, by various reaction mechanisms. The first reaction step proceeds as following: $MoS_2 + x \cdot Li^+ + x \cdot e^- \leftrightarrow Li_xMoS_2$, is kinetically fast and studies suggest it is also highly reversible within the range of 3.0 – 1.1 V vs. Li/Li^+.[2,636] This gives MoS_2 a desirable range of safe operating voltage window of 1.9 V. However, when MoS_2 is used only as an intercalation host, the

capacity is much lower, up to 25% compared to the conversion scenario. Below 1.1 V, additionally to the formation of intermediate metastable sulphides, there can be several electrochemical reactions. Several research groups have proposed theories for the complex mechanism of lithium intercalation into MoS_2 under deep discharge. It was shown that MoS_2 can be reduced to metallic Mo and Li_2S at 0.01 V vs. Li/Li^+.[637] It was also observed that during the transition from 2H phase to the lithiated 1T phase, the conversion reactions intensify at around 0.5 V, initially leading to fragmentation of the MoS_2 layers, followed after by disintegration into LiS_2 and Mo nanoparticles.[362] In contrast, other theories suggest that the storage mechanisms of lithium into MoS_2 is a reversible phase transformation conversion mechanism between MoS_2 and Mo/Li_2S.[638–644]

Another theory describes an analogous conversion mechanism for MoS_2 observed in lithium-sulphur batteries, owing to the Li_2S formation during the first discharge cycle, with the further reaction being a reversible conversion between Li_2S and elemental sulphur.[645–649] It is assumed that when the MoS_2/Li cell is under deep discharge, the metallic Mo is inactive and Li_2S with sulphur form the electrochemical reaction couple. Another study has come with an explanation that single-crystalline MoS_2 nanosheets may not hold the standard 2H or 1T phase during the first lithiation, but transform to multi-crystalline nanosheets of many molybdenum nanograins embedded within a Li_2S matrix, with a layer of up to 9 nm thickness of uniform Li_2S on the lithiated electrode. In the delithiation process, the molybdenum nanograins and the Li_2S layer convert to many lamellar nanograins of MoS_2, suggesting a completely reversible phase conversion between MoS_2 nanograins and molybdenum nanograins alongside the formation and decomposition of Li_2S.[626] In the range of 0.5 – 0.1 V, these reactions correspond with decomposition of the electrolyte and majority of electrode active material forming a gel-like matrix of molybdenum nanoparticles. The generation of

molybdenum atoms and the subsequent reversible reaction with lithium to form Li_xMo is thought to provide an extra capacity contribution of the MoS_2 nanosheets, further supporting the claim, as precipitation of molybdenum at the atomic scale in the Li_2S matrix can in theory accommodate a large amount of Li^+.[650] The full contact of the molybdenum nanograins with the Li_2S matrix may enable a reversible reaction cycle during the charge and discharge processes through molybdenum to Li_xMo to molybdenum to 1T-MoS_2, which could be the cause of greatly improved cycle stability and reliability of MoS_2 nanosheets. In view of these multiple contradictory theories, a thorough study to provide a verifiable mechanism of the electrochemical reaction between MoS_2 and Li is needed.

As well as Li-ion batteries, rechargeable sodium-ion batteries have shown great potential for electric energy storage in mass-scale due to abundant nature and therefore low cost of sodium, negative redox potential and lower toxicity, together with the ease of recovery and recyclability.[651–653] It is believed that Na-ion batteries will become commercially viable as an alternative to Li-ion, due to reduced cost and greater environmental sustainability.[277] Another major advantage to Na-ion batteries is the higher half-reaction potential for sodium relative to lithium, which provides the capability for using water-based electrolytes as an alternative to organic electrolytes, pushing commercially viable energy storage some way towards environmentally green batteries.[654] However, the practicalities of applying Na-ion batteries is limited due to a lower specific capacity, lower energy density, and lower rate capability compared to Li-ions, caused by the intrinsic large ionic radius and heavier atomic mass of Na ions.[654,655] Two-dimensional layered transition metal dichalcogenides are a promising option for anode materials for Na-ion batteries, with MoS_2 standing out due to its favourable intercalation structure for Na ions and high theoretical reversible capacity, comparable to that of Li-ion batteries.[656,657] MoS_2 shows low electronic conductivity and volume expansion during

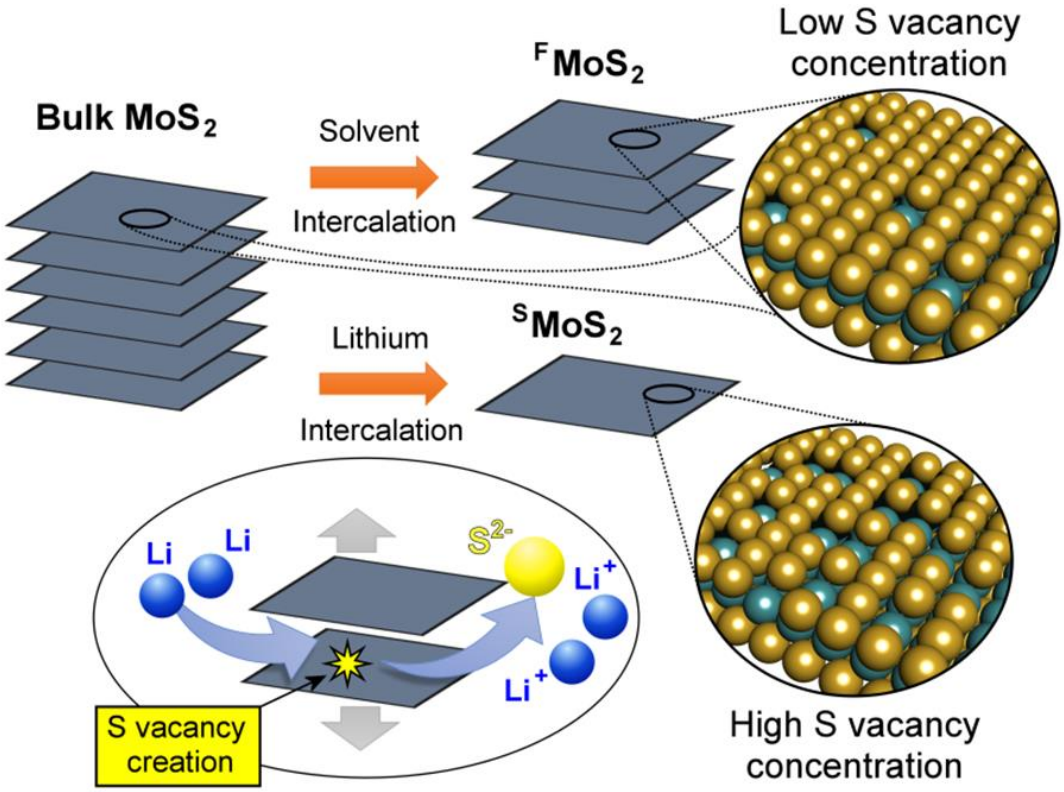
repeated sodiation/desodiation processes, similarly to those in Li-ion batteries, causing pulverisation and loose contact of active material, leading to rapid capacity fading.[658]

The aim of this research project is to investigate and summarize the differences between bulk, few-layers thick nanosheets, and monolayer nanosheets of MoS_2. Many different strategies were employed to tackle the shortcomings of MoS_2 anodes. Among all, nanostructured MoS_2 active materials have been demonstrated to vastly outperform the bulk material and retain capacity over many cycles.[20,35,37,40,43,58–67] Some even showed higher specific capacity than the theoretical value for the MoS_2 conversion reaction. This demonstrates the significant attractiveness of 2D nanomaterials and how the change in their physicochemical properties translates into desirability for applications in energy storage systems. A comparative study of single-layer nanosheets and several-layers thick nanosheets with their precursor multilayer bulk MoS_2 has been done to address the understanding of the stability and lithiation-delithiation mechanism. In addition, a simple reductive doping method of the 1T single-layer MoS_2 nanosheets with tin precursor was attempted to study impact of increased interlayer spacing in restacked single-layer nanosheets as well as the degree of accommodating the large expansion for high lithium uptake element that is tin.

6.2 Results and discussion

A straight-forward organolithium chemistry was used to intercalate lithium in between the planes of MoS_2 layered structure. Sonic wave assisted top-down chemical exfoliation method was utilised by introducing lithiated MoS_2 to water media, where exfoliated monolayers are suspended. Removal of the unexfoliated parts led to the synthesis of 1T phase monolayer MoS_2 under ambient conditions, which would preserve the 1T phase from reconstruction to the more thermodynamically stable 2H phase of its precursor. Few-layer thick MoS_2

nanosheets were synthesized via sonic wave assisted top-down physical exfoliation method using hydrazine penetration in the planes of bulk MoS_2 and consequent decomposition into N_2 and H_2 gases. This yielded a mixture of stable 2H and 1T phases across and within individual nanosheets. The two synthesis methods are illustrated in the Scheme 6.1. Both as-prepared nanosheets were compared with their precursor analogue, the bulk 2H phase MoS_2, for lithiation and delithiation capability and properties.



Scheme 6.1 Illustration of the top-down physical and chemical exfoliation sonochemical synthesis of few-layer and single-layer MoS_2 nanosheets from their bulk analogue. Adapted from a study on Co-doped MoS_2 monolayer catalyst by Liu, Tsang et.al. [554]

6.2.1 Structural Characterisation of as-prepared MoS_2 Nanosheets

Powder X-ray diffraction characterization method was used to determine crystallinity of the synthesized MoS_2 nanosheets and examine their crystalline structure. XRD diffractograms showing the crystalline arrangement in different MoS_2 samples is presented in Figure 6.1.

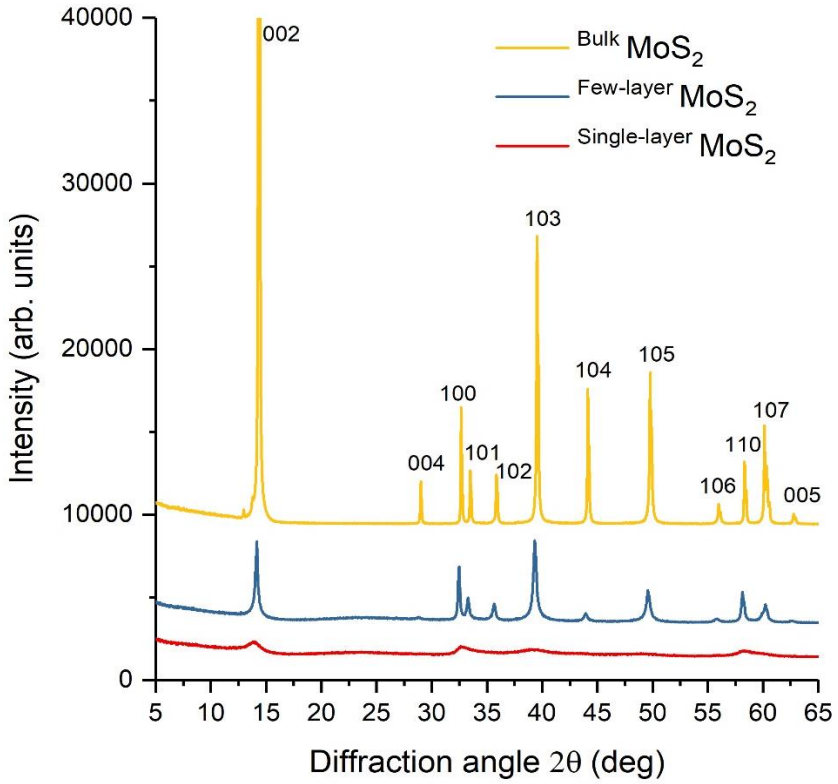


Figure 6.1 XRD diffractogram showing crystalline arrangement pattern in different MoS_2 samples.

Hydrazine exfoliation of MoS_2 typically yields several layers thick nanosheets and the XRD pattern follows that of 2H phase of the bulk counterpart, although changes in intensity of the diffraction peak is apparent, reflective of the reduced number of layers. Disappearance of (004) and reduction in intensity of the (002) interlayer-related diffraction peaks confirm several layer-thick nanosheets were obtained. In contrast, chemically exfoliated material using organolithium species typically result in large number of single-layer nanosheets, but few layers thick nanosheets can also be present. In addition, phase change from semiconducting 2H phase to metallic 1T phase is expected due to structural changes as a result of the lithium intercalation during the exfoliation process. Changes in structure lead to loss of long-range repetitive pattern and the diffraction peaks nearly vanish. In general, to identify a reduced number of layers, the (002) diffraction peak represents a repetitive pattern across the basal planes of nanosheets and is perpendicular to the basal planes of MoS_2, and

therefore can be a good indicator of the reduced number sheets in exfoliated MoS_2 flakes. It was previously reported that single-layer nanosheets get restacked and may return from 1T to 2H phase, however, this was not observed and 1T phase of exfoliated MoS_2 monolayers remained stable upon restacking.[573,574,660] The lack of other peaks shows that the material lacks long range crystallinity, and this was expected for 2D materials.

In order to confirm the exfoliated nature of MoS_2 nanosheets, and the exfoliation efficiency from their bulk analogue, transmission electron microscopy (TEM) images were recorded (Figure 6.2).

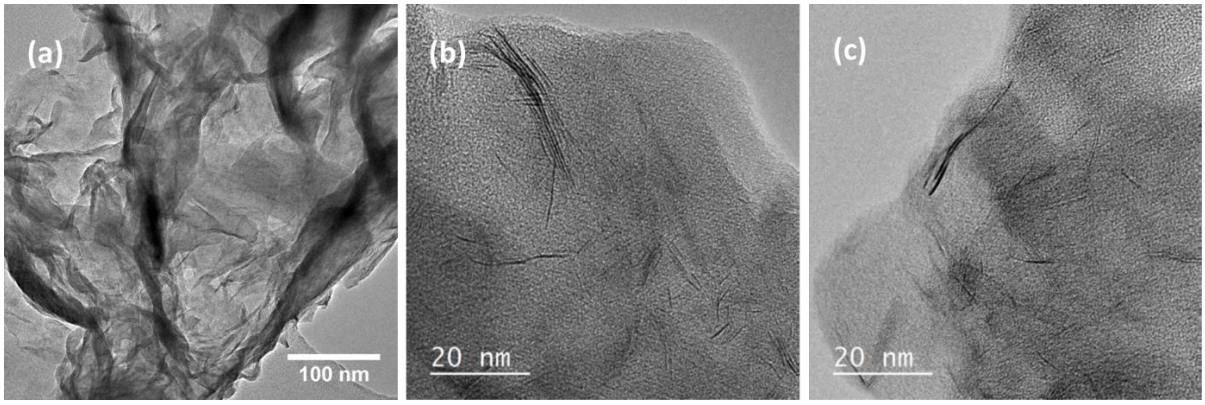


Figure 6.2 TEM images of a) bulk, b) few-layers and c) single-layer MoS2 nanosheets.

The TEM image of bulk MoS_2 reveals its layered but heavily stacked structure with lateral size varying from 0.5 to 2µm. It is evident from Figure 6.2b that hydrazine exfoliation of bulk MoS_2 led to thinner nanolayers. Fringes of several layers thick nanosheets can be observed. On the other hand, large number of very thin nanosheets were observed across the examined sample for single-layer MoS_2. The predominance of single layers is obvious upon inspection of multiple images across different areas of the material, while few bilayers were also present. Many of the nanosheets appearing as bilayers had an increased gap between the two

monolayers, with extended interlayer spacing of 9.2-9.3 Å. The measurements indicate these were two monolayers formerly exfoliated that since restacked back together.

Raman spectroscopy is known as a powerful non-destructive technique for characterization of crystalline structures of single-layer nanosheets and bulk MoS_2. As presented in Figure 5.5, two most significant vibrational modes of 2H phase MoS_2 are E_{2g} and A_{1g}. E_{2g} arises from in-plane vibrations of two sulphur atoms with respect to the molybdenum, while A_{1g} corresponds to the out-of-plane vibrations of S atoms in opposite directions.[565] The origin of the 2LA(M) peak is ascribed to a second-order longitudinal acoustic phonon peak, however, it has been proposed that it can overlap with an additional peak referring to the first-order optical phonon vibration denoted as A_{2u}.[566,567]

Upon exfoliation of MoS_2 nanosheets structural changes to the MoS_2 basal planes from 2H phase to 1T phase take place. The 1T phase has relatively lower in-plane symmetry, leading to loss of long-range structural features that could be observed by powder diffraction. 1T phase for single layer MoS_2 nanosheets with characteristic Raman modes of E_{1g}, and low-frequency phonon modes J_1, J_2 and J_3 are clearly observed. The appearances of these characteristic peaks for 1T phase are attributed to the longitudinal acoustic phonon modes. A_{1g} mode characteristic for out of plane stretches in semiconducting 2H phase and 2LA(M) longitudinal acoustic phonon mode are lost.[568,569] Raman spectra of exfoliated few-layer MoS_2 nanosheets showed presence of characteristics of both phases and confirm that these are indeed composed of a mixture of 2H and 1T phases. While predominantly of 2H phase, the 1T metallic phase is generally found around structural defect sites, such as sulphur vacancies.

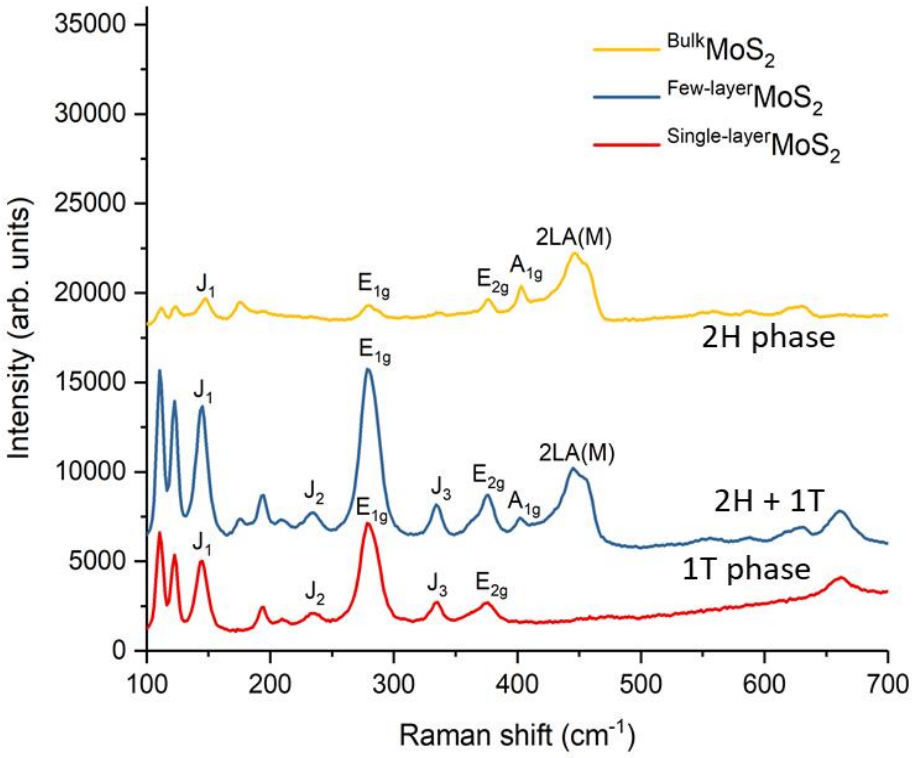


Figure 6.3 Raman spectra showing different phases present in MoS_2 samples.

X-ray photoelectron spectroscopy (XPS) of bulk and single-layer MoS_2 nanosheets was used to identify the structural composition of the two polymorphs and the chemical state of Mo and S in the material. Intensities were normalised and binding energy scales were corrected. XPS is a widely accepted surface-sensitive quantitative spectroscopic analysis technique to monitor elemental composition of the material, and their chemical state as well as the overall electronic structure. The binding energies of the MoS_2 samples can distinguish between the semiconducting 2H trigonal prismatic phase and the metallic 1T octahedral phase as both Mo 3d and S 2p regions for the 1T phase appear at binding energy 0.8 eV lower than for the 2H polymorph.[573] This was indeed the case as Figure 6.4 shows. Mo 3d and S 2p regions specifically depict the shift in binding energy between metallic 1T phase of single-layer MoS_2 and semiconducting 2H phase of bulk MoS_2. 2H phase bulk MoS_2 characteristic peaks of Mo $3d_{3/2}$ and $3d_{5/2}$ appeared at 232.5 eV and 229.1 eV, respectively. Corresponding characteristic

peaks of 1T phase of single-layer MoS_2 were shifted to lower binding energy by 0.8 eV, appearing at 231.7 eV and 228.3 eV for Mo $3d_{3/2}$ and $3d_{5/2}$ region, respectively. In addition, the symmetry of the peaks in both regions indicate that both samples exist entirely in their corresponding phase. It was previously reported that liquid exfoliation of the MoS_2 nanosheets may result in the formation of MoO_3 and indeed a trace amount of Mo^{6+} species have been detected.[574,575] There is a very small peak observed in the Mo 3d region at 235.6 eV (bulk) and 234.8 eV (single-layer) that indicate a presence of small amount of Mo^{6+} species. However, this small peak is observed in both of the samples. It is hypothesized that it refers to sulphur enriched MoS_3 species.[576] The S 2p region further supports these observations as a shift in binding energy of the 1T phase single-layer MoS_2 to lower binding energy values compared to 2H phase of the bulk MoS_2. The XPS scan of the 1T phase showed 2 distinct sulphur $2p_{1/2}$ and $2p_{3/2}$ peaks at 162.6 eV and 161.4 eV, respectively. A difference of 0.8 eV of the corresponding S $2p_{1/2}$ and $2p_{3/2}$ peaks of the 2H phase. A detailed peak fitting and deconvolution analysis was not performed, however, the symmetry of the peaks of each phase with respect to the other is additional evidence to Raman spectral phase analysis. A small, broad peak at 168 eV in S 2p region indicates that there may be a very small content of what might correspond to sulphate species in the bulk MoS_2 sample, however, no apparent sulphate species were observed in the 1T single-layer MoS_2 XPS spectrum.

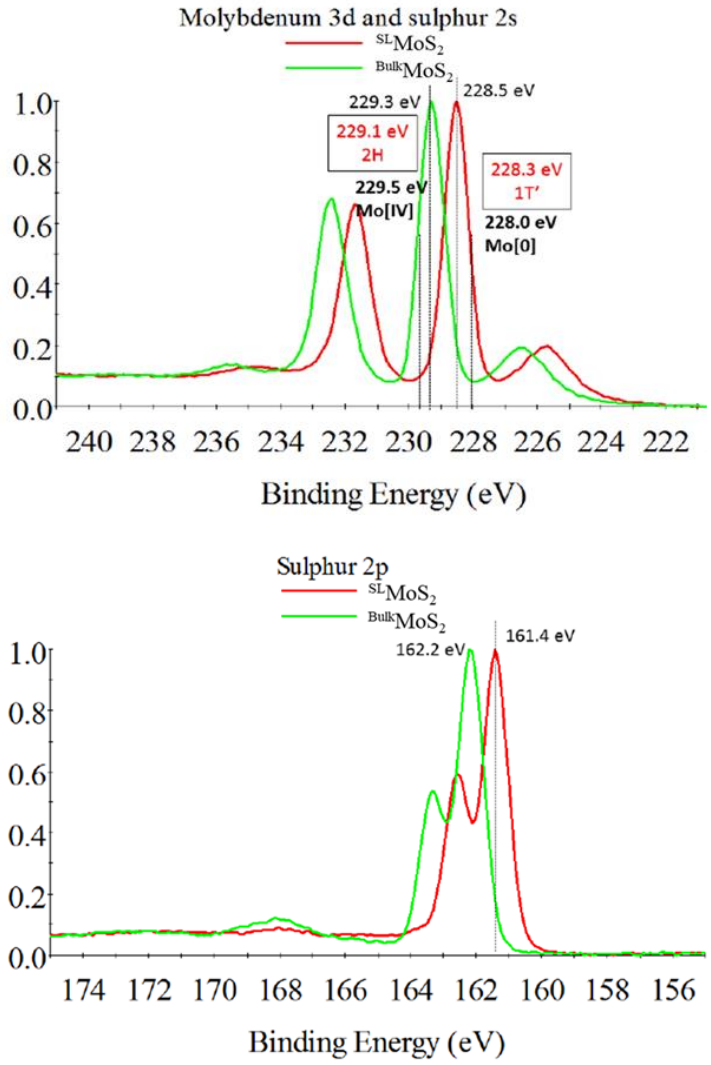


Figure 6.4 Mo 3d and S 1s and 2p regions of XPS spectra of bulk and single-layer MoS_2.

Electron paramagnetic resonance (EPR) can be used as a measuring tool for accounting for unpaired electrons on unsaturated defective sites and across basal planes where quantitative, structural, and dynamic information can be inferred, and therefore can reflect the phase nature of the MoS_2 nanosheets. The metallic 1T phase, often resulting from sulphur vacancies on or other structural interference caused to basal planes in the material layered structure, leads to increased number of delocalised electrons, while the semiconducting 2H phase offers limited number of unpaired electrons at the basal plane edges and structural defects. It is important to mention that defects usually result in local change of the 2H to the 1T phase, and therefore the extent of 1T phase present in the sample can be extracted from EPR spectra

of MoS_2 nanosheets. The EPR spectra of the bulk, few-layer and single-layer nanosheets (g factor of 2.0) are displayed in Figure 6.5 and summarized in Table 6.1 together with Brunauer–Emmett–Teller surface analysis technique values.

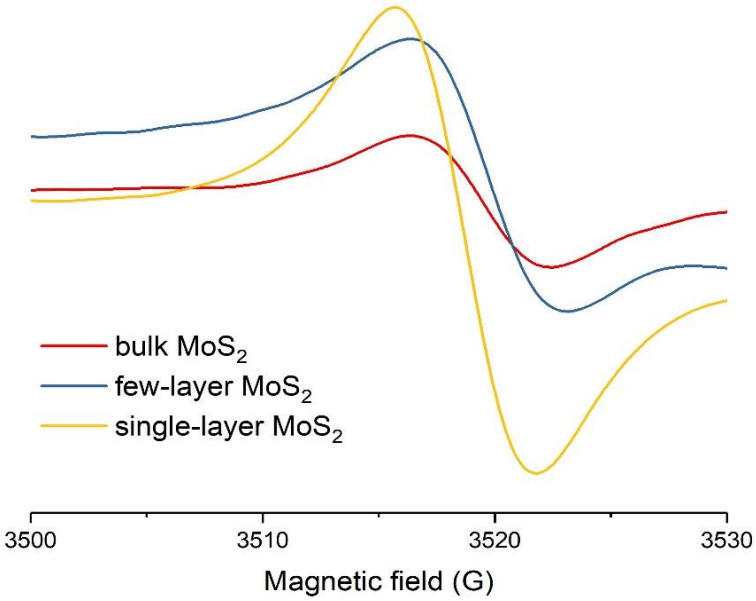


Figure 6.5 EPR analysis of MoS_2 nanosheet and bulk materials.

Surprisingly, a large quantity of unpaired electrons is observed in bulk MoS_2 sample (4.73×10^{15} g^{-1}) given its small surface area revealed by BET (25.0 $m^2 \cdot g^{-1}$), mostly located at multilayer flake edges and crystallite interfaces. On the other hand, few-layer MoS_2 showed twice as many unpaired electrons (8.54×10^{15} g^{-1}) compared to the bulk phase material, while three times as much surface area was gained performing physical exfoliation from bulk into few-layer thick nanosheets and restacking as indicated by BET (25.0 $m^2 \cdot g^{-1}$). This increase can be directly related to the basal plane structural imperfections resulting in local presence of unpaired electrons of the metallic 1T phase. By contrast, restacked single-layer MoS_2 nanosheets showed further increase in measured surface area by BET (30.5 $m^2 \cdot g^{-1}$), while additional 2.5 fold increase in unpaired electron was recorded by EPR (18.36×10^{15} g^{-1}). This confirms the trend of transformation of the semiconducting trigonal prismatic 2H phase into

the octahedral 1T phase upon chemical exfoliation of bulk MoS_2 into monolayers. It also demonstrates that organochemical lithiation of the bulk material results in structural perturbation of the constituent layers, and results in phase transition that remains stable after delithiation and restacking of individual nanosheets.

Table 6.1 Comparison of the BET surface area and the EPR analysis of unpaired electrons in MoS_2 samples.

sample	BET ($m^2 \cdot g^{-1}$)	EPR [V_s] at g = 2.0 spin counts $\cdot g^{-1}$
Bulk MoS_2	8.4	4.73×10^{15}
Few-layer MoS_2	25.0	8.54×10^{15}
Single-layer MoS_2	30.5	18.36×10^{15}

Packing of the active material, mixing with the additives and good contact with the electrode surface are some of the crucial factors for electrode to perform well. This is particularly important so that the electron transfer from and to the active material is efficient. Scanning electron microscopy (SEM) is a surface analytical technique that scans the surface of a sample with a focused beam of electrons rendering information about the surface topography and composition of the sample. Energy-dispersive X-ray spectroscopy (EDX), on the other hand, is an analytical technique used for the chemical elemental characterization, displaying a unique set of peaks for each element in its electromagnetic emission spectrum. When SEM imaging is coupled with EDX, individual elements that the sample is composed of, and their precise locations can be identified.

SEM-EDX images of ink-casted and calendered electrodes made of different MoS_2 samples as the active material, carbon super C65 as a conductive additive, and fluorinated thermoplastic

copolymers as a binder resin are shown in Figure 6.6. SEM images show that nanosheet size and thickness in particular play a vital role in packing of the active material on the electrode surface. Bulk MoS_2 large particulate size can be seen and influenced poor mixing with additives which in turn resulted in not very homogeneous casting of the sample. In contrast, both few-layer and single-layer MoS_2 show highly homogeneous evenly-dispersed casting over the electrode surface. Thin nanosheets get easily mixed with conductive additive and the binder to provide good electric connectivity, and this alone makes these two-dimensional MoS_2 nanomaterials more promising candidates for improved electrode performance.

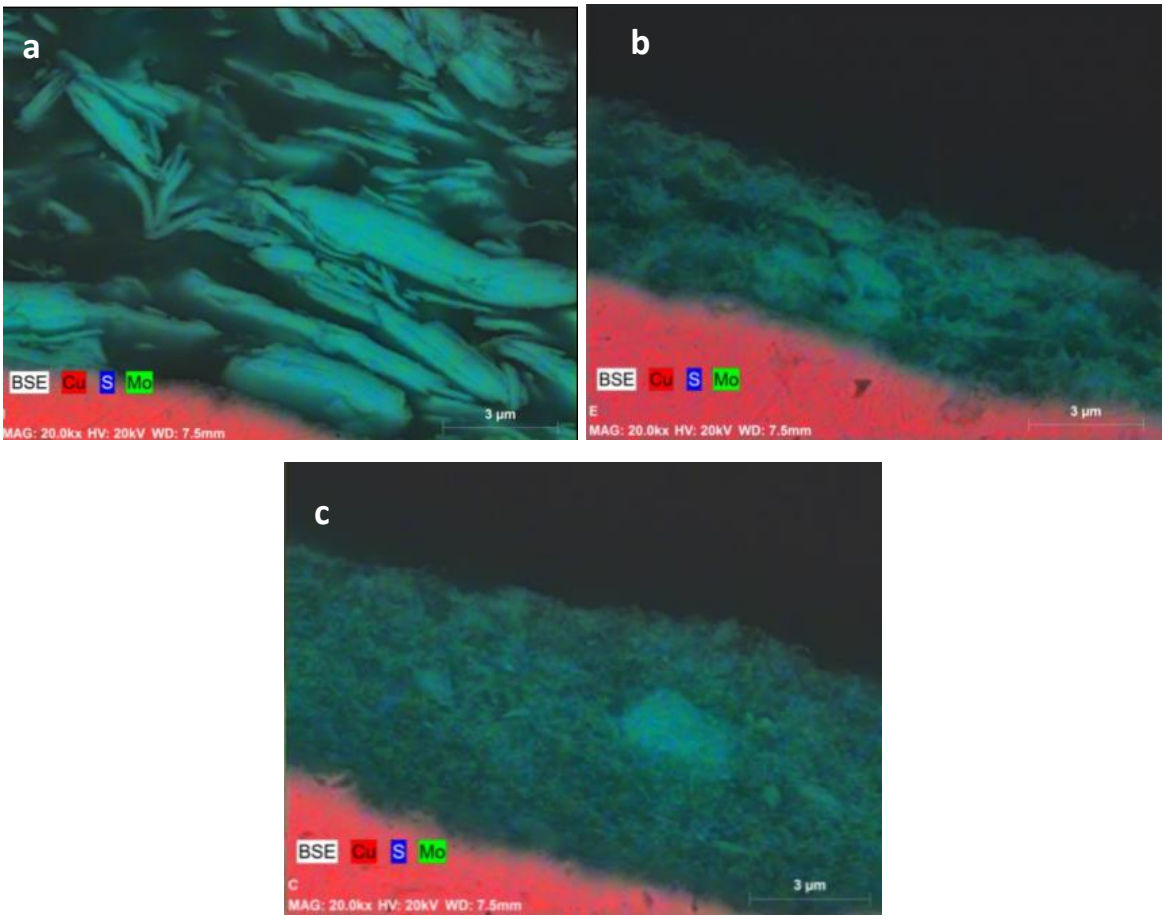


Figure 6.6 SEM coupled with EDX images showing freshly prepared calendered electrodes a) bulk, b) few-layer, and c) single-layer MoS_2 active materials.

6.2.2 Performance of MoS_2 Nanosheets as Anode Materials for Lithium-Ion Batteries

One of the key attributes for desirable and efficient lithiation is easy access and diffusion of lithium ions across the electrode material. The high surface to volume ratio of exfoliated MoS_2 nanosheets offers advantages such as a tight electrode/electrolyte interaction, a short diffusion path for Li^+ ions and electrons and improved conductivity.[661] A method of studying this is via charge-discharge cycling of lithium half-cells at various current rates. Galvanostatic charge-discharge cycling test of bulk, few-layer and single-layer MoS_2 is shown in Figure 6.7.

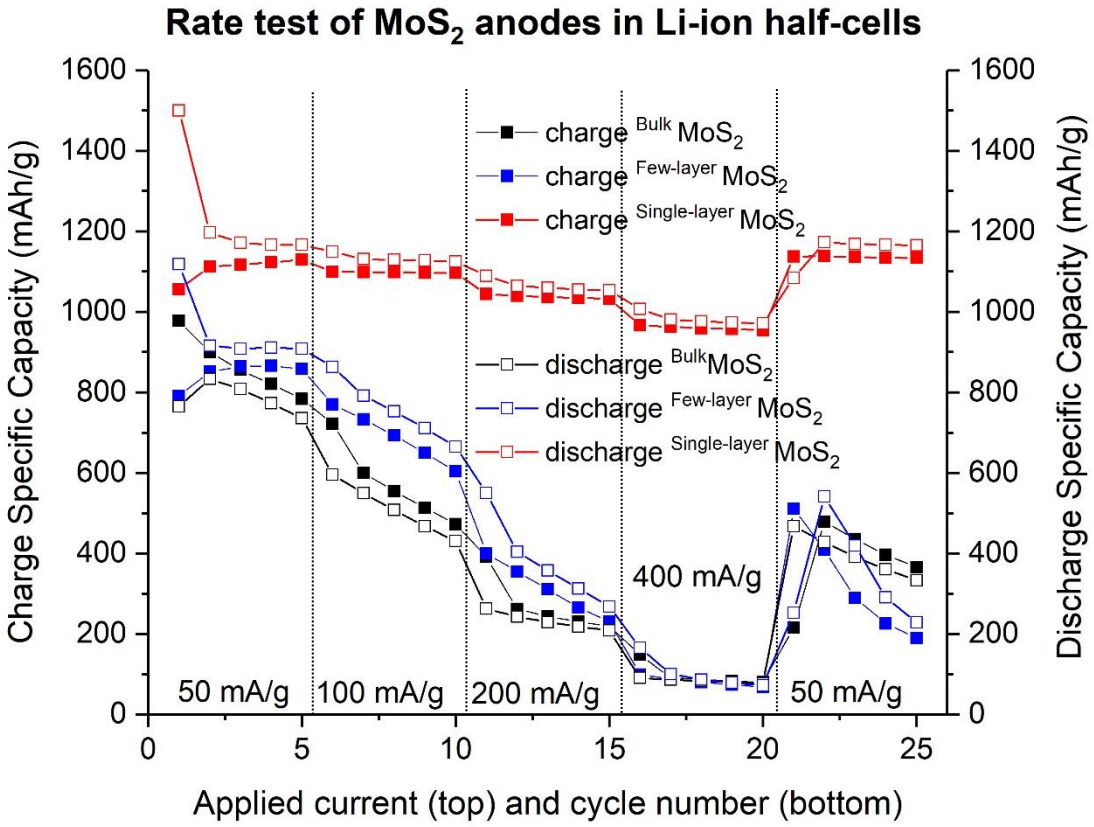


Figure 6.7 Galvanostatic rate performance of bulk, few-layer, and single-layer MoS_2 negative electrodes in Li-ion cells. Each electrode was cycled 5 times at applied currents of 50, 100, 200, 400 and again at 50 mA/g.

This experiment was performed using a standard procedure involving coin 2032 half cells and was run on a Maccor 3 instrument operated by Maccor software. Each experiment was repeated three times and the average of each type of cells was plotted. All three samples

showed initial irreversible loss of capacity during the first cycle. This is attributed to the formation of solid electrolyte interface on the surface of the electrode.[662–664] Bulk MoS_2 electrodes showed capacity fading and poor rate as a result of low ionic conductivity, fast material degradation, volume variation, unwanted irreversible Li_2S conversion and a possible added issue with sulphur disintegration and insulation of the newly formed SEI layer and within individual sheets, and this observation is in agreement with literature.[665,666]

Electrodes made of few-layer thick nanosheets of MoS_2 showed slower capacity fading and slightly improved rate performance at lower current rates. The enhanced performance can be attributed to the improvement in accessibility of lithium occupational sites in MoS_2 lattice and diffusivity of lithium ions across MoS_2 layers, but it can also be linked to the presence of some of the more stable 1T metallic phase MoS_2. However, the capacity faded fast with increasing current rates and irreversible capacity loss issue similar to the bulk MoS_2 was observed. In addition, the capacity loss of the few-layer MoS_2 beyond that of bulk material was observed when low current cycling was reintroduced. This could be linked to faster and easier diffusion of lithium ions leading to more dynamic disintegration of the 2H phase and formation of a fine insulating layer across the more exposed exfoliated layers than would happen in the bulk material.

In contrast, exfoliated and restacked single-layer 1T metallic phase MoS_2 showed significantly higher capacity retention capability even at high current rates as well as greater rate stability. The metallic character of the 1T phase of the single layer MoS_2 incorporates a quick electron transfer while the increased in-plane bonds facilitate lithium ions more readily without the addition structural strain taking place in the 2H phase.[667] In addition, larger exposed surface area and ionic diffusion across the basal planes of 1T phase also contribute to the much

improved cycling ability of the single layer MoS_2 electrode.[668] Furthermore, any sulphur vacancies, structural defects or grain boundaries of neighbouring crystallites were previously shown not to be hindering lithium diffusion.[669,670] Higher uniformity and increased mechanical strength at atomic thickness of the single-layer 1T phase MoS_2 proves highly advantageous when operating at higher currents.[671] This result clearly shows the durability of single-layer MoS_2, and makes it a very promising candidate as the material of choice for long duration intercalation anodes.

Figure 6.8. shows voltage vs capacity curves of first three charge-discharge cycles of the three studied MoS_2 electrodes. The charge-discharge voltage curves of the 1st, 2nd and 3rd cycles were plotted and compared in Figure 6.8, and differential analysis of the voltage curves for all three samples can be found in Appendix Figure A6.1 that exhibited the over-capacity phenomenon in the experiments. The discharge voltage curve profiles appeared to show plateaus at 2.1 V, 1.2 V and 0.5 V except for the initial discharge cycle where there is a plateau around 0.7-0.6 V and is associated with formation of SEI during the first discharge cycle. In general, electrochemical processes above 1.0 V are typically associated with Li^+ intercalation and de-intercalation, while below this mark means insertion of Li^+ ions into the MoS_2 crystal lattice. A typical plateau around 0.5 V and below is linked to fragmentation of MoS_2 nanosheets and formation of insulating Li_2S and Mo nanoclusters. Upon charging, corresponding anodic peaks appear around 1.7 V and 2.3 V, the former is associated with reversible reaction of Mo back to MoS_2 and a conversion reaction of Li_2S to sulphur. These are particularly related to the 2H semiconducting phase of bulk MoS_2 and indeed that is what was observed.

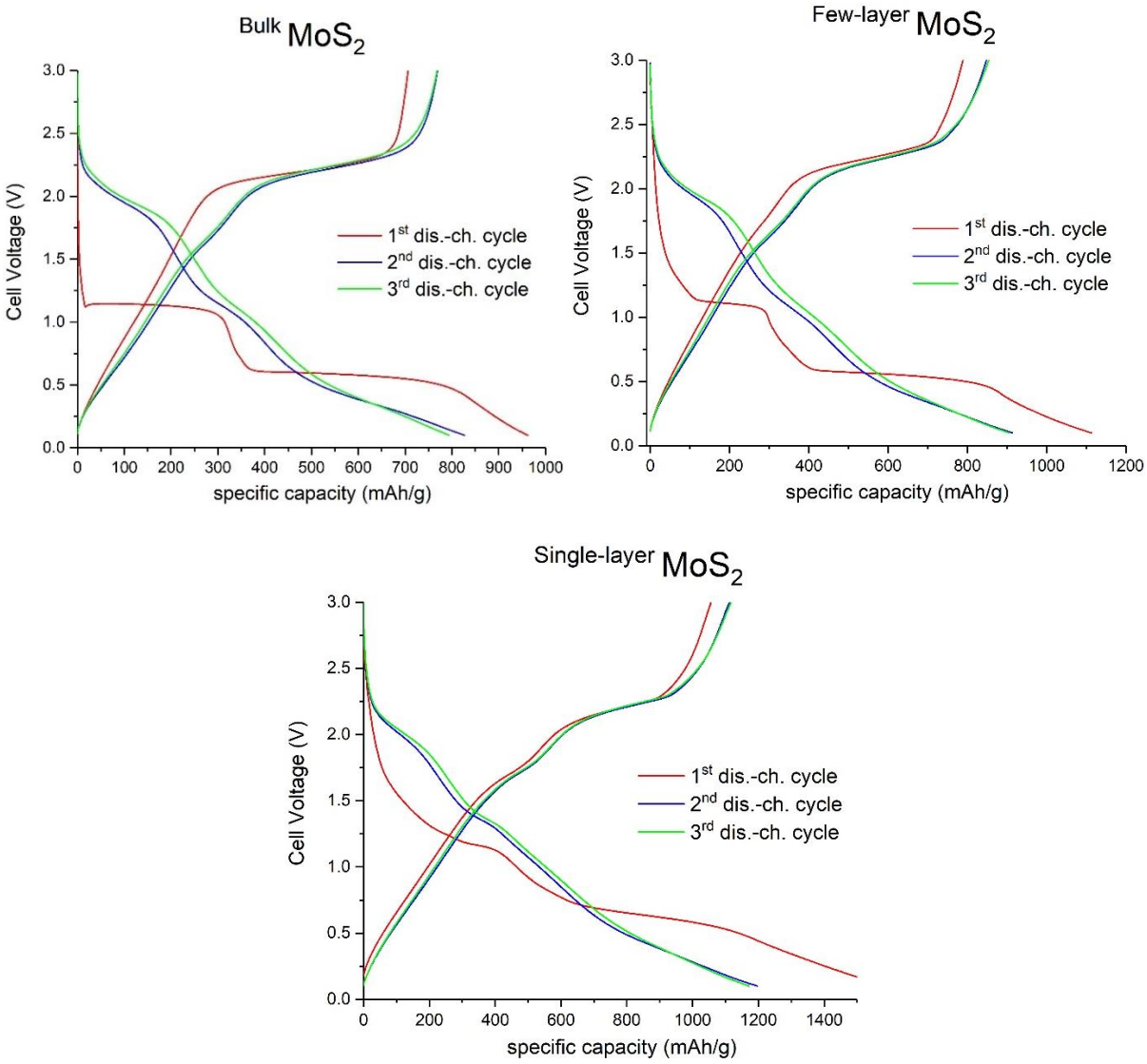


Figure 6.8 Voltage vs capacity curves of first three charge-discharge cycles at 50 mA/g current applied to bulk, few-layer, and single-layer MoS_2 electrodes.

$^{Few\text{-}layer}MoS_2$ also followed this trend although with a noticeable shift to lower potentials, and this can be particularly seen in the discharge cycle. The lower potential values as well as slightly more sloping plateaus mean there is a lower energy barrier for the diffusion of Li^+ ions across the basal planes of MoS_2 and to react with MoS_2 crystal lattice as Li^+ finds it easier and consequently creates less strain on MoS_2 material. It should be noted that $^{Few\text{-}layer}MoS_2$ possesses both phases 2H semiconducting phase and some areas of metallic 1T phase. 1T phase is typically created by structural perturbation, often caused by lithium, either in form

of electrochemical intercalation, or in form of a reaction with organolithium compounds. Nevertheless, it appears that if this phase is created in slow motion and homogeneously across the basal planes, it remains stable and enables easier diffusion and reversable hosting Li^+ ions. It tends to host Li^+ ions by a further but smaller structural change to 1T' phase, and this is discussed in more detail in the AC-TEM and Ptychography analytical image reconstruction section below.

Nevertheless, this phenomenon is particularly obvious in $^{Single\text{-}layer}MoS_2$ material which consists of predominantly metallic 1T phase, where easier intercalation, diffusion, and hosting of Li^+ ions result in outstanding stability and almost two-fold increase in Li^+ hosting capability (or better known as the materials cycling capacity) of this remarkable MoS_2 nanomaterial. Furthermore, the flexibility and ultrathin nature of $^{Single\text{-}layer}MoS_2$ nanosheets help the material accommodate substantial structure and volume expansion during the Li^+ intercalation/de-intercalation. This leads to a formidable stability of the material when high current densities were applied. This makes $^{Single\text{-}layer}MoS_2$ nanosheet highly promising prospective nanomaterial for use in battery system where rapid charging and high current densities are desirable.

The same trend was observed for all three samples when different current densities were applied, and can be seen in Figure 6.9 and in Appendix Figure A6.2.

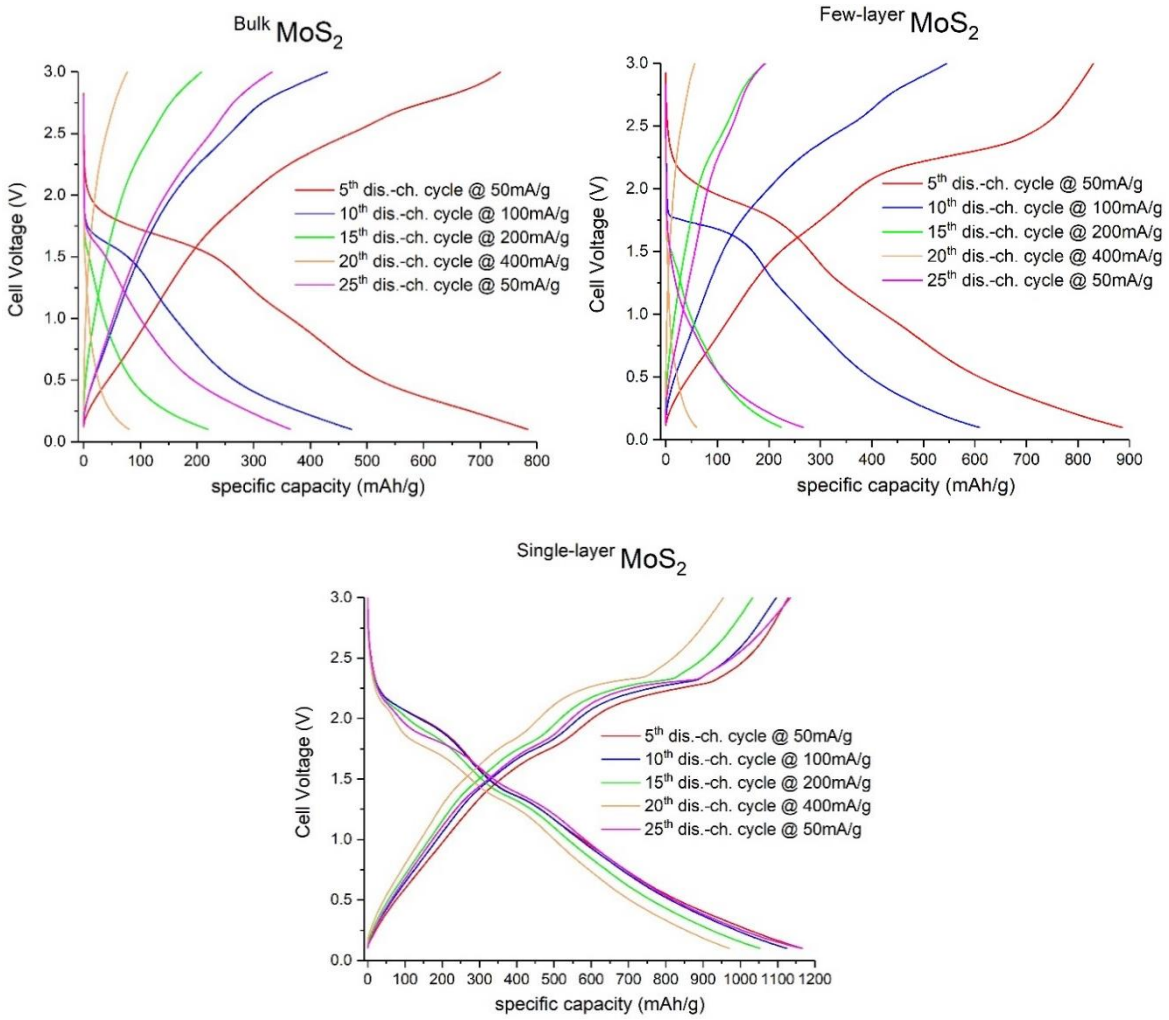


Figure 6.9 Voltage vs capacity curves of each fifth cycle at different applied currents. These curves show retention of capacity and indicate lithium storage mechanism in each active material.

By combining synchrotron X-ray powder diffraction (SXRD) together with galvanostatic cycling experiments using specially designed cells, we can look into the detail of the structural changes in few-layer MoS_2 and single-layer MoS_2 electrode materials during the initial discharge at 100 mA/g current rate. SXRD technique is applied in short, monochromatic, high intensity beam pulses during the discharge cycle to probe the internal structure of the electrode in operation. Multiple XRD patterns were obtained throughout the first discharge

and the most appropriate patterns reflecting the most representative changes in the voltage curves are shown in the Figure 6.10.

Observations of discharge cycling of $^{\text{Few-layer}}MoS_2$ nanosheets showed how the material started losing its crystalline 2H phase structure below 1.0 V. This is in stark contrast to $^{\text{Single-layer}}MoS_2$ nanosheets where the in-plane (102) Bragg reflection remains visible down to 0.5 V, confirming that $^{\text{Single-layer}}MoS_2$ does not fragment and decompose into Li_2S and molybdenum nanoclusters as widely accepted as a plausible conversion mechanism.[283,344,547,649,650,672]

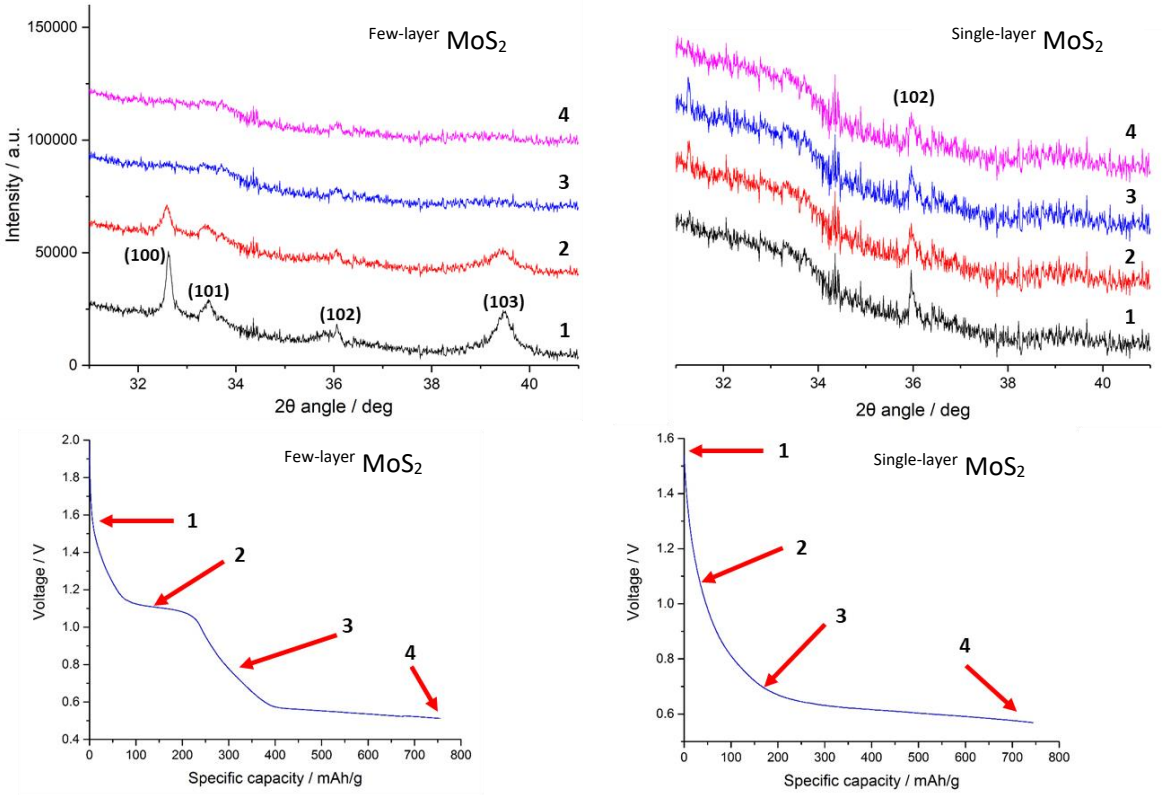


Figure 6.10 In-situ monitoring lithiation of MoS_2 active material during the first discharge cycle at 100 mA/g current. Synchrotron XRD technique is applied in short, monochromatic, high intensity beam pulses during the discharge cycle to probe the internal structure of the electrode in operation. The XRD patterns in the upper graphs represent each highlighted point on the discharge curve below.

To further address the lithiation and delithiation process, MoS_2 nanosheets were lithiated chemically with n-butyllithium and exfoliated under inert atmosphere in anhydrous acetonitrile to preserve lithium ions on the basal planes. As prepared nanosheets were imaged by spherical aberration corrected scanning transmission electron microscopy (C_s-STEM) coupled with electron energy loss spectroscopy (EELS) and analysed using image reconstruction technique called ptychography. This technique is based on quantitative analysis of multiple phase images and their compositional contrast formed simultaneously with incoherent signals. Computational analysis of the phase images consequently may reveal the exact position where lithium is present.

At first, a quick assessment of the nanoflakes for presence of lithium was made by identifying a large clump of lithiated MoS_2 flakes. Employing EELS to the STEM imaging can analyse the energy lost by the electrons scattered from the sample, and represents a powerful tool that can extract sample properties from nanostructures such as electronic structure and sample composition.[673] Unlike many common spectroscopic techniques, EELS is capable of detecting the presence of lithium, and when coupled with STEM it can confirm the presence of lithium in a specific nanoscale region of the sample. Figure 6.11 shows annular dark-field C_s-STEM (ADF C_s-STEM) image of a large restacked MoS_2 flake and corresponding EELS scan. The signal intensity for lithium K-edge peak appear in the energy range of 60-65 eV and revealed presence of a significant amount of lithium in the sample. This is important evidence of the presence of lithium, providing information to be used for more in-detail study of the STEM images. However, the sample proved to be unstable under longer beam irradiation times.

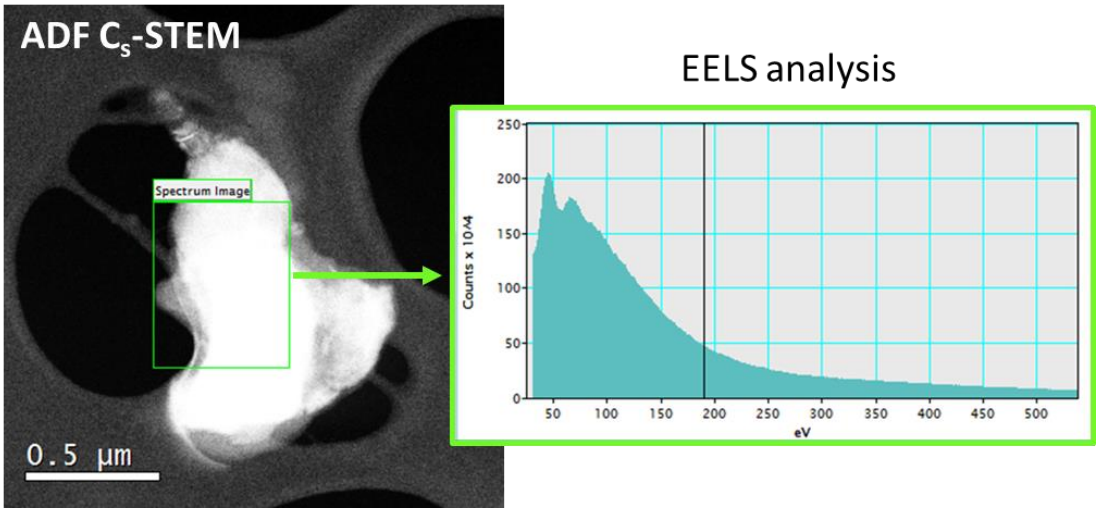


Figure 6.11 ADF C_s-STEM coupled with EELS analysis shows large lithium content in lithiated single-layer MoS_2.

Using phase-contrast high-resolution ADF C_s-STEM images has been demonstrated to provide the least damaging electron beam imaging, where radiation damage to the sample might be a limiting factor.[674] Recent progress in low intensity beam and low dose application for STEM ptychographic imaging reconstruction of monolayer MoS_2 demonstrated that a lattice resolution can be achieved.[675] A high degree of compositional sensitivity to both heavy and light elements simultaneously at atomic resolution is achieved by employing annular dark-field (ADF) detection. ADF detectors are capable of collecting the intensity of relatively high-angle scattering, which in turn results in an image with atomic-number contrast (Z-contrast). When these phase images are combined with ptychographic phase imaging, a full reconstruction of the ADF C_s-STEM images can be achieved through a deconvolution approach. This fast non-iterative method is called Wigner-distribution deconvolution ptychography.[676] Reconstructed phase images using the Wigner-distribution deconvolution ptychographic method are shown in Figure 6.12, exhibiting 1T′ metastable distorted phase domains of Li_xMoS_2.

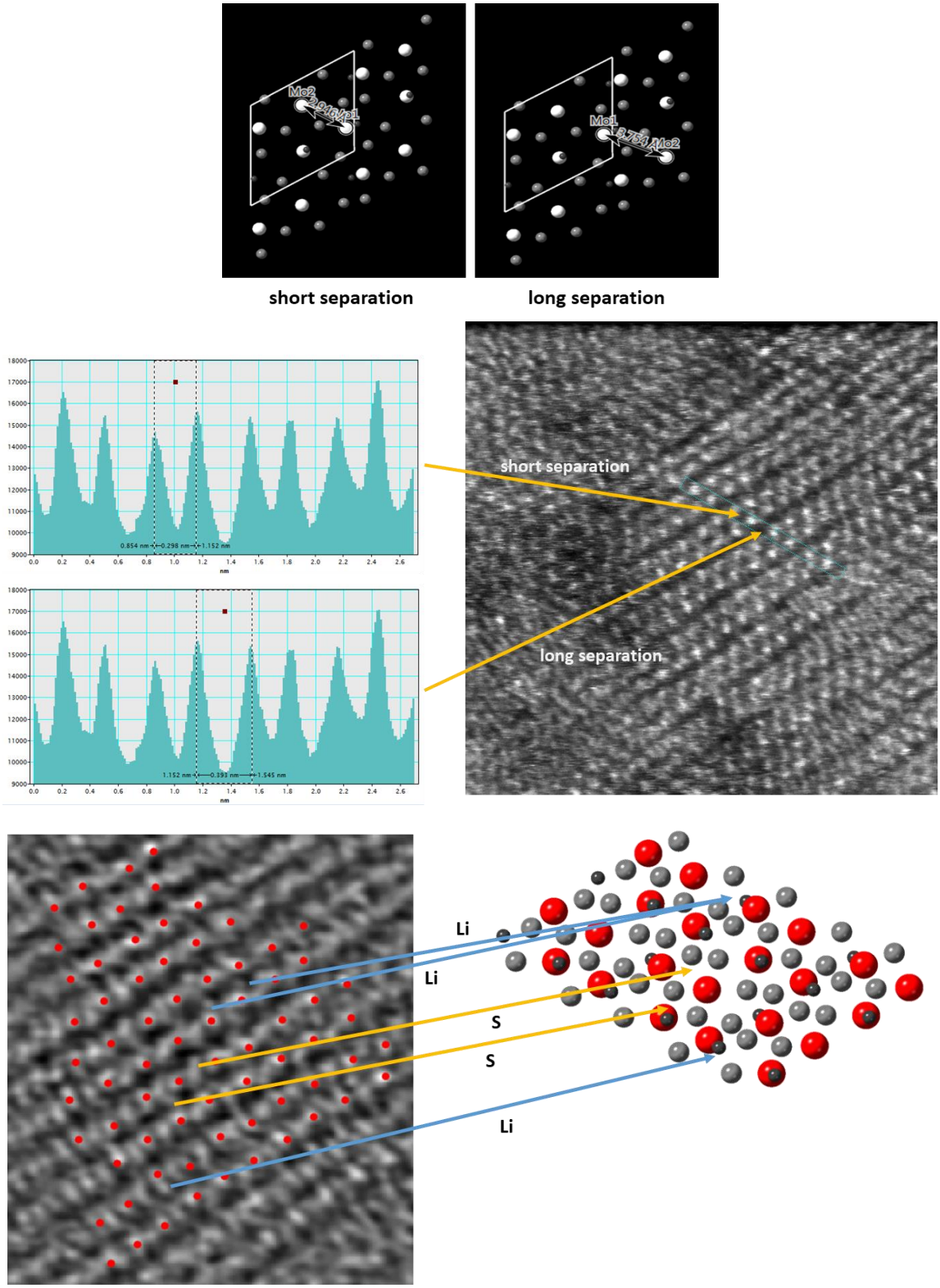


Figure 6.12 Ptychographic analysis performed on ADF C_s-STEM images of lithiated single-layer MoS_2. Line profile showing alternating shorter and longer separation gap between Mo atoms. Modelled crystal structure of the lithiated MoS_2 was applied to ADF C_s-STEM image. The atom colours in the model are as follows - S: Light grey, Mo: red, Li: black

The lithium intercalation dramatically modified the MoS_2 structure due to the decrease in binding energy between individual elements and creates a 1T' phase domain of low symmetry that is stabilized by the presence of lithium ions. As mentioned earlier, the first structural change is the transition to the octahedrally coordinated 1T phase caused by electron transfer from intercalated Li^+, upon further lithiation, the 1T phase undergoes further distortion to form the 1T' phase in order to lower the system overall energy. Further lithiation would lead to a loss of long-range order and this was demonstrated in broadening and disappearance of the XRD pattern as observed in Figure 6.1. However, Figure 6.12 shows an altered lattice with stripes of two different distances between Mo atoms but indeed with a pattern. This is in stark contrast to Figure 6.6 where 1T MoS_2 phase is shown. Applying lithiated 1T' MoS_2 model structure from the Inorganic Crystal Structure Database to collected ADF C_s-STEM images was used to determine the location of lithium atoms. 1T' MoS_2 phase is a distorted version of 1T phase originally believed to be highly metastable, but recent research showed 1T' phase can be stabilised by electron donation through lithium ion intercalation into the lattice.[348–351] As highlighted by arrows in the Figure 6.12 lithium atoms appear as dumbbells within larger (and brighter in the image) molybdenum atoms. The sample, however, suffered from long time exposure to the electron beam which made imaging over a prolonged period of time that would result in clearer atomic resolution difficult. 1T' phase proved to be less stable and lithium ions highly volatile under extended electron doses that resulted in movement of lithium atoms as well as gradual relaxation of molybdenum atoms from 1T' distorted octahedral arrangement.

6.2.3 Impact of calender press on the electrochemical performance of single-layer MoS_2 electrodes in Lithium-Ion Batteries

The calendering of electrodes is an essential process used in industry to maximize the volumetric capacity of each electrode in Li-ion battery cells through the compaction of the electrode materials components with current collector metal sheet between two large calender rollers.[677,678] This process aims at improving the final electrode energy density as well as electronic conductivity of the electrodes. In contrast, overcalendering of the conductive carbon, active material, and binder closer together might have a negative impact on ionic conductivity of the electrode as well as it might lead to particle pulverization and reduced cycle life as a result of parasitic side reactions and loss of active material.[679]

Electrodes made of the $^{Single\text{-}layer}MoS_2$ material of 0.1 mm thickness calendered to 1 g/cm^3 and 2 g/cm^3 loadings together with a 0.2 mm thick electrode active material with loading of 1 g/cm^3 were tested, analysed and compared for their respective electrochemical performances. 0.1 mm thick 1 g/cm^3 electrodes were used as a standard testing thickness and loading as it corresponds to the testing procedure usually adopted for testing anode materials on smaller scales. However, larger loadings are highly desirable in order to accommodate larger amounts of lithium ions in a cell and reduce the overall manufacturing costs. Electrodes of 0.2 mm thickness with the same loading (1 g/cm^3) were prepared from the same ink slurry and calendered to the desired thickness and loading. Average data from galvanostatic rate performances of three cells per each sample are shown in Figure 6.13. It can be seen that the performance of the 0.2 mm thick electrodes rapidly deteriorated with every cycle, and quicker at higher currents. This can be explained by the less effective ionic diffusion within the thicker electrode, and interaction of lithium ions with the MoS_2 was not homogeneous across the

whole electrode. Such a scenario would lead to a higher stress at and close to the electrode interface with electrolyte as the lithium ions would not penetrate deep enough within the electrode material resulting in material pulverization and MoS_2 material degradation, particularly at higher rates. In addition, electron transfer also appears less efficient as packing porosity and material packing would influence transfer efficiency to the copper current collector.

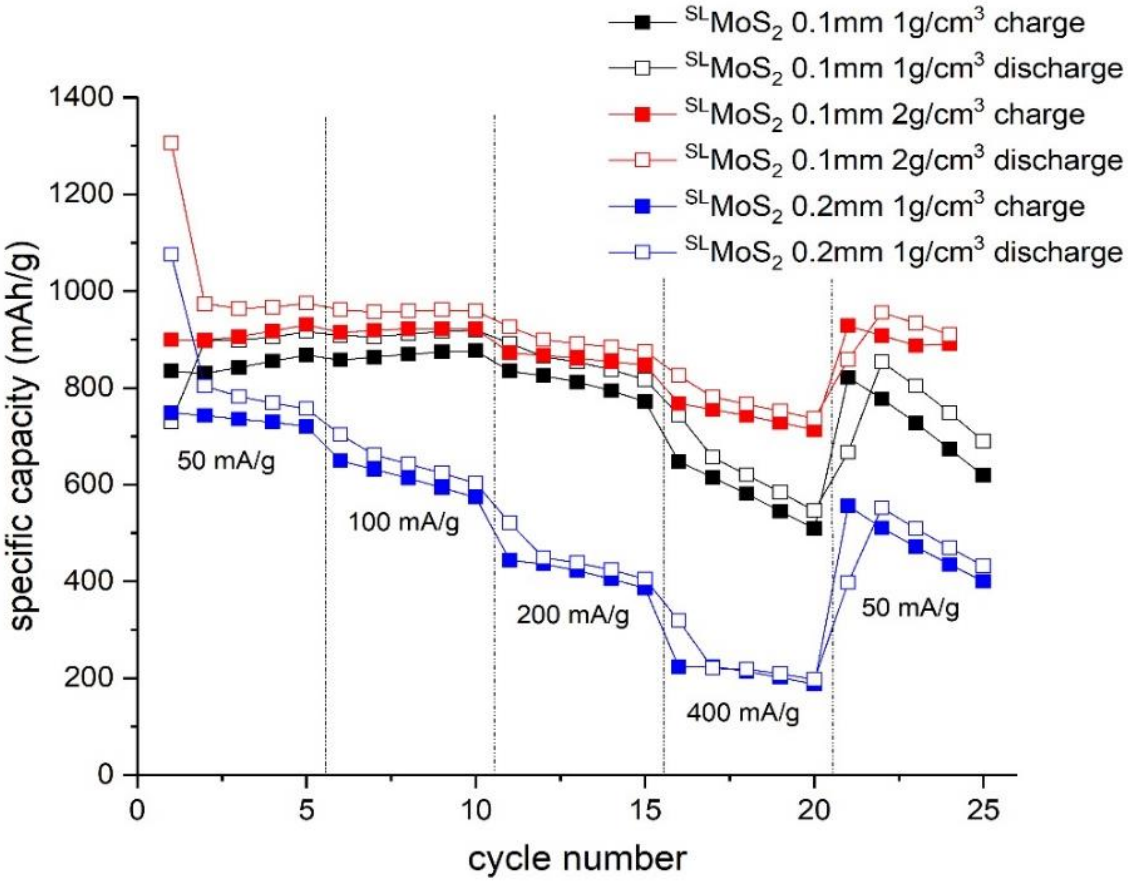


Figure 6.13 The effect of loading and calender press upon the performance of single-layer MoS_2 negative electrodes. The galvanostatic rate performance of electrodes made of three different castings of the same single-layer MoS_2 ink. Thickness and loading of each electrode is denoted in the legend of the graph. Each electrode was cycled 5 times at applied currents of 50, 100, 200, 400 and again at 50 mA/g.

The 0.1 mm thick $^{Single\text{-}layer}MoS_2$ electrode calendered to 2 g/cm^3 loading were prepared by subjecting the standard 0.1 mm thick 1 g/cm^3 $^{Single\text{-}layer}MoS_2$ electrodes to further increase in

pressure by the calendering machine. In contrast, as prepared electrodes showed a significant improvement in cycling ability and durability during higher currents. The anticipated lowest porosity within the mixed electrode material together with an enhanced contact of the conductive carbon additive and polyvinylidene fluoride polymer binder with and around the active material would ensure more effective electron transfer to the current collector, while better contact of the active material would ensure more homogeneous lithium ion diffusion across the active material, and consequently, reducing a localized stress on the material. This clearly shows that the electrode material mixture packing is absolutely essential for good electrochemical performance and individual electrode stability.

There is a corresponding increase in volumetric capacity and cycling stability with increased degree of calendering of the active 2D nanosheet material with binder and conductivity promoter necessary for achieving enhanced performance of the electrodes for future practical applications. The trend clearly shows that calendering improves the electrochemical performance and overall cycle life of the electrochemical cell and can be attributed to the combined contribution of lower polarization arising from mass transport limitations, and increased percentage of electronic and ionic connections within the electrode packed material mixture. The enhanced mechanical properties of the electrode after calendering would play an important role in further improvement of the capacity retention of the cell during cycling.

6.2.4 Performance of MoS_2 Nanosheets as Anode Materials for Sodium-Ion Batteries

Similarly to the previously studied employment of MoS_2 electrodes in Li-ion cells, an easy access and diffusion of larger sodium ions across the electrode material for more efficient sodiation of the electrode active material are highly desirable. This can be a particular game

changer as sodium is more abundant material, however, the larger atomic radius resulting in larger strains in electrode material upon intercalation are key limiting factors for Na-ion electrochemistry to overtake Li-ion in the market. Also, here the high surface to volume ratio of exfoliated MoS_2 nanosheets would offer similar advantages for hosting sodium ions such as a tight electrode/electrolyte interaction, a short diffusion path for Na^+ ions and electrons resulting in largely improved conductivity. Charge-discharge galvanostatic cycling of Na-ion half-cells at various current rates was performed on the same electrodes made of bulk, few-layer and single-layer MoS_2 active materials with conductive carbon additive and polymer binder. Their electrochemical rate performances are shown in Figure 6.14.

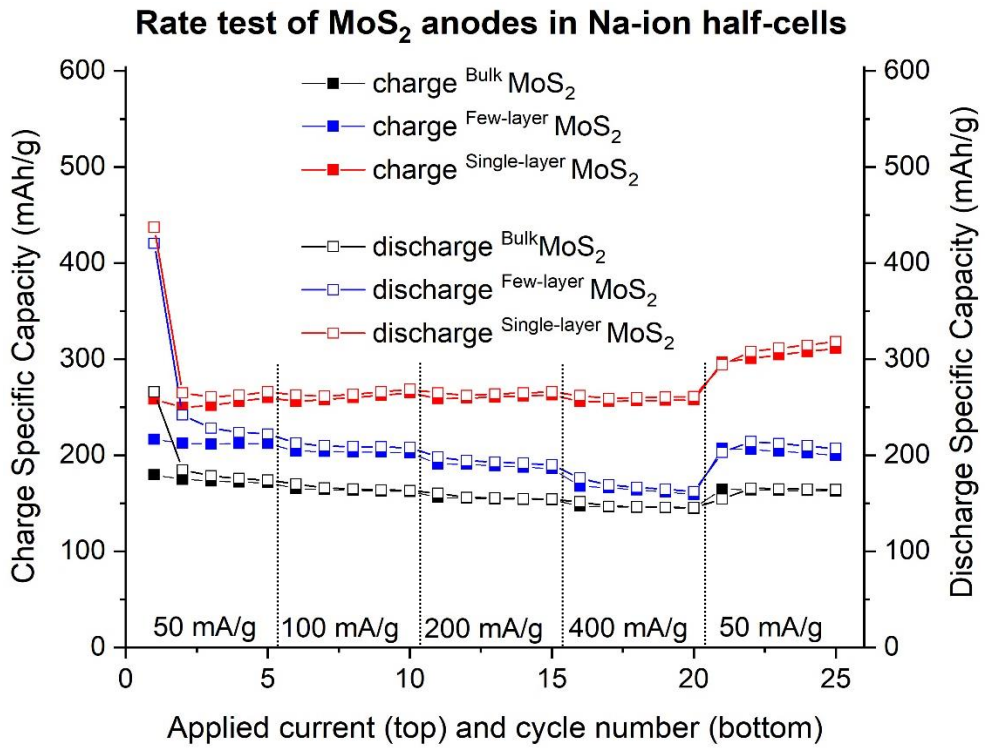


Figure 6.14 Galvanostatic rate performance of bulk, few-layer, and single-layer MoS_2 negative electrodes in Na-ion cells. Each electrode was cycled 5 times at applied currents of 50, 100, 200, 400 and again at 50 mA/g.

Testing was performed using the standard procedure with coin 2032 half cells, and was run on Maccor 3 instrument operated by Maccor software. Each electrode material was tested

three times and the average of each type of cells has been plotted and analysed. Like the Li-ion experiment, all three samples showed initial irreversible loss of capacity during the first cycle attributed to the formation of solid electrolyte interface on the surface of the electrodes.[662–664] $^{Bulk}MoS_2$ electrodes showed significantly less capacity fading and better rate performance compared to Li-ion experiment, however, it is important to note that the overall amount of achieved sodiation of the electrode material is considerably lower than in the case of lithiation too. This is in contrast to previous studies on the mechanism of sodium storage in MoS_2 that confirmed the Li-ion scenario of an initial intercalation process followed by a conversion reaction during further discharging.[680–682] While the intercalation process does not lead to a substantial change of the MoS_2 crystal structure, interlayer expansion was observed together with a shift of phase transition from 2H to 1T phase, a process that was documented in Li-ion chemistry as well. Further conversion reaction is attributed to a loss of the long-range crystalline structure of MoS_2 and formation of insulating Na_2S and Mo nanoclusters, where reversible conversion of these products is generally considered to be unfavourable. However, $^{Bulk}MoS_2$ electrodes in this project showed good capacity retention although smaller sodium storage capability. This could be a result of lower ionic conductivity as well as poorer electron transfer, and higher energy barrier for larger sodium ions to diffuse across the basal planes of the $^{Bulk}MoS_2$.

In the same manner with Li-ion results, electrodes made of few-layer thick nanosheets of MoS_2 showed slightly improved capacity as well as better cycling performance at lower current rates. This observation can be linked to the enhanced accessibility of sodium occupational sites in MoS_2 lattice and diffusivity of sodium ions across increased surface area of MoS_2 layers. Furthermore, it can also be associated with the presence of the more stable 1T metallic phase MoS_2. However, like the Li-ion cycling results, the capacity also faded with

increasing current rates and some irreversible capacity loss issue was observed. It is important to state that the overall capacity loss was much smaller than in Li-ion cells, however, this could be partially due to reduced sodiation amount creating smaller strain on the MoS_2 crystal structure. This could also be partially linked to the faster and easier diffusion of sodium ions leading to more dynamic intercalation and de-intercalation of the nanosheets.

Resembling the previous Li-ion results, the single-layer 1T metallic phase MoS_2 electrodes showed significantly higher capacity retention capability even at high current rates and a greater rate stability as well. The metallic character of the 1T phase of the $^{Single\text{-}layer}MoS_2$ incorporates a quick electron transfer while the increased in-plane bonds facilitate movement of sodium ions more readily without the additional structural strain and higher energy threshold barriers. In addition, larger exposed surface area and sodium-ion diffusion across the basal planes of the 1T phase also contribute to the much-improved cycling ability of the single layer MoS_2 electrode. Any present sulphur vacancies, structural defects or grain boundaries of neighbouring crystallites should not to be hindering diffusion.[669,670] Higher uniformity and increased mechanical strength of the one-molecule thick 1T phase MoS_2 nanosheets provides a considerable advantage when higher currents are used.[671] Thus, $^{Single\text{-}layer}MoS_2$ makes a highly promising candidate as the material of choice for sodium intercalation anodes, that can help the sodium-ion chemistry to reduce the technological gap in pursuit of the Li-ion battery market.

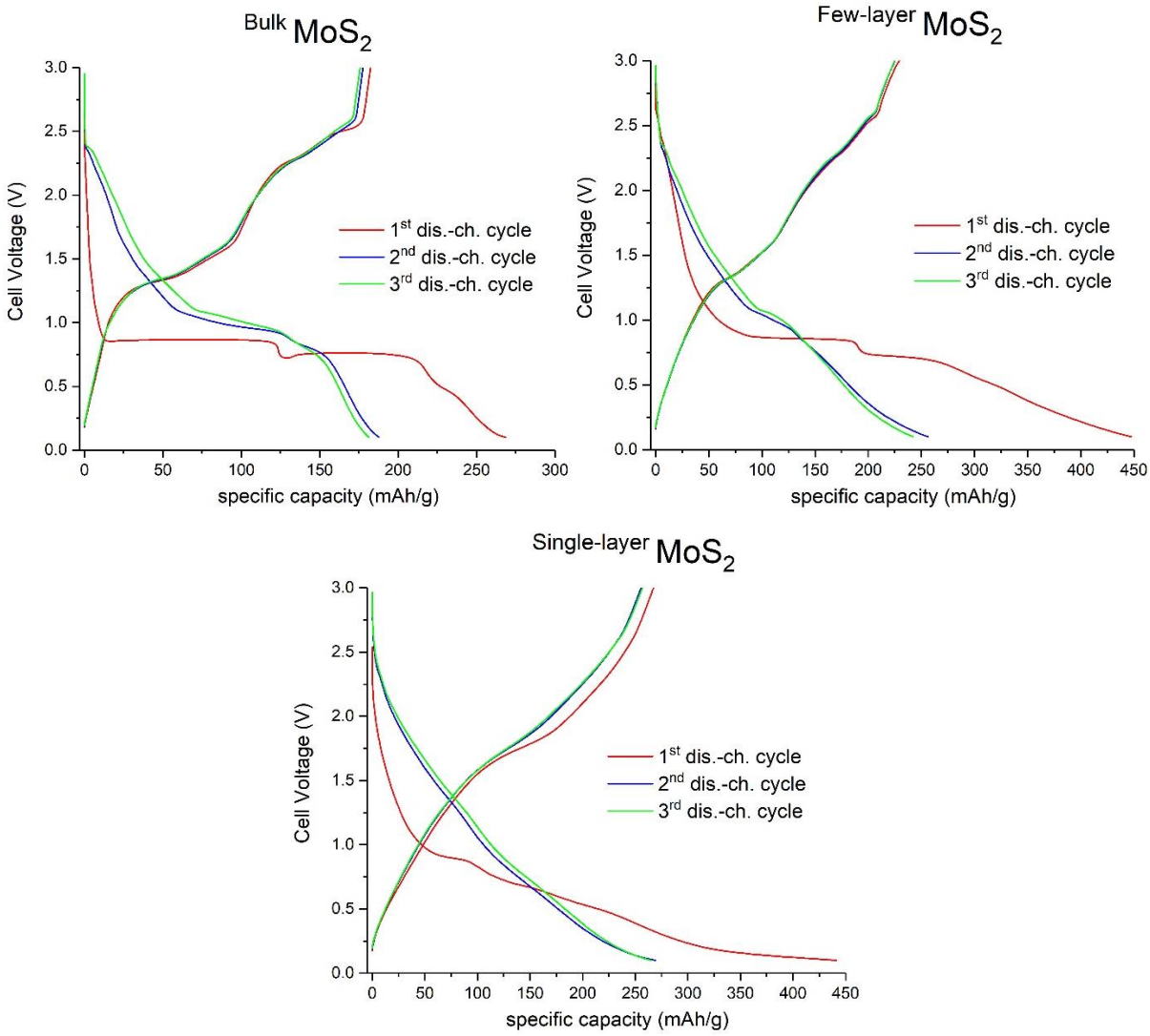


Figure 6.15 Voltage vs capacity curves of first three charge-discharge cycles at 50 mA/g current applied to bulk, few-layer, and single-layer MoS_2 electrodes in Na-ion cells.

Figures 6.15 and 6.16 show voltage vs capacity curves of first three charge-discharge cycles at 50 mA/g current, and fifth cycle at different current density rates, both applied to bulk, few-layer, and single-layer MoS_2 electrodes in Na-ion cells. In contrast to Li-ion, MoS_2 electrodes in Na-ion cells show discharge plateaus at 0.93V and 0.8V, however, it was suggested that sodium insertion of MoS_2 to Na_xMoS_2 over $x > 0.5$ led to distortion and the formation of zigzag-like MoS_2.[2,658,680,683,684] Voltage curves observed for $^{Bulk}MoS_2$, and $^{Few\text{-}layer}MoS_2$ nanosheets, however, showed slower degradation of the MoS_2 electrodes for both materials than it was previous seen in Li-ion cells. Moreover, there was no obvious degradation

observed for restacked $^{Single\text{-}layer}MoS_2$ nanosheets during different current rate cycles. It can be argued that the mechanism of stability and cycling ability to host Na^+ ions would follow the same trend. Sodium has a larger diameter than lithium which would result in higher strain on the sample, but it can be observed that sodiation of the electrodes remains smaller under identical testing conditions. Which also results in lower overall capacity of the MoS_2 electrodes in comparison to the Li-ion experiment.

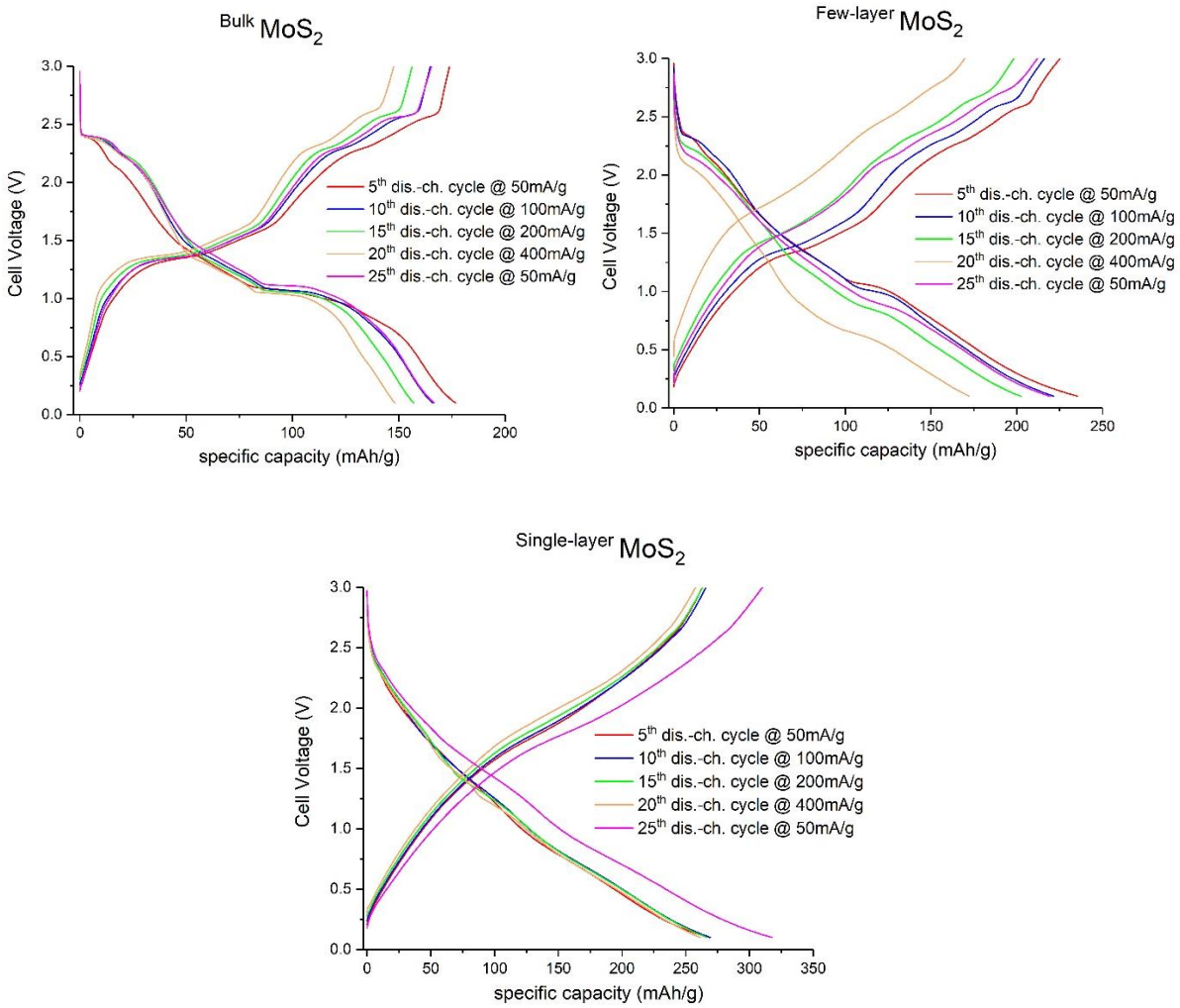


Figure 6.16 Voltage vs capacity curves of each fifth cycle at different applied currents. These curves show retention of capacity and indicate lithium storage mechanism in each MoS_2 active material in Na-ion cells.

6.2.5 Tin-doped MoS_2 Nanocomposite as Anode Materials for Lithium-Ion Batteries

In view of using the properties of single layers to avoid the restacking problem and to improve accessibility of individual monolayers to the environment, opening up the interlayer spacing by functionalization and pillaring of the 2D materials can address the stability and intercalation issues. In this regard, inserting large number of single atoms and small nanoclusters of elements with high lithium uptake in-between of the exfoliated nanosheets can accommodate larger portion of lithium. In addition, the increased interlayer spacings between the layers would provide better lithium-ion diffusion, which in turn would result in quicker lithiation and delithiation rates, and reduction of the charge barrier that the lithium ions have to overcome to get accommodated within the electrode active material. Tin-based (Sn) materials are strong candidates for high-capacity electrode materials for the next-generation lithium-ion batteries as they possess high volumetric capacity and relatively low working potential for alloying and de-alloying with alkali metal ions. The most significant drawback of Sn-based materials that keep them from wide employment in Li-ion batteries is the large volume change of Sn upon Li insertion and extraction leading to material pulverization and capacity loss. A sophisticated nanostructure design could mitigate the volume change of Sn and improve diffusion of Li^+ ions and electrons across the basal planes to the current collector.[685] $1T^{\text{Single-layer}}MoS_2$ have the potential to accommodate Sn volume changes while they can effectively facilitate electron transfer and simultaneously protect Sn nanoparticles from joining together into bulk during battery cycling.

Unpaired electrons at unsaturated and defect sites on basal planes and edges of individual nanosheets can be utilised for functionalization or doping of the MoS_2 material. Single atom doping on single-layer MoS_2 nanosheets was successfully demonstrated by Liu et.al., who

employed Co-doped single-layer MoS_2 as highly performing catalyst in hydrodeoxygenation.[554] However, these were predominantly 2H phase monolayers. As exfoliation of the bulk material promotes the number of unpaired electrons and sulphur vacancies on basal planes, these are targeted by electron deficient positively charged species. The cationic species are stabilised on the basal planes via electron affinity to the substrate and remain stable. When impregnating solution is diluted enough, further nucleation to nanoparticles can be surpassed. It is also expected that the larger number of exposed sulphur vacancies and other defect sites would allow further uptake of positively charge precursor species, which in turn can lead to higher loadings on the exfoliated single-layer material. However, it can be very delicate to find the right balance in doing so.

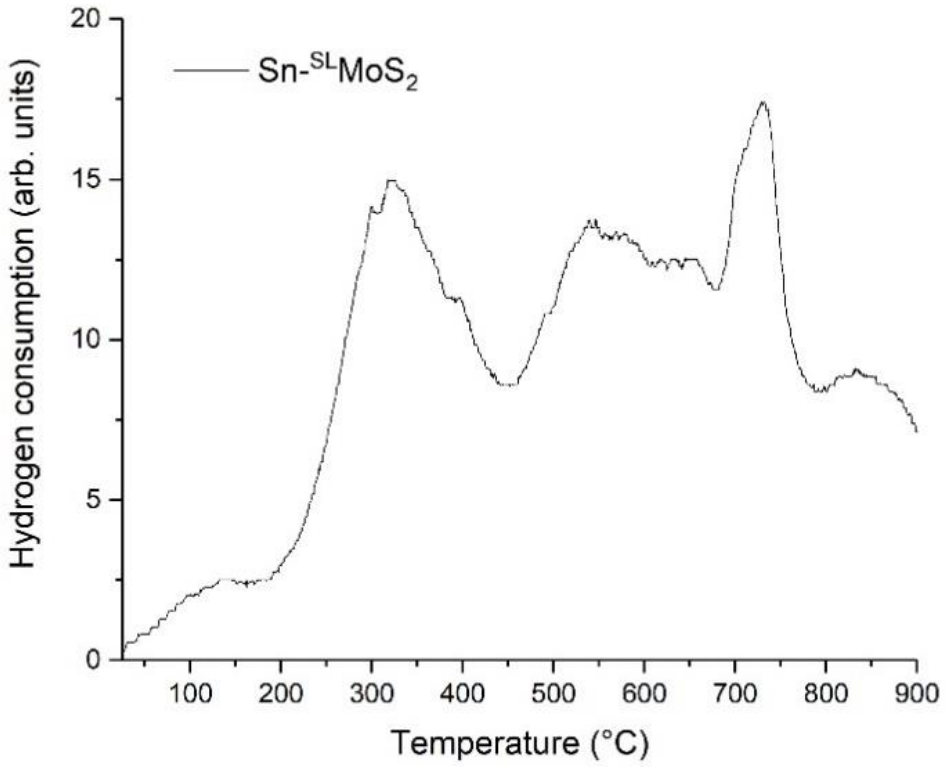


Figure 6.17 Temperature-programmed reduction (TPR) of Sn doped single-layer MoS_2.

One of the aspects of doping is to adsorb species active in accommodating lithium on the surface of the MoS_2 nanosheets. It is important to note that adsorbed precursor species are

often in their oxidized form. To promote reduction of the precursor species to their metallic state, sodium borohydride is used as a reducing agent. However, this often is not enough and further reduction under a flow of reducing gas and elevated temperatures is needed. To investigate the reduction temperature of the tin species, temperature programmed reduction was employed using hydrogen flow as a reducing agent.

First of all, it is noteworthy that reduction of the expected oxidized species of tin oxide would happen at very high temperatures of 1600°C.[686,687] However, high temperatures are known to cause a phase change of the metallic 1T MoS_2. High temperatures are also generally known to cause sintering into larger nanoparticles. Therefore, a reduction temperature study using hydrogen gas was performed to identify a temperature threshold compromise for reducing oxidized species. Given the assumption that they would be either single or several molecule large features on the surface, lower reducing temperatures might do the trick. Figure 6.17 shows TPR profiles of Sn-doped single-layer MoS_2 sample.

The TPR profile of Sn-doped single-layer MoS_2 shows a dominant peak at around 320°C. The large hydrogen consumption peak can be associated with reduction of the single entity oxidised tin species. There also are two other reduction peaks that can be observed at around 550°C and 750°C. The 750°C peak is generally associated with reduction of larger SnO_2 structures, while the broad peak at 550°C can potentially be related to a phase change of the 1T MoS_2. Taking into account the preservation of the metallic 1T phase and the observation of the main hydrogen consumption peak at 320°C, reduction calcination temperature for Sn-doped single-layer MoS_2 samples was decided to be tested by step calcination at increasing temperature and monitoring by PXRD.

Heating of the samples was set as follows; first the freshly deposited dopant on $^{Single\text{-}layer}MoS_2$ was examined by PXRD, then submitted to mild calcination at 80°C for 2 hours under continuous flow of 5 % hydrogen in argon reducing gas. This was followed by another PXRD scan and submitting the sample to calcination at 300 °C for 2 hours under continuous flow of 5 % hydrogen in argon reducing gas. As before, the sample was examined by PXRD and then submitted for further calcination at 400°C for 2 hours under continuous flow of 5 % hydrogen in argon reducing gas. The resulting XRD patterns are summarized in Figure 6.18.

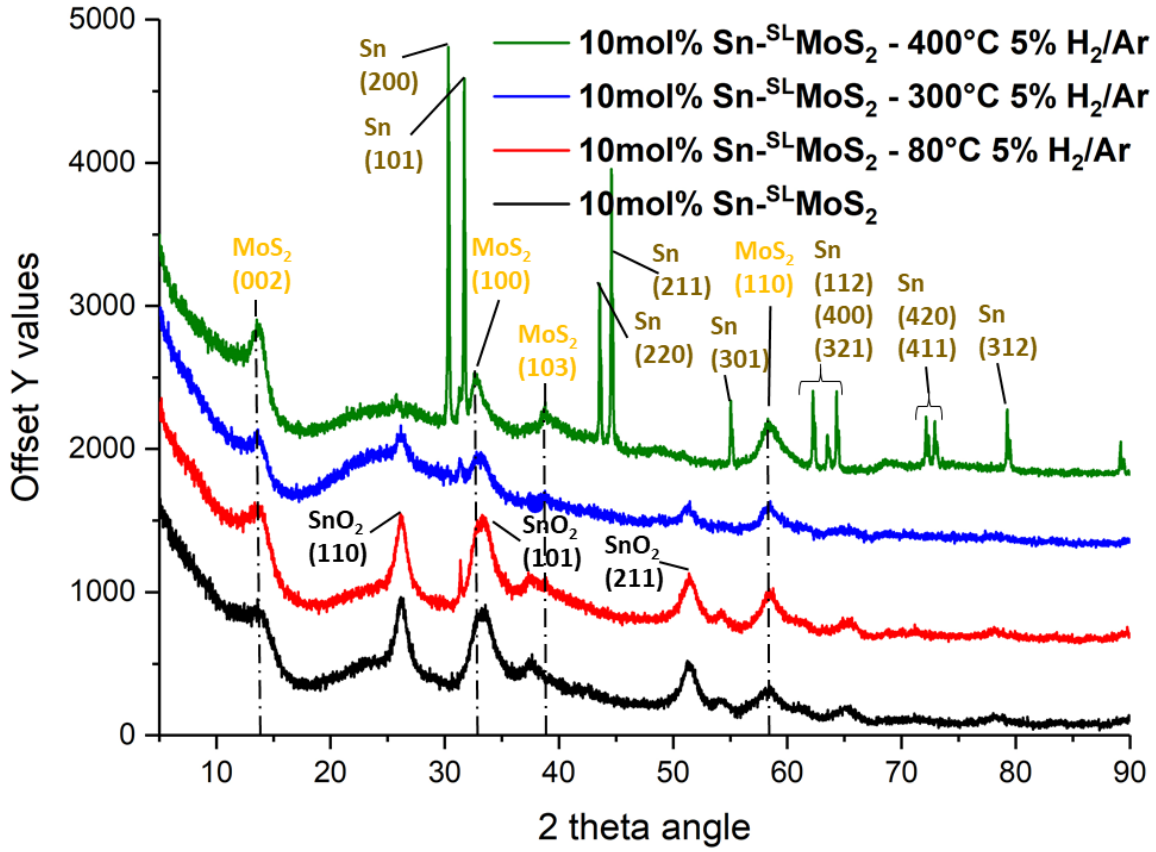


Figure 6.18 PXRD patterns as-prepared and calcined Sn doped single-layer MoS_2 samples.

Sn-doped and restacked single-layer MoS_2 nanosheets showed typical patterns observed for 1T phase $^{SL}MoS_2$ samples. Contrary to expectation, no shift in the 2θ angle to lower values that would refer to increased interlayer spacing was observed. The formation of small SnO_2 nanoparticles can be determined from the pattern of uncalcined sample as characteristic

(110), (101) and (211) reflections of SnO_2 were observed. This shows that tin species are largely oxidized and many formed small nanoparticles. Submitting of this sample to a mild heat of 80°C under reducing 5% hydrogen gas had no impact on the structure of the nanosheets or tin oxide features. However, calcination at 300 °C under the same reducing conditions revealed reduced intensity of SnO_2 but no obvious tin metal peaks were observed. This result suggested that 300 °C temperature was not sufficiently high to help achieve full reduction of the tin oxide into metallic tin single atoms and nanoparticles. In fact, this supports the TPR result where the reduction peak highly overlaps 300 °C but the maximum is reached at around 320 °C. Increasing temperature to 400 °C under the same reducing conditions and time revealed a complete reduction of SnO_2 into metallic tin nanoparticles but unfortunately also their growth, as the new sharp peaks associated with metallic tin confirmed.

In order to investigate the stability of the 1T phase upon doping with tin, and the impact of the calcination temperature and reduction conditions, Raman spectra of non-calcined doped $^{\text{Single-layer}}MoS_2$ and their counterparts calcined at 400°C under flow of 5% hydrogen in argon were recorded and compared to single-layer 1T phase precursor MoS_2 nanosheets. Raman spectra of all samples are displayed in Figure 6.19. It is easy to see that all characteristic Raman modes of E_{1g}, and low-frequency phonon modes J_1, J_2 and J_3 were observed in all samples. This confirmed that there was no phase change of the metallic octahedral phase upon any of the treatment and proved the 1T phase to be highly stable under these reaction conditions.

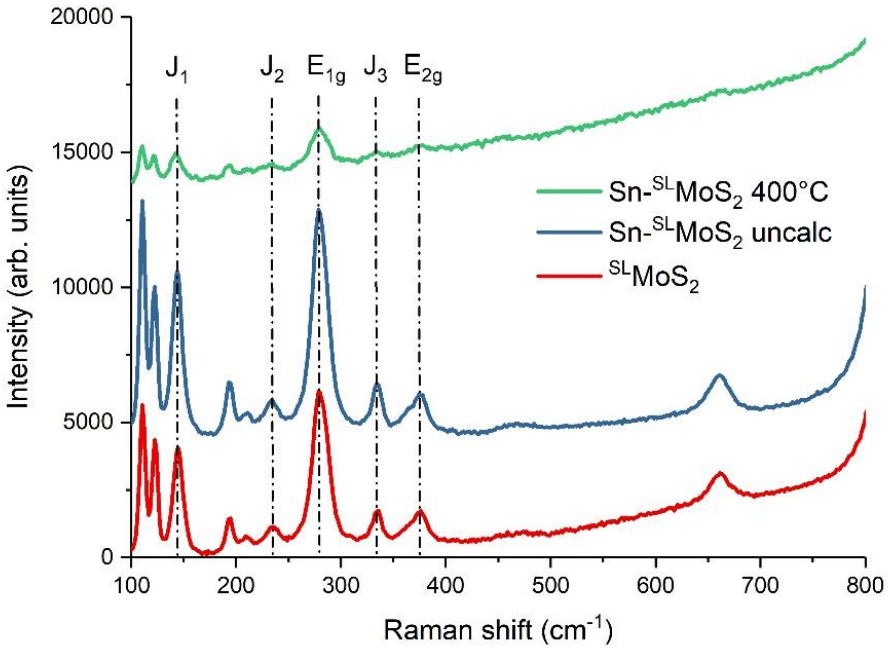


Figure 6.19 Raman spectra showing Sn-doped and undoped single-layer MoS_2 samples.

XPS spectra of both samples was recorded to provide further insight into the samples chemical composition and to account for the amount of the dopant deposited on single-layer MoS_2 sample. Figure 6.20. shows Sn 3d XPS region of both doped-samples before calcination. The Sn 3d region signal appears at 487 eV and together with the valence band signal indicating the presence of SnO_2 species and corresponds to XRD observation. Elemental analysis of Sn-doped single-layer MoS_2 determined surface tin content in the sample as 9.3 wt.%.

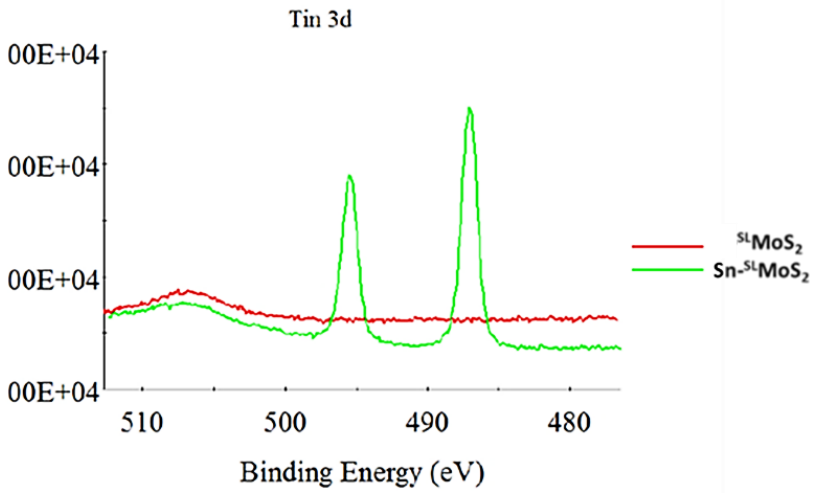


Figure 6.20 Sn 3d region of XPS spectra of Sn-doped single-layer MoS_2 samples.

A scanning transmission electron microscope (STEM) enables very high-resolution electron imaging capable to depict individual atoms and molecules, and makes a highly attractive tool to study materials elemental structure and an ideal probe for detecting individual Sn single atoms on the single-layer MoS_2 surface. Figure 6.21 shows high-resolution STEM imaging of the uncalcined Sn-doped MoS_2 nanosheets. Single atoms sitting on the basal planes were observed, and some of the typical positions are highlighted in the top left image. In order to visualize the single atom presence, blue shading was used to improve contrast between atoms. It has been previously demonstrated that Pd single atoms can be stabilised on basal planes of MoS_2 either as a sulphur site substitute atom or at a Mo atop site.[564]

Stabilisation of single atomic unit on basal planes of MoS_2 was aimed to be achieved by reduction of the oxidized precursor species and reducing the level of formation of SnO_2 species. Single Sn atoms were indeed observed as both a sulphur site substitute atom and as atop site above Mo within the lattice. Illustration of these atomic arrangements from the top view perspective is presented in Figure 6.21. Line profiles of both arrangements identified in the images were analysed, and each assigned to either the atop or the substitute sites. The atop site line profiles showed an added extra atomic feature along the Mo and S repetitive pattern within the lattice. The substitute site can be determined by an added height to the pattern of S and Mo and such feature is shown by the corresponding line profile. Thus, it can be concluded that impregnation method for depositing single Sn moiety on MoS_2 nanosheets was partially successful, although it has to be highlighted that the presence of SnO_2 nanoparticles was clearly identified by XRD method.

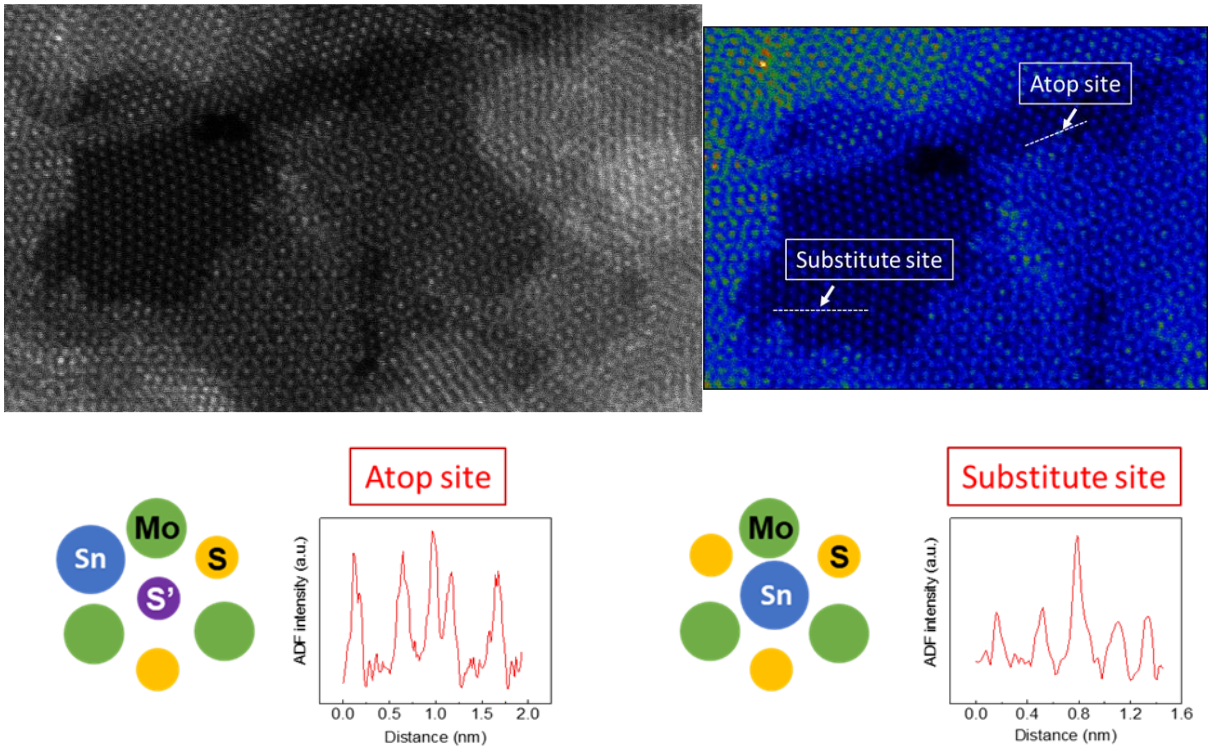


Figure 6.21 STEM images and illustration of preferred stable sites of Sn single atoms on single-layer MoS_2 basal planes. Line profiles confirm the location and presence of Sn single-atom sites.

The galvanostatic charge-discharge (specific capacity vs. voltage) cycling test of Sn-doped $^{\text{Single-layer}}MoS_2$ samples measured at 50, 100, 200, 400 and again 50 mA/g in the voltage range of 0.01–3.00 V (*vs.* Li/Li^+) are shown in Figure 6.22. The experiment was performed using the same standard procedure involving the coin 2032 half cells and using the Maccor 3 galvanostat. The average performance of three repeated cycling experiments per each sample at different current rates is shown. As seen previously, both samples showed initial irreversible loss of capacity during the first cycle, linked to the formation of solid electrolyte interface on the surface of the electrode material. The use of elemental Sn nanoparticles is preferred over SnO_2 nanoparticles as they can, in principle, eliminate the irreversible capacity loss associated with the decomposition of tin compounds in the first lithiation cycle. However, the preparation of nanosized Sn particles is difficult.[688]

The theoretical specific capacity of Sn is 993.4 mAh/g, according to the reversible reaction $Sn+xLi^{+}+xe^{-}\leftrightarrow Li_xSn$ ($0\leq x\leq 4.4$).[689] In contrast, the theoretical specific capacity for SnO_2 active material is 780 mAh/g, and covers both conversion and alloying/dealloying reactions.[685] It should be noted that the conversion reaction of SnO_2 to Sn is mostly considered irreversible but SnO_2 nanostructures have been found to give specific capacity as high as 1,484 mAh/g.[690,691] However, metallic Sn formed from SnO_2 result in large volume changes in the range of 250% in lithiation and delithiation processes.

Sn-doped $^{Single\text{-}layer}MoS_2$ uncalcined nanocomposite material possesses large number of SnO_2 species resulted in an initial specific capacity of 1192 mAh/g that is less than that of pure $^{Single\text{-}layer}MoS_2$ and more than that of SnO_2. However, this initial capacity suffered a drop to 879 mAh/g and kept losing its capacity in a very dramatic way even at low current rates of 50 mA/g. This is in a stark contrast to expectations of enhances interlayer spacing for easier Li-ion diffusion, accommodating structural strain within Sn species across the basal planes of $^{Single\text{-}layer}MoS_2$ and facilitating increased electron transfer. It is clear that the opposite effect took place and instead SnO_2 species must have reacted during its conversion together with MoS_2. Based on the widely accepted chemical reaction of SnO_2 with lithium ions involving a two-step conversion mechanism of $SnO_2 + 4Li^{+} + 4e^{-} \rightarrow Sn + 2Li_2O$ and $Sn + xLi^{+} + xe^{-} \rightarrow Li_xSn$ ($0\leq x\leq 4.4$), it appears the Li_2O formation could be highly unfavourable for stability of $^{Single\text{-}layer}MoS_2$ nanosheets.[692] This shows that $^{Single\text{-}layer}MoS_2$ did not function as a physical barrier to protect SnO_2 species from stress-induced pulverization, quite the opposite SnO_2 appeared to weaken the improved stability and durability of the $^{Single\text{-}layer}MoS_2$ electrode.

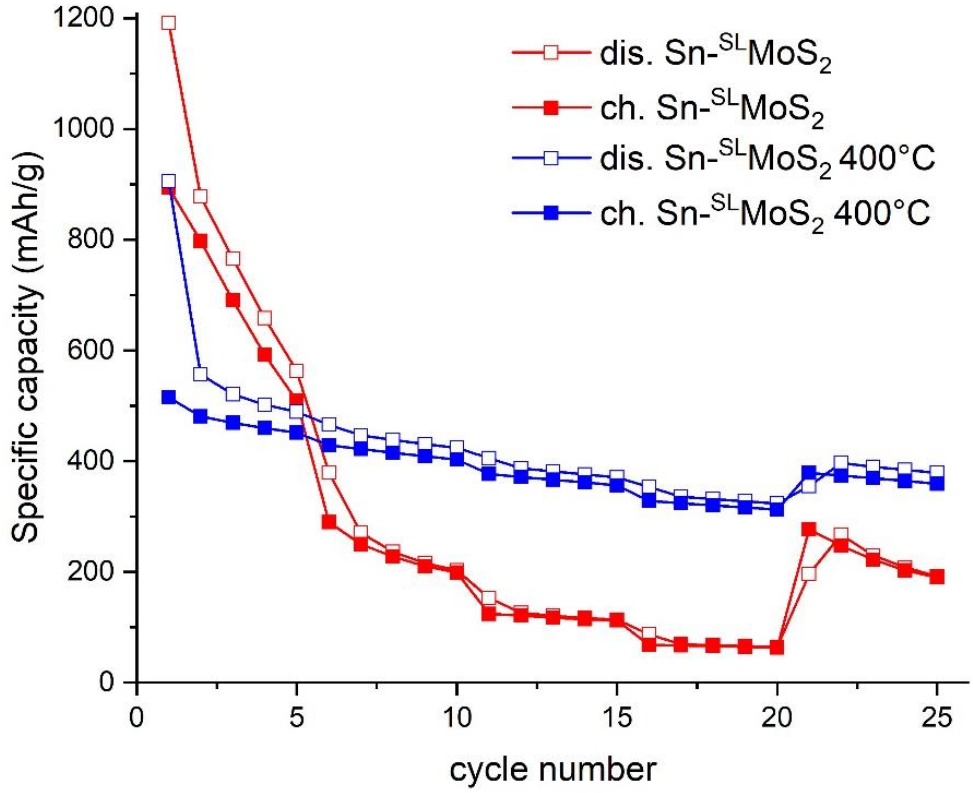


Figure 6.22 Galvanostatic rate performance of Sn-doped single-layer MoS_2 negative electrodes in Li-ion cells. Each electrode was cycled 5 times at applied currents of 50, 100, 200, 400 and again at 50 mA/g.

On the other hand, the Sn-doped $^{Single\text{-}layer}MoS_2$ nanocomposite calcined at 400 °C showed significant improvement in the cycling ability compared to the non-calcined SnO_2 on $^{Single\text{-}layer}MoS_2$. It retained its capacity in every subsequent cycle after the initial drop in capacity typically associated with SEI formation, where the capacity dropped to about 550 mAh/g. Remarkably, the reversible capacity can be observed even when the current rate cycling is higher, indicating that the unique structure of Sn-doped $^{Single\text{-}layer}MoS_2$ nanocomposite can to an extent preserve the integrity of the electrode material. However, the overall capacity of the system was again much lower than what it would be expected from the combination of two high capacity materials.

Figure 6.23 depicts voltage vs capacity curves of the first three charge-discharge cycles of both Sn-doped MoS_2 nanocomposites, however, it is not fully clear what would cause this unexpected electrochemical storage behaviour, nevertheless the impact on the cycling stability of $^{SL}MoS_2$ can be seen. However, lithiation of tin species into tin-lithium alloy can be seen within the region of 0.9 to 0.6 V and several smaller plateaus indicate several stages of lithiation and delithiation of tin.

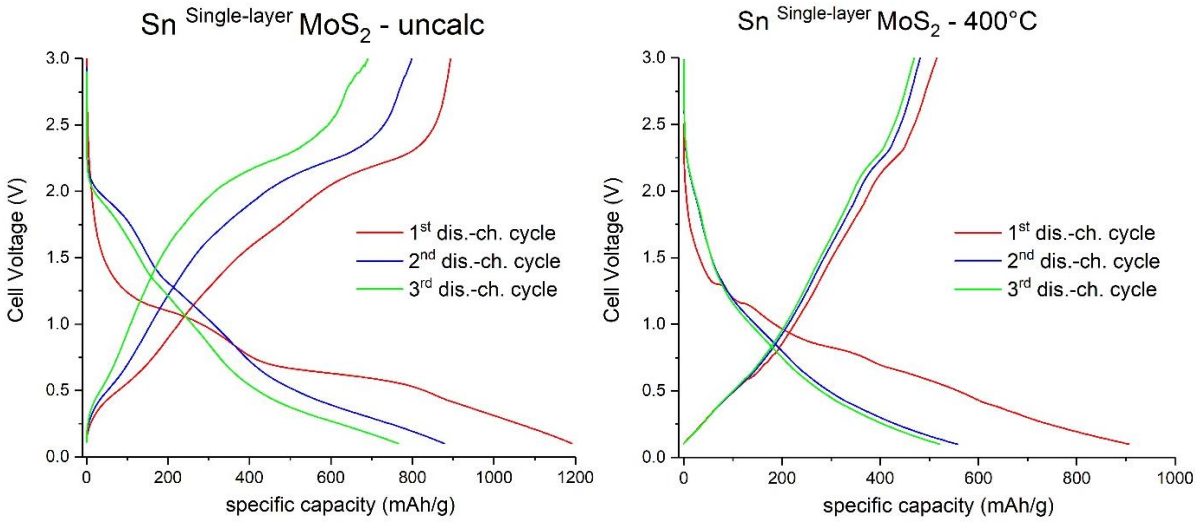


Figure 6.23 Voltage vs capacity curves of the first three charge-discharge cycles at 50 mA/g current applied to Sn-doped single-layer MoS_2 electrodes in Li-ion cells.

6.3 Conclusion

The aim of this work described within this chapter was to synthesise, characterise and analyse the performance of MoS_2 nanosheets in the application of battery energy storage. Few-layer thick MoS_2 nanosheets were synthesized via a sonic wave assisted top-down physical exfoliation method using hydrazine penetration in the planes of bulk MoS_2 and consequent decomposition into N_2 and H_2 gases. This yielded a mixture of stable 2H and 1T phases across and within individual nanosheets. Single-layer MoS_2 nanosheets were synthesized through treatment of a bulk MoS_2 precursor with organolithium and followed by sonic wave assisted

top-down chemical exfoliation method and reaction with water media, where exfoliated monolayers are suspended.

Exfoliated nanosheet MoS_2 nanosheets in this work were thoroughly characterized with analytical techniques for their properties using HRTEM, STEM, BET, EPR, XPS and Raman spectroscopy and metallic and semiconducting phases of bulk, few-layer and single-layer nanosheets were elucidated. XPS and Raman together with atomic arrangements in STEM confirmed predominance of 1T phase in single-layer MoS_2, while a proportion of 1T phase and 2H phase was shown in physically exfoliated few-layer MoS_2. All three materials were tested as negative electrodes in Li-ion and Na-ion coin cells and outstanding improvement in capacity retention and structural stability towards lithiation and de-lithiation, and higher density current rate performance were shown for exfoliated nanosheets, and the metallic single-layer 1T phase in particular, in both alkali-ion battery cells.

Their improved structural stability and electrochemical performance in lithiation and de-lithiation of the nanosheets were further analysed with help of highly sophisticated characterisation tools such as short, monochromatic, high intensity collimated beam pulse synchrotron XRD coupled with state of the art galvanostatic set-up, and in the case of single-layer MoS_2, also with phase-contrast of high-resolution ADF C_s-STEM with image reconstruction and Wigner-distribution deconvolution ptychography tool and coupled with elemental analysis tool EELS. The former revealed structural stability and crystal structure retention under large amount of lithiation of the material contrasting with materials degradation of the few-layer MoS_2. Small electron beam intensity dose was applied for latter STEM ptychographic imaging reconstruction of lithiated monolayer MoS_2, where and a crystal lattice resolution was achieved. This was particularly difficult due to the volatility of lithium

under electron beams. A high degree of compositional sensitivity to both heavy molybdenum and light lithium and sulphur elements simultaneously at atomic resolution was achieved and lithium presence and location within the crystal structure leading to 1T′ metastable phase distortion of Li_xMoS_2 of the metallic 1T phase was demonstrated. The lithium intercalation modifies the MoS_2 structure due to the decrease of binding energy between individual elements and formation of 1T' phase domain of low symmetry stabilized by the presence of lithium ions.

Tin based materials possess high volumetric capacity and relatively low working potential for alloying and de-alloying with alkali metal ions, however, they suffer from large volume changes of Sn upon alloying with lithium leading to material pulverization and consequently capacity loss, and prevent them from wider employment in commercial battery cells. In view of the successful Pd doping of 1T phase MoS_2 in the catalysis section 5, as well as in light of the structural flexibility and stability of the 1T phase and its conductive nature, it was adopted for functionalization and pillaring with tin species to accommodate the stability linked to volume expansion of tin.

The nanocomposite Sn-doped single-layer MoS_2 material was synthesized by doping and followed by reduction of tin species with sodium borohydride, and additionally also via reductive heat treatment. As-prepared as well as heat-treated nanocomposites were thoroughly characterized by XRD, XPS, Raman spectroscopy, TPR and STEM imaging to reveal successful synthesis of the nanocomposites, and presence of SnO_2 species and metallic Sn species respectively. STEM showed single Sn atoms as well as larger nanoparticles being present within the sample. Single Sn atoms were observed as both a sulphur site substitute atom or as atop site above Mo within the lattice. XRD and XPS further showed how Sn species

reduced from oxide to their metallic form upon reductive heat treatment with hydrogen. Raman spectroscopy together with STEM imaging confirm that the nature of MoS_2 1T phase was preserved.

This sophisticated nanocomposite design, however, did not follow the promising anticipation and did not lead to mitigation of the volume change issues caused by Sn. In addition, the increased interlayer spacing with Sn species appeared to affect the extraordinary electrochemical performance of the 1T phase single-layer MoS_2 seen previously. This was especially true for uncalcined nanocomposite with SnO_2 species, where single-layer 1T phase MoS_2 did not function as a physical barrier to protect SnO_2 species from stress-induced pulverization, while SnO_2 emanated to weaken the stability and durability of the $^{SL}MoS_2$ host material.

In contrast, Sn-doped $^{SL}MoS_2$ nanocomposite calcined at 400 °C under 5 % hydrogen gas in argon showed significant improvement in the cycling ability compared to the the non-calcined SnO_2 on $^{SL}MoS_2$ indicating that the combined structure of Sn-doped $^{SL}MoS_2$ nanocomposite can lead to a well-performing electrode material. However, the overall capacity of the system resulted in lower lithium uptake and smaller overall capacity when compared to the original ambition and expectations from combining high capacity Sn species with highly-promising metallic 1T phase MoS_2 2D nanomaterial.

Tables 6.2 and 6.3 compare the performance of MoS_2 samples tested in this work with some of the best performing MoS_2 electrode materials in Li-ion and Na-ion batteries recently published in the literature. As seen, single-layer MoS_2 with 1T exposed phase depict comparable specific capacities at low current densities.

Table 6.2 Performance comparison of MoS_2 samples tested in this work with some of the best performing MoS_2 electrode materials in Li-ion batteries recently published in literature.

Material structure	MoS_2 Phase	Specific capacity	At current density	References
Bulk MoS_2	2H (Semiconductor)	736 mA·h·g^{-1} 91 mA·h·g^{-1}	0.05 A·g^{-1} 0.4 A·g^{-1}	This work
1T few-layer MoS_2	2H and 1T MoS_2	908 mA·h·g^{-1} 165 mA·h·g^{-1}	0.05 A·g^{-1} 0.4 A·g^{-1}	This work
1T single-layer MoS_2	1T (Metallic)	1167 mA·h·g^{-1} 1007 mA·h·g^{-1}	0.05 A·g^{-1} 0.4 A·g^{-1}	This work
Sn-doped 1T ^{SL} MoS_2 untreated (SnO_2 content)	1T (Metallic)	898 mA·h·g^{-1} 87 mA·h·g^{-1}	0.05 A·g^{-1} 0.4 A·g^{-1}	This work
Sn-doped 1T ^{SL} MoS_2 H_2 treated 400°C	1T (Metallic)	557 mA·h·g^{-1} 353 mA·h·g^{-1}	0.05 A·g^{-1} 0.4 A·g^{-1}	This work
Nanotube-like MoS_2 over graphene	1T (Metallic)	666 mA·h·g^{-1}	3.5 A·g^{-1}	Nanoscale, 9, 21, 6 2017[693]
MoS_2 over carbon cloth	1T (Metallic)	1789 mA·h·g^{-1} 853 mA·h·g^{-1}	0.1 A·g^{-1} 1 A·g^{-1}	Journal of Materials Chemistry A, 5, 27, 7 2017[694]
1T MoS_2 + ($NiMoO_4$)	1T (Metallic)	941 mA·h·g^{-1}	0.5 C	ACS Applied Materials & Interfaces, 11, 47, 11 2019[695]
Pure MoS_2	1T (Metallic)	1150 mA·h·g^{-1} 935 mA·h·g^{-1}	A·g^{-1} 5 A·g^{-1}	Advanced Energy Materials, 8, 15, 5 2018[696]

Table 6.3 Performance comparison of MoS_2 samples tested in this work with some of the best performing MoS_2 electrode materials in Na-ion batteries recently published in literature.

Material structure	MoS_2 Phase	Specific capacity	At current density	References
1T few-layer MoS_2	2H and 1T MoS_2	228 mA·h· g^{-1} 176 mA·h· g^{-1}	0.05 A· g^{-1} 0.4 A· g^{-1}	This work
1T single-layer MoS_2	1T (Metallic)	318 mA·h· g^{-1} 262 mA·h· g^{-1}	0.05 A· g^{-1} 0.4 A· g^{-1}	This work
Bulk MoS_2	2H (Semiconductor)	185 mA·h· g^{-1} 151 mA·h· g^{-1}	0.05 A· g^{-1} 0.4 A· g^{-1}	This work
MoS_2-graphene-MoS_2	1T (Metallic)	313 mA·h· g^{-1} 175 mA·h· g^{-1}	0.05 A· g^{-1} 2 A· g^{-1}	Advanced Functional Materials, 27, 40, 10 2017[697]
Dual phase of 2H and 1T MoS_2	2H and 1T MoS_2	300mA·h· g^{-1} 220mA·h· g^{-1}	0.5 A· g^{-1} 2 A· g^{-1}	Journal of Materials Chemistry A, 8, 4, 1 2020[698]
MoS_2 and amorphous carbon	2H and 1T MoS_2	563 mA·h· g^{-1} 485 mA·h· g^{-1}	0.2 A· g^{-1} 2 A· g^{-1}	ACS Nano, 12, 12, 12578 2018[699]

6.4 Future Outlook

In summary, bulk, few-layer and single-layer MoS_2 nanosheets were synthesized and analysed for their suitability as an electrode active material in Li-ion and Na-ion batteries. Exfoliated nanosheets showed particularly convincing electrochemical stability and how lithium diffusion and local strains influence it. Nevertheless, further improvements could be made via sophisticated engineering of these 2D nanomaterials into targeted 3D nanocomposite structures with further enhanced electrochemical properties in order to improve the lifetime

and performance capabilities of present day battery cells. Pillaring and doping through sulphur vacancies within the MoS_2 basal planes are the two most obvious starting points. Unfortunately, combining tin with MoS_2 nanosheets did not result in synergistic enhanced properties, however, electron conducting materials such as conjugated organic molecules and single metal atoms could revolutionise how we create essential parts of current battery systems.

General Conclusions

Throughout this thesis, the main objectives of the research have been on synthesis, characterization, and successful applications of developing novel nanosized inorganic structures in order to gain a better understanding on how they can contribute to a more efficient and more environmentally friendly world.

The first part of this thesis concentrated around development of solid acid catalyst replacement for highly corrosive mineral acids or solvent swellable polymeric acids. Very small titania nanoparticles were successfully synthesized from a titanium precursor and characterized for their physical properties and Lewis acidity. Functionalisation with sulphate species introduced highly Brønsted acidic protons on the surface of as-prepared small nanoparticles. Heat treatment resulted in an increase in crystallinity which led to highly stable and superacidic nanoparticles. These nanoparticles were characterized by a sensitive characterization tool of probe-assisted NMR spectroscopy and shone light onto the amount and strength of acid sites in sulphated titania. Sulphated titania nanoparticles calcined at 450 °C outperformed sulphated commercial titania and even highly acidic commercial polymeric resin Amberlyst-15 in a model esterification reaction of levulinic acid. Lewis acidity was tested in pyruvaldehyde hydrolysis to lactic acid and demonstrated the amount and strength of Lewis acid sites of the novel nanoparticulate titania.

In later chapters, 2-dimensional nanosheet materials have been studied for their appealing properties as an active and selective catalysts and as a battery active material. These were prepared by more robust top down methods with potential to scale up for various industrial interest. A sequence of steps was put in place to optimize the yield and each sample was characterized for their morphology and potential physicochemical properties.

The first series of materials synthesized via top down method was chemical exfoliation of layered dichalcogenides, which showed a great potential for functionalization via induced defect sites, or scaling up the synthesis process for large scale manufacturing. In addition, sequential separation and filtration method was improved to yield larger quantities and higher sample purity. Overall, the single-layer MoS_2 samples were almost entirely made of monolayers, however, it was important to achieve a stable metallic phase for better electronic properties, particularly for use as catalyst support or electrode material.

Palladium chemistry is an essential part of everyday manufacturing and catalytic processes and heterogeneous Pd catalysts are becoming more popular due to their benign environmental aspects and recyclability. Palladium catalysts can be further tailored for specific catalysed reactions either by increasing their surface to volume ratio, alloying them with another substance, or by coupling them with a catalyst support material. Electronically conducting, cheap and non-toxic single-layer MoS_2 nanosheets with large number of defect sites where single Pd atoms and nanoparticles can be stabilised were synthesized and tested with great success in a series of industrially important reactions such as organic coupling reactions or partial hydrogenations of unsaturated acetylenes. This was achieved by introducing defect sites within the lattice and perturbation of the atomic arrangement in the more abundant semiconducting 2H phase. MoS_2 nanosheet supports facilitate electron transfer in and out of Pd active sides, and stabilisation of very small Pd nanoparticles and single atoms further increased their reactivity. However, it can also hinder certain reactions and become selective towards one type of product such as partial hydrogenation reaction. This catalyst was particularly performing well in non-aqueous solutions, but it showed good activity in water-based mixtures as well, making it an appealing system for wider applications.

Finally, the MoS_2 nanosheets showed enhanced cycling stability and capacity as compared to the bulk material. Further functionalisation with metal nanoparticles, single atoms and pillaring agents did not seem to yield the desired improved characteristics of these newly engineered nanostructures. Further experiments are required to explore this area.

Future perspectives

The research of this thesis offers a basis for the understanding of tailoring various nanomaterials for use in a range of heterogeneous catalytic reactions and in energy storage media, all highly sought after in pursuit of green chemistry and a better environment. There is scope for each material to reach further applications and studying each individual scenario could lead to a discovery of further unknown capabilities of these novel nanomaterials. In particular, further attention could be paid to extending the study of solid acids in more demanding but economically very attractive transesterification reactions. Optimisation of Pd content on MoS_2 nanosheets and their activity in organic coupling reactions beyond Suzuki and Heck could be of great interest. And last but not least, stacking single layer MoS_2 with other layered materials as 3D nano-structural composites to reach even higher current density and larger specific capacities of electrodes in pseudo capacitors and batteries is worthy of exploration.

References

1 S. Lubik, *Nanotechnol. Perceptions*, 2008, **4**, 225–238.

2 T. Eldridge, *Nanotechnol. Now*, 2014, **6**, 1501937.

3 G. A. Ozin, A. Arsenault and L. Cademartiri, *Nanochemistry: A Chemical Approach to Nanomaterials*, RSC Publishing, 2nd editio., 2008.

4 C. McGovern, *Nanotechnol. Perceptions*, 2010, **6**, 155–178.

5 R. Mas-Ballesté, C. Gómez-Navarro, J. Gómez-Herrero and F. Zamora, *Nanoscale*, 2011, 3, 20–30.

6 C. K. Chua, A. H. Loo and M. Pumera, *Chem. - A Eur. J.*, 2016, **22**, 14336–14341.

7 O. Lamiel-Garcia, A. Cuko, M. Calatayud, F. Illas and S. T. Bromley, *Nanoscale*, 2017, **9**, 1049–1058.

8 B. P. Isaacoff and K. A. Brown, *Nano Lett.*, 2017, **17**, 6508–6510.

9 M. Rabiee, *Introduction to Nanomaterials in Medicine*, IOP Publishing, 2019.

10 M. Soni, P. Mehta, A. Soni and G. K. Goswami, *IOSR J. Biotechnol. Biochem.*, **4**, 78–83.

11 S. Kanchi and S. Ahmed, *Green metal nanoparticles : synthesis, characterization and their applications*, .

12 M. S. Chavali and M. P. Nikolova, *SN Appl. Sci.*, 2019, **1**, 607.

13 C. C. Koch, *Nanostructured Materials: Processing, Properties, and Applications*, William Andrew, 2nd editio., 2007.

14 M. C. Roco, *Nanoparticles and nanotechnology research, Journal of Nanoparticle Research*, 1999, vol. 1.

15 J. H. Clark and C. N. Rhodes, *Clean Synthesis Using Porous Inorganic Solid Catalysts and Supported Reagents*, 2000.

16 J. H. Clark, *Green Chem.*, 1999, **1**, 1–8.

17 P. Anastas and J. Warner, *Green Chemistry: Theory and Practice*, Oxford University Press, 1998.

18 P. Tundo and P. Anastas, *Green Chemistry: Challenging Perspectives*, Oxford University Press, 1st edn., 2000.

19 A. Carrero, G. Vicente, R. Rodríguez, M. Linares and G. L. Del Peso, *Catal. Today*, 2011, **167**, 148–153.

20 D. E. López, K. Suwannakarn, D. A. Bruce and J. G. Goodwin, *J. Catal.*, 2007, **247**, 43–50.

21 N. Bothe, F. Döscher, J. Klein and H. Widdecke, *Polymer (Guildf).*, 1979, **20**, 850–854.

22 J. Y. Park, D. K. Kim and J. S. Lee, in *Bioresource Technology*, Elsevier Ltd, 2010, vol. 101.

23 I. F. Teixeira, B. T. W. Lo, P. Kostetskyy, M. Stamatakis, L. Ye, C. C. Tang, G. Mpourmpakis and S. C. E. Tsang, *Angew. Chemie Int. Ed.*, 2016, **55**, 13061–13066.

24 L. Ye, I. Teixeira, B. T. W. Lo, P. Zhao and S. C. Edman Tsang, *Chem. Commun.*, 2017, **53**, 9725–9728.

25 M. Moreno-Recio, J. Santamaría-González and P. Maireles-Torres, *Chem. Eng. J.*, 2016, **303**, 22–30.

26 T. D. Swift, H. Nguyen, Z. Erdman, J. S. Kruger, V. Nikolakis and D. G. Vlachos, *J. Catal.*, 2016, **333**, 149–161.

27 J. F. Haw, in *Physical Chemistry Chemical Physics*, 2002, vol. 4, pp. 5431–5441.

28 J. Gardy, A. Osatiashtiani, O. Céspedes, A. Hassanpour, X. Lai, A. F. Lee, K. Wilson and M. Rehan, *Appl. Catal. B Environ.*, 2018, **234**, 268–278.

29 C. A. Trickett, T. M. Osborn Popp, J. Su, C. Yan, J. Weisberg, A. Huq, P. Urban, J. Jiang, M. J. Kalmutzki, Q. Liu, J. Baek, M. P. Head-Gordon, G. A. Somorjai, J. A. Reimer and O. M. Yaghi, *Nat. Chem.*, 2019, **11**, 170–176.

30 T. Okuhara, *Chem. Rev.*, 2002, **102**, 3641–3666.

31 P. G. Bruce, B. Scrosati and J. M. Tarascon, *Angew. Chemie Int. Ed.*, 2008, **47**, 2930–2946.

32 E. Pomerantseva and Y. Gogotsi, *Nat. Energy 2017 27*, 2017, **2**, 1–6.

33 N. Nitta, F. Wu, J. T. Lee and G. Yushin, *Mater. Today*, 2015, 18, 252–264.

34 A. B. Yaroslavtsev, T. L. Kulova and A. M. Skundin, *Russ. Chem. Rev.*, 2015, **84**, 826–852.

35 L. P. Yu, X. H. Zhou, L. Lu, X. L. Wu and F. J. Wang, *ChemSusChem*, 2020, **13**, 5361–5407.

36 X. Zang, T. Wang, Z. Han, L. Li and X. Wu, *Nano*, 2019, **14**, 1930001.

37 L. Cong, H. Xie and J. Li, *Adv. Energy Mater.*, 2017, **7**, 1601906.

38 M. Velický and P. S. Toth, *Appl. Mater. Today*, 2017, **8**, 68–103.

39 K. S. Chen, I. Balla, N. S. Luu and M. C. Hersam, *ACS Energy Lett.*, 2017, **2**, 2026–2034.

40 K. T. Lee and J. Cho, *Nano Today*, 2011, **6**, 28–41.

41 M. Jana, R. Xu, X. B. Cheng, J. S. Yeon, J. M. Park, J. Q. Huang, Q. Zhang and H. S. Park, *Energy Environ. Sci.*, 2020, **13**, 1049–1075.

42 V. Bansal, P. Poddar, A. Ahmad and M. Sastry, *J. Am. Chem. Soc.*, 2006, **128**, 11958–11963.

43 B. Zhang, *Physical Fundamentals of Nanomaterials*, Elsevier, 2018.

44 M. Darwish and A. Mohammadi, in *Nanotechnology in Environmental Science*, Wiley-VCH Verlag, 2018, vol. 1–2, pp. 315–350.

45 O. Carp, C. L. Huisman and A. Reller, *Prog. Solid State Chem.*, 2004, 32, 33–177.

46 S. Di Mo and W. Y. Ching, *Phys. Rev. B*, 1995, **51**, 13023–13032.

47 A. L. Linsebigler, G. Lu and J. T. Yates, *Chem. Rev.*, 1995, **95**, 735–758.

48 Z. Xu, J. Wu, T. Wu, Q. Bao, X. He, Z. Lan, J. Lin, M. Huang, Y. Huang and L. Fan, *Energy Technol.*, 2017, **5**, 1820–1826.

49 I. Mora-Seró and J. Bisquert, *Nano Lett.*, 2003, **3**, 945–949.

50 K. Tanaka, M. F. V. Capule and T. Hisanaga, *Chem. Phys. Lett.*, 1991, **187**, 73–76.

51 P. Nyamukamba, O. Okoh, H. Mungondori, R. Taziwa and S. Zinya, in *Titanium Dioxide - Material for a Sustainable Environment*, InTech, 2018.

52 T. Parangi and M. K. Mishra, *Comments Inorg. Chem.*, 2019, 39, 90–126.

53 R. Arroyo, R. Rodríguez and P. Salinas, *J. Non. Cryst. Solids*, 1993, **163**, 90–96.

54 U. Diebold, *Surf. Sci. Rep.*, 2003, 48, 53–229.

55 H. Hattori and Y. Ono, *Solid Acid Catalysis*, Jenny Stanford Publishing, 2015.

56 P. Gupta and S. Paul, *Catal. Today*, 2014.

57 J. H. Clark, *Acc. Chem. Res.*, 2002, **35**, 791–797.

58 A. Takagaki, C. Tagusagawa, S. Hayashi, M. Hara and K. Domen, *Energy Environ. Sci.*, 2010, **3**, 82–93.

59 W. Shi and J. Li, *Catal. Letters*, 2013, **143**, 1285–1293.

60 K. Kaur, R. K. Wanchoo and A. P. Toor, *Ind. Eng. Chem. Res.*, 2015, **54**, 3285–3292.

61 Y. Kim, J. Kim, H. W. Kim, T. W. Kim, H. J. Kim, H. Chang, M. B. Park and H. J. Chae, *ACS Catal.*, 2019, **9**, 9398–9410.

62 J. Gardy, M. Rehan, A. Hassanpour, X. Lai and A. S. Nizami, *J. Environ. Manage.*, 2019, **249**, 109316.

63 C. R. S. de Oliveira, M. A. Batistella, A. A. Ulson de Souza and S. M. de A. G. Ulson de Souza, *Powder Technol.*, 2021, **381**, 366–380.

64 M. R. S. Farisya, R. Irmawati, I. N. Shafizah, Y. H. Taufiq-Yap, E. N. Muhamad, S. L. Lee and N. Salamun, *Catalysts*, 2021, **11**, 1542.

65 K. M. Lee, C. F. Kait, J. W. Lim and G. B. Teh, *Springer Proc. Complex.*, 2021, 85–95.

66 S. J. Sekewael, R. A. Pratika, L. Hauli, A. K. Amin, M. Utami and K. Wijaya, *Catalysts*, 2022, **12**, 191.

67 B. Lowe, J. Gardy and A. Hassanpour, *Catalysts*, 2022, **12**, 223.

68 A. K. Dalai, R. Sethuraman, S. P. R. Katikaneni and R. O. Idem, *Ind. Eng. Chem. Res.*, 1998, **37**, 3869–3878.

69 S. M. Jung and P. Grange, *Catal. Today*, 2000, **59**, 305–312.

70 Q. Yang, C. Xie, Z. Xu, Z. Gao and Y. Du, *J. Phys. Chem. B*, 2005, **109**, 5554–5560.

71 Y. Hu, B. Guo, Y. Fu, Y. Ren, G. Tang, X. Chen, B. Yue and H. He, *Chem. Commun.*, 2015,

51, 14219–14222.

72 H. Zhao, P. Jiang, Y. Dong, M. Huang and B. Liu, *New J. Chem.*, 2014, **38**, 4541–4548.

73 H. Zhao, P. Jiang, Y. Dong, M. Huang and B. Liu, *React. Kinet. Mech. Catal.*, 2014, **113**, 445–458.

74 W. Shi and J. Li, *React. Kinet. Mech. Catal.*, 2014, **111**, 215–233.

75 C. Meng, G. P. Cao, X. K. Li, Y. Z. Yan, E. Y. Zhao, L. Y. Hou and H. Y. Shi, *React. Kinet. Mech. Catal.*, 2017, **121**, 719–734.

76 R. Gómez, T. López, E. Ortiz-Islas, J. Navarrete, E. Sánchez, F. Tzompanztzi and X. Bokhimi, *J. Mol. Catal. A Chem.*, 2003, **193**, 217–226.

77 W. Hua, Y. Xia, Y. Yue and Z. Gao, *J. Catal.*, 2000, **196**, 104–114.

78 R. M. de Almeida, L. K. Noda, N. S. Gonçalves, S. M. P. Meneghetti and M. R. Meneghetti, *Appl. Catal. A Gen.*, 2008, **347**, 100–105.

79 X. Bokhimi, A. Morales, E. Ortíz, T. López, R. Gómez and J. Navarrete, *J. Sol-Gel Sci. Technol.*, 2004, **29**, 31–40.

80 E. Ortiz-Islas, R. Gomez, T. Lopez, J. Navarrete, D. H. Aguilar and P. Quintana, in *Applied Surface Science*, Elsevier, 2005, vol. 252, pp. 807–812.

81 J. L. Ropero-Vega, A. Aldana-Pérez, R. Gómez and M. E. Niño-Gómez, *Appl. Catal. A Gen.*, 2010, **379**, 24–29.

82 E. A. Guseinova, M. R. Salaev, N. T. Alieva and K. Y. Adzhamov, *Chem. Technol. Fuels Oils*, 2018, **54**, 132–139.

83 E. Ortiz-Islas, T. López, J. Navarrete, X. Bokhimi and R. Gómez, in *Journal of Molecular Catalysis A: Chemical*, 2005, vol. 228, pp. 345–350.

84 M. Waqif, J. Bachelier, O. Saur and J. C. Lavalley, *J. Mol. Catal.*, 1992, **72**, 127–138.

85 A. Mantilla, G. Ferrat, A. López-Ortega, E. Romero, F. Tzompantzi, M. Torres, E. Ortíz-Islas and R. Gómez, in *Journal of Molecular Catalysis A: Chemical*, 2005, vol. 228, pp. 333–338.

86 C. X. Tian, Y. Yang and H. Pu, *Appl. Surf. Sci.*, 2011, **257**, 8391–8395.

87 M. Yan, F. Chen, J. Zhang and M. Anpo, *J. Phys. Chem. B*, 2005, **109**, 8673–8678.

88 I. Nowak and M. Ziolek, *Chem. Rev.*, 1999, **99**, 3603–3624.

89 A. Corma, *Chem. Rev.*, 1995, **95**, 559–614.

90 G. Busca, *Phys. Chem. Chem. Phys.*, 1999, **1**, 723–736.

91 G. Busca, *Catal. Today*, 1998, **41**, 191–206.

92 C. A. Emeis, *J. Catal.*, 1993, **141**, 347–354.

93 M. Niwa, K. Suzuki, K. Isamoto and N. Katada, *J. Phys. Chem. B*, 2006, **110**, 264–269.

94 H. Knözinger, H. Krietenbrink and P. Ratnasamy, *J. Catal.*, 1977, **48**, 436–439.

95 M. Niwa and N. Katada, *Chem. Rec.*, 2013, **13**, 432–455.

96 M. Takeuchi, T. Tsukamoto, A. Kondo and M. Matsuoka, *Catal. Sci. Technol.*, 2015, **5**, 4587–4593.

97 M. Hunger, *Catal. Rev. - Sci. Eng.*, 1997, **39**, 345–393.

98 Z.-W. Yu, A.-M. Zheng, Q. Wang, S.-J. Huang, F. Deng and S.-B. Liu, *Chinese J. Magn. Reson.*, 2010, **27**, 485– 515.

99 J. Čejka, A. Corma and S. Zones, *Zeolites and Catalysis: Synthesis, Reactions and Applications*, Wiley-VCH, 2010, vol. 1–2.

100 S. Li and F. Deng, in *Annual Reports on NMR Spectroscopy*, Academic Press Inc., 2013, vol. 78, pp. 1–54.

101 A. Zheng, S. J. Huang, Q. Wang, H. Zhang, F. Deng and S. Bin Liu, *Cuihua Xuebao/Chinese J. Catal.*, 2013, 34, 436–491.

102 A. Zheng, S. Bin Liu and F. Deng, *Solid State Nucl. Magn. Reson.*, 2013, 55–56, 12–27.

103 Y. Jiang, J. Huang, W. Dai and M. Hunger, *Solid State Nucl. Magn. Reson.*, 2011, 39, 116–141.

104 M. Zhang, S. Xu, J. Li, Y. Wei, Y. Gong, Y. Chu, A. Zheng, J. Wang, W. Zhang, X. Wu, F. Deng and Z. Liu, *J. Catal.*, 2016, **335**, 47–57.

105 X. Su, S. Xu, P. Tian, J. Li, A. Zheng, Q. Wang, M. Yang, Y. Wei, F. Deng and Z. Liu, *J. Phys. Chem. C*, 2015, 150127131937009.

106 H. Pfeifer and H. Ernst, *Annu. Reports NMR Spectrosc.*, 1994, **28**, 91–187.

107 C. Lieder, S. Opelt, M. Dyballa, H. Henning, E. Klemm and M. Hunger, *J. Phys. Chem. C*, 2010, **114**, 16596–16602.

108 J. Huang, Y. Jiang, V. R. Reddy Marthala, Y. S. Ooi, J. Weitkamp and M. Hunger, *Microporous Mesoporous Mater.*, 2007, **104**, 129–136.

109 Y. Chu, Z. Yu, A. Zheng, H. Fang, H. Zhang, S. J. Huang, S. Bin Liu and F. Deng, *J. Phys. Chem. C*, 2011, **115**, 7660–7667.

110 E. F. Rakiewicz, A. W. Peters, R. F. Wormsbecher, K. J. Sutovich and K. T. Mueller, *J. Phys. Chem. B*, 1998, **102**, 2890–2896.

111 J. P. Osegovic and R. S. Drago, *J. Phys. Chem. B*, 2000, **104**, 147–154.

112 J. P. Osegovic and R. S. Drago, *J. Catal.*, 1999, **182**, 1–4.

113 Q. Zhao, W. H. Chen, S. J. Huang, Y. C. Wu, H. K. Lee and S. Bin Liu, *J. Phys. Chem. B*, 2002, **106**, 4462–4469.

114 A. Zheng, L. Chen, J. Yang, M. Zhang, Y. Su, Y. Yue, C. Ye and F. Deng, *J. Phys. Chem. B*, 2005, **109**, 24273–24279.

115 C. Tagusagawa, A. Takagaki, S. Hayashi and K. Domen, *J. Phys. Chem. C*, 2009, **113**, 7831–7837.

116 C. Tagusagawa, A. Takagaki, A. Iguchi, K. Takanabe, J. N. Kondo, K. Ebitani, S. Hayashi, T. Tatsumi and K. Domen, *Angew. Chemie Int. Ed.*, 2010, **49**, 1128–1132.

117 A. Zheng, H. Zhang, X. Lu, S. Bin Liu and F. Deng, *J. Phys. Chem. B*, 2008, **112**, 4496–4505.

118 A. Zheng, S. J. Huang, W. H. Chen, P. H. Wu, H. Zhang, H. K. Lee, L. C. De Ménorval, F. Deng and S. Bin Liu, *J. Phys. Chem. A*, 2008, **112**, 7349–7356.

119 M. Hunger, *Solid State Nucl. Magn. Reson.*, 1996, 6, 1–29.

120 A. Zheng, S. J. Huang, S. Bin Liu and F. Deng, *Phys. Chem. Chem. Phys.*, 2011, **13**, 14889–14901.

121 A. Zheng, F. Deng and S. Bin Liu, in *Annual Reports on NMR Spectroscopy*, Academic Press Inc., 2014, vol. 81, pp. 47–108.

122 A. Zheng, S. Li, S. Bin Liu and F. Deng, *Acc. Chem. Res.*, 2016, **49**, 655–663.

123 D. H. Barich, J. B. Nicholas, T. Xu and J. F. Haw, *J. Am. Chem. Soc.*, 1998, **120**, 12342–12350.

124 J. F. Haw, T. Xu, J. B. Nicholas and P. W. Goguen, *Nature*, 1997, **389**, 832–835.

125 J. Yang, M. J. Janik, D. Ma, A. Zheng, M. Zhang, M. Neurock, R. J. Davis, C. Ye and F. Deng, *J. Am. Chem. Soc.*, 2005, **127**, 18274–18280.

126 S. Li, A. Zheng, Y. Su, H. Zhang, L. Chen, J. Yang, C. Ye and F. Deng, *J. Am. Chem. Soc.*, 2007, **129**, 11161–11171.

127 H. Fang, A. Zheng, Y. Chu and F. Deng, *J. Phys. Chem. C*, 2010, **114**, 12711–12718.

128 J. H. Lunsford, W. P. Rothwell and W. Shen, *J. Am. Chem. Soc.*, 1985, **107**, 1540–1547.

129 H. M. Kao, C. Y. Yu and M. C. Yeh, *Microporous Mesoporous Mater.*, 2002, **53**, 1–12.

130 A. Zheng, H. Zhang, L. Chen, Y. Yue, C. Ye and F. Deng, *J. Phys. Chem. B*, 2007, **111**, 3085–3089.

131 J. F. Haw, I. S. Chuang, B. L. Hawkins and G. E. Maciel, *J. Am. Chem. Soc.*, 1983, **105**, 7206–7207.

132 H. Guenter, *NMR Spectroscopy: Basic Principles, Concepts and Applications in Chemistry, 3rd Edition*, Wiley-VCH Verlag GmbH & Co. KGaA, 2013.

133 H. Zhang, H. Yu, A. Zheng, S. Li, W. Shen and F. Deng, *Environ. Sci. Technol.*, 2008, **42**, 5316–5321.

134 J. Yang, M. Zhang, F. Deng, Q. Luo, D. Yi and C. Ye, *Chem. Commun.*, 2003, **3**, 884–885.

135 L. Baltusis, J. S. Frye and G. E. Maciel, *J. Am. Chem. Soc.*, 1987, **109**, 40–46.

136 H. Yu, H. Fang, H. Zhang, B. Li and F. Deng, *Catal. Commun.*, 2009, **10**, 920–924.

137 J. Xu, A. Zheng, J. Yang, Y. Su, J. Wang, D. Zeng, M. Zhang, C. Ye and F. Deng, *J. Phys. Chem. B*, 2006, **110**, 10662–10671.

138 J. Wang, N. Yu, A. Zheng, J. Yang, D. Wu, Y. Sun, C. Ye and F. Deng, *Microporous Mesoporous Mater.*, 2006, **89**, 219–226.

139 W. Hu, Q. Luo, Y. Su, L. Chen, Y. Yue, C. Ye and F. Deng, *Microporous Mesoporous Mater.*, 2006, **92**, 22–30.

140 H. M. Kao, P. C. Chang, Y. W. Liao, L. P. Lee and C. H. Chien, *Microporous Mesoporous Mater.*, 2008, **114**, 352–364.

141 F. Deng, Y. Du, C. Ye, J. Wang, T. Ding and H. Li, *J. Phys. Chem.*, 1995, **99**, 15208–15214.

142 G. Yang, X. Lan, J. Zhuang, D. Ma, L. Zhou, X. Liu, X. Han and X. Bao, *Appl. Catal. A Gen.*, 2008, **337**, 58–65.

143 B. Zhao, H. Pan and J. H. Lunsford, *Langmuir*, 1999, **15**, 2761–2765.

144 A. Zheng, S. Li, S.-B. Liu and F. Deng, *Acc. Chem. Res.*, 2016, **49**, 655–663.

145 D. Astruc, *Nanoparticles and Catalysis*, Wiley-VCH, 2008.

146 A. Roucoux, J. Schulz and H. Patin, *Chem. Rev.*, 2002, **102**, 3757–3778.

147 S. Gurunathan, E. Kim, J. Han, J. Park and J.-H. Kim, *Molecules*, 2015, **20**, 22476–22498.

148 K. Ravindra, L. Bencs and R. Van Grieken, *Sci. Total Environ.*, 2004, 318, 1–43.

149 S. Cheong, J. D. Watt and R. D. Tilley, *Nanoscale*, 2010, 2, 2045–2053.

150 D. Astruc, *Inorg. Chem.*, 2007, 46, 1884–1894.

151 A. T. Bell, *Science*, 2003, **299**, 1688–1691.

152 C. R. Hammond, *CRC Handbook of Chemistry and Physics, 86th Edition*, CRC Press, 86th edn., 2005.

153 D. C. Powers and T. Ritter, *Top. Organomet. Chem.*, 2011, **503**, 129–156.

154 W. Chen, S. Shimada and M. Tanaka, *Science*, 2002, **295**, 308–310.

155 R. H. Crabtree, *Science*, 2002, 295, 288–289.

156 N. Miyaura and A. Suzuki, *Chem. Rev.*, 1995, **95**, 2457–2483.

157 https://www.nobelprize.org/prizes/chemistry/2010/summary/ - The Nobel Prize in Chemistry 2010.

158 P. B. Kettler, *Org. Process Res. Dev.*, 2003, 7, 342–354.

159 S. Saravanamurugan, O. Nguyen Van Buu and A. Riisager, *ChemSusChem*, 2011, **4**, 723–726.

160 R. Narayanan and M. A. El-Sayed, *J. Phys. Chem. B*, 2005, **109**, 12663–12676.

161 T. Teranishi and M. Miyake, *Chem. Mater.*, 1998, **10**, 594–600.

162 M. M. Demir, M. A. Gulgun, Y. Z. Menceloglu, B. Erman, S. S. Abramchuk, E. E. Makhaeva, A. R. Khokhlov, V. G. Matveeva and M. G. Sulman, *Macromolecules*, 2004, **37**, 1787–1792.

163 E. Bustelo, C. Guérot, A. Hercouet, B. Carboni, L. Toupet and P. H. Dixneuf, *J. Am. Chem. Soc.*, 2005, **127**, 11582–11583.

164 D. J. M. Snelders, G. van Koten and R. J. M. Klein Gebbink, *J. Am. Chem. Soc.*, 2009, **131**, 11407–11416.

165 T. Fujihara, S. Yoshida, H. Ohta and Y. Tsuji, *Angew. Chemie Int. Ed.*, 2008, **47**, 8310–8314.

166 W. A. Herrmann, K. Öfele, S. K. Schneider, E. Herdtweck and S. D. Hoffmann, *Angew. Chemie Int. Ed.*, 2006, **45**, 3859–3862.

167 G. Altenhoff, R. Goddard, C. W. Lehmann and F. Glorius, *Angew. Chemie Int. Ed.*, 2003, **42**, 3690–3693.

168 A. K. Diallo, C. Ornelas, L. Salmon, J. Ruiz Aranzaes and D. Astruc, *Angew. Chemie Int. Ed.*, 2007, **46**, 8644–8648.

169 R. Martin and S. L. Buchwald, *Acc. Chem. Res.*, 2008, 41, 1461–1473.

170 A. F. Littke and G. C. Fu, *Angew. Chemie - Int. Ed.*, 2002, 41, 4176–4211.

171 L. Yin and J. Liebscher, *Chem. Rev.*, 2007, 107, 133–173.

172 M. Blanco, D. Mosconi, C. Tubaro, A. Biffis, D. Badocco, P. Pastore, M. Otyepka, A. Bakandritsos, Z. Liu, W. Ren, S. Agnoli and G. Granozzi, *Green Chem.*, 2019, **21**, 5238–5247.

173 K. S. Siddiqi and A. Husen, *Nanoscale Res. Lett.*, 2016, **11**, 482.

174 Y. Li, E. Boone and M. A. El-Sayed, *Langmuir*, 2002, **18**, 4921–4925.

175 I. Saldan, Y. Semenyuk, I. Marchuk and O. Reshetnyak, *J. Mater. Sci.*, 2015, 50, 2337–2354.

176 A. B. Patil and B. M. Bhanage, *J. Nanosci. Nanotechnol.*, 2013, **13**, 5061–5068.

177 N. Jamwal, R. K. Sodhi, P. Gupta and S. Paul, *Int. J. Biol. Macromol.*, 2011, **49**, 930–935.

178 J. Lichtenberger, D. Lee and E. Iglesia, *Phys. Chem. Chem. Phys.*, 2007, **9**, 4902–4906.

179 S. Horinouchi, Y. Yamanoi, T. Yonezawa, T. Mouri and H. Nishihara, *Langmuir*, 2006, **22**, 1880–1884.

180 J. Cookson, *Platin. Met. Rev.*, 2012, 56, 83–98.

181 C. Xu, L. Cheng, P. Shen and Y. Liu, *Electrochem. commun.*, 2007, **9**, 997–1001.

182 M. Yamauchi, R. Ikeda, H. Kitagawa and M. Takata, *J. Phys. Chem. C*, 2008, **112**, 3294–3299.

183 Q. Zeng, J. S. Cheng, X. F. Liu, H. T. Bai and J. H. Jiang, *Biosens. Bioelectron.*, 2011, **26**, 3456–3463.

184 S. Mubeen, T. Zhang, B. Yoo, M. A. Deshusses and N. V. Myung, *J. Phys. Chem. C*, 2007, **111**, 6321–6327.

185 J. W. M. Frenken and P. Stoltze, *Phys. Rev. Lett.*, 1999, **82**, 3500–3503.

186 Y. W. Jun, J. H. Lee, J. S. Choi and J. Cheon, *J. Phys. Chem. B*, 2005, **109**, 14795–14806.

187 B. L. Cushing, V. L. Kolesnichenko and C. J. O'Connor, *Chem. Rev.*, 2004, **104**, 3893–3946.

188 E. E. Finney and R. G. Finke, *J. Colloid Interface Sci.*, 2008, **317**, 351–374.

189 D. M. P. Mingos and R. H. Crabtree, *Comprehensive organometallic chemistry III*, Elsevier, 2007.

190 A. Roucoux, in *Surface and Interfacial Organometallic Chemistry and Catalysis*, Springer-Verlag, 2005, pp. 261–279.

191 J. A. Widegren and R. G. Finke, *J. Mol. Catal. A Chem.*, 2003, 191, 187–207.

192 W. Yu, M. D. Porosoff and J. G. Chen, *Chem. Rev.*, 2012, 112, 5780–5817.

193 N. Toshima, in *Nanoscale Materials*, Kluwer Academic Publishers, 2006, pp. 79–96.

194 K. Philippot and B. Chaudret, *Comptes Rendus Chim.*, 2003, 6, 1019–1034.

195 M. Liu, W. Yu and H. Liu, *J. Mol. Catal. A Chem.*, 1999, **138**, 295–303.

196 W. Yu, M. Liu, H. Liu, X. Ma and Z. Liu, *J. Colloid Interface Sci.*, 1998, **208**, 439–444.

197 H. Bönnemann, G. Braun, W. Brijoux, R. Brinkmann, A. S. Tilling, K. Seevogel and K. Siepen, *J. Organomet. Chem.*, 1996, **520**, 143–162.

198 V. Marvaud, C. Decroix, A. Scuiller, F. Tuyèras, C. Guyard-Duhayon, J. Vaissermann, J. Marrot, F. Gonnet and M. Verdaguer, *Chem. - A Eur. J.*, 2003, **9**, 1692–1705.

199 A. Corma, D. Das, H. García and A. Leyva, *J. Catal.*, 2005, **229**, 322–331.

200 D. Sanhes, E. Raluy, S. Rétory, N. Saffon, E. Teuma and M. Gómez, *Dalt. Trans.*, 2010, **39**, 9719–9726.

201 J. G. De Vries, *Dalt. Trans.*, 2006, 421–429.

202 A. H. M. de Vries, F. J. Parlevliet, L. Schmieder-van de Vondervoort, J. H. M. Mommers, H. J. W. Henderickx, M. A. M. Walet and J. G. de Vries, *Adv. Synth. Catal.*, 2002, **344**, 996–1002.

203 A. Balanta, C. Godard and C. Claver, *Chem. Soc. Rev.*, 2011, 40, 4973–4985.

204 H. Geissler, in *Transition Metals for Organic Synthesis*, Wiley-VCH Verlag GmbH, Weinheim, Germany, pp. 158–183.

205 K. Kohler, S. Prockl and W. Kleist, *Curr. Org. Chem.*, 2006, **10**, 1585–1601.

206 M. T. Reetz, R. Breinbauer and K. Wanninger, *Tetrahedron Lett.*, 1996, **37**, 4499–4502.

207 A. Biffis, P. Centomo, A. Del Zotto and M. Zecca, *Chem. Rev.*, 2018, 118, 2249–2295.

208 V. M. Wall, A. Eisenstadt, D. J. Ager and S. A. Laneman, *Platin. Met. Rev.*, 1999, **43**, 138.

209 L. Djakovitch, K. Khler and J. G. de Vries, in *Nanoparticles and Catalysis*, Wiley-VCH

Verlag GmbH & Co. KGaA, Weinheim, Germany, pp. 303–348.

210 M. Seki, *Recent advances in Pd/C-catalyzed coupling reactions*, 2006.

211 A. Biffis, M. Zecca and M. Basato, *J. Mol. Catal. A Chem.*, 2001, **173**, 249–274.

212 F. A. Lewis, *Int. J. Hydrogen Energy*, 1995, **20**, 587–592.

213 L. Zaluski, A. Zaluska, P. Tessier, J. O. Ström-Olsen and R. Schulz, *J. Alloys Compd.*, 1995, **217**, 295–300.

214 P. P. Mardilovich, Y. She, Y. H. Ma and M.-H. Rei, *AIChE J.*, 1998, **44**, 310–322.

215 P. Munnik, P. E. De Jongh and K. P. De Jong, *Chem. Rev.*, 2015, 115, 6687–6718.

216 B. D. Adams and A. Chen, *Mater. Today*, 2011, 14, 282–289.

217 H. Huang, S. Bao, Q. Chen, Y. Yang, Z. Jiang, Q. Kuang, X. Wu, Z. Xie and L. Zheng, *Nano Res.*, 2015, **8**, 2698–2705.

218 A. Borodziński and G. C. Bond, *Catal. Rev.*, 2008, **50**, 379–469.

219 A. Borodziński and G. C. Bond, *Catal. Rev.*, 2006, **48**, 91–144.

220 S. A. Nikolaev, L. N. Zanaveskin, V. V Smirnov, V. A. Averyanov and K. L. Zanaveskin, *Russ. Chem. Rev.*, 2009, **78**, 231–247.

221 M. Kuhn, M. Lucas and P. Claus, *Ind. Eng. Chem. Res.*, 2015, **54**, 6683–6691.

222 M. Kuhn, M. Lucas and P. Claus, *Chem. Eng. Technol.*, 2015, **38**, 61–67.

223 A. Pachulski, R. Schödel and P. Claus, *Appl. Catal. A Gen.*, 2012, **445**–**446**, 107–120.

224 A. Pachulski, R. Schödel and P. Claus, *Appl. Catal. A Gen.*, 2011, **400**, 14–24.

225 D. Astruc, F. Lu and J. R. Aranzaes, *Angew. Chemie Int. Ed.*, 2005, **44**, 7852–7872.

226 R. Ye, T. J. Hurlburt, K. Sabyrov, S. Alayoglu and G. A. Somorjai, *Proc. Natl. Acad. Sci. U. S. A.*, 2016, 113, 5159–5166.

227 G. Chen, C. Xu, X. Huang, J. Ye, L. Gu, G. Li, Z. Tang, B. Wu, H. Yang, Z. Zhao, Z. Zhou, G. Fu and N. Zheng, *Nat. Mater.*, 2016, **15**, 564–569.

228 M. García-Mota, J. Gómez-Díaz, G. Novell-Leruth, C. Vargas-Fuentes, L. Bellarosa, B. Bridier, J. Pérez-Ramírez and N. López, *Theor. Chem. Acc.*, 2011, **128**, 663–673.

229 M. García-Mota, B. Bridier, J. Pérez-Ramírez and N. López, *J. Catal.*, 2010, **273**, 92–102.

230 Y. Jin, A. K. Datye, E. Rightor, R. Gulotty, W. Waterman, M. Smith, M. Holbrook, J. Maj and J. Blacksony, *J. Catal.*, 2001, **203**, 292–306.

231 N. A. Khan, S. Shaikhutdinov and H. J. Freund, *Catal. Letters*, 2006, **108**, 159–164.

232 B. Yang, R. Burch, C. Hardacre, G. Headdock and P. Hu, *J. Catal.*, 2013, **305**, 264–276.

233 M. Armbrüster, M. Behrens, F. Cinquini, K. Föttinger, Y. Grin, A. Haghofer, B. Klötzer, A. Knop-Gericke, H. Lorenz, A. Ota, S. Penner, J. Prinz, C. Rameshan, Z. Révay, D. Rosenthal, G. Rupprechter, P. Sautet, R. Schlögl, L. Shao, L. Szentmiklósi, D. Teschner,

D. Torres, R. Wagner, R. Widmer and G. Wowsnick, *ChemCatChem*, 2012, **4**, 1048–1063.

234 W. Ludwig, A. Savara, K. H. Dostert and S. Schauermann, *J. Catal.*, 2011, **284**, 148–156.

235 F. Studt, F. Abild-Pedersen, T. Bligaard, R. Z. Sørensen, C. H. Christensen and J. K. Nørskov, *Science*, 2008, **320**, 1320–1322.

236 H. Zhou, M. Liao, S.-W. Huang, L. Zhou, K. Qiu and C. W. Wong, *Laser Photon. Rev.*, 2016, **10**, 1054–1061.

237 J. Feng, Y. Liu, M. Yin, Y. He, J. Zhao, J. Sun and D. Li, *J. Catal.*, 2016, **344**, 854–864.

238 Q. Feng, S. Zhao, Y. Wang, J. Dong, W. Chen, D. He, D. Wang, J. Yang, Y. Zhu, H. Zhu, L. Gu, Z. Li, Y. Liu, R. Yu, J. Li and Y. Li, *J. Am. Chem. Soc.*, 2017, **139**, 7294–7301.

239 F. M. McKenna and J. A. Anderson, *J. Catal.*, 2011, **281**, 231–240.

240 F. M. McKenna, R. P. K. Wells and J. A. Anderson, *Chem. Commun.*, 2011, **47**, 2351–2353.

241 F. M. McKenna, L. Mantarosie, R. P. K. Wells, C. Hardacre and J. A. Anderson, *Catal. Sci. Technol.*, 2012, **2**, 632–638.

242 A. J. McCue, F. M. McKenna and J. A. Anderson, *Catal. Sci. Technol.*, 2015, **5**, 2449–2459.

243 Y. K. Gulyaeva, V. V. Kaichev, V. I. Zaikovskii, E. V. Kovalyov, A. P. Suknev and B. S. Bal'Zhinimaev, *Catal. Today*, 2015, **245**, 139–146.

244 Y. K. Gulyaeva, V. V. Kaichev, V. I. Zaikovskii, A. P. Suknev and B. S. Bal'zhinimaev, *Appl. Catal. A Gen.*, 2015, **506**, 197–205.

245 H. Yi, H. Du, Y. Hu, H. Yan, H.-L. Jiang and J. Lu, *ACS Catal.*, 2015, **5**, 2735–2739.

246 Y. Liu, J. Zhao, Y. He, J. Feng, T. Wu and D. Li, *J. Catal.*, 2017, **348**, 135–145.

247 J. Osswald, K. Kovnir, M. Armbrüster, R. Giedigkeit, R. E. Jentoft, U. Wild, Y. Grin and R. Schlögl, *J. Catal.*, 2008, **258**, 219–227.

248 G. X. Pei, X. Y. Liu, A. Wang, L. Li, Y. Huang, T. Zhang, J. W. Lee, B. W. L. Jang and C. Y. Mou, *New J. Chem.*, 2014, **38**, 2043–2051.

249 A. J. McCue, A. Guerrero-Ruiz, C. Ramirez-Barria, I. Rodríguez-Ramos and J. A. Anderson, *J. Catal.*, 2017, **355**, 40–52.

250 S. A. Nikolaev and V. V. Smirnov, *Catal. Today*, 2009, 147.

251 A. Cooper, B. Bachiller-Baeza, J. A. Anderson, I. Rodríguez-Ramos and A. Guerrero-Ruiz, *Catal. Sci. Technol.*, 2014, **4**, 1446–1455.

252 A. J. McCue, R. T. Baker and J. A. Anderson, *Faraday Discuss.*, 2016, **188**, 499–523.

253 C. Ma, Y. Du, J. Feng, X. Cao, J. Yang and D. Li, *J. Catal.*, 2014, **317**, 263–271.

254 G. X. Pei, X. Y. Liu, A. Wang, A. F. Lee, M. A. Isaacs, L. Li, X. Pan, X. Yang, X. Wang, Z. Tai, K. Wilson and T. Zhang, *ACS Catal.*, 2015, **5**, 3717–3725.

255 N. J. Ossipoff and N. W. Cant, *J. Catal.*, 1994, **148**, 125–133.

256 B. Bridier, N. López and J. Pérez-Ramírez, *J. Catal.*, 2010, **269**, 80–92.

257 B. Bridier, N. López and J. Pérez-Ramírez, *Dalt. Trans.*, 2010, **39**, 8412–8419.

258 B. Bridier and J. Pérez-Ramírez, *J. Am. Chem. Soc.*, 2010, **132**, 4321–4327.

259 G. Vilé, D. Baudouin, I. N. Remediakis, C. Copéret, N. López and J. Pérez-Ramírez, *ChemCatChem*, 2013, **5**, 3750–3759.

260 G. Vilé, B. Bridier, J. Wichert and J. Pérez-Ramírez, *Angew. Chemie Int. Ed.*, 2012, **51**, 8620–8623.

261 J. Carrasco, G. Vilé, D. Fernández-Torre, R. Pérez, J. Pérez-Ramírez and M. V. Ganduglia-Pirovano, *J. Phys. Chem. C*, 2014, **118**, 5352–5360.

262 D. Albani, M. Capdevila-Cortada, G. Vilé, S. Mitchell, O. Martin, N. López and J. Pérez-Ramírez, *Angew. Chemie Int. Ed.*, 2017, **56**, 10755–10760.

263 G. Vilé, P. Dähler, J. Vecchietti, M. Baltanás, S. Collins, M. Calatayud, A. Bonivardi and J. Pérez-Ramírez, *J. Catal.*, 2015, **324**, 69–78.

264 A. J. McCue, C. J. McRitchie, A. M. Shepherd and J. A. Anderson, *J. Catal.*, 2014, **319**, 127–135.

265 A. J. McCue, A. M. Shepherd and J. A. Anderson, *Catal. Sci. Technol.*, 2015, **5**, 2880–2890.

266 A. J. McCue, A. Gibson and J. A. Anderson, *Chem. Eng. J.*, 2016, **285**, 384–391.

267 G. Kyriakou, M. B. Boucher, A. D. Jewell, E. A. Lewis, T. J. Lawton, A. E. Baber, H. L. Tierney, M. Flytzani-Stephanopoulos and E. C. H. Sykes, *Science*, 2012, **335**, 1209–1212.

268 Q. Fu and Y. Luo, *ACS Catal.*, 2013, **3**, 1245–1252.

269 A. J. McCue and J. A. Anderson, *J. Catal.*, 2015, **329**, 538–546.

270 J. A. Delgado, O. Benkirane, C. Claver, D. Curulla-Ferré and C. Godard, *Dalt. Trans.*, 2017, 46, 12381–12403.

271 B. Bachiller-Baeza, A. Iglesias-Juez, E. Castillejos-López, A. Guerrero-Ruiz, M. Di Michiel, M. Fernández-García and I. Rodríguez-Ramos, *ACS Catal.*, 2015, **5**, 5235–5241.

272 B. Bachiller-Baeza, J. Peña-Bahamonde, E. Castillejos-López, A. Guerrero-Ruiz and I. Rodríguez-Ramos, *Catal. Today*, 2015, **249**, 63–71.

273 V. V. Singh, U. Kumar, S. N. Tripathi and A. K. Singh, *Dalt. Trans.*, 2014, **43**, 12555–12563.

274 C. Du, P. Li, F. Yang, G. Cheng, S. Chen and W. Luo, *ACS Appl. Mater. Interfaces*, 2018, **10**, 753–761.

275 A. J. McCue, A. Guerrero-Ruiz, I. Rodríguez-Ramos and J. A. Anderson, *J. Catal.*, 2016, **340**, 10–16.

276 X. Zhao, L. Zhou, W. Zhang, C. Hu, L. Dai, L. Ren, B. Wu, G. Fu and N. Zheng, *Chem*, 2018,

4, 1080–1091.

277 D. Larcher and J. M. Tarascon, *Nat. Chem.*, 2015, 7, 19–29.

278 J. Vetter, P. Novák, M. R. Wagner, C. Veit, K. C. Möller, J. O. Besenhard, M. Winter, M. Wohlfahrt-Mehrens, C. Vogler and A. Hammouche, *J. Power Sources*, 2005, **147**, 269–281.

279 C. Schultz, S. Vedder, M. Winter and S. Nowak, Investigation of the decomposition of organic solvent-based lithium ion battery electrolytes with liquid chromatography-mass spectrometry, https://www.spectroscopyasia.com/article/investigation-decomposition-organic-solvent-based-lithium-ion-battery-electrolytes-liquid.

280 J. B. Goodenough and K. S. Park, *J. Am. Chem. Soc.*, 2013, 135, 1167–1176.

281 J. B. Goodenough and Y. Kim, *Chem. Mater.*, 2010, 22, 587–603.

282 M. Armand and J. M. Tarascon, *Nature*, 2008, 451, 652–657.

283 T. Kim, W. Song, D. Y. Son, L. K. Ono and Y. Qi, *J. Mater. Chem. A*, 2019, 7, 2942–2964.

284 M. Arbabzadeh, J. X. Johnson, G. A. Keoleian, P. G. Rasmussen and L. T. Thompson, *Environ. Sci. Technol.*, 2016, **50**, 1046–1055.

285 M. A. Pellow, C. J. M. Emmott, C. J. Barnhart and S. M. Benson, *Energy Environ. Sci.*, 2015, **8**, 1938–1952.

286 A. Bilich, K. Langham, R. Geyer, L. Goyal, J. Hansen, A. Krishnan, J. Bergesen and P. Sinha, *Environ. Sci. Technol.*, 2017, **51**, 1043–1052.

287 A. Mishra, A. Mehta, N. M. Nadagoudad, S. S. Shuklac, S. Basu, S. J. Malode, N. P. Shetti and M. T. Aminabhavi, *Mater. Sci. Energy Technol.*, 2018, **1**, 182–187.

288 H. Vikström, S. Davidsson and M. Höök, *Appl. Energy*, 2013, **110**, 252–266.

289 E. Petrucco, *Johnson Matthey Technol. Rev.*, 2019, **63**, 134–139.

290 eLNO | Johnson Matthey, https://matthey.com/en/products-and-services/battery-materials/elno-next-generation-battery-material, (accessed 17 January 2020).

291 M. Ting, M. Burigana, L. Zhang, Y. Z. Finfrock, S. Trabesinger, A. Jonderian and E. McCalla, *Chem. Mater.*, 2020, **32**, 849–857.

292 J. Y. Liu, X. X. Li, J. R. Huang, J. J. Li, P. Zhou, J. H. Liu and X. J. Huang, *J. Mater. Chem. A*, 2017, 5, 5977–5994.

293 Y. Hao, S. Wang, Y. Shao, Y. Wu and S. Miao, *Adv. Energy Mater.*, 2019, 1902836.

294 J. Billaud, F. Bouville, T. Magrini, C. Villevieille and A. R. Studart, *Nat. Energy*, 2016, 1.

295 L. Pan, Y. Zhang, F. Lu, Y. Du, Z. Lu, Y. Yang, T. Ye, Q. Liang, Y. Bando and X. Wang, *Energy Storage Mater.*, 2019, **19**, 39–47.

296 A. Casimir, H. Zhang, O. Ogoke, J. C. Amine, J. Lu and G. Wu, *Nano Energy*, 2016, 27, 359–376.

297 D. H. Youn, S. K. Stauffer, P. Xiao, H. Park, Y. Nam, A. Dolocan, G. Henkelman, A. Heller

and C. B. Mullins, *ACS Nano*, 2016, **10**, 10778–10788.

298 C. Ma, Y. Zhao, J. Li, Y. Song, J. Shi, Q. Guo and L. Liu, *Carbon N. Y.*, 2013, 64, 553–556.

299 K. Wang, Y. Jin, S. Sun, Y. Huang, J. Peng, J. Luo, Q. Zhang, Y. Qiu, C. Fang and J. Han, *ACS Omega*, 2017, **2**, 1687–1695.

300 H. Zheng, Q. Qu, L. Zhang, G. Liu and V. S. Battaglia, *RSC Adv.*, 2012, **2**, 4904–4912.

301 Z. Yan, Q. Hu, G. Yan, H. Li, K. Shih, Z. Yang, X. Li, Z. Wang and J. Wang, *Chem. Eng. J.*, 2017, **321**, 495–501.

302 L. Zhang and C. Chen, *Prog. Chem.*, 2011, **23**, 275–283.

303 P. G. Bruce, B. Scrosati and J.-M. Tarascon, *Angew. Chemie Int. Ed.*, 2008, **47**, 2930–2946.

304 V. Aravindan, Y.-S. Lee and S. Madhavi, *Adv. Energy Mater.*, 2015, **5**, 1402225.

305 H. Kang, Y. Liu, K. Cao, Y. Zhao, L. Jiao, Y. Wang and H. Yuan, *J. Mater. Chem. A*, 2015, 3, 17899–17913.

306 Y. Zhao, L. P. Wang, M. T. Sougrati, Z. Feng, Y. Leconte, A. Fisher, M. Srinivasan and Z. Xu, *Adv. Energy Mater.*, 2017, 7.

307 Z. J. Han, N. Yabuuchi, K. Shimomura, M. Murase, H. Yui and S. Komaba, *Energy Environ. Sci.*, 2012, **5**, 9014–9020.

308 N. D. Rago, J. K. Basco, A. Vu, J. Li, K. Hays, Y. Sheng, D. L. Wood and I. Bloom, *J. Power Sources*, 2019, 435.

309 X. Li, M. Gu, S. Hu, R. Kennard, P. Yan, X. Chen, C. Wang, M. J. Sailor, J. G. Zhang and J. Liu, *Nat. Commun.*, 2014, 5.

310 L. Pan, H. Wang, D. Gao, S. Chen, L. Tan and L. Li, *Chem. Commun.*, 2014, **50**, 5878–5880.

311 C. K. Chan, H. Peng, G. Liu, K. McIlwrath, X. F. Zhang, R. A. Huggins and Y. Cui, *Nat. Nanotechnol.*, 2008, **3**, 31–35.

312 S. Yoon and A. Manthiram, *Chem. Mater.*, 2009, **21**, 3898–3904.

313 D. E. Demirocak and B. Bhushan, *J. Power Sources*, 2015, **280**, 256–262.

314 C. R. Birkl, M. R. Roberts, E. McTurk, P. G. Bruce and D. A. Howey, *J. Power Sources*, 2017, **341**, 373–386.

315 M. M. Kabir and D. E. Demirocak, *Int. J. Energy Res.*, 2017, **41**, 1963–1986.

316 M. Broussely, P. Biensan, F. Bonhomme, P. Blanchard, S. Herreyre, K. Nechev and R. J. Staniewicz, in *Journal of Power Sources*, 2005, vol. 146, pp. 90–96.

317 P. Arora, R. E. White and M. Doyle, *J. Electrochem. Soc.*, 1998, **145**, 3647–3667.

318 K. Sato, M. Noguchi, A. Demachi, N. Oki and M. Endo, *Science*, 1994, **264**, 556–558.

319 P. K. Nayak, T. R. Penki, B. Markovsky and D. Aurbach, *ACS Energy Lett.*, 2017, **2**, 544–

548.

320 J. Ming, Z. Cao, W. Wahyudi, M. Li, P. Kumar, Y. Wu, J.-Y. Hwang, M. N. Hedhili, L. Cavallo, Y.-K. Sun and L.-J. Li, *ACS Energy Lett.*, 2018, **3**, 335–340.

321 T. Abe, H. Fukuda, Y. Iriyama and Z. Ogumi, *J. Electrochem. Soc.*, 2004, **151**, A1120.

322 G. R. Li, H. Xu, X. F. Lu, J. X. Feng, Y. X. Tong and C. Y. Su, *Nanoscale*, 2013, **5**, 4056–4069.

323 J. S. Chen and X. W. D. Lou, *Small*, 2013, **9**, 1877–1893.

324 M. Simões, Y. Surace, S. Yoon, C. Battaglia, S. Pokrant and A. Weidenkaff, *J. Power Sources*, 2015, **291**, 66–74.

325 M. R. Palacín, *Chem. Soc. Rev.*, 2009, **38**, 2565–2575.

326 J. N. Tiwari, R. N. Tiwari and K. S. Kim, *Prog. Mater. Sci.*, 2012, 57, 724–803.

327 J. Jiang, Y. Li, J. Liu and X. Huang, *Nanoscale*, 2011, 3, 45–58.

328 J. Guo and J. Liu, *RSC Adv.*, 2014, **4**, 12950–12957.

329 Y. Zeng, Y. Han, Y. Zhao, Y. Zeng, M. Yu, Y. Liu, H. Tang, Y. Tong and X. Lu, *Adv. Energy Mater.*, 2015, **5**, 1402176.

330 M. S. Balogun, M. Yu, C. Li, T. Zhai, Y. Liu, X. Lu and Y. Tong, *J. Mater. Chem. A*, 2014, **2**, 10825–10829.

331 X.-F. Lu, X.-Y. Chen, W. Zhou, Y.-X. Tong and G.-R. Li, *ACS Appl. Mater. Interfaces*, 2015, **7**, 14843–14850.

332 M. S. Balogun, W. Qiu, Y. Luo, H. Meng, W. Mai, A. Onasanya, T. K. Olaniyi and Y. Tong, *Nano Res.*, 2016, 9, 2823–2851.

333 M. Yu, W. Qiu, F. Wang, T. Zhai, P. Fang, X. Lu and Y. Tong, *J. Mater. Chem. A*, 2015, 3, 15792–15823.

334 B. L. Ellis, P. Knauth and T. Djenizian, *Adv. Mater.*, 2014, **26**, 3368–3397.

335 R. Raccichini, A. Varzi, S. Passerini and B. Scrosati, *Nat. Mater.*, 2015, **14**, 271–279.

336 M. Chhowalla, H. S. Shin, G. Eda, L. J. Li, K. P. Loh and H. Zhang, *Nat. Chem.*, 2013, 5, 263–275.

337 Y. Zhong, T. Shi, Y. Huang, S. Cheng, C. Chen, G. Liao and Z. Tang, *Nanoscale Res. Lett.*, 2019, 14.

338 J. Tian, Z. Yang, Z. Yin, Z. Ye, J. Wang, C. Cui and W. Qian, *Chem. Rec.*, 2019, **19**, 1256–1262.

339 J. Zhu, R. Duan, S. Zhang, N. Jiang, Y. Zhang and J. Zhu, *J. Korean Phys. Soc.*, 2014, 3, 1–8.

340 M. Li, J. Lu, Z. Chen and K. Amine, *Adv. Mater.*, 2018, **30**, 1800561.

341 S. Goriparti, E. Miele, F. De Angelis, E. Di Fabrizio, R. Proietti Zaccaria and C. Capiglia, *J.*

Power Sources, 2014, 257, 421–443.

342 X. Xu, W. Liu, Y. Kim and J. Cho, *Nano Today*, 2014, 9, 604–630.

343 H. Wang, H. Feng and J. Li, *Small*, 2014, **10**, 2165–2181.

344 J. Wang, L. Zhang, K. Sun, J. He, Y. Zheng, C. Xu, Y. Zhang, Y. Chen and M. Li, *Chem. Eng. J.*, 2019, **372**, 665–672.

345 T. Stephenson, Z. Li, B. Olsen and D. Mitlin, *Energy Environ. Sci.*, 2014, 7, 209–231.

346 C. Sun, K. Zhao, Y. He, J. Zheng, W. Xu, C. Zhang, X. Wang, M. Guo, L. Mai, C. Wang and M. Gu, *ACS Appl. Mater. Interfaces*, 2019, **11**, 20762–20769.

347 L. Wang, Z. Xu, W. Wang and X. Bai, *J. Am. Chem. Soc.*, 2014, **136**, 6693–6697.

348 J. Heising and M. G. Kanatzidis, *J. Am. Chem. Soc.*, 1999, **121**, 638–643.

349 F. Wypych and R. Schöllhorn, *J. Chem. Soc. Chem. Commun.*, 1992, 1386–1388.

350 G. Gao, Y. Jiao, F. Ma, Y. Jiao, E. Waclawik and A. Du, *J. Phys. Chem. C*, 2015, **119**, 13124–13128.

351 X. Qian, J. Liu, L. Fu and J. Li, *Science*, 2014, **346**, 1344–1347.

352 S. Yan, W. Qiao, X. He, X. Guo, L. Xi, W. Zhong and Y. Du, *Appl. Phys. Lett.*, 2015, 106.

353 G. Eda, T. Fujita, H. Yamaguchi, D. Voiry, M. Chen and M. Chhowalla, *ACS Nano*, 2012, **6**, 7311–7317.

354 M. Calandra, *Phys. Rev. B - Condens. Matter Mater. Phys.*, 2013, **88**, 245428.

355 U. Krishnan, M. Kaur, K. Singh, M. Kumar and A. Kumar, *Superlattices Microstruct.*, 2019, 128, 274–297.

356 H. Jiang, D. Ren, H. Wang, Y. Hu, S. Guo, H. Yuan, P. Hu, L. Zhang and C. Li, *Adv. Mater.*, 2015, **27**, 3687–3695.

357 D. Kong, H. He, Q. Song, B. Wang, W. Lv, Q. H. Yang and L. Zhi, *Energy Environ. Sci.*, 2014, **7**, 3320–3325.

358 L. Wang, Z. Xu, W. Wang and X. Bai, *J. Am. Chem. Soc.*, 2014, **136**, 6693–6697.

359 Y. Diao, K. Xie, S. Xiong and X. Hong, *J. Electrochem. Soc.*, 2012, **159**, A421–A425.

360 L. Suo, Y. S. Hu, H. Li, M. Armand and L. Chen, *Nat. Commun.*, 2013, **4**, 1–9.

361 X. Chen, J. He, D. Srivastava and J. Li, *Appl. Phys. Lett.*, 2012, **100**, 263901.

362 C. George, A. J. Morris, M. H. Modarres and M. De Volder, *Chem. Mater.*, 2016, **28**, 7304–7310.

363 H. Yu, C. Zhu, K. Zhang, Y. Chen, C. Li, P. Gao, P. Yang and Q. Ouyang, *J. Mater. Chem. A*, 2014, **2**, 4551–4557.

364 Z. Bai, Y. Zhang, Y. Zhang, C. Guo and B. Tang, *Chem. - A Eur. J.*, 2015, **21**, 18187–18191.

365 S. Ding, D. Zhang, J. S. Chen and X. W. Lou, *Nanoscale*, 2012, **4**, 95–98.

366 J. Guo, X. Chen, S. Jin, M. Zhang and C. Liang, *Catal. Today*, 2015, **246**, 165–171.

367 J. Wang, D. Chao, J. Liu, L. Li, L. Lai, J. Lin and Z. Shen, *Nano Energy*, 2014, **7**, 151–160.

368 Q. Li, E. C. Walter, W. E. Van Der Veer, B. J. Murray, J. T. Newberg, E. W. Bohannan, J. A. Switzer, J. C. Hemminger and R. M. Penner, *J. Phys. Chem. B*, 2005, **109**, 3169–3182.

369 Y. Li, D. Wu, Z. Zhou, C. R. Cabrera and Z. Chen, *J. Phys. Chem. Lett.*, 2012, **3**, 2221–2227.

370 H. Liu, D. Su, R. Zhou, B. Sun, G. Wang and S. Z. Qiao, *Adv. Energy Mater.*, 2012, **2**, 970–975.

371 T. Stephenson, Z. Li, B. Olsen and D. Mitlin, *Energy Environ. Sci.*, 2014, 7, 209–231.

372 K. D. Rasamani, F. Alimohammadi and Y. Sun, *Mater. Today*, 2017, 20, 83–91.

373 Y. Waseda, E. Matsubara and K. Shinoda, *X-Ray Diffraction Crystallography Introduction, Examples and Solved Problems*, Springer Berlin, 2014.

374 J. W. Niemantsverdriet, *Spectroscopy in Catalysis: An Introduction: Third Edition*, Wiley-VCH, 2007.

375 D. B. Williams and C. B. Carter, *Transmission electron microscopy: A textbook for materials science*, Springer US, 2009.

376 L. Reimer and H. (Helmut) Kohl, *Transmission electron microscopy : physics of image formation*, Springer, 2010.

377 M. R. Armstrong, K. Boyden, N. D. Browning, G. H. Campbell, J. D. Colvin, W. J. DeHope, A. M. Frank, D. J. Gibson, F. Hartemann, J. S. Kim, W. E. King, T. B. LaGrange, B. J. Pyke, B. W. Reed, R. M. Shuttlesworth, B. C. Stuart and B. R. Torralva, *Ultramicroscopy*, 2007, **107**, 356–367.

378 R. J. Keyse, A. J. Garratt-Reed, P. J. Goodhew and G. W. Lorimer, *Introduction to Scanning Transmission Electron Microscopy*, Routledge, 2018.

379 P. D. Nellist, in *Scanning Transmission Electron Microscopy*, Springer New York, New York, NY, 2011, pp. 91–115.

380 J. D. Rodenburg and R. H. T. Bates, *Philos. Trans. R. Soc. London. Ser. A Phys. Eng. Sci.*, 1992, **339**, 521–553.

381 V. W. Hoppe, *Beugung im Inhomogenen Prim˜irstrahlwellenfeld. I. Prinzip einer Phasenmessung von Elektronenbeugungsinterferenzen*, 1969, vol. 25.

382 S. Gao, P. Wang, F. Zhang, G. T. Martinez, P. D. Nellist, X. Pan and A. I. Kirkland, *Nat. Commun.*, 2017, 8.

383 Y. K. Peng, Y. Hu, H. L. Chou, Y. Fu, I. F. Teixeira, L. Zhang, H. He and S. C. E. Tsang, *Nat. Commun.*, 2017, 8.

384 J. A. Iggo, *NMR spectroscopy in inorganic chemistry*, Oxford University Press, 1999.

385 M. Mehta, *J. Chem. Educ.*, 2002, **79**, 677.

386 M. J. Duer, *Solid-state NMR spectroscopy : principles and applications*, Blackwell Science, 2002.

387 C. H. . Lunsford, J. H.; Sang, H.; Campbell, S. M.; Liang and R. G. Anthony, *Catal. Lett.*, 1994, **27**, 305.

388 B. Odom, D. Hanneke, B. D'urso and G. Gabrielse, *Phys. Rev. Lett.*

389 J. M. Mermet, *J. Anal. At. Spectrom.*, 2005, 20, 11–16.

390 A. Stefánsson, I. Gunnarsson and N. Giroud, *Anal. Chim. Acta*, 2007, **582**, 69–74.

391 S. Skujins, *Handbook for ICP-AES (Varian-Vista), A Short Guide to Vista Series ICP-AES Operation*, Zug, 1.0., 1998.

392 D. J. (Derek J. . Gardiner, P. R. (Pierre R. . Graves and H. J. (Heather J. . Bowley, *Practical Raman spectroscopy*, Springer-Verlag, 1989.

393 S. Vyazovkin, in *Characterization of Materials*, John Wiley & Sons, Inc., Hoboken, NJ, USA, 2012.

394 S. Brunauer, P. H. Emmett and E. Teller, *J. Am. Chem. Soc.*, 1938, **60**, 309–319.

395 I. Langmuir, *J. Am. Chem. Soc.*, 1918, **40**, 1361–1403.

396 T. Suzuki and T. Okuhara, *Microporous Mesoporous Mater.*, 2001, **43**, 83–89.

397 K. A. Jadav, *Design a Residential PV Power System with Battery Energy Storage*, 2015.

398 H. Yang, R. N. Rutte, L. Jones, M. Simson, R. Sagawa, H. Ryll, M. Huth, T. J. Pennycook, M. L. H. Green, H. Soltau, Y. Kondo, B. G. Davis and P. D. Nellist, *Nat. Commun.*, 2016, **7**, 1–8.

399 H. Yang, I. MacLaren, L. Jones, G. T. Martinez, M. Simson, M. Huth, H. Ryll, H. Soltau, R. Sagawa, Y. Kondo, C. Ophus, P. Ercius, L. Jin, A. Kovács and P. D. Nellist, *Ultramicroscopy*, 2017, **180**, 173–179.

400 J. Q. Bond, D. M. Alonso, D. Wang, R. M. West and J. A. Dumesic, *Science*, 2010, **327**, 1110–1114.

401 J. N. Chheda, G. W. Huber and J. A. Dumesic, *Angew. Chemie Int. Ed.*, 2007, **46**, 7164–7183.

402 H. Joshi, B. R. Moser, J. Toler, W. F. Smith and T. Walker, *Biomass and Bioenergy*, 2011, **35**, 3262–3266.

403 E. S. Olson, M. R. Kjelden, A. J. Schlag and R. K. Sharma, 2001, pp. 51–63.

404 C. Sasikala, C. V. Ramana and P. R. Rao, *Biotechnol. Prog.*, 1994, **10**, 451–459.

405 Z. Dabrowski, M. Kwaśny, J. Kamiński, M. Bełdowicz, L. Lewicka, B. Obukowicz, M. Kaliszewski and E. Pirozyńska, *Acta Pol. Pharm. - Drug Res.*, 2003, **60**, 219–224.

406 S. Saravanamurugan and A. Riisager, *Catal. Commun.*, 2012, **17**, 71–75.

407 L. Peng, L. Lin, H. Li and Q. Yang, *Appl. Energy*, 2011, **88**, 4590–4596.

408 L. Peng, L. Lin, J. Zhang, J. Shi and S. Liu, *Appl. Catal. A Gen.*, 2011, **397**, 259–265.

409 D. R. Fernandes, A. S. Rocha, E. F. Mai, C. J. A. Mota and V. Teixeira Da Silva, *Appl. Catal. A Gen.*, 2012, 199–204.

410 J.-P. Lange, W. D. van de Graaf and R. J. Haan, *ChemSusChem*, 2009, **2**, 437–441.

411 M. Mascal and E. B. Nikitin, *Green Chem.*, 2010, **12**, 370–373.

412 Z. Zhang, R. Yang, S. Zhang, H. Zhao and X. Hua, *J. Food Eng.*, 2011, **105**, 112–118.

413 G. Pasquale, P. Vázquez, G. Romanelli and G. Baronetti, *Catal. Commun.*, 2012, **18**, 115–120.

414 A. Lee, N. Chaibakhsh, M. B. A. Rahman, M. Basri and B. A. Tejo, *Ind. Crops Prod.*, 2010, **32**, 246–251.

415 D. R. Fernandes, A. S. Rocha, E. F. Mai, C. J. A. Mota and V. Teixeira Da Silva, *Appl. Catal. A Gen.*, 2012, **425**–**426**, 199–204.

416 J. J. Bozell and G. R. Petersen, *Green Chem.*, 2010, 12, 539–554.

417 C. Chang, G. Xu and X. Jiang, *Bioresour. Technol.*, 2012, **121**, 93–99.

418 T. Okuhara, *Chem. Rev.*, 2002, **102**, 3641–3666.

419 E. C. Njagi, H. C. Genuino, C. H. Kuo, S. Dharmarathna, A. Gudz and S. L. Suib, *Microporous Mesoporous Mater.*, 2015, **202**, 68–72.

420 J. H. Clark, *Acc. Chem. Res.*, 2002, **35**, 791–797.

421 K. Tanabe and W. F. Hölderich, *Appl. Catal. A Gen.*, 1999, **181**, 399–434.

422 M. Hunger, *Zeolite Characterization and Catalysis*, 2009.

423 Z. Ma, Y. Yue, X. Deng and Z. Gao, *J. Mol. Catal. A Chem.*, 2002, **178**, 97–104.

424 X. Song and A. Sayari, *Catal. Rev. - Sci. Eng.*, 1996, **38**, 329–412.

425 H. T. Kreissl, K. Nakagawa, Y. K. Peng, Y. Koito, J. Zheng and S. C. E. Tsang, *J. Catal.*, 2016, **338**, 329–339.

426 M. S. Chavali and M. P. Nikolova, *SN Appl. Sci.*, 2019, **1**, 607.

427 Y. Koito, G. J. Rees, V. Hanna, John, M. J. M. Li, Y.-K. Peng, T. Puchtler, R. Taylor, T. Wang, H. Kobayashi, I. F. Teixeira, M. A. Khan, H. T. Kreissl and S. C. E. Tsang, *ACS Catal.*

428 D. Himmel, S. K. Goll, I. Leito and I. Krossing, *Angew. Chemie - Int. Ed.*, 2010, **49**, 6885–6888.

429 T. Ohno, K. Sarukawa, K. Tokieda and M. Matsumura, *J. Catal.*, 2001, **203**, 82–86.

430 T. Ohno, K. Sarukawa, K. Tokieda and M. Matsumura, *J. Catal.*, 2001, **203**, 82–86.

431 D. O. Scanlon, C. W. Dunnill, J. Buckeridge, S. A. Shevlin, A. J. Logsdail, S. M. Woodley, C. R. A. Catlow, M. J. Powell, R. G. Palgrave, I. P. Parkin, G. W. Watson, T. W. Keal, P. Sherwood, A. Walsh and A. A. Sokol, *Nat. Mater.*, 2013, **12**, 798–801.

432 R. M. de Almeida, L. K. Noda, N. S. Gonçalves, S. M. P. Meneghetti and M. R. Meneghetti, *Appl. Catal. A Gen.*, 2008, **347**, 100–105.

433 X. H. Lin, X. J. Yin, J. Y. Liu and S. F. Yau Li, *Appl. Catal. B Environ.*, 2017, **203**, 731–739.

434 N. A. S. Ramli, D. Sivasubramaniam and N. A. S. Amin, *BioEnergy Res.*, 2017, **10**, 1105–1116.

435 S. Bagheri, K. Shameli and S. B. Abd Hamid, *J. Chem.*, , DOI:10.1155/2013/848205.

436 S. S. El-Deen, A. M. Hashem, A. E. Abdel Ghany, S. Indris, H. Ehrenberg, A. Mauger and C. M. Julien, *Ionics (Kiel).*, 2018, **24**, 2925–2934.

437 V. H. Castrejón-Sánchez, E. Camps and M. Camacho-López, *Superf. y Vacío*, 2014, **27**, 88–92.

438 N. Bouanimba, N. Laid, R. Zouaghi and T. Sehili, *Int. J. Chem. React. Eng.*, 2018, 16.

439 G. Wang, L. Xu, J. Zhang, T. Yin and D. Han, *Int. J. Photoenergy*, 2012, 2012.

440 A. Corma, A. Martïnez and C. Martínez, *Appl. Catal. A Gen.*, 1996, **144**, 249–268.

441 H. Esteban Benito, T. Del Ángel Sánchez, R. García Alamilla, J. M. Hernández Enríquez, G. Sandoval Robles and F. Paraguay Delgado, *Brazilian J. Chem. Eng.*, 2014, **31**, 737–745.

442 X-ray Photoelectron Spectroscopy (XPS) Reference Pages: Titanium, http://www.xpsfitting.com/2008/09/titanium.html.

443 P. Goswami and J. N. Ganguli, *RSC Adv.*, 2013, **3**, 8878–8888.

444 NIST X-ray Photoelectron Spectroscopy (XPS) Database, Version 3.5, https://srdata.nist.gov/xps/.

445 M. C. Biesinger, B. P. Payne, B. R. Hart, A. P. Grosvenor, N. S. McIntryre, L. W. M. Lau and R. S. C. Smart, *J. Phys. Conf. Ser.*, 2008, **100**, 012025.

446 M. C. Biesinger, L. W. M. Lau, A. R. Gerson and R. S. C. Smart, *Appl. Surf. Sci.*, 2010, **257**, 887–898.

447 Q. Yang, C. Xie, Z. Xu, Z. Gao and Y. Du, *J. Phys. Chem. B*, 2005, **109**, 5554–5560.

448 S. Liu, M. Zhu and M. Iqbal, *Catal. Surv. from Asia*, 2020, **24**, 196–206.

449 K. M. A. Santos, E. M. Albuquerque, L. E. P. Borges and M. A. Fraga, *Mol. Catal.*, 2018, **458**, 198–205.

450 Y. Niu, L. K. Yeung and R. M. Crooks, *J. Am. Chem. Soc.*, 2001, **123**, 6840–6846.

451 C. Premi and N. Jain, *RSC Adv.*, 2016, **6**, 74961–74967.

452 J. Huang, T. Jiang, B. Han, H. Gao, Y. Chang, G. Zhao and W. Wu, *Chem. Commun.*, 2003, **3**, 1654–1655.

453 O. M. Wilson, M. R. Knecht, J. C. Garcia-Martinez and R. M. Crooks, *J. Am. Chem. Soc.*, 2006, **128**, 4510–4511.

454 Z. Hou, N. Theyssen and W. Leitner, *Green Chem.*, 2007, **9**, 127–132.

455 J. Yang, C. Tian, L. Wang and H. Fu, *J. Mater. Chem.*, 2011, **21**, 3384–3390.

456 N. Hussain, A. Borah, G. Darabdhara, P. Gogoi, V. K. Azhagan, M. V. Shelke and M. R. Das, *New J. Chem.*, 2015, **39**, 6631–6641.

457 J. Hu, Y. Wang, M. Han, Y. Zhou, X. Jiang and P. Sun, *Catal. Sci. Technol.*, 2012, **2**, 2332–2340.

458 P. D. Stevens, G. Li, J. Fan, M. Yen and Y. Gao, *Chem. Commun.*, 2005, 4435–4437.

459 C. Yi and R. Hua, *Catal. Commun.*, 2006, **7**, 377–379.

460 J. Michalik, M. Narayna and L. Kevan, *J. Phys. Chem.*, 1985, **89**, 4553–4560.

461 W. M. H. Sachtler, F. A. P. Cavalcanti and Z. Zhang, *Catal. Letters*, 1991, **9**, 261–271.

462 V. Arun, N. Sridevi, P. P. Robinson, S. Manju and K. K. M. Yusuff, *J. Mol. Catal. A Chem.*, 2009, **304**, 191–198.

463 S. Niembro, A. Shafir, A. Vallribera and R. Alibés, *Org. Lett.*, 2008, **10**, 3215–3218.

464 Y. Li, X. M. Hong, D. M. Collard and M. A. El-Sayed, *Org. Lett.*, 2000, **2**, 2385–2388.

465 J. Hu and Y. Liu, *Langmuir*, 2005, **21**, 2121–2123.

466 R. Narayanan and M. A. El-Sayed, *J. Am. Chem. Soc.*, 2003, **125**, 8340–8347.

467 K. Mennecke, R. Cecilia, T. N. Glasnov, S. Gruhl, C. Vogt, A. Feldhoff, M. A. L. Vargas, C. O. Kappe, U. Kunz and A. Kirschning, *Adv. Synth. Catal.*, 2008, **350**, 717–730.

468 L. Xu, W. Chen and J. Xiao, *Organometallics*, 2000, **19**, 1123–1127.

469 R. R. Deshmukh, R. Rajagopal and K. V. Srinivasan, *Chem. Commun.*, 2001, **1**, 1544–1545.

470 X. Yang, Z. Fei, D. Zhao, H. A. Wee, Y. Li and P. J. Dyson, *Inorg. Chem.*, 2008, **47**, 3292–3297.

471 C. Premi and N. Jain, *European J. Org. Chem.*, 2013, **2013**, 5493–5499.

472 N. T. S. Phan, M. Van Der Sluys and C. W. Jones, *Adv. Synth. Catal.*, 2006, **348**, 609–679.

473 P. R. R. Vadaparthi, C. Pavan Kumar, K. Kumar, A. Venkanna, V. Lakshma Nayak, S. Ramakrishna and K. S. Babu, *Med. Chem. Res.*, 2015, **24**, 2871–2878.

474 P. C. Rodrigues, B. D. Fontes, B. B. M. Torres, W. S. Sousa, G. C. Faria, D. T. Balogh, R. M. Faria and L. Akcelrud, *J. Appl. Polym. Sci.*, 2015, **132**, 42579.

475 S. Das, S. Jana, B. Dutta and S. Koner, *Res. Chem. Intermed.*, 2015, **41**, 4825–4832.

476 I. Favier, D. Madec, E. Teuma and M. Gomez, *Curr. Org. Chem.*, 2011, **15**, 3127–3174.

477 A. Fihri, M. Bouhrara, B. Nekoueishahraki, J. M. Basset and V. Polshettiwar, *Chem. Soc. Rev.*, 2011, 40, 5181–5203.

478 J. Hassan, M. Sévignon, C. Gozzi, E. Schulz and M. Lemaire, *Chem. Rev.*, 2002, **102**,

1359–1469.

479 Y. Li, E. Boone and M. A. El-Sayed, *Langmuir*, 2002, **18**, 4921–4925.

480 X. Chen, G. Wu, J. Chen, X. Chen, Z. Xie and X. Wang, *J. Am. Chem. Soc.*, 2011, **133**, 3693–3695.

481 G. M. Scheuermann, L. Rumi, P. Steurer, W. Bannwarth and R. Mülhaupt, *J. Am. Chem. Soc.*, 2009, **131**, 8262–8270.

482 M. Chen, Z. Zhang, L. Li, Y. Liu, W. Wang and J. Gao, *RSC Adv.*, 2014, **4**, 30914–30922.

483 M. Amini, A. Tarassoli, S. Yousefi, S. Delsouz-Hafshejani, M. Bigdeli and M. Salehifar, *Chinese Chem. Lett.*, 2014, **25**, 166–168.

484 J. P. Wolfe, R. A. Singer, B. H. Yang and S. L. Buchwald, *J. Am. Chem. Soc.*, 1999, **121**, 9550–9561.

485 Y. Li and M. A. El-Sayed, *J. Phys. Chem. B*, 2001, **105**, 8938–8943.

486 M. Bakherad, A. Keivanloo, B. Bahramian and S. Jajarmi, *J. Organomet. Chem.*, 2013, **724**, 206–212.

487 Y. H. Qin, Yue-Jiang, H. H. Yang, X. S. Zhang, X. G. Zhou, L. Niu and W. K. Yuan, *J. Power Sources*, 2011, **196**, 4609–4612.

488 Y. S. Feng, X. Y. Lin, J. Hao and H. J. Xu, *Tetrahedron*, 2014, **70**, 5249–5253.

489 S. Keesara, S. Parvathaneni, G. Dussa and M. R. Mandapati, *J. Organomet. Chem.*, 2014, **765**, 31–38.

490 L. Shao and C. Qi, *Fibers Polym.*, 2014, **15**, 2233–2237.

491 M. Ghiaci, D. Valikhani and Z. Sadeghi, *Chinese Chem. Lett.*, 2012, **23**, 887–890.

492 H. Yang, D. Shi, S. F. Ji, D. N. Zhang and X. F. Liu, *Chinese Chem. Lett.*, 2014, **25**, 1265–1270.

493 S. Jadhav, A. Kumbhar and R. Salunkhe, *Appl. Organomet. Chem.*, 2015, **29**, 339–345.

494 F.-X. Felpin, T. Ayad and S. Mitra, *European J. Org. Chem.*, 2006, **2006**, 2679–2690.

495 F. X. Felpin, *Synlett*, 2014, **25**, 1055–1067.

496 E. Cini, E. Petricci and M. Taddei, *Catalysts*, 2017, **7**, 89.

497 M. D. Bowman, J. R. Schmink, C. M. McGowan, C. M. Kormos and N. E. Leadbeater, *Org. Process Res. Dev.*, 2008, **12**, 1078–1088.

498 F. Giacalone, V. Campisciano, C. Calabrese, V. La Parola, L. F. Liotta, C. Aprile and M. Gruttadauria, *J. Mater. Chem. A*, 2016, **4**, 17193–17206.

499 M. Seki, *J. Synth. Org. Chem. Japan*, 2006, **64**, 853–866.

500 X. Y. Zhou, X. Chen and L. G. Wang, *Synth.*, 2017, **49**, 5364–5370.

501 E. J. García-Suárez, P. Lara, A. B. García, M. Ojeda, R. Luque and K. Philippot, *Appl. Catal. A Gen.*, 2013, **468**, 59–67.

502 T. Hattori, A. Tsubone, Y. Sawama, Y. Monguchi and H. Sajiki, *Catalysts*, 2015, **5**, 18–25.

503 S. Horikoshi and N. Serpone, *Catal. Sci. Technol.*, 2014, 4, 1197–1210.

504 Y.-Q. Yuan and S.-R. Guo, *Synth. Commun.*, 2012, **42**, 1059–1069.

505 B. Schmidt and M. Riemer, *J. Org. Chem.*, 2014, **79**, 4104–4118.

506 J. S. Freundlich and H. E. Landis, *Tetrahedron Lett.*, 2006, **47**, 4275–4279.

507 M. Dighe, S. Lonkar and M. Degani, *Synlett*, 2013, **24**, 347–350.

508 D. Schils, F. Stappers, G. Solberghe, R. van Heck, M. Coppens, D. Van den Heuvel, P. Van der Donck, T. Callewaert, F. Meeussen, E. De Bie, K. Eersels and E. Schouteden, *Org. Process Res. Dev.*, 2008, **12**, 530–536.

509 P. Mpungose, Z. Vundla, G. Maguire and H. Friedrich, *Molecules*, 2018, **23**, 1676.

510 N. A. Dobson, G. Eglinton, M. Krishnamurti, R. A. Raphael and R. G. Willis, *Tetrahedron*, 1961, **16**, 16–24.

511 S. P. Thomas and M. D. Greenhalgh, in *Comprehensive Organic Synthesis: Second Edition*, Elsevier Ltd., 2014, vol. 8, pp. 564–604.

512 F. A. Carey and R. J. Sundberg, in *Advanced Organic Chemistry*, Springer US, Boston, MA, pp. 1–117.

513 H. Lebel and V. Paquet, *J. Am. Chem. Soc.*, 2004, **126**, 11152–11153.

514 S. M. Sadrameli, *Fuel*, 2015, 140, 102–115.

515 Y. Ji, H. Yang and W. Yan, *Mol. Catal.*, 2018, **448**, 91–99.

516 G. Vilé, D. Albani, N. Almora-Barrios, N. López and J. Pérez-Ramírez, *ChemCatChem*, 2016, **8**, 21–33.

517 P. R. Ellis, C. M. Brown, P. T. Bishop, D. Ievlev, J. Yin, K. Cooke and R. E. Palmer, *Catal. Struct. React.*, 2018, **4**, 1–8.

518 Y. Yabe, T. Yamada, S. Nagata, Y. Sawama, Y. Monguchi and H. Sajiki, *Adv. Synth. Catal.*, 2012, **354**, 1264–1268.

519 M. W. Tew, H. Emerich and J. A. Van Bokhoven, *J. Phys. Chem. C*, 2011, **115**, 8457–8465.

520 Z. Shao, C. Li, X. Chen, M. Pang, X. Wang and C. Liang, *ChemCatChem*, 2010, **2**, 1555–1558.

521 F. Alonso, I. Osante and M. Yus, *Tetrahedron*, 2007, **63**, 93–102.

522 F. Alonso, I. Osante and M. Yus, *Adv. Synth. Catal.*, 2006, **348**, 305–308.

523 R. Nishio, M. Sugiura and S. Kobayashi, *Org. Biomol. Chem.*, 2006, **4**, 992–995.

524 H. S. La Pierre, J. Arnold and F. D. Toste, *Angew. Chemie*, 2011, **123**, 3986–3989.

525 C. R. Lederhos, J. M. Badano, M. E. Quiroga, P. C. L'Argentière and F. Coloma-Pascual, *Quim. Nova*, 2010, **33**, 816–820.

526 M. J. MacCarrone, C. R. Lederhos, G. Torres, C. Betti, F. Coloma-Pascual, M. E. Quiroga and J. C. Yori, *Appl. Catal. A Gen.*, 2012, **441**–**442**, 90–98.

527 C. R. Lederhos, J. M. Badano, N. Carrara, F. Coloma-Pascual, M. C. Almansa, D. Liprandi and M. Quiroga, *Sci. World J.*, 2013, **2013**, 528453.

528 D. Teschner, E. Vass, M. Hävecker, S. Zafeiratos, P. Schnörch, H. Sauer, A. Knop-Gericke, R. Schlögl, M. Chamam, A. Wootsch, A. S. Canning, J. J. Gamman, S. D. Jackson, J. McGregor and L. F. Gladden, *J. Catal.*, 2006, **242**, 26–37.

529 K. J. Hu, S. R. Plant, P. R. Ellis, C. M. Brown, P. T. Bishop and R. E. Palmer, *Phys. Chem. Chem. Phys.*, 2014, **16**, 26631–26637.

530 P. Albers, J. Pietsch and S. F. Parker, *J. Mol. Catal. A Chem.*, 2001, **173**, 275–286.

531 M. Cordoba, F. Coloma-Pascual, M. E. Quiroga and C. R. Lederhos, *Ind. Eng. Chem. Res.*, 2019, **58**, 17182–17194.

532 H. Lindlar, *Helv. Chim. Acta*, 1952, **35**, 446–450.

533 H. Lindlar and R. Dubuis, in *Organic Syntheses*, John Wiley & Sons, Inc., Hoboken, NJ, USA, 2003, pp. 89–89.

534 J. Rajaram, A. P. S. Narula, H. P. S. Chawla and S. Dev, *Tetrahedron*, 1983, **39**, 2315–2322.

535 J. J. Brunet and P. Caubere, *J. Org. Chem.*, 1984, **49**, 4058–4060.

536 H. Sajiki, S. Mori, T. Ohkubo, T. Ikawa, A. Kume, T. Maegawa and Y. Monguchi, *Chem. - A Eur. J.*, 2008, **14**, 5109–5111.

537 Y. Lee, Y. Motoyama, K. Tsuji, S.-H. Yoon, I. Mochida and H. Nagashima, *ChemCatChem*, 2012, **4**, 778–781.

538 T. Mitsudome, M. Yamamoto, Z. Maeno, T. Mizugaki, K. Jitsukawa and K. Kaneda, *J. Am. Chem. Soc.*, 2015, **137**, 13452–13455.

539 K. S. Novoselov, A. K. Geim, S. V. Morozov, D. Jiang, Y. Zhang, S. V. Dubonos, I. V. Grigorieva and A. A. Firsov, *Science*, 2004, **306**, 666–669.

540 X. Huang, Z. Yin, S. Wu, X. Qi, Q. He, Q. Zhang, Q. Yan, F. Boey and H. Zhang, *Small*, 2011, **7**, 1876–1902.

541 A. K. Geim and K. S. Novoselov, *Nat. Mater.*, 2007, **6**, 183–191.

542 Q. H. Wang, K. Kalantar-Zadeh, A. Kis, J. N. Coleman and M. S. Strano, *Nat. Nanotechnol.*, 2012, 7, 699–712.

543 H. Zeng, J. Dai, W. Yao, D. Xiao and X. Cui, *Nat. Nanotechnol.*, 2012, **7**, 490–493.

544 A. Splendiani, L. Sun, Y. Zhang, T. Li, J. Kim, C. Y. Chim, G. Galli and F. Wang, *Nano Lett.*, 2010, **10**, 1271–1275.

545 Z. Yin, H. Li, H. Li, L. Jiang, Y. Shi, Y. Sun, G. Lu, Q. Zhang, X. Chen and H. Zhang, *ACS Nano*, 2012, **6**, 74–80.

546 C. Sun, K. Zhao, Y. He, J. Zheng, W. Xu, C. Zhang, X. Wang, M. Guo, L. Mai, C. Wang and M. Gu, *ACS Appl. Mater. Interfaces*, 2019, **11**, 20762–20769.

547 C. George, A. J. Morris, M. H. Modarres and M. De Volder, *Chem. Mater.*, 2016, **28**, 7304–7310.

548 S. Wang, G. Deng, J. Gu, W. Hua, X. Jia and K. Xi, *Appl. Catal. A Gen.*, 2015, **508**, 80–85.

549 H. H. Shin, E. Kang, H. Park, T. Han, C. H. Lee and D. K. Lim, *J. Mater. Chem. A*, 2017, **5**, 24965–24971.

550 J. Ji, Y. Li, W. Fu, Z. Cui, J. Shen and M. Ye, *J. Colloid Interface Sci.*, 2017, **505**, 983–994.

551 T. H. M. Lau, S. Wu, R. Kato, T.-S. Wu, J. Kulhavý, J. Mo, J. Zheng, J. S. Foord, Y.-L. Soo, K. Suenaga, M. T. Darby and S. C. E. Tsang, *ACS Catal.*, 2019, **9**, 7527–7534.

552 N. Singh, G. Jabbour and U. Schwingenschlögl, *Eur. Phys. J. B*, 2012, **85**, 392.

553 T. H. M. Lau, X. Lu, J. Kulhavý, S. Wu, L. Lu, T. S. Wu, R. Kato, J. S. Foord, Y. L. Soo, K. Suenaga and S. C. E. Tsang, *Chem. Sci.*, 2018, **9**, 4769–4776.

554 G. Liu, A. W. Robertson, M. M. J. Li, W. C. H. Kuo, M. T. Darby, M. H. Muhieddine, Y. C. Lin, K. Suenaga, M. Stamatakis, J. H. Warner and S. C. E. Tsang, *Nat. Chem.*, 2017, **9**, 810–816.

555 R. Kappera, D. Voiry, S. E. Yalcin, B. Branch, G. Gupta, A. D. Mohite and M. Chhowalla, *Nat. Mater.*, 2014, **13**, 1128–1134.

556 A. Ambrosi, Z. Sofer and M. Pumera, *Small*, 2015, **11**, 605–612.

557 Y. Yin, J. Han, Y. Zhang, X. Zhang, P. Xu, Q. Yuan, L. Samad, X. Wang, Y. Wang, Z. Zhang, P. Zhang, X. Cao, B. Song and S. Jin, *J. Am. Chem. Soc.*, 2016, **138**, 7965–7972.

558 G. Gao, Y. Jiao, F. Ma, Y. Jiao, E. Waclawik and A. Du, *J. Phys. Chem. C*, 2015, **119**, 13124–13128.

559 K. Chang, X. Hai, H. Pang, H. Zhang, L. Shi, G. Liu, H. Liu, G. Zhao, M. Li and J. Ye, *Adv. Mater.*, 2016, **28**, 10033–10041.

560 M. A. Lukowski, A. S. Daniel, F. Meng, A. Forticaux, L. Li and S. Jin, *J. Am. Chem. Soc.*, 2013, **135**, 10274–10277.

561 D. Voiry, M. Salehi, R. Silva, T. Fujita, M. Chen, T. Asefa, V. B. Shenoy, G. Eda and M. Chhowalla, *Nano Lett.*, 2013, **13**, 6222–6227.

562 T. Jia, A. Kolpin, C. Ma, R. Chau-Ting Chan, W. M. Kwok and S. C. E. Tsang, *Chem. Commun.*, 2014, **50**, 1185–1188.

563 H. Li, S. Wang, H. Sawada, G. G. D. Han, T. Samuels, C. S. Allen, A. I. Kirkland, J. C. Grossman and J. H. Warner, *ACS Nano*, 2017, **11**, 3392–3403.

564 T. H. M. Lau, S. Wu, R. Kato, T.-S. Wu, J. Kulhavý, J. Mo, J. Zheng, J. S. Foord, Y.-L. Soo, K. Suenaga, M. T. Darby and S. C. E. Tsang, *ACS Catal.*, 2019, **9**, 7527–7534.

565 H. Li, Q. Zhang, C. C. R. Yap, B. K. Tay, T. H. T. Edwin, A. Olivier and D. Baillargeat, *Adv. Funct. Mater.*, 2012, **22**, 1385–1390.

566 E. Er, H. L. Hou, A. Criado, J. Langer, M. Möller, N. Erk, L. M. Liz-Marzán and M. Prato, *Chem. Mater.*, 2019, **31**, 5725–5734.

567 G. L. Frey, R. Tenne, M. J. Matthews, M. S. Dresselhaus and G. Dresselhaus, *Phys. Rev. B - Condens. Matter Mater. Phys.*, 1999, **60**, 2883–2892.

568 K. C. Knirsch, N. C. Berner, H. C. Nerl, C. S. Cucinotta, Z. Gholamvand, N. McEvoy, Z. Wang, I. Abramovic, P. Vecera, M. Halik, S. Sanvito, G. S. Duesberg, V. Nicolosi, F. Hauke, A. Hirsch, J. N. Coleman and C. Backes, *ACS Nano*, 2015, **9**, 6018–6030.

569 E. E. Benson, H. Zhang, S. A. Schuman, S. U. Nanayakkara, N. D. Bronstein, S. Ferrere, J. L. Blackburn and E. M. Miller, *J. Am. Chem. Soc.*, 2018, **140**, 441–450.

570 P. Joensen, E. D. Crozier, N. A. Alberding and R. F. Frindt, *J. Phys. C Solid State Phys.*, 1987, **20**, 4043.

571 H. Huang, Y. Cui, Q. Li, C. Dun, W. Zhou, W. Huang, L. Chen, C. A. Hewitt and D. L. Carroll, *Nano Energy*, 2016, **26**, 172–179.

572 K. D. Rasamani, F. Alimohammadi and Y. Sun, *Mater. Today*, 2017, **20**, 83–91.

573 M. Acerce, D. Voiry and M. Chhowalla, *Nat. Nanotechnol.*, 2015, **10**, 313–318.

574 K. Leng, Z. Chen, X. Zhao, W. Tang, B. Tian, C. T. Nai, W. Zhou and K. P. Loh, *ACS Nano*, 2016, **10**, 9208–9215.

575 S. Kim, W. Park, D. Kim, J. Kang, J. Lee, H. Y. Jang, S. H. Song, B. Cho and D. Lee, *Nanomaterials*, 2020, **10**, 1045.

576 H. Ye, L. Ma, Y. Zhou, L. Wang, N. Han, F. Zhao, J. Deng, T. Wu, Y. Li and J. Lu, *PNAS*, 2017, **114**, 13091–13096.

577 J. P. Wolfe and J. Jack Li, *Tetrahedron Org. Chem. Ser.*, 2007, **26**, 1–35.

578 S. McCarthy, D. C. Braddock and J. D. E. T. Wilton-Ely, *Coord. Chem. Rev.*, 2021, **442**, 213925.

579 B. Van Vaerenbergh, J. Lauwaert, P. Vermeir, J. W. Thybaut and J. De Clercq, *React. Chem. Eng.*, 2020, **5**, 1556–1618.

580 Libor Červený, *Chem. Eng. Commun.*, 1989, **83**, 31–63.

581 L. Yin and J. Liebscher, *Chem. Rev.*, 2006, **107**, 133–173.

582 M. Pagliaro, V. Pandarus, R. Ciriminna, F. Béland and P. DemmaCarà, *ChemCatChem*, 2012, **4**, 432–445.

583 Á. Molnár, *Chem. Rev.*, 2011, **111**, 2251–2320.

584 P. P. Mpungose, Z. P. Vundla, G. E. M. Maguire and H. B. Friedrich, *Mol. A J. Synth. Chem. Nat. Prod. Chem.*, 2018, **23**, 1–24.

585 Y. Monguchi, T. Ichikawa and H. Sajiki, *Chem. Pharm. Bull*, 2017, **65**, 2–9.

586 Q. A. Chen, Z. S. Ye, Y. Duan and Y. G. Zhou, *Chem. Soc. Rev.*, 2012, **42**, 497–511.

587 P. Veerakumar, P. Thanasekaran, K. L. Lu, S. Bin Liu and S. Rajagopal, *ACS Sustain. Chem.*

Eng., 2017, **5**, 6357–6376.

588 C. J. Crawford, Y. Qiao, Y. Liu, D. Huang, W. Yan, P. H. Seeberger, S. Oscarson and S. Chen, *Org. Process Res. Dev.*, 2021, 25, 1573–1578.

589 C. Chen, R. Felton, J. C. Buffet and D. O'Hare, *Chem. Commun.*, 2015, **51**, 3462–3465.

590 C. Chen, C. F. H. Byles, J. C. Buffet, N. H. Rees, Y. Wu and D. O'Hare, *Chem. Sci.*, 2016, **7**, 1457–1461.

591 D. Blakemore, *RSC Drug Discov. Ser.*, 2015, **1**, 1–69.

592 G. P. McGlacken and I. J. S. Fairiamb, *European J. Org. Chem.*, 2009, **2009**, 4011–4029.

593 B. Lin, X. Wu, L. Xie, Y. Kang, H. Du, F. Kang, J. Li and L. Gan, *Angew. Chemie Int. Ed.*, 2020, **59**, 20348–20352.

594 W. Liu, Y. Magnin, D. Förster, J. Bourgon, T. Len, F. Morfin, L. Piccolo, H. Amara and C. Zlotea, *J. Mater. Chem. A*, 2021, **9**, 10354–10363.

595 X. Guo, Z. Hu, J. Lv, H. Li, Q. Zhang, L. Gu, W. Zhou, J. Zhang and S. Hu, *Nano Res.*, 2021, **15**, 1288–1294.

596 J. Fan, X. Cui, S. Yu, L. Gu, Q. Zhang, F. Meng, Z. Peng, L. Ma, J. Y. Ma, K. Qi, Q. Bao and W. Zheng, *ACS Nano*, 2019, **13**, 12987–12995.

597 M. Evans, Metal Hydrides - Chemistry LibreTexts, https://chem.libretexts.org/Bookshelves/Inorganic_Chemistry/Supplemental_Modules_and_Websites_(Inorganic_Chemistry)/Organometallic_Chemistry_(Evans)/Organometallic_Ligands/Metal_Hydrides.

598 T. Chen, C. Foo and S. C. E. Tsang, *Chem. Sci.*, 2021, **12**, 517–532.

599 A. de Lambert de Boisjan, C. Allemann and L. Fadini, *Helv. Chim. Acta*, 2021, **104**, e2100035.

600 T. Maegawa, Y. Kitamura, S. Sako, T. Udzu, A. Sakurai, A. Tanaka, Y. Kobayashi, K. Endo, U. Bora, T. Kurita, A. Kozaki, Y. Monguchi and H. Sajiki, *Chem. – A Eur. J.*, 2007, **13**, 5937–5943.

601 J. Sherwood, J. H. Clark, I. J. S. Fairlamb and J. M. Slattery, *Green Chem.*, 2019, **21**, 2164–2213.

602 P. J. Dyson and P. G. Jessop, *Catal. Sci. Technol.*, 2016, **6**, 3302–3316.

603 F. M. Pang, C. E. Seng, T. T. Teng and M. H. Ibrahim, *J. Mol. Liq.*, 2007, **136**, 71–78.

604 M. S. Alam, B. Ashokkumar and A. Mohammed Siddiq, *J. Mol. Liq.*, 2018, **251**, 458–469.

605 M. M. Heravi, M. Ghavidel and L. Mohammadkhani, *RSC Adv.*, 2018, **8**, 27832–27862.

606 N. T. S. Phan, M. Van Der Sluys and C. W. Jones, *Adv. Synth. Catal.*, 2006, **348**, 609–679.

607 S. R. Sanjaykumar, B. D. Mukri, S. Patil, G. Madras and M. S. Hegde, *J. Chem. Sci. 2011 1231*, 2011, **123**, 47–54.

608 B. Yuan, Y. Pan, Y. Li, B. Yin and H. Jiang, *Angew. Chemie Int. Ed.*, 2010, **49**, 4054–4058.

609 H. H. Shin, E. Kang, H. Park, T. Han, C. H. Lee and D. K. Lim, *J. Mater. Chem. A*, 2017, **5**, 24965–24971.

610 C. Amatore and A. Jutand, *Acc. Chem. Res.*, 2000, **33**, 314–321.

611 T. Pavloudis, J. Kioseoglou and R. E. Palmer, *Phys. Chem. Chem. Phys.*, 2022, **24**, 3231–3237.

612 V. Dusastre and L. Martiradonna, *Nat. Mater.*, 2016, 16, 15.

613 R. Schlögl, *Top. Catal.*, 2016, **59**, 772–786.

614 R. Eisenberg, H. B. Gray and G. W. Crabtree, *Proc. Natl. Acad. Sci.*, 2019, 201821674.

615 A. Stoddart, *Nat. Rev. Mater.*, 2018, 3, 18021.

616 V. Etacheri, R. Marom, R. Elazari, G. Salitra and D. Aurbach, *Energy Environ. Sci.*, 2011, 4, 3243–3262.

617 H. Wang, D. Yu, C. Kuang, L. Cheng, W. Li, X. Feng, Z. Zhang, X. Zhang and Y. Zhang, *Chem*, 2019, 5, 313–338.

618 S. Yan, W. Qiao, X. He, X. Guo, L. Xi, W. Zhong and Y. Du, *Appl. Phys. Lett.*, 2015, 106, 012408.

619 H. Zhang, H. Zhao, M. A. Khan, W. Zou, J. Xu, L. Zhang and J. Zhang, *J. Mater. Chem. A*, 2018, 6, 20564–20620.

620 H. Wang, X. Liang, J. Wang, S. Jiao and D. Xue, *Nanoscale*, 2020, 12, 14–42.

621 K. S. Novoselov, A. K. Geim, S. V. Morozov, D. Jiang, Y. Zhang, S. V. Dubonos, I. V. Grigorieva and A. A. Firsov, *Science*, 2004, **306**, 666–669.

622 D. Nasr Esfahani, O. Leenaerts, H. Sahin, B. Partoens and F. M. Peeters, *J. Phys. Chem. C*, 2015, **119**, 10602–10609.

623 J. W. Jiang, *Front. Phys.*, 2015, 10, 287–302.

624 H. Wang, C. Li, P. Fang, Z. Zhang and J. Z. Zhang, *Chem. Soc. Rev.*, 2018, 47, 6101–6127.

625 D. Voiry, A. Mohite and M. Chhowalla, *Chem. Soc. Rev.*, 2015, 44, 2702–2712.

626 Q. Su, S. Wang, M. Feng, G. Du and B. Xu, *Sci. Rep.*, 2017, **7**, 1–10.

627 J. Zhou, J. Qin, X. Zhang, C. Shi, E. Liu, J. Li, N. Zhao and C. He, *ACS Nano*, 2015, **9**, 3837–3848.

628 C. N. R. Rao, K. Gopalakrishnan and U. Maitra, *ACS Appl. Mater. Interfaces*, 2015, **7**, 7809–7832.

629 L. Hu, Y. Ren, H. Yang and Q. Xu, *ACS Appl. Mater. Interfaces*, 2014, **6**, 14644–14652.

630 M. R. Gao, Y. F. Xu, J. Jiang and S. H. Yu, *Chem. Soc. Rev.*, 2013, 42, 2986–3017.

631 S. Gong, G. Zhao, N. Zhang and K. Sun, *ChemElectroChem*, 2019, **6**, 3393–3400.

632 D. Sun, D. Ye, P. Liu, Y. Tang, J. Guo, L. Wang and H. Wang, *Adv. Energy Mater.*, 2018, **8**, 1702383.

633 D. M. Soares and G. Singh, *Nanotechnology*, 2020, **31**, 145403.

634 M. Wang, Y. H. Xu, F. Lu, Z. Zhu, J. Y. Dong, D. L. Fang, J. Zhou, Y. J. Yang, Y. T. Zhong, S. M. Chen, Y. Bando, D. Golberg and X. Wang, *ChemElectroChem*, 2019, **6**, 1475–1484.

635 H. Huang, Y. Cui, Q. Li, C. Dun, W. Zhou, W. Huang, L. Chen, C. A. Hewitt and D. L. Carroll, *Nano Energy*, 2016, **26**, 172–179.

636 J. B. Cook, H. S. Kim, T. C. Lin, C. H. Lai, B. Dunn and S. H. Tolbert, *Adv. Energy Mater.*, 2017, **7**, 1601283.

637 J. Xiao, D. Choi, L. Cosimbescu, P. Koech, J. Liu and J. P. Lemmon, *Chem. Mater.*, 2010, **22**, 4522–4524.

638 Q. Wang and J. Li, *J. Phys. Chem. C*, 2007, **111**, 1675–1682.

639 H. Hwang, H. Kim and J. Cho, *Nano Lett.*, 2011, **11**, 4826–4830.

640 K. Chang and W. Chen, *Chem. Commun.*, 2011, **47**, 4252–4254.

641 J. Yao, B. Liu, S. Ozden, J. Wu, S. Yang, M. T. F. Rodrigues, K. Kalaga, P. Dong, P. Xiao, Y. Zhang, R. Vajtai and P. M. Ajayan, *Electrochim. Acta*, 2015, **176**, 103–111.

642 M. Yang, S. Ko, J. S. Im and B. G. Choi, *J. Power Sources*, 2015, **288**, 76–81.

643 Z. Wang, T. Chen, W. Chen, K. Chang, L. Ma, G. Huang, D. Chen and J. Y. Lee, *J. Mater. Chem. A*, 2013, **1**, 2202–2210.

644 X. Zhou, L. J. Wan and Y. G. Guo, *Chem. Commun.*, 2013, **49**, 1838–1840.

645 X. Fang, C. Hua, X. Guo, Y. Hu, Z. Wang, X. Gao, F. Wu, J. Wang and L. Chen, *Electrochim. Acta*, 2012, **81**, 155–160.

646 V. H. Pham, K. H. Kim, D. W. Jung, K. Singh, E. S. Oh and J. S. Chung, *J. Power Sources*, 2013, **244**, 280–286.

647 H. Yamin and E. Peled, *J. Power Sources*, 1983, **9**, 281–287.

648 J. Zhou, J. Qin, X. Zhang, C. Shi, E. Liu, J. Li, N. Zhao and C. He, *ACS Nano*, 2015, **9**, 3837–3848.

649 U. K. Sen, P. Johari, S. Basu, C. Nayak and S. Mitra, *Nanoscale*, 2014, **6**, 10243–10254.

650 L. Wang, Q. Zhang, J. Zhu, X. Duan, Z. Xu, Y. Liu, H. Yang and B. Lu, *Energy Storage Mater.*, 2019, **16**, 37–45.

651 C. Vaalma, D. Buchholz, M. Weil and S. Passerini, *Nat. Rev. Mater.*, 2018, 3, 1–11.

652 S. W. Kim, D. H. Seo, X. Ma, G. Ceder and K. Kang, *Adv. Energy Mater.*, 2012, 2, 710–721.

653 B. Dunn, H. Kamath and J. M. Tarascon, *Science*, 2011, 334, 928–935.

654 V. Palomares, P. Serras, I. Villaluenga, K. B. Hueso, J. Carretero-González and T. Rojo, *Energy Environ. Sci.*, 2012, 5, 5884–5901.

655 H. Pan, Y. S. Hu and L. Chen, *Energy Environ. Sci.*, 2013, 6, 2338–2360.

656 Z. Hu, L. Wang, K. Zhang, J. Wang, F. Cheng, Z. Tao and J. Chen, *Angew. Chemie - Int. Ed.*, 2014, **53**, 12794–12798.

657 S. H. Choi, Y. N. Ko, J. K. Lee and Y. C. Kang, *Adv. Funct. Mater.*, 2015, **25**, 1780–1788.

658 T. Eldridge, *Nanotechnol. Now*, 2014, **25**, 1393–1403.

659 Y. Jiao, A. Mukhopadhyay, Y. Ma, L. Yang, A. M. Hafez and H. Zhu, *Adv. Energy Mater.*, 2018, **8**, 1702779.

660 G. Du, Z. Guo, S. Wang, R. Zeng, Z. Chen and H. Liu, *Chem Commun*, 2010, **46**, 1106–1108.

661 E. Benavente, M. A. Santa Ana, F. Mendizábal and G. González, *Coord. Chem. Rev.*, 2002, **224**, 87–109.

662 Z. Wang, T. Chen, W. Chen, K. Chang, L. Ma, G. Huang, D. Chen and J. Y. Lee, *J. Mater. Chem. A*, 2013, **1**, 2202–2210.

663 L. Yang, S. Wang, J. Mao, J. Deng, Q. Gao, Y. Tang and O. G. Schmidt, *Adv. Mater.*, 2013, **25**, 1180–1184.

664 H. Jiang, D. Ren, H. Wang, Y. Hu, S. Guo, H. Yuan, P. Hu, L. Zhang and C. Li, *Adv. Mater.*, 2015, **27**, 3687–3695.

665 E. Cha, D. K. Kim and W. Choi, *Front. Energy Res.*, 2021, 9.

666 C. D. Quilty, L. M. Housel, D. C. Bock, M. R. Dunkin, L. Wang, D. M. Lutz, A. Abraham, A. M. Bruck, E. S. Takeuchi, K. J. Takeuchi and A. C. Marschilok, *ACS Appl. Energy Mater.*, 2019, **2**, 7635–7646.

667 L. Zhang, D. Sun, J. Kang, J. Feng, H. A. Bechtel, L.-W. Wang, E. J. Cairns and J. Guo, *Nano Lett.*, 2018, **18**, 1466–1475.

668 Y. Li, D. Wu, Z. Zhou, C. R. Cabrera and Z. Chen, *J. Phys. Chem. Lett.*, 2012, **3**, 2221–2227.

669 W. Choi, N. Choudhary, G. H. Han, J. Park, D. Akinwande and Y. H. Lee, *Mater. Today*, 2017, **20**, 116–130.

670 X. Sun and Z. Wang, *Beilstein J. Nanotechnol. 8270*, 2017, **8**, 2711–2718.

671 E. Cha, M. D. Patel, J. Park, J. Hwang, V. Prasad, K. Cho and W. Choi, *Nat. Nanotechnol.*, 2018, **13**, 337–343.

672 C. Sun, K. Zhao, Y. He, J. Zheng, W. Xu, C. Zhang, X. Wang, M. Guo, L. Mai, C. Wang and M. Gu, *ACS Appl. Mater. Interfaces*, 2019, **11**, 20762–20769.

673 R. F. Egerton, *Ultramicroscopy*, 2007, **107**, 575–586.

674 L. Jones, *IOP Conf. Ser. Mater. Sci. Eng.*, 2016, **109**, 012008.

675 J. Song, C. S. Allen, S. Gao, C. Huang, H. Sawada, X. Pan, J. Warner, P. Wang and A. I. Kirkland, *Sci. Rep.*, 2019, **9**, 1–8.

676 H. Yang, I. MacLaren, L. Jones, G. T. Martinez, M. Simson, M. Huth, H. Ryll, H. Soltau, R.

Sagawa, Y. Kondo, C. Ophus, P. Ercius, L. Jin, A. Kovács and P. D. Nellist, *Ultramicroscopy*, 2017, **180**, 173–179.

677 W. Haselrieder, S. Ivanov, D. K. Christen, H. Bockholt and A. Kwade, *ECS Trans.*, 2013, **50**, 59–70.

678 E. N. Primo, M. Chouchane, M. Touzin, P. Vazquez and A. A. Franco, *J. Power Sources*, 2021, **488**, 229361.

679 R. Sim, S. Lee, W. Li and A. Manthiram, *ACS Appl. Mater. Interfaces*, 2021, **13**, 42898–42908.

680 T. Eldridge, *Nanotechnol. Now*, 2014, **11**, 473–481.

681 Y. X. Wang, S. L. Chou, D. Wexler, H. K. Liu and S. X. Dou, *Chem. – A Eur. J.*, 2014, **20**, 9607–9612.

682 Q. Li, Z. Yao, J. Wu, S. Mitra, S. Hao, T. S. Sahu, Y. Li, C. Wolverton and V. P. Dravid, *Nano Energy*, 2017, **38**, 342–349.

683 T. Eldridge, *Nanotechnol. Now*, 2014, **38**, 342–349.

684 T. Eldridge, *Nanotechnol. Now*, 2014, **11**, 473–481.

685 H. Mou, W. Xiao, C. Miao, R. Li and L. Yu, *Front. Chem.*, 2020, **8**, 141.

686 R. A. Gardner, *J. Solid State Chem.*, 1974, **9**, 336–344.

687 B.-S. Kim, J. Lee, H.-S. Yoon and S.-K. Kim, *Mater. Trans.*, 2011, **52**, 1814–1817.

688 Y. Wang, J. Y. Lee and T. C. Deivaraj, *J. Electrochem. Soc.*, 2004, **151**, A1804.

689 K. T. Lee, Y. S. Jung and S. M. Oh, *J. Am. Chem. Soc.*, 2003, **125**, 5652–5653.

690 H. X. Zhang, C. Feng, Y. C. Zhai, K. L. Jiang, Q. Q. Li and S. S. Fan, *Adv. Mater.*, 2009, **21**, 2299–2304.

691 C. Kim, M. Noh, M. Choi, J. Cho and B. Park, *Chem. Mater.*, 2005, **17**, 3297–3301.

692 J. R. Dahn, R. E. Mar and A. Abouzeid, *J. Electrochem. Soc.*, 2005, **153**, A361.

693 T. Xiang, Q. Fang, H. Xie, C. Wu, C. Wang, Y. Zhou, D. Liu, S. Chen, A. Khalil, S. Tao, Q. Liu and L. Song, *Nanoscale*, 2017, **9**, 6975–6983.

694 M. Wu, J. Zhan, K. Wu, Z. Li, L. Wang, B. Geng, L. Wang and D. Pan, *J. Mater. Chem. A*, 2017, **5**, 14061–14069.

695 Z. Li, X. Zhan, W. Zhu, S. Qi and P. V. Braun, *ACS Appl. Mater. Interfaces*, 2019, **11**, 44593–44600.

696 Y. Jiao, A. Mukhopadhyay, Y. Ma, L. Yang, A. M. Hafez and H. Zhu, *Adv. Energy Mater.*, 2018, **8**, 1702779.

697 X. Geng, Y. Jiao, Y. Han, A. Mukhopadhyay, L. Yang and H. Zhu, *Adv. Funct. Mater.*, 2017, **27**, 1702998.

698 J. Wu, J. Liu, J. Cui, S. Yao, M. Ihsan-Ul-Haq, N. Mubarak, E. Quattrocchi, F. Ciucci and J.

K. Kim, *J. Mater. Chem. A*, 2020, **8**, 2114–2122.

699 Q. Pan, Q. Zhang, F. Zheng, Y. Liu, Y. Li, X. Ou, X. Xiong, C. Yang and M. Liu, *ACS Nano*, 2018, **12**, 12578–12586.

Appendix

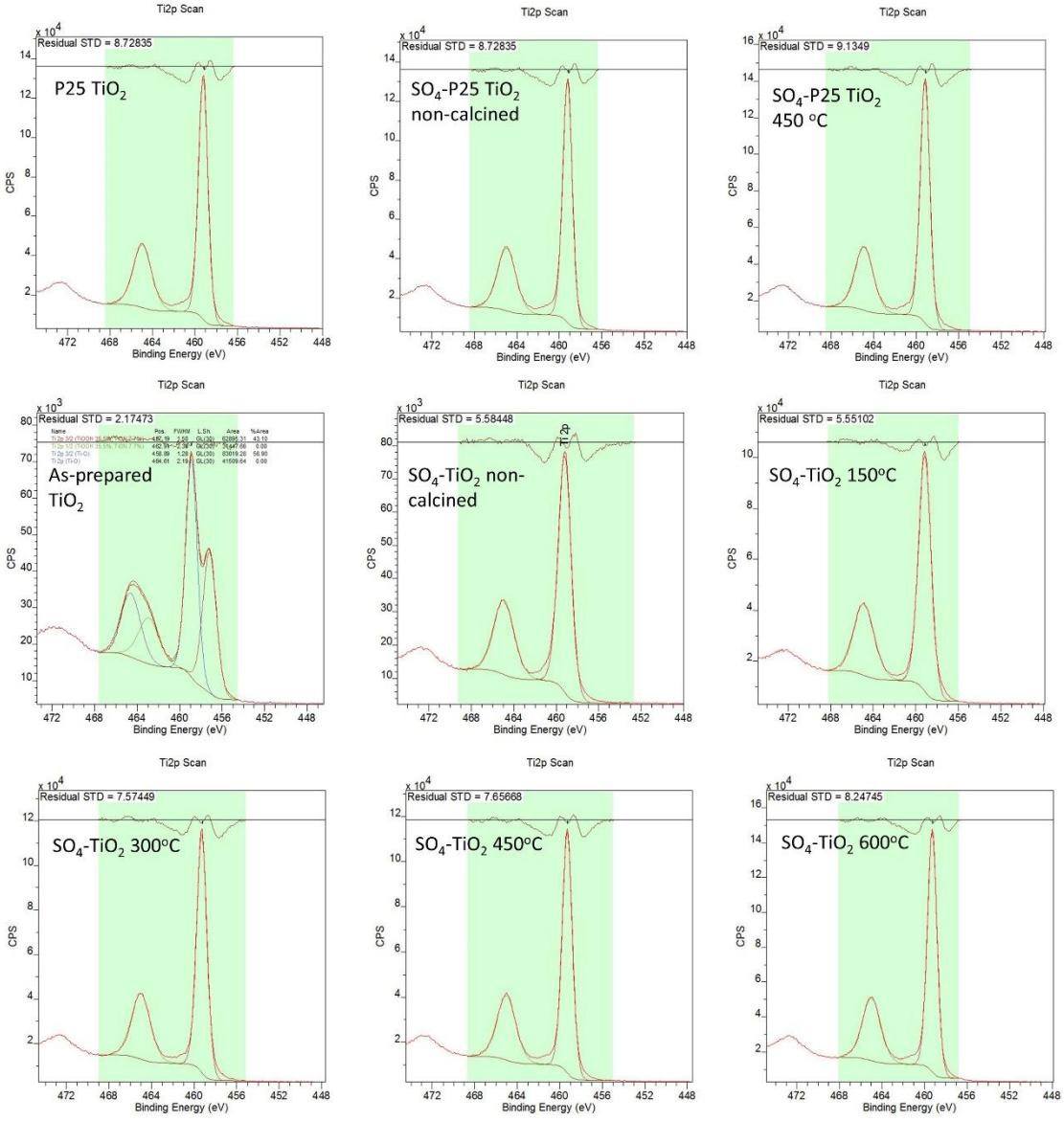


Figure A4.1. Deconvoluted Ti 2p XPS spectra of titania catalysts

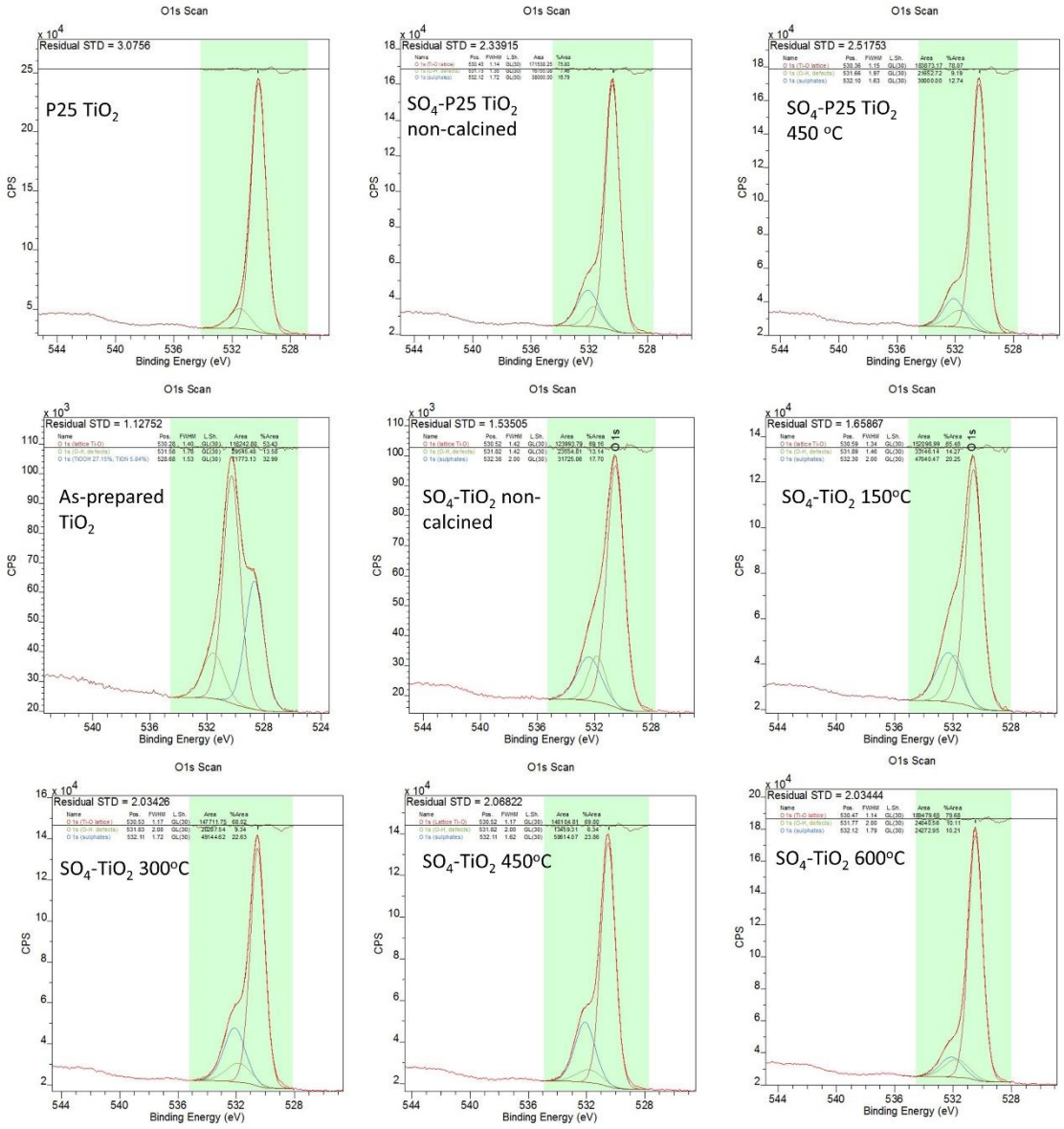


Figure A4.2. Deconvoluted O 1s XPS spectra of titania catalysts

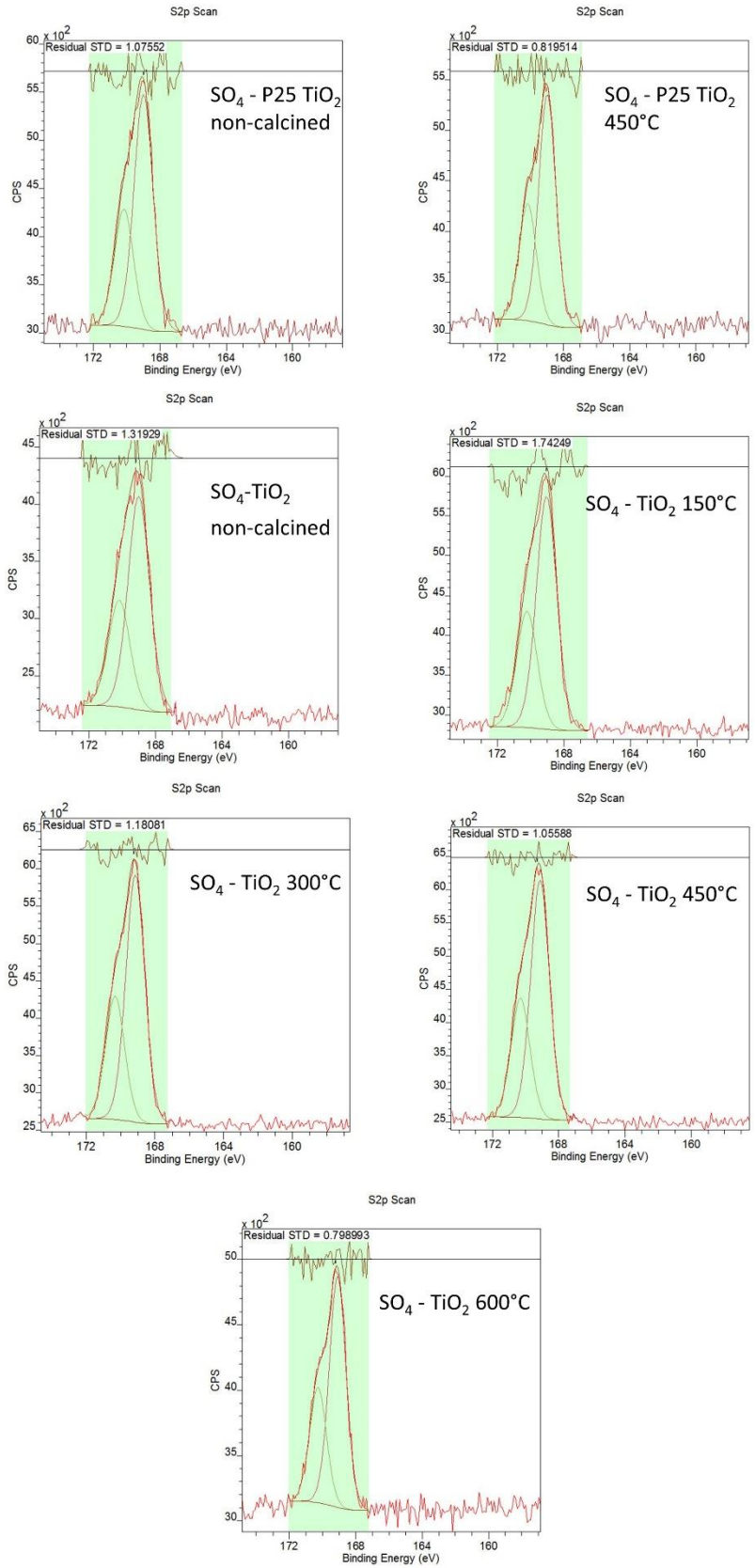


Figure A4.3. Deconvoluted S 2p XPS spectra of titania catalysts

To investigate the reduction temperature of the palladium species deposited on the surface of MoS_2 material, temperature programmed reduction was employed using hydrogen flow as a reducing agent. Palladium is also known as a hydrogen scavenger that couples with hydrogen to produce an alloy of palladium with hydrogen called palladium hydride - PdH_x, a metallic version of palladium that contains metallic hydrogen within its crystal lattice. This property makes Pd metal nanoparticles a highly desirable candidate for hydrogenation reactions.

Figure A5.1. shows TPR profiles of Pd-doped bulk and Pd-doped single-layer MoS_2 samples. It is important to note that both samples were not dried enough before they were subjected to the characterisation process. This is obvious in the first negative hydrogen consumption peak as water molecules are released from the sample around 100°C. Interestingly, there is no obvious hydrogen consumption peak in the bulk MoS_2 sample despite ICP-AES analysis confirmed the presence of Pd (Table A5.1). Observation of a small and very broad flat peak with maximum around 300°C can be ascribed to slow and steady uptake of hydrogen to form palladium hydride within Pd^0 deposited on bulk MoS_2. Unlike Pd-doped bulk MoS_2, TPR profile of Pd-doped single-layer MoS_2 shows two distinct peaks in hydrogen consumption. The first appear at 120°C and can be ascribed to the reduction of highly dispersed PdO (although $NaBH_4$ was used to reduce Pd^{2+} to Pd^0 during the preparation of Pd-doped MoS_2 nanosheets, the samples were not kept under inert condition; therefore, small amount of surface oxidation is expected), while second peak with maximum at 300°C represents the temperature at which hydrogen uptake to PdH_x is most efficient, but also is generally required temperature threshold for reducing any remaining positively charged palladium species. Therefore, calcination temperature for Pd-doped MoS_2 samples was decided to be set at 300°C for 2 hours under continuous flow of 5 % hydrogen gas in argon.

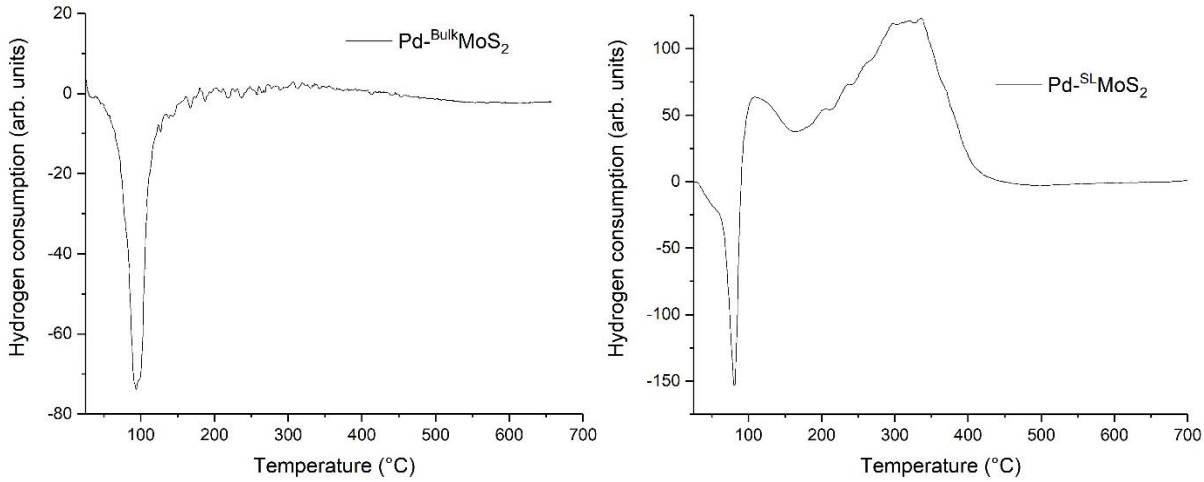
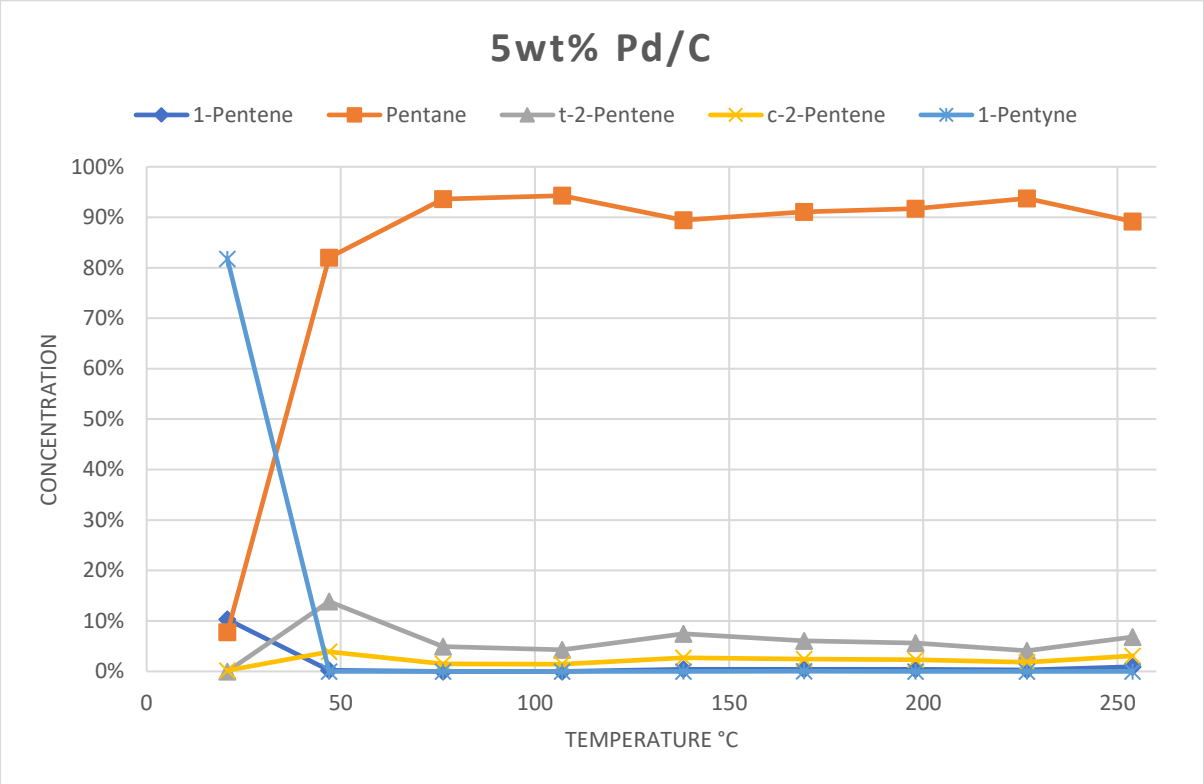


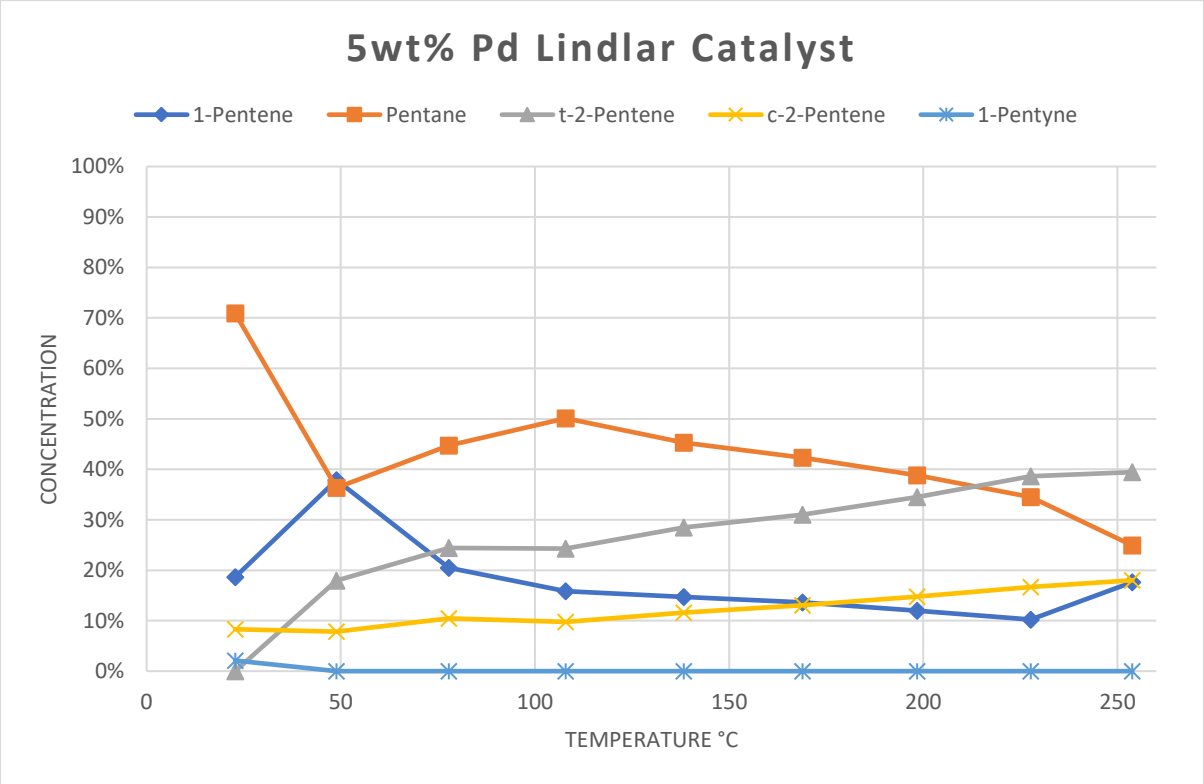
Figure A5.1. Temperature-programmed reduction (TPR) of Pd-doped bulk and single-layer MoS_2.

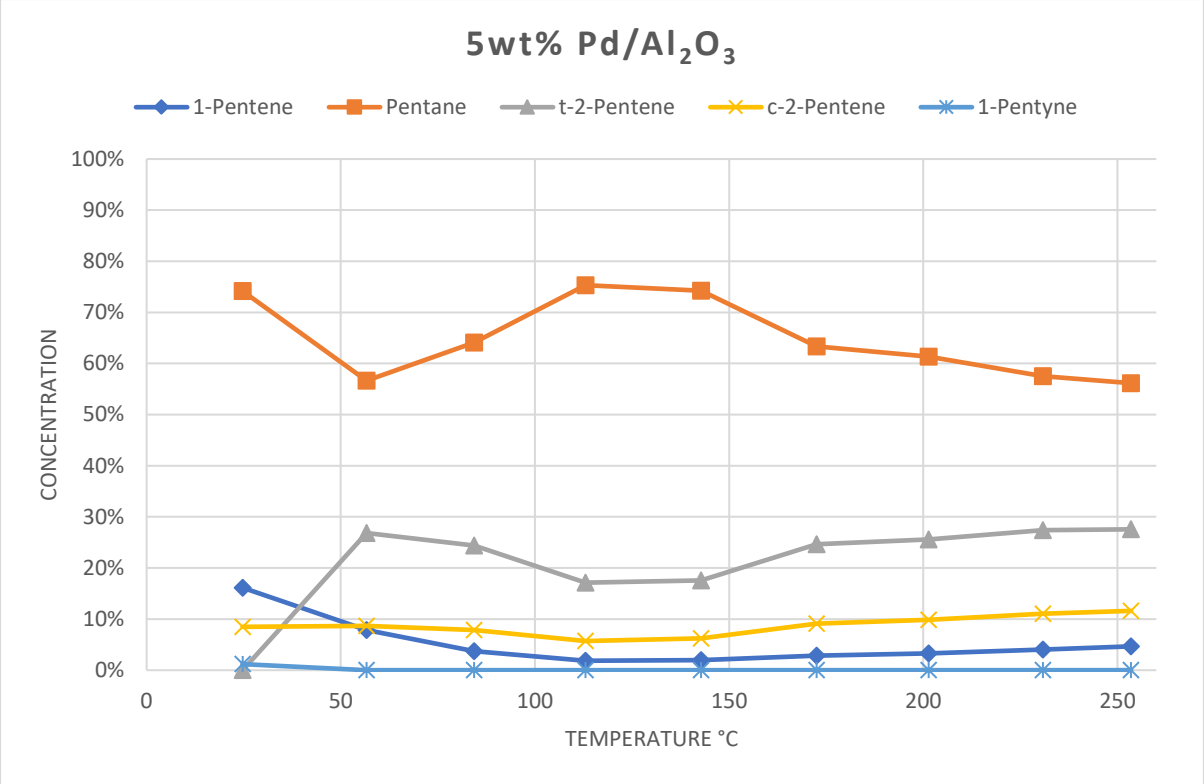
Table A5.1. ICP-AES results of Pd-doped bulk and single-layer MoS_2

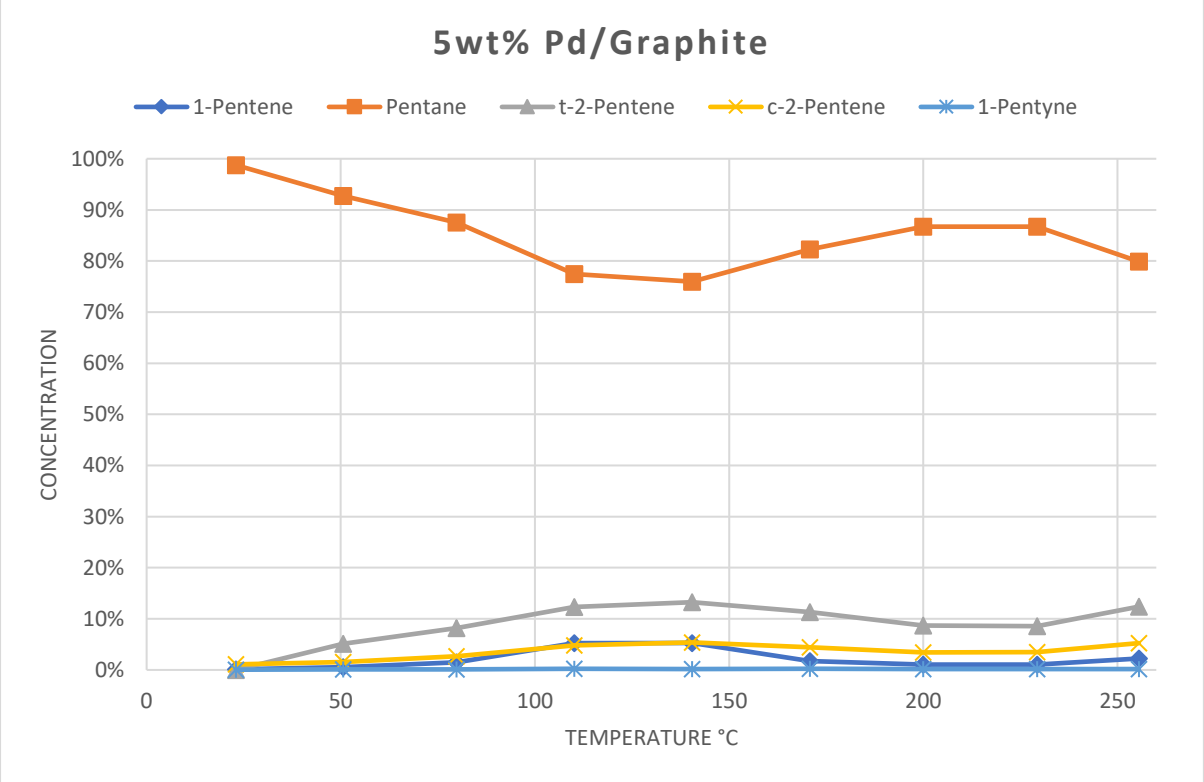
Sample Name	**%Mo**	**%S**	**%Pd**
Pd $^{Bulk}MoS_2$	30.8	22.6	30.2
Pd $^{SL}MoS_2$	45.1	29.4	25.3

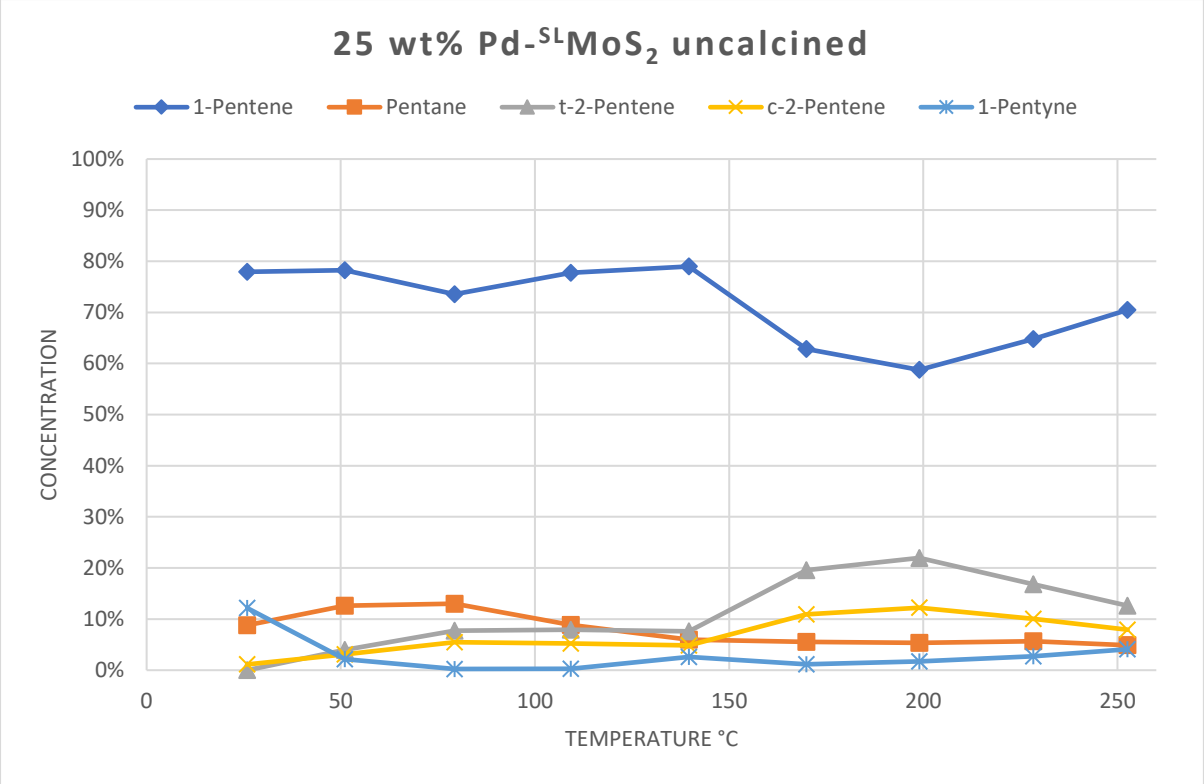
Figure A5.2. Rates of conversion and products of hydrogenation of 1-pentyne in 40 % H_2/He using Pd-based catalysts at different temperatures.

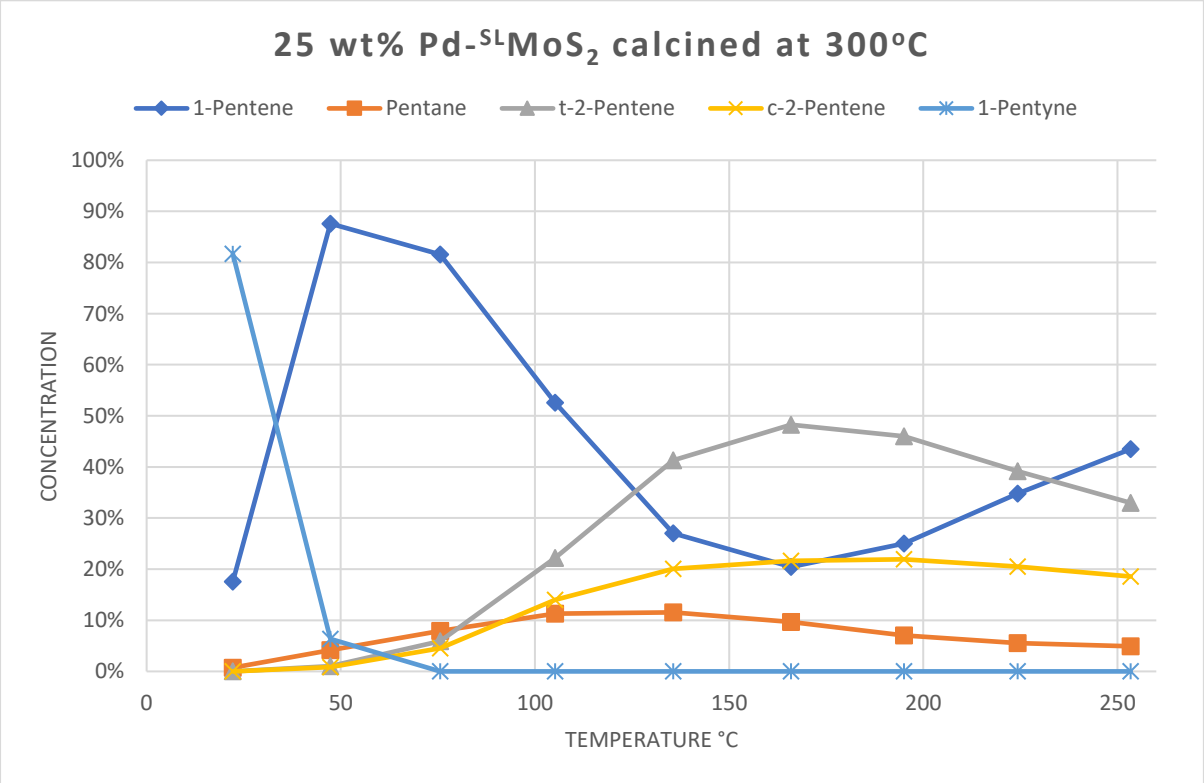


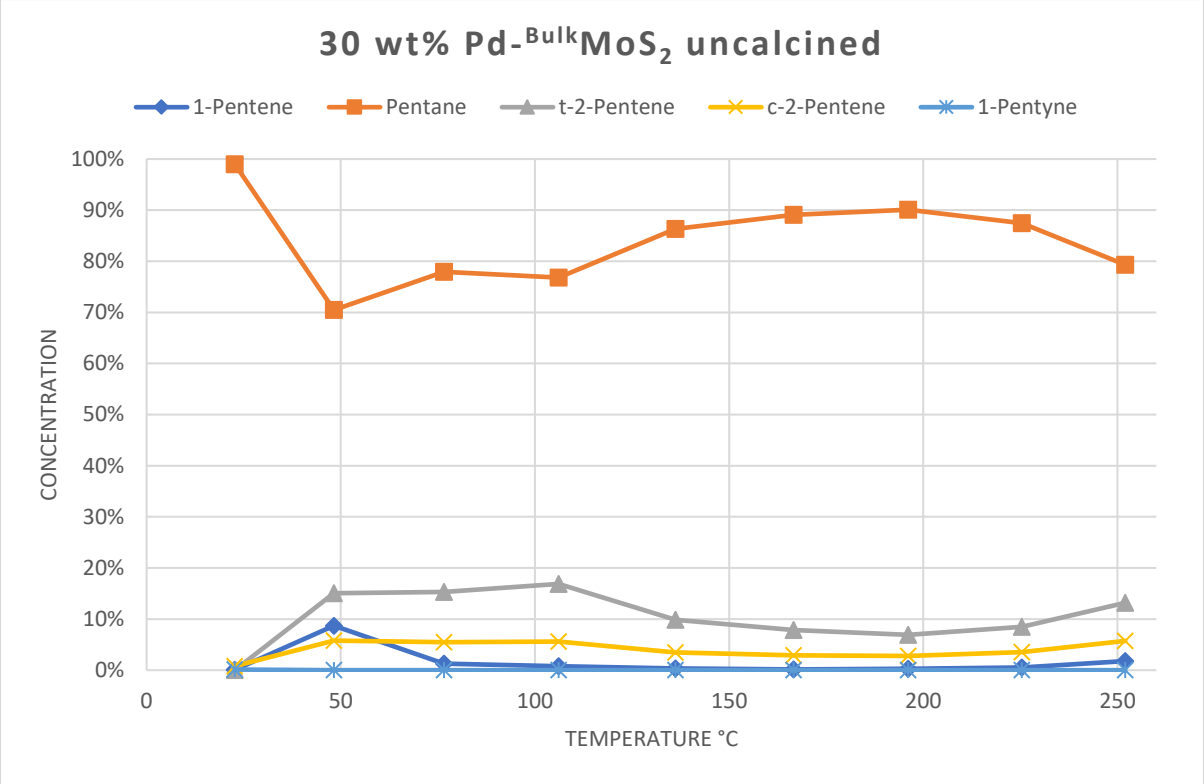


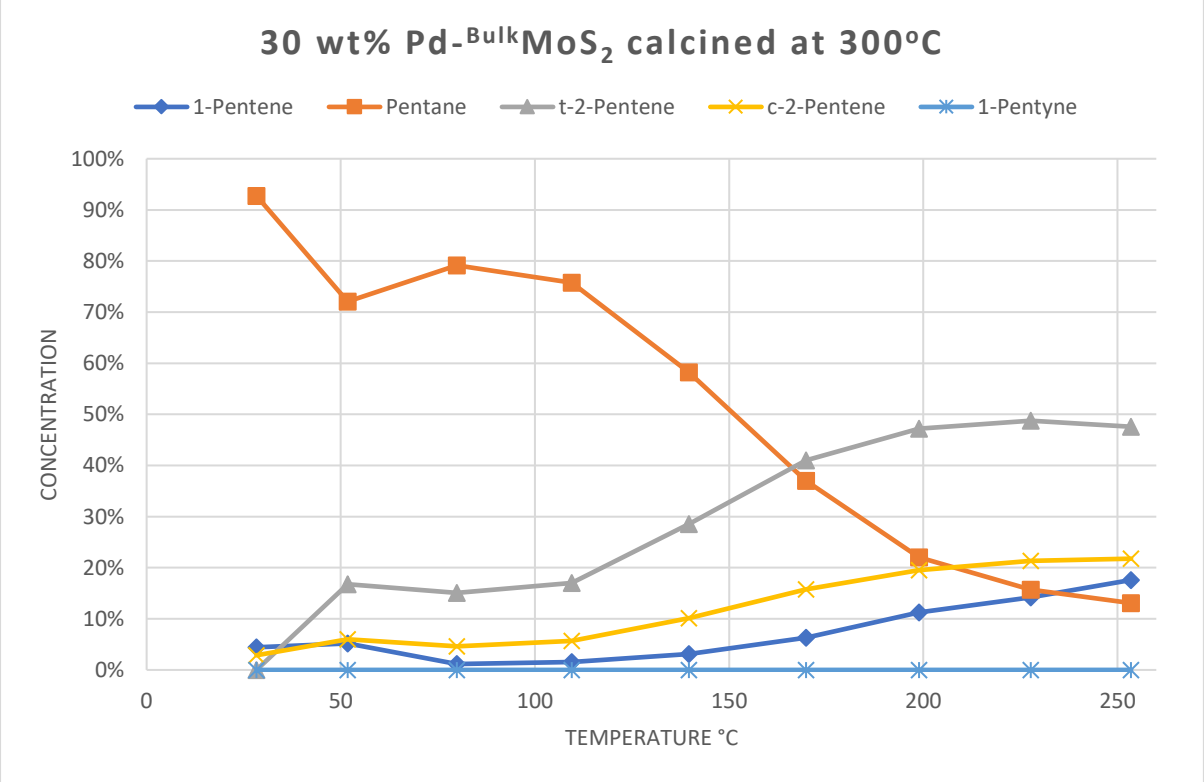

5wt% Pd/Al2O3
1-Pentene
Pentane
t-2-Pentene
c-2-Pentene
1-Pentyne
100%
90%
80%
70%
60%
50%
40%
30%
20%
10%
0%
CONCENTRATION
0
50
100
150
200
250
TEMPERATURE °C

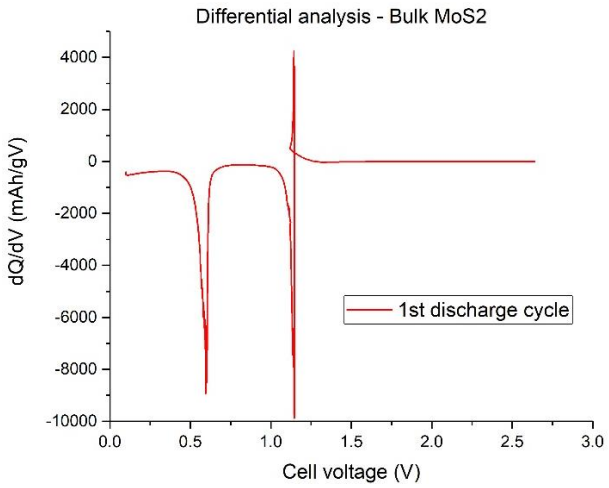

5wt% Pd/Graphite
1-Pentene
Pentane
t-2-Pentene
c-2-Pentene
1-Pentyne
100%
90%
80%
70%
60%
50%
40%
30%
20%
10%
0%
CONCENTRATION
0
50
100
150
200
250
TEMPERATURE °C

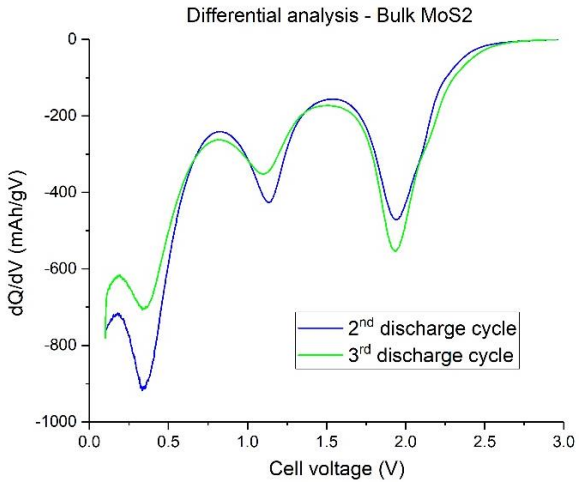

25 wt% Pd-SLMoS2 uncalcined
1-Pentene
Pentane
t-2-Pentene
c-2-Pentene
1-Pentyne
100%
90%
80%
70%
60%
50%
40%
30%
20%
10%
0%
CONCENTRATION
0
50
100
150
200
250
TEMPERATURE °C

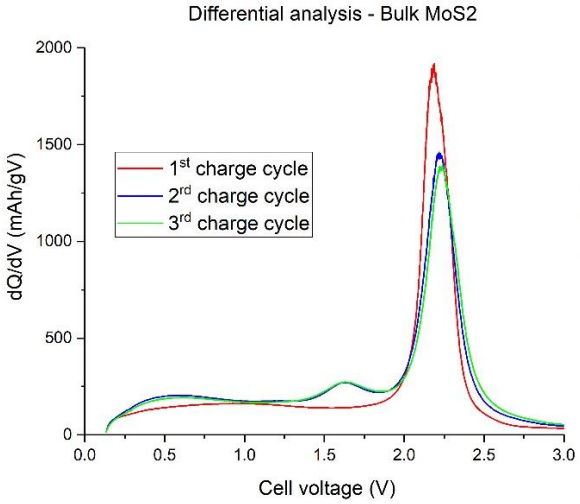

25 wt% Pd-SLMoS2 calcined at 300°C
1-Pentene
Pentane
t-2-Pentene
c-2-Pentene
1-Pentyne
100%
90%
80%
70%
60%
50%
40%
30%
20%
10%
0%
CONCENTRATION
0
50
100
150
200
250
TEMPERATURE °C

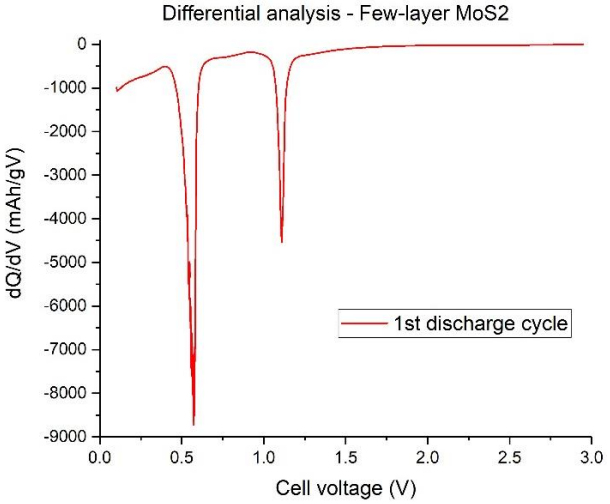

30 wt% Pd-BulkMoS2 uncalcined
1-Pentene
Pentane
t-2-Pentene
c-2-Pentene
1-Pentyne
100%
90%
80%
70%
60%
50%
40%
30%
20%
10%
0%
CONCENTRATION
0
50
100
150
200
250
TEMPERATURE °C

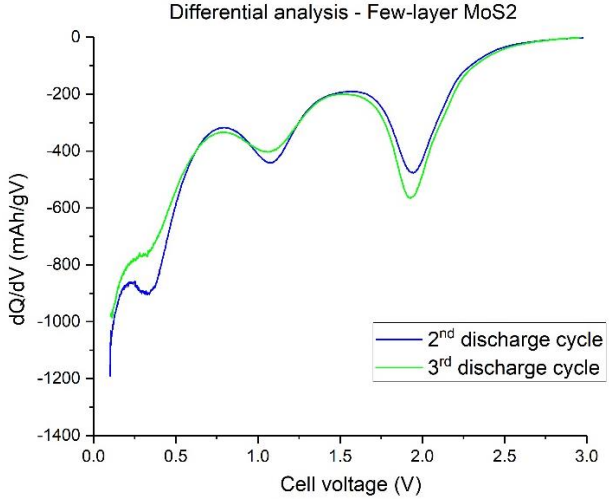

30 wt% Pd-BulkMoS2 calcined at 300°C
1-Pentene
Pentane
t-2-Pentene
c-2-Pentene
1-Pentyne
100%
90%
80%
70%
60%
50%
40%
30%
20%
10%
0%
CONCENTRATION
0
50
100
150
200
250
TEMPERATURE °C

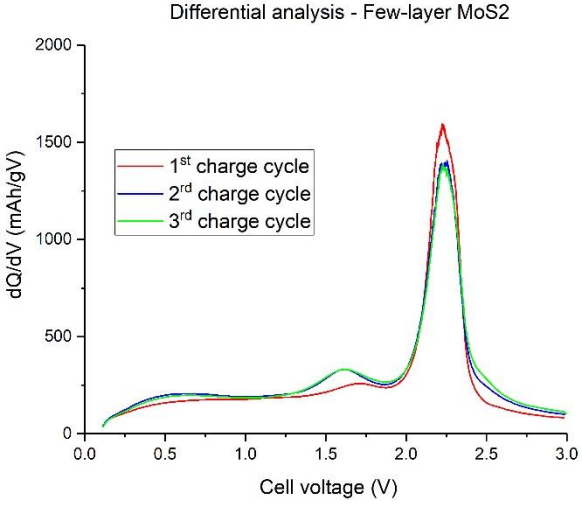

Differential analysis - Bulk MoS2
dQ/dV (mAh/gV)
Cell voltage (V)
1st discharge cycle


Differential analysis - Bulk MoS2
dQ/dV (mAh/gV)
Cell voltage (V)
2nd discharge cycle
3rd discharge cycle


Differential analysis - Bulk MoS2
dQ/dV (mAh/gV)
Cell voltage (V)
1st charge cycle
2rd charge cycle
3rd charge cycle


Differential analysis - Few-layer MoS2
dQ/dV (mAh/gV)
Cell voltage (V)
1st discharge cycle


Differential analysis - Few-layer MoS2
dQ/dV (mAh/gV)
Cell voltage (V)
2nd discharge cycle
3rd discharge cycle


Differential analysis - Few-layer MoS2
dQ/dV (mAh/gV)
Cell voltage (V)
1st charge cycle
2rd charge cycle
3rd charge cycle

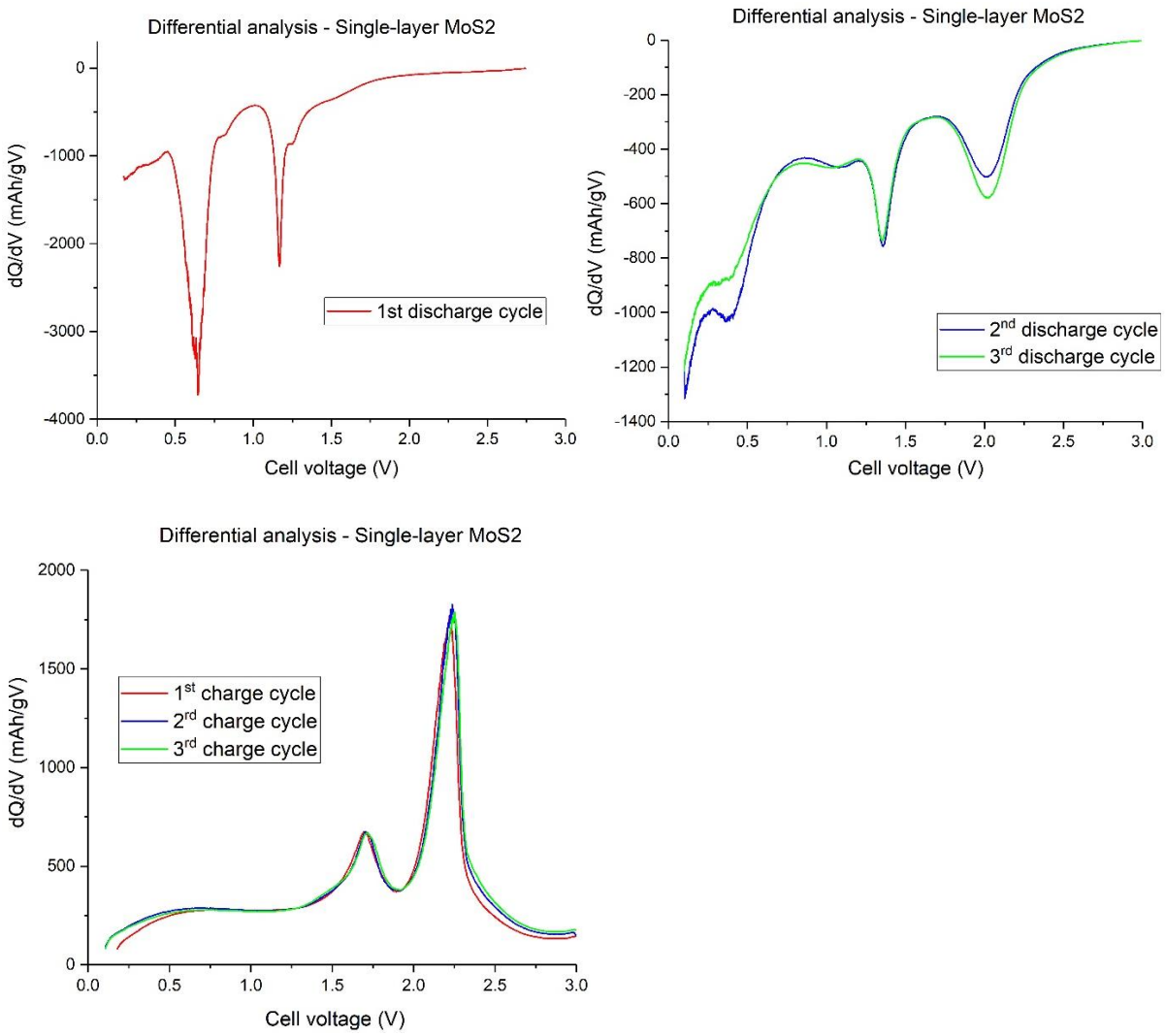


Figure A6.1. Differential analysis of first three charge-discharge cycles at 50 mA/g applied current for bulk, few-layer and single-layer MoS_2 electrodes in Li-ion cells.

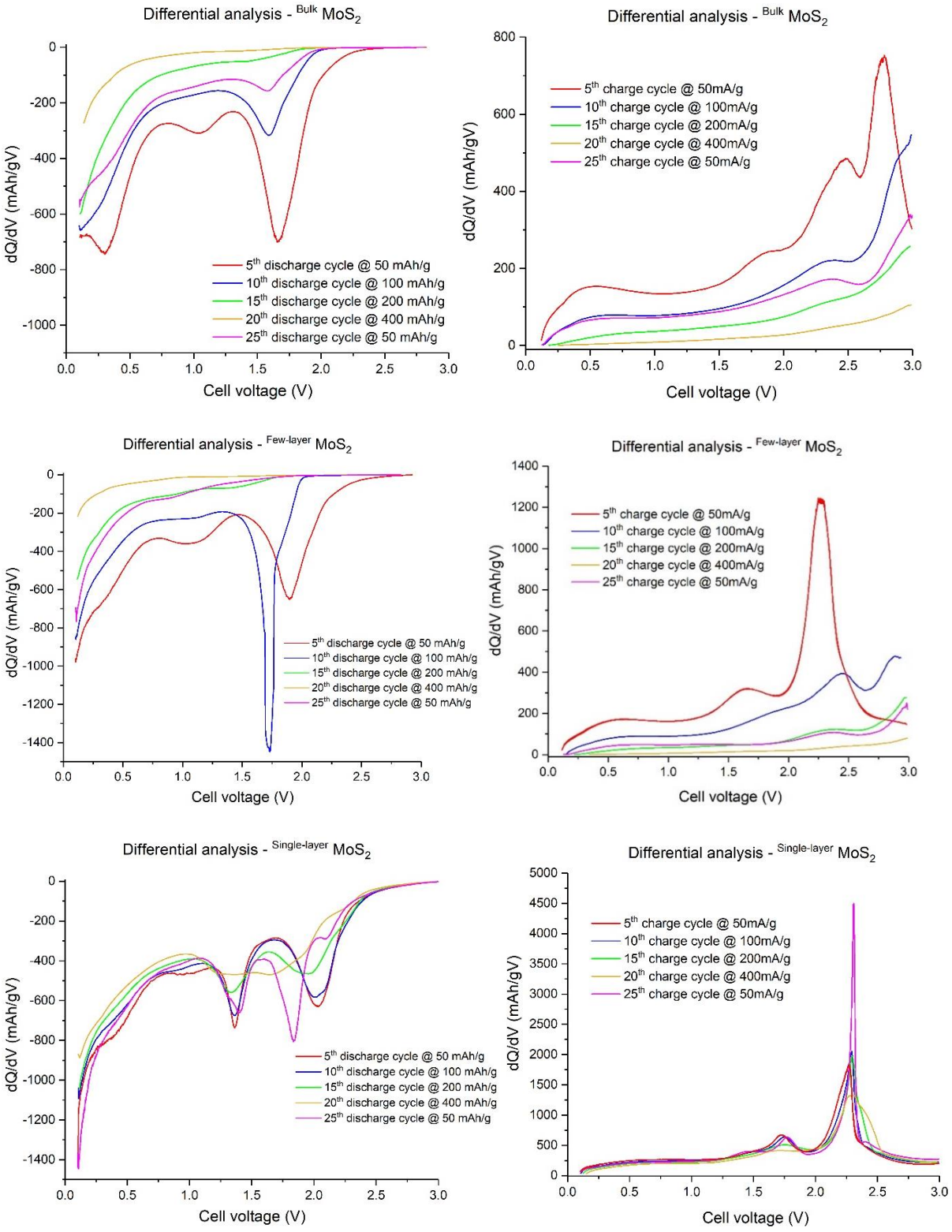
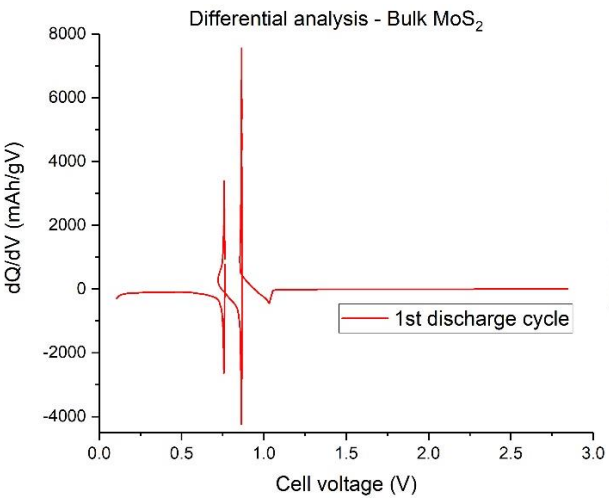
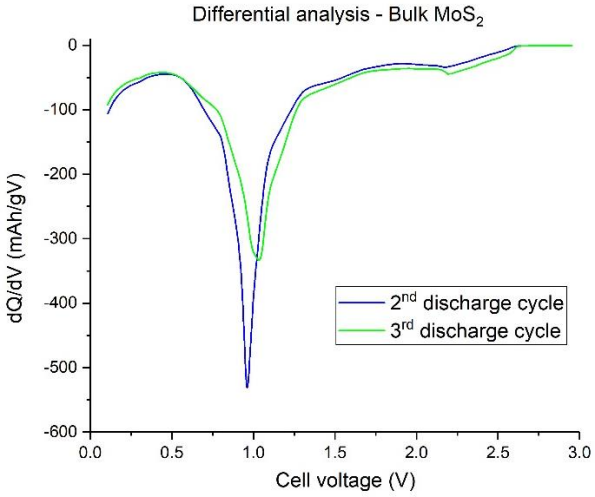
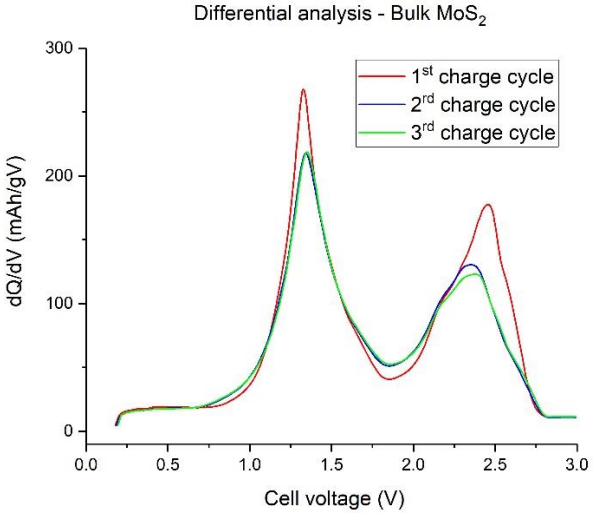
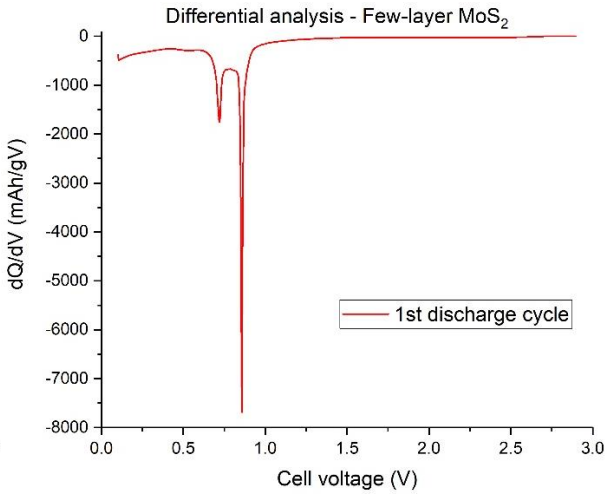


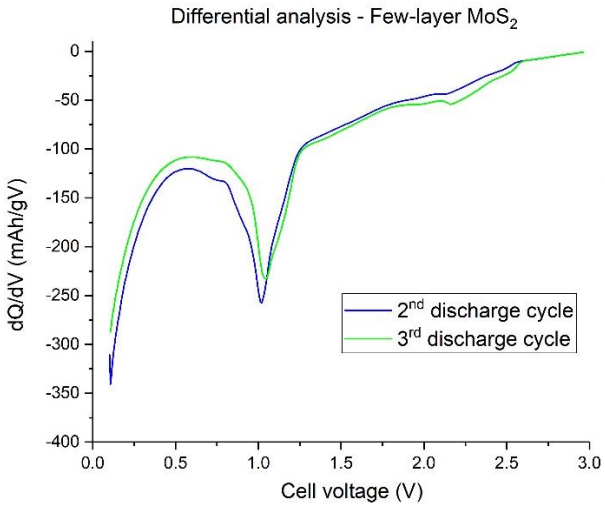
Figure A6.2. Differential analysis of fifth charge-discharge cycle per each applied current for bulk, few-layer and single-layer MoS_2 electrodes in Li-ion cells.

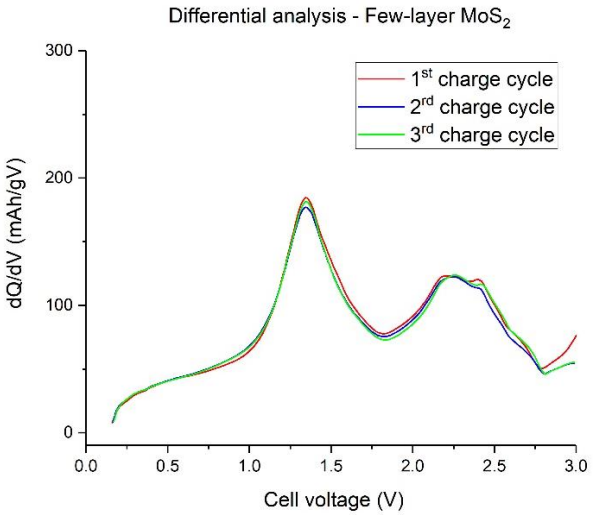

Differential analysis - Bulk MoS2
dQ/dV (mAh/gV)
Cell voltage (V)
1st discharge cycle


Differential analysis - Bulk MoS2
dQ/dV (mAh/gV)
Cell voltage (V)
2nd discharge cycle
3rd discharge cycle


Differential analysis - Bulk MoS2
dQ/dV (mAh/gV)
Cell voltage (V)
1st charge cycle
2rd charge cycle
3rd charge cycle


Differential analysis - Few-layer MoS2
dQ/dV (mAh/gV)
Cell voltage (V)
1st discharge cycle


Differential analysis - Few-layer MoS2
dQ/dV (mAh/gV)
Cell voltage (V)
2nd discharge cycle
3rd discharge cycle


Differential analysis - Few-layer MoS2
dQ/dV (mAh/gV)
Cell voltage (V)
1st charge cycle
2rd charge cycle
3rd charge cycle

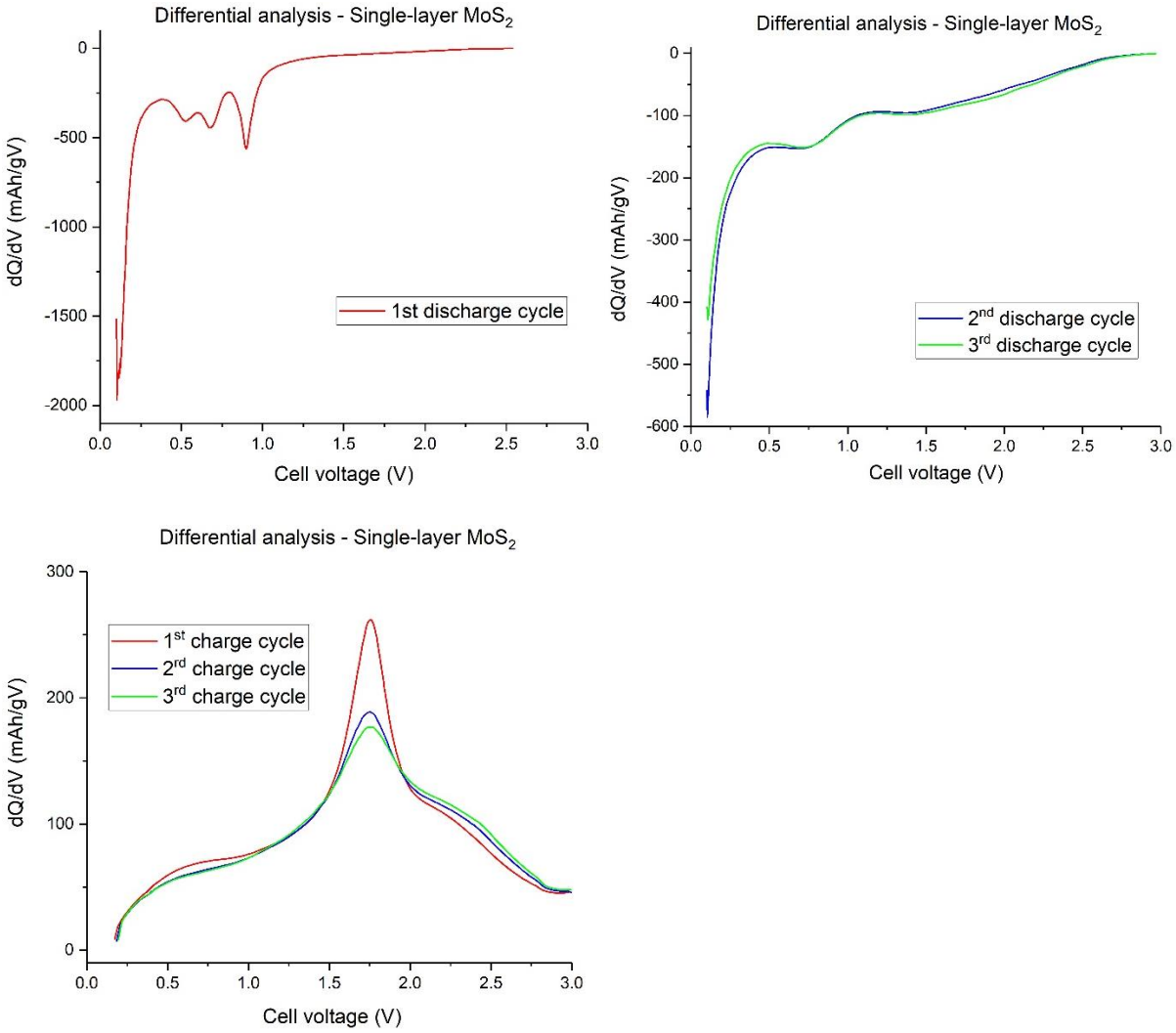


Figure A6.3. Differential analysis of first three charge-discharge cycles at 50 mA/g applied current for bulk, few-layer and single-layer MoS_2 electrodes in Na-ion cells.

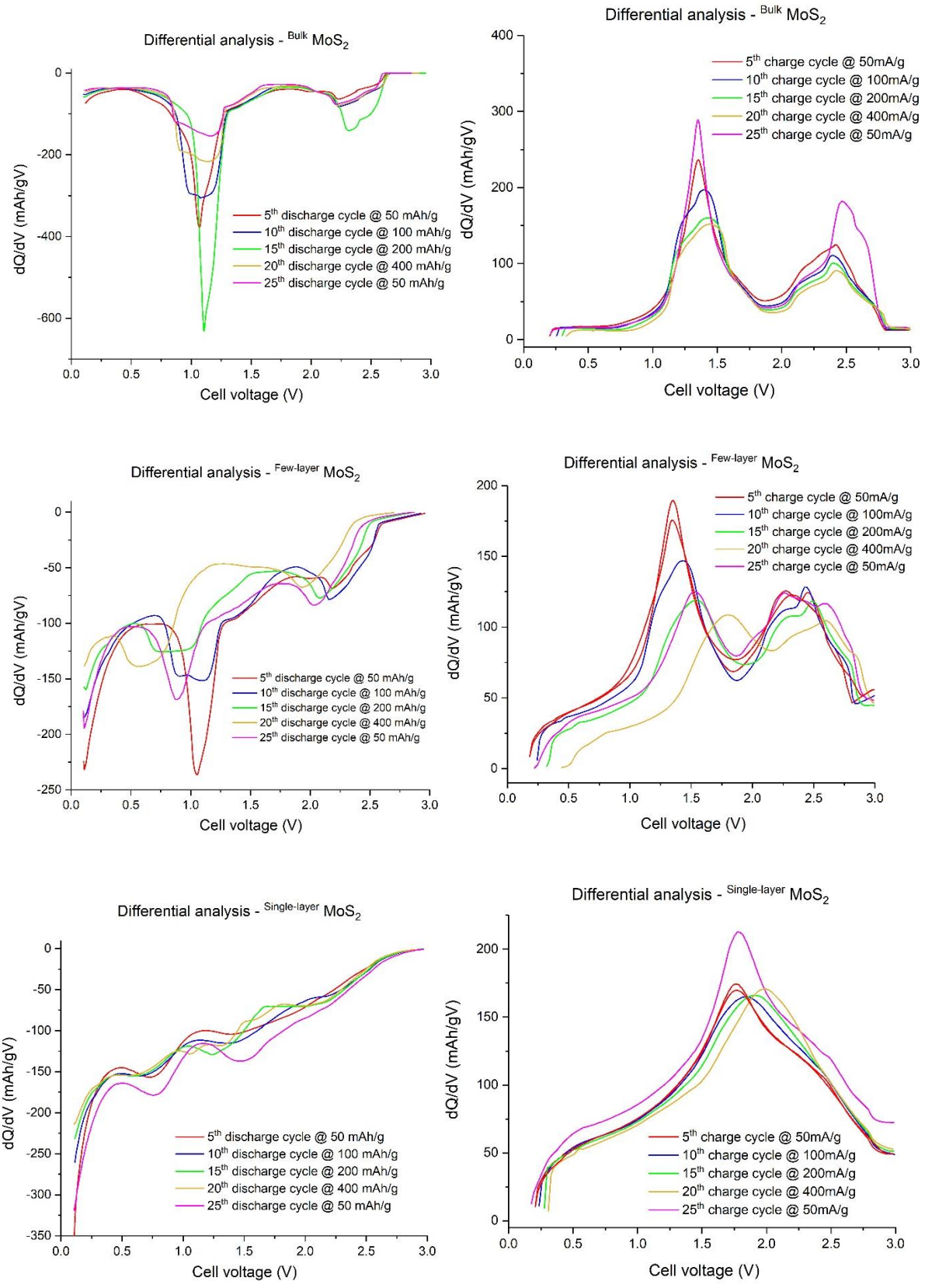


Figure A6.4. Differential analysis of fifth charge-discharge cycle per each applied current for bulk, few-layer and single-layer MoS_2 electrodes in Na-ion cells.

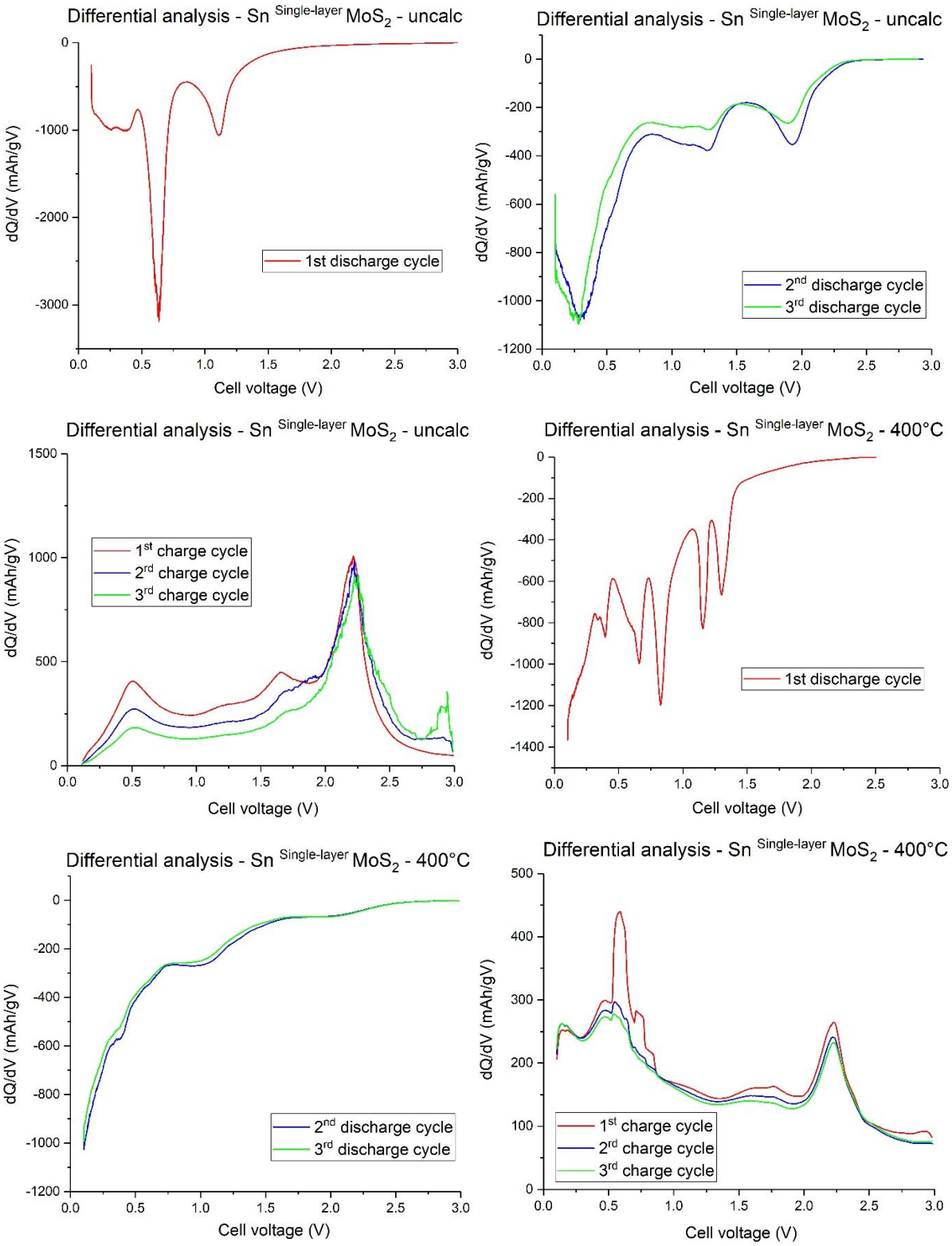


Figure A6.5. Differential analysis of the first three charge-discharge cycles at 50 mA/g applied current for Sn-doped single-layer MoS_2 electrodes in Li-ion cells.